Cool Stars in the Galaxy – A ROSAT and ASCA View.

John E. Morley

Thesis submitted to the University of Leicester
for the degree of Doctor of Philosophy

March 1999
~~November 1998~~

X-Ray Astronomy Group
Department of Physics and Astronomy
University of Leicester

ProQuest LLC
789 East Eisenhower Parkway
P.O. Box 1346
Ann Arbor, MI 48106-1346

Declaration

I hereby declare that no part of this thesis has been previously submitted to this or any other University as part of the requirement for a higher degree. The work described herein was conducted by the undersigned except for contributions from colleagues as acknowledged in the text.

John E. Morley,
November 1998

"We are all in the gutter, but some of us are looking at the stars"

Oscar Wilde.

Publications

Morley J.E., Pye J.E., Warwick R.S., Pilkington J., 1996, 'Rontgenstrahlung from the Universe' Proc. Wurzburg conference. "On the Galactic Plane: A Deep ROSAT Survey in the Third Quadrant 180 <l<280"

Morley J.E., Pye J.P., McGale P.A., Hodgkin S.T., Barstow M.A., Makashima K., 1996, accepted Conference Proceedings of the 9th Cambridge Cool Stars Workshop. "A ROSAT and ASCA View of VW Cep."

Pye J.P., McGale P.A., Morley J.E.,Hodgkin S.T., Barstow M.A., Makashima K., 1996, accepted Conference Proceedings of the 9th Cambridge Cool Stars Workshop. "ROSAT and ASCA Spectral Surveys of W UMa-type Contact Binaries"

Dedicated, with love, to my family, without whom questions on the fundamental nature of the Universe wouldn't really have meant much. Thank You.

Cool Stars in the Galaxy – A ROSAT and ASCA View.

John E. Morley

ABSTRACT

This thesis describes work undertaken using data from the ROSAT and ASCA missions, in order to study the coronal x-ray emission of cool, late type stars. Chapters 1 and 2 summarise the emission processes involved and the methods by which the x-rays are detected and analysed, including a discussion of the ROSAT and ASCA missions.

Chapter 3 details a deep soft x-ray survey of the Galactic Plane using the ROSAT Position Sensitive Proportional Counter. The data consist of 9 fields, each of $\approx$ 10ks exposure, pointed at positions on or very close to the plane. Presented are the source list, number-flux relation and the x-ray to optical flux ratios. I present the results of source count modelling which suggest $\approx$ 50% stellar and $\approx$ 8% extra-galactic contributions. The nature of the unidentified population is discussed.

Chapter 4 discusses the temporal variability of the x-ray emission of stars in the Hyades cluster. The data consist of 13 PSPC fields, each of $\approx$20ks exposure, targeted in the central regions of the cluster. Little evidence is present to suggest long term variability, though 14 do exhibit short term variability. Time resolved spectra of detected flares are presented. Flare modelling results suggest flare loop heights of $\approx$ 1—2 solar radii.

Chapters 5 details observations, obtained using the ASCA satellite, of 3 sources, VW Cep, SW Lac and 44i Boo. These observations form part of an ongoing survey of W UMa systems. Spectral and temporal results are compared to a previous ROSAT survey. I show that the observed systems have a high temperature component comparable with that seen in RS CVn and BY Dra systems. I also provide evidence for non-solar metal abundances in these systems.

Finally in Chapter 6 I summarise this work and discuss the future of x-ray astronomy in the field of cool stars.

Contents

Chapter 1

Introduction

1.1 Solar-Stellar X-ray Astronomy

During the 1960's and 70's rocket-based observations (Vaiana *et al.* 1968) and high resolution instruments on Skylab (Reeves 1976, Vaiana *et al.* 1973) showed the solar corona to be composed of complex loop structures associated with underlying photospheric and chromospheric features, in particular magnetic field structures.

Also in the 1970's, the detection of X-ray quiescent and flaring emission from late-type stars opened up stellar activity as a viable field of study. This led to the discovery that stars of nearly all spectral types are surrounded by tenuous, high temperature ($T \approx 10^6$—10^7K) coronae, emitting most of their radiation in the soft X-ray band. Since then solar and stellar observations have been used in conjunction, the high detail available in solar measurements allowing a close-up view of the physical phenomena and the stellar observations effectively providing a method of 'varying' solar parameters. This has allowed the evolution of stellar activity to be studied in terms of mass and age.

1.2 The Sun as a Star

This thesis deals mainly with emission from stellar sources, however an understanding of the solar corona is useful when considering the stellar equivalents. Figure 1.1 shows a soft X-ray image of the solar corona obtained using the Japanese Yohkoh satellite. The bright regions are active (emit in the X-ray band) whilst the dark regions are much less so. The large dark polar regions are coronal holes, regions which when compared to their surroundings have lower temperatures (10^6K cf $\approx 3\times10^6$K) and densities (by a factor of >3). Also clearly visible are loop structures on the solar surface.

Most of the solar coronal X-ray emission comes from many topologically closed magnetic structures (loops). These structures arise from the coupling of differential rotation and convection with existing magnetic fields, forming a regenerative magnetic dynamo. Flux tubes are created which rise to the surface and form loops. Golub *et al.* (1981) derived a scaling law relating magnetic field (B) to loop pressure (p) and length (L); $p \propto B^{2/7}L^{-1/7}$. The basic loop model is that of a one dimensional mini-atmosphere, where the energy input is redistributed by thermal conduction and lost by radiation. A stable loop structure results from heating which causes the loop to fill with chromospheric material which maintains a balance between energy gains and losses (Rosner *et al.* 1978, Withbroe 1981).

This still leaves the question of how the corona is heated. Dissipation of electric currents from closed field lines, micro-flaring and magneto-hydrodynamic waves are all potential heating mechanisms. As yet there is no agreement as to the actual mechanisms responsible. Polar regions with open magnetic field lines have a much lower X-ray flux than areas with closed field lines (Maxson and Vaiana 1977) and it is from these regions that the high speed solar wind arises. It is possible that in these regions atmospheric heating by acoustic shock waves occurs (Ulmschneider 1991). Indeed it is likely that there is a basal level of acoustic heating in all regions and stars (Schmitt 1996).

The Sun may be used as a point of comparison with other stars of similar structure. However it should be noted that in the earliest X-ray surveys the Sun was found to be near the lower end of the observed range of X-ray luminosities for late-type stars[1].

[1]For the Sun $L_x \sim 10^{27}$ erg s^{-1}, whereas the observed stellar maximum X-ray luminosity is in the region

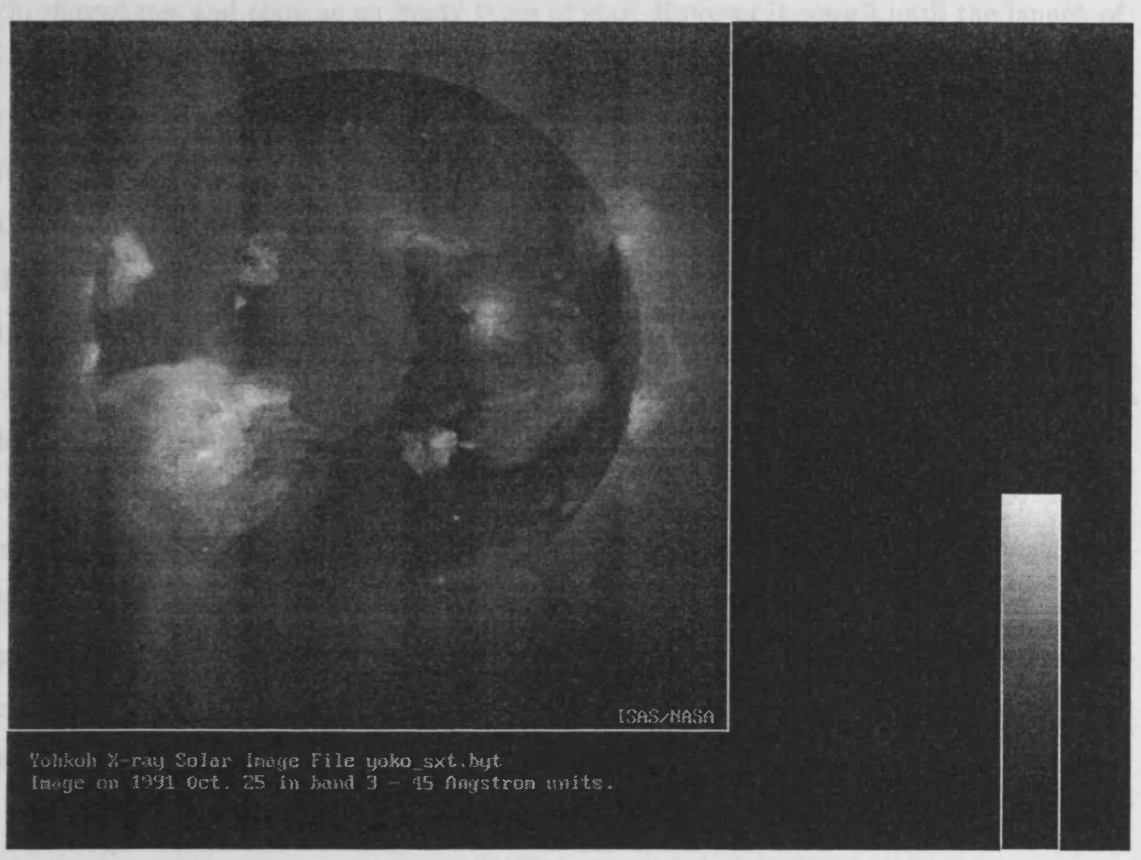

Figure 1.1: Yohkoh soft X-ray image of the Sun. Clearly visible are active regions, large scale loops connecting active regions, coronal holes and coronal loop structures.

1.3 Discovery of Stellar Coronae

The first 'normal' late-type stellar X-ray source was detected on a 1974 rocket flight and reported by Catura *et al.* (1975). It was only a short while later that the first attempt to model the corona of another star was made (Haisch and Linsky, 1976). The IUE satellite allowed stellar ultraviolet spectral (1175—2000$\AA$) observations to be used to detect chromospheres and coronae on many types of star. However it wasn't until the launch of the Einstein Imaging Proportional Counter (IPC) that the field of stellar X-ray astronomy truly came into its own with the discovery of over 1000 coronal sources. Prior to this point it was expected that only the very nearest of stars could be detected in X-rays. By scaling the solar X-ray flux and considering the effect of the inter-stellar medium the limiting distance for observing stellar coronae was calculated to be $\approx$9pc. Einstein showed our Sun to be relatively dim in X-rays as compared to most other late-type stars, hence more were visible out to much greater distances than expected. Indeed the ROSAT all-sky survey has detected tens of thousands of coronal X-ray sources. Another unexpected result was obtained by Holt *et al.* (1979) using the Einstein Solid State Spectrometer (SSS). X-ray emission lines detected using the SSS indicated the presence of plasma in coronae with temperatures of up to 24×10^6K, a figure much higher than had been previously anticipated . By the early 1980's it was possible to show that most late-type stars had solar like coronae, indeed X-ray emission was detected over most of the HR diagram (see Linsky 1990, Vaiana 1990).

1.4 X-ray Emission on the HR Diagram

One of the first stellar discoveries made using the Einstein observatory was that most stars are X-ray emitters. The X-ray properties of early-type stars were found to be very different from those of late-type stars and X-ray emission was found even outside of the main sequence. Summarised below are the details of the X-ray emission across the HR diagram, which is shown (reproduced from Linsky 1990) in Figure 1.2.

---

of $L_x\sim10^{31}$ erg s^{-1}. However there are still $\approx$30—40% of nearby main sequence G-type stars less X-ray luminous than our Sun (Schmitt 1996).

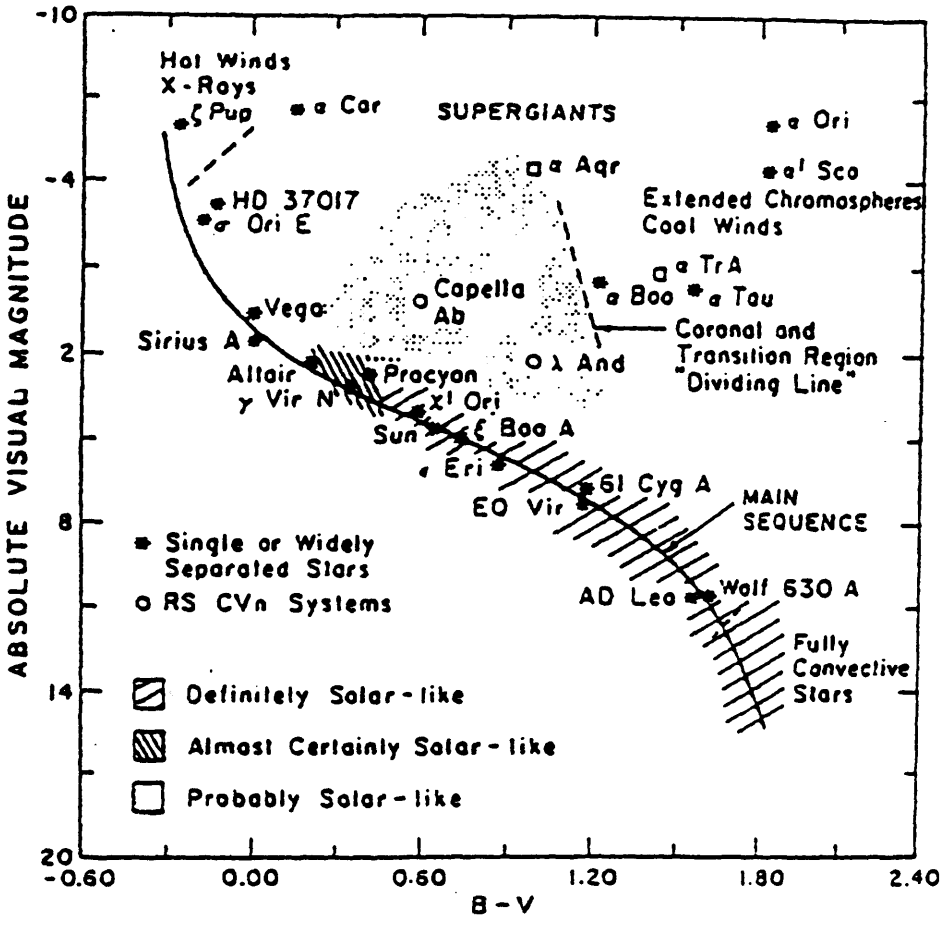

Figure 1.2: Summary of stellar activity through the HR diagram, derived from optical, UV and X-ray observations. Shown are the main sequence and regions where wind-shocks occur. Some representative stars are shown. Figure adapted from Linsky 1990.

Main Sequence:

- **O-B Stars:** Early-type stars of spectral types O and B are vigorous X-ray emitters with X-ray luminosities ranging from 10^{26}erg s^{-1} to 10^{34}erg s^{-1}. There is a dependence of X-ray luminosity on bolometric luminosity (e.g. Sciortino *et al.* 1990) best represented by $L_x \approx L_{BOL}{}^{-7}$, with no dependence on luminosity class. No dynamo action, as seen in stars with outer convection zones, should be possible. X-ray emission most likely originates from shock-heated material in a strong stellar wind.

- **A-type Dwarfs:** Stars in the range B7 to A5 are probably not X-ray emitters, at least not at levels greater than $\approx 10^{27}$erg s^{-1}. Any detections of X-rays from these star categories so far have been shown to be due to a faint secondary companion. For late A to early F-type stars Schmitt *et al.* (1985) reports on a survey of shallow convection zone stars and concludes that stellar coronae are first detectable at spectral type F0V.

- **Late-type Dwarfs:** All late-type dwarfs from spectral type F to M emit X-rays in the 10^{26}erg s^{-1} to 10^{31}erg s^{-1} range. For each spectral type there is a large range of emission levels (spanning 3—4 orders of magnitude). This spread is widest for M-dwarfs and narrowest for F-dwarfs. A number of X-ray luminosity functions for late-type stars are presented in Appendix A, these being used in Chapter 3 of this thesis. Stars beyond dM4 are fully convective, as such they are expected to produce magnetic flux via a distributive dynamo (Rosner, 1980) or fibril dynamo (Weiss, 1993) rather than a shell dynamo. Since M-dwarfs are the most common stars it is expected that they may represent a major contribution to the soft X-ray background.

Giants and Super-Giants:

Only the late-type giants and supergiants (spectral types earlier than around K2III) have been detected in the X-ray band (Ayres *et al.* 1981). This point is known as the Coronal Dividing Line, which lies between stars with high-temperature transition regions and coronae (to the left of the line) and stars which have only extended chromospheres (to the

right). Stars to the right of the line also have massive low-velocity cool winds (Linsky and Haisch 1979) making the line also known as the Wind Dividing Line.

Close Binaries:

- **RS CVn's:** This class consists of an evolved G/K IV star with an F/G IV/V companion. These are the most luminous non-degenerate stars in the X-ray regime, with L_x in the range of 10^{30}erg s^{-1} to several times 10^{31}erg s^{-1}. Their high X-ray luminosity is consistent with their high rotation rate caused by tidal synchronism of orbital and rotational motions (periods less than a day up to weeks). Within the class itself there is little evidence of a rotation rate dependence. RS CVn's are characterised by strong, long-duration flares in the X-ray, UV and radio bands (e.g. Tsuru *et al.* 1989). A full discussion of their X-ray properties is given in Majer *et al.* (1986).

- **Algols:** Algol itself consists of a B8V primary with a K2IV secondary which fills its Roche lobe. The system has a period of 2.87 days. Observations suggest a large scale for the X-ray emitting region (White *et al.* 1986). Such systems are discussed in White and Marshal (1983) with their large X-ray flaring activity discussed in Stern *et al.* (1992). A more recent ASCA Algol survey is presented by Singh *et al.* (1996).

- **W UMa's:** Not as bright as RS CVn's despite their shorter periods (6—8 hours), these stars share a common outer envelope, giving both components similar effective temperatures (and thus spectral type) despite mass ratios of <1. The first X-ray survey of W UMa systems was reported by Cruddace and Dupree (1984) from Einstein observations. A more recent survey using ROSAT pointed observations was performed by McGale *et al.* (1996) and the work presented in Chapter 5 of this thesis begins the work of extending the ROSAT W UMa survey using observations performed with ASCA.

- **BY Dra, UV Cet Type Systems:** These are active, rapidly rotating, single or binary dK/dM stars. Their X-ray luminosities are comparable with young rapidly rotating dK/dM stars in clusters such as the Hyades and Pleiades. For a deeper discussion see Jeffries and Bromage (1993).

Pre-Main Sequence Stars:

These still contracting stars have relatively high X-ray luminosities (10^{29}erg s^{-1} to 10^{31}erg s^{-1}), possibly due to their large surface areas. They exhibit high levels of variability on timescales as short as one day.

1.5 Observing Coronal Properties

1.5.1 Spatial Structure

Obtaining spatial structure information is normally not possible in all cases except the Sun. Some information can be obtained from eclipsing binary systems where the modelling of eclipses can provide insight into the spatial extent and structure of coronae. This technique was first used by Swank and White (1980) using an Einstein observation of the RS CVn binary AR Lac. They concluded that compact coronal structures were present on both components and identified an extended corona around the K0IV secondary. Whilst valuable, studies like these must be coordinated with optical and UV measurements in order to understand stellar atmospheres from chromosphere to corona.

Some surface structure may be obtained by modelling. If a standard solar-like atmospheric model with X-ray emission associated with active regions is used to model a stellar surface, then it emerges that even on F and G-type stars the fractional surface coverage of dark spots on young stars can be up to ten times greater than on the Sun (Radick *et al.* 1990).

1.5.2 Temperatures

Considering the lack of spatial resolution and the modest spectral resolution generally available it is at best difficult to determine the properties of stellar coronal plasma. With sufficient signal to noise in a spectrum it is clear that single component temperature models are usually inadequate, with at least a bimodal temperature model being required. It is not yet clear, in general, whether the bimodality is instrumental in origin, as suggested by

Majer *et al.* (1986), or physical; White *et al.* (1990) argued that eclipsing binary systems provide evidence of spatially separated structures in coronae. Swank (1985) argued for the physicality of bimodality due to the better fits of a bimodal model over those using a continuous emission measure model. In this thesis, where spectral fitting is required, both continuous emission models and multi-temperature models are used, the fit results of each being presented.

1.5.3 Variability

From our knowledge of the temporal behaviour of solar X-ray emission there are essentially three processes which would be expected to cause the X-ray luminosity of a star to vary; orbital and rotational modulation (timescale—days-weeks), stellar activity cycles (timescale—years-decades), active region evolution (timescale—hours-days) and flaring (timescale—minutes-hours). However so far few examples of large-scale variations in the quiescent emissions of stars have been recorded. Barstow *et al.* (1992) reported periodic rotational variability of the emission from the active binaries BY Dra and HR1099.

An optical search for a stellar analog of the 11-year solar cycle was begun by O.C Wilson in 1966. The HK project was designed to investigate variations in the Ca II H and K lines in 91 main sequence stars in the spectral range F5 to M2 (Wilson 1978). Continued monitoring of these stars has shown that the majority of dwarf stars exhibit behaviour which is possibly cyclic with 2.5 to 20 year periods. Such a project in the X-ray band is at the moment not feasible, however Gagne *et al.* (1995) discuss variability of the Pleiades on timescales of weeks to $\approx$10 years, finding evidence of both short-term (flaring) and long-term variability, possibly arising due to stellar cycles. A similar study is presented in Chapter 4 of this thesis, for stars in the Hyades cluster. Hyads detected in ROSAT pointed observations are analysed for short-term variability and then compared to previous Einstein observations in order to check for long-term variations.

1.5.4 Flares

Analysis of Einstein, EXOSAT and ROSAT data has shown stellar flaring to be a common occurence. The duration and energy of a flare may vary over many orders of magnitude. Timescales range from ≈10 seconds (on the nearby flare star UV Ceti - Schmitt *et al.* 1993) to 10 days (in the case of the RS CVn system CF Tuc - Kürster 1994) though typically a flare will last from a few minutes to a few hours. Total flare energies are in the range of 10^{30} to 10^{34} erg for dMe stars and 10^{35} to 10^{37} erg for RS CVn and pre-main sequence (PMS) systems, as compared to the solar-flare range of 10^{28} to 10^{31} erg. Flares contribute significantly to the instantaneous power of a star, with a flare power to bolometric emission ratio of typically 5% for a Pleiades K2 dwarf (Schmitt *et al.* 1993), ≈7% for a late-type M dwarf and up to 8% in the case of Speedy Mic (Bromage *et al.* 1992). Details of flares on Hyades stars and W UMa systems are presented in Chapters 4 and 5 respectively of this thesis.

In addition to these bright flares, quiescent X-ray emission from late-type stars often show low amplitude fluctuations on time-scales of a few minutes to days (Ambruster *et al.* 1987, Pallavicini 1988). It has been postulated that this behaviour is attributed to the chaotic behaviour of magnetic field lines dissipating magnetic energy at the stellar surface. It is a possibility that coronal heating may occur due to such continuous low-level activity (Parker 1988). Such microflaring has been seen on the Sun in hard X-rays (Lin *et al.* 1984) and attempts at detection of stellar microflares have been made (Collura *et al.* 1988). At this point their existence and coronal heating contribution cannot be ruled out.

1.6 The Age-Rotation-Activity Relation

With the discovery that coronal X-ray emission is a common feature of late-type stars, the question arose as to how two stars, identical in spectral type, may differ dramatically in coronal output. As activity is related to the magnetic dynamo effect in a star, rotation had to play a significant part in the equation. This relation was first reported in RS CVn systems (Walter and Bowyer 1981) and was generalised as $L_x \approx 10^{27}(v.sin(i))^2$, with v

in km s^{-1} (Pallavicini *et al.* 1981). This relation was found to hold up to a 'saturation' velocity where a star would run out of surface area to accommodate active regions (Fleming *et al.* 1989). Clearly such a relation must be subject to a certain amount of dispersion as we see solar variations in 'quiescent' X-ray output (by factors of ≈5—10) without any rotational velocity change. Figure 1.3 demonstrates this rotation-emission relation.

The relatively old (≈5×10^9year) Sun rotates slowly (v_{EQ}≈2km s^{-1}) as compared to younger stars (≈150km s^{-1} for a solar like star when it first reaches the main sequence. This phenomenon is clearly visible when looking at samples of stars in nearby open clusters. The youngest cluster, α Persei (age ≈50Myr) has rapid rotators (v.sin(i)>100km s^{-1}) at all spectral types. The Pleiades (age ≈70Myr) has rotational velocities of v.sin(i)≥50km s^{-1} in the K and M dwarfs but no G dwarfs have rotational velocities this high. By the time we reach the age of the Hyades (age ≈600Myr) all the G and K dwarfs rotate slowly (v.sin(i)≤10km s^{-1}) with the M dwarfs having v.sin(i)≈15—20km s^{-1}. No matter which cluster we observe, the majority of stars with spectral types later than G0 are slow rotators (v.sin(i)≤10km s^{-1}) (Stauffer *et al.* 1994).

This slowing down of stars with age is attributed to magnetic braking from the magnetised stellar wind (though as yet there have been no observations of solar like winds from F, G, K or M dwarfs) with the more massive stars braking more efficiently (Stauffer *et al.* 1994).

Wilson and Woolley (1970) found that Ca II emission was related to stellar age in late-type main sequence stars and showed statistically that stars of differing velocities showed different H and K line strengths. It is likely that evolutionary changes in stellar rotation can account for changes in chromospheric activity levels. Skumanich (1972) proposed a rotation and Ca II emission decay relation of $\tau^{-1/2}$ where τ is the main sequence age.

1.7 Thesis Outline

The remainder of this thesis is laid out as follows. In Chapter 2 I discuss the mechanisms by which a hot, optically thin plasma emits at X-ray wavelengths and how this emission is detected by the instruments on board the ROSAT and ASCA satellites.

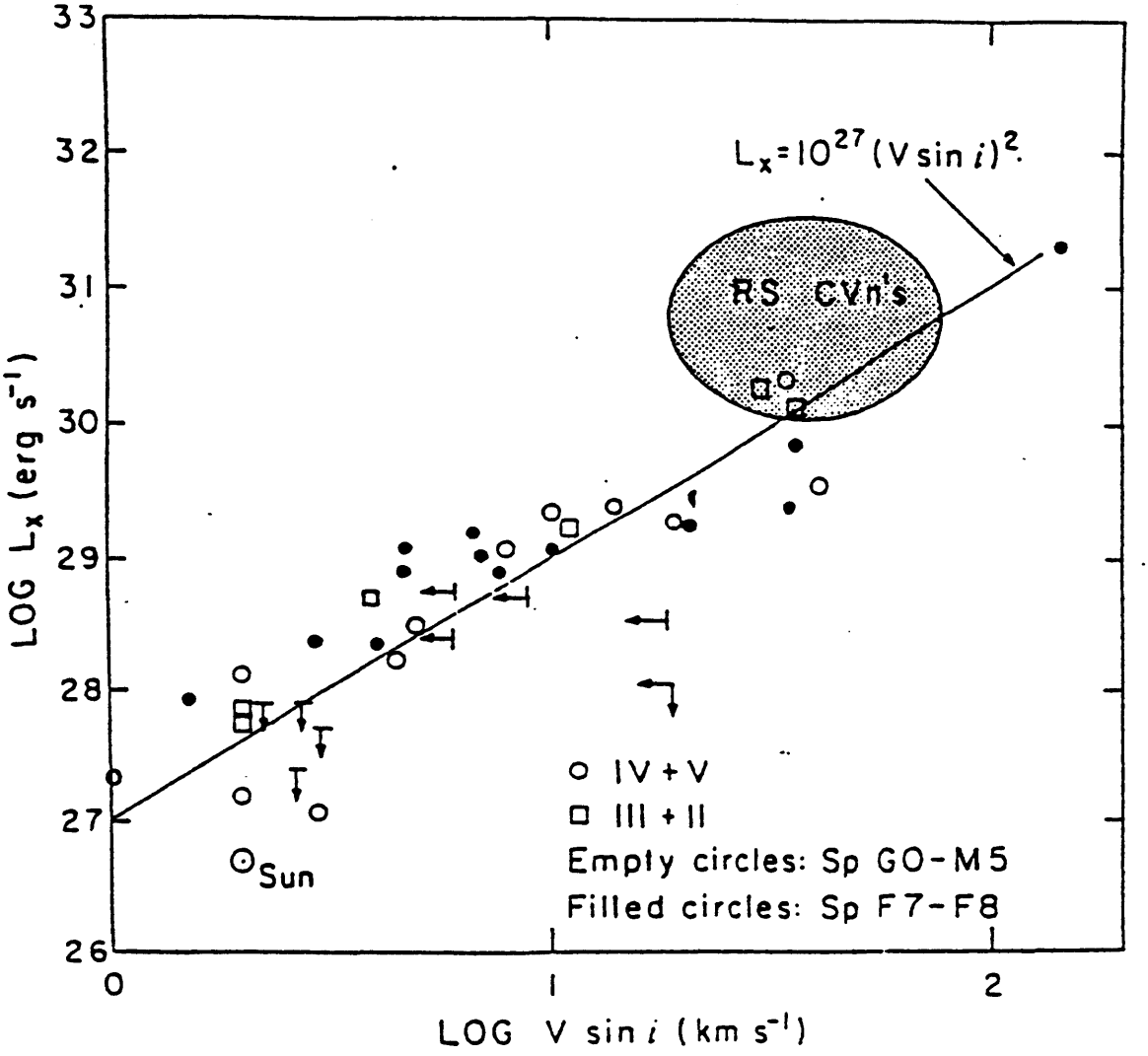

Figure 1.3: Soft x-ray luminosity versus rotation rate. Despite the diversity of stellar types in the sample, the correlation can be seen to remain strong. Figure adapted from Pallavicini *et al.* (1982).

Chapter 3 reports a deep survey of the Galactic Plane in the third quadrant using ROSAT PSPC pointed observations. The data consist of 9 fields each of ≈10ks exposure. The catalogue of X-ray sources is presented, as are the number-flux relation, X-ray to optical ratios and modelling of the source populations.

In Chapter 4 I discuss a ROSAT survey of the Hyades open star cluster. The survey consists of 13 pointed PSPC observations each of ≈20ks exposure. I present the results of a variability study (long and short-term) and examine the behaviour of the flare events observed.

Chapter 5 presents ASCA spectral and temporal results for three W UMa type contact binaries (VW Cep, ,44i Boo and SW Lac). These are initial results from an on-going survey which so far has accumulated data on 7 such systems.

Finally in Chapter 6 I conclude with a summary of results from the previous chapters and a discussion of future missions and their likely contributions to stellar X-ray astronomy.

Chapter 2

Observation and Analysis of Coronal X-ray Emission

2.1 Stellar X-ray Astronomy Pre-ROSAT

During the 1940's and '50's sounding rocket flights were used to make the first detections of the Sun at X-ray wavelengths. A rocket flight in 1974 first detected Capella in the soft X-ray band (Catura *et al.* 1975). The first X-ray survey was performed by HEAO-1 in 1978, though this was a non-imaging instrument. This was used to identify RS CVn systems as the first class of stellar[1] X-ray source. The Einstein Observatory (HEAO-2) was launched in 1978 and carried the first imaging X-ray instruments in orbit. On board were an imaging proportional counter (IPC), a high resolution imager (HRI) and three spectrometers; the solid state spectrometer (SSS), the objective grating spectrometer (OGS) and the focal-plane crystal spectrometer (FPCS). Prior to the launch of this satellite few stellar X-ray sources were known. The IPC detected over 1000 stellar sources and was used to show that X-ray emission was common throughout the entire HR-diagram (see Chapter 1). It was observations made using the IPC which showed that acoustic heating could not account for the observed levels of X-ray emission. The SSS was used to confirm the existence of thermal line emission (Holt *et al.* 1979) and indicated the existence of plasma in the

[1]From now on, unless stated otherwise, the term 'stellar' refers to non-degenerate late-type stars.

temperature range 6—24$\times 10^6$K.

EXOSAT was launched in 1983 and remained functional for 3 years. Its highly eccentric orbit allowed for uninterrupted observations lasting several days. Instruments carried were: a low energy (LE) experiment capable of imaging but with no intrinsic spectral resolution, a medium energy array (ME) covering the 1 to 20keV band with moderate spectral resolution and a transmission grating spectrometer (TGS) used for studying line complexes with a 3Å resolution in the 10-300Å (0.04-1.2keV) range.

In operation between 1987 and 1991, *Ginga* detected several coronal sources with the large area counter (LAC). The LAC was an array of 8 proportional counters with a peak effective area of $\approx$4000cm^2, sensitive in the 1.2—37keV range. Tsuru *et al.* (1989) found evidence using *Ginga* observations for a lower than expected, and variable, FeXXV—XXVI equivalent width during and between two flares on UX Ari.

These and other instruments flown pre-ROSAT are described in Table 2.1. These provided the grounding upon which current observations build, allowing our understanding of stellar coronal emission to grow.

2.2 The ROSAT Mission

On June 1st 1990 ROSAT was launched. The on-board instrumentation was: the positional sensitive proportional counter (PSPC) provided by the Max-Plank Institut für Extraterrestriche Physik (MPE), the high-resolution imager (HRI) provided by NASA and the wide-field camera (WFC) provided by the University of Leicester. Figure 2.1 shows the location of the instrumentation on board the satellite.

The ROSAT X-ray telescope (XRT) consists of 4 nested grazing incidence Wolter Type 1 mirrors with a minimum aperture of 83.5cm and focal length of 240cm. The mirrors are made from a glass ceramic coated with a thin layer of gold. Typical grazing angles are between 1 and 2 degrees. Mounted on a carousel in the XRT focal plane are 2 redundant PSPC's and the HRI.

Table 2.1: X-ray orbiting detectors flown pre-ROSAT (adapted from Bradt, Ohashi & Pounds, 1992).

Mission	Dates	X-ray Instruments
OSO-3	1967–1968	H
OSO-5	1969–1972	H
Vela Series	1969–1979	M
OSO-7	1971–1973	M, H
Copernicus	1972–1981	M, C
ANS	1974–1976	L, M, C, B
Ariel V	1974–1980	M, B, Pol, SM, MC
SAS-3	1975–1979	L, M, MC, C
OSO-8	1975–1978	L, M, H, B, Pol
HEAO-1	1977–1979	L, M, H, MC
Einstein (HEAO-2)	1978–1981	F, IPC, HRI, B, SSS, M, TG
Ariel VI	1979–1981	L, M, C
Hakucho	1979–1984	M, MC, SM
Tenma	1983–1984	L, M, G, C, SM, MC
EXOSAT	1983–1986	L, M, G, F, TG
Ginga (ASTRO-C)	1987–1991	M, SM
Röntgen/Kvant	1987–	M, H, CM, G
Granat	1989–	M, H, CM
ROSAT	1990–	F, HRI, IPC, WFC

Key B - Bragg crystal spectroscopy; C - collector (reflecting); CM - coded-mask imaging; F - focusing optics; G - gas scintillation proportional counter; H - high-energy (10-200 keV) crystal scintillator; HRI - high resolution imager; IPC - imaging proportional counter; L - low-energy (0.1-1 keV) proportional counter; M - medium energy (1-20 keV) proportional counter; MC modulation collimator; Pol - polarimetry; SM - sky monitor; SSS - solid-state spectrometer; TG - transmission gratings; WFC - EUV wide-field camera.

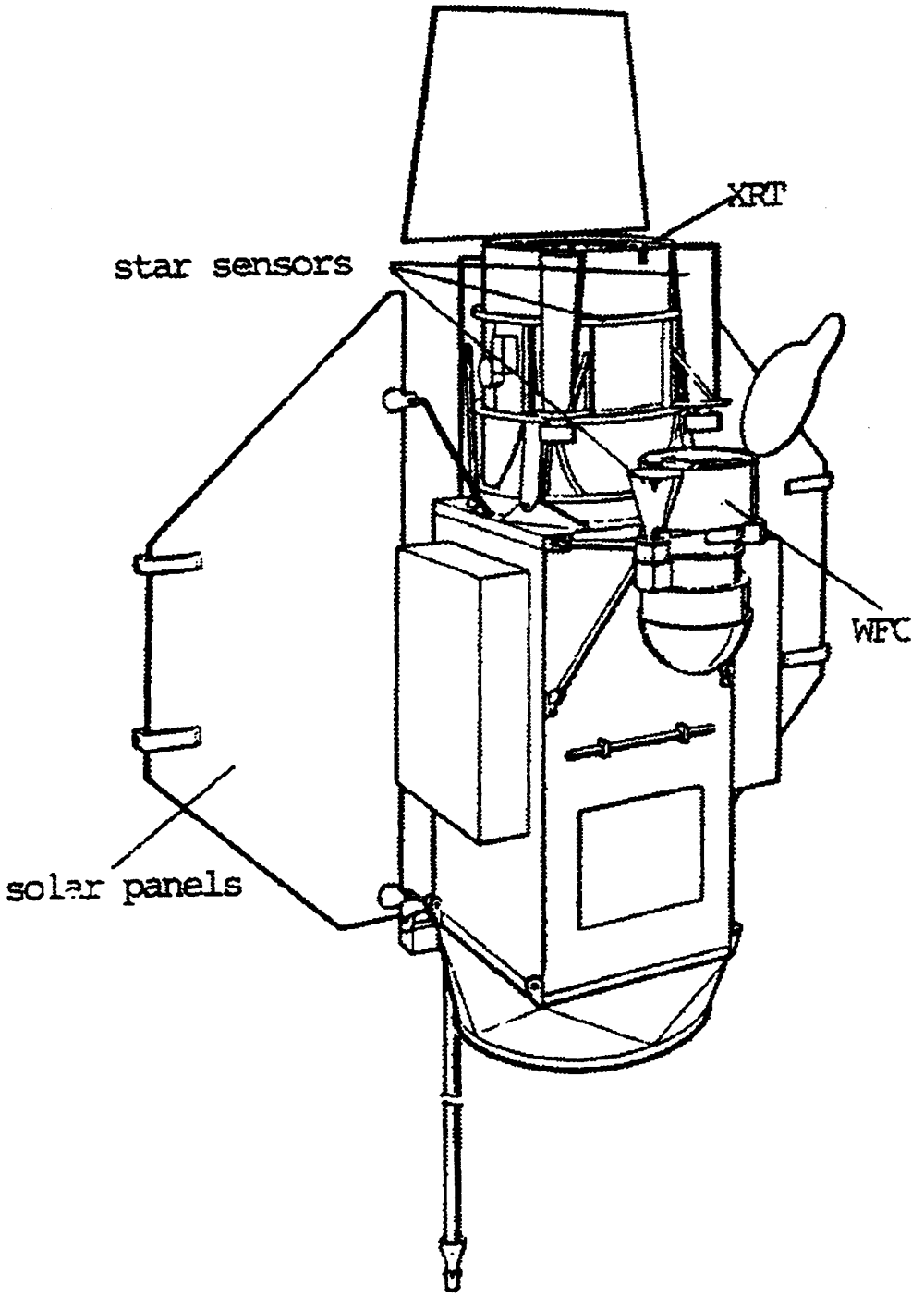

Figure 2.1: The ROSAT satellite with main components indicated.

The satellite has a circular orbit at an altitude of ≈575km and an inclination of 53°, with an orbital period of ≈95 minutes. It is controlled from the German Satellite Operations Center (GSOC) at Weilheim. Five to six ground contacts each day allow for downloading of data and issuing of telemetry commands. Attitude control is accurate to 1 arcmin. Using onboard CCD star sensors the pointing direction can be reconstructed at GSOC to a precision of ~5 arcsec. During observations made using the PSPC the pointing direction was 'wobbled' over ±3arcmins with a 400 second period. This prevented shadowing of X-ray sources by the opaque wire of the PSPC window-support grid.

The ROSAT mission had two scientific goals, the first being to carry out complete far EUV and soft X-ray all-sky surveys. This was to be followed by pointed observations in both wavebands of individual targets with long exposure times. After an initial calibration phase the all-sky survey commenced in July of 1990, finishing on January 25th 1991. The sky was scanned by rotating ROSAT on an axis, once per orbit, so that its 2 coaligned telescopes always looked away from the earth, hence observing the sky in a series of great circles passing over both ecliptic poles. Upon the completion of the all-sky surveys, the pointed, guest observer (GO), phase began. The PSPC was available for use until the end of 1993, with the WFC and HRI still in operation at the time of writing (August 1996). A full description of the ROSAT X-ray telescope and its detectors can be found in Trümper (1983).

The work presented in Chapters 3 and 4 of this thesis involved the analysis of data obtained using the PSPC during the pointed phase of the mission.

2.3 The PSPC

The PSPC (see Pfeffermann *et al.* 1986) is a conventional multiwire proportional counter with a cathode strip readout scheme for position determination. An 1141cm^2 sensitive area subtends an angle of 2° at the XRT focus. The operational energy range is 0.1—2.5keV. The PSPC entrance window is polypropylene coated with carbon and Lexan to reduce UV transmission. A 4 position filter wheel is located in front of the detector, with settings for standard observations, background particle monitoring, observations using a

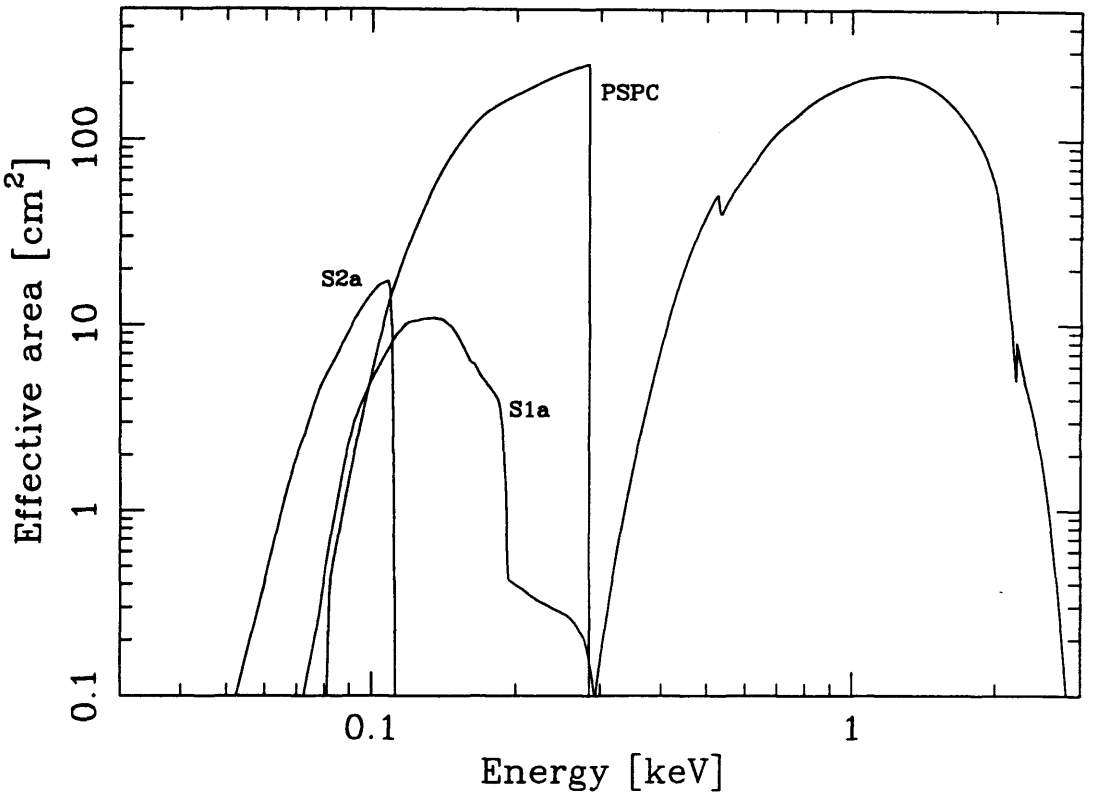

Figure 2.2: The response curves for the combinations of PSPC/XMA and WFC (S1 and S2 filters).

boron filter allowing an increase in low energy spectral resolution and a fourth position with radioactive sources used for spectral calibrations. The PSPC gas supply is a mixture of Argon, Xenon and Methane and absorbs ≈100% of the incident photons with energies below 2keV. The detector quantum efficiency is thus determined by the transmission of the viewing window. The response curves for the combinations of PSPC with the X-ray mirror assembly (XMA) (and WFC for comparison) are shown in Figure 2.2. The PSPC effective area falls off gradually with increasing off-axis angle. This drop becomes much more rapid beyond an angle of ≈50arcmin, as can be seen in Figure 2.3.

Pulse heights of events are recorded in the detector, digitised on board into 256 channels and corrected for temporal and spatial gain variations on the ground. The events are placed into pulse-height invariant (PI) channels. These channels are generally binned-up

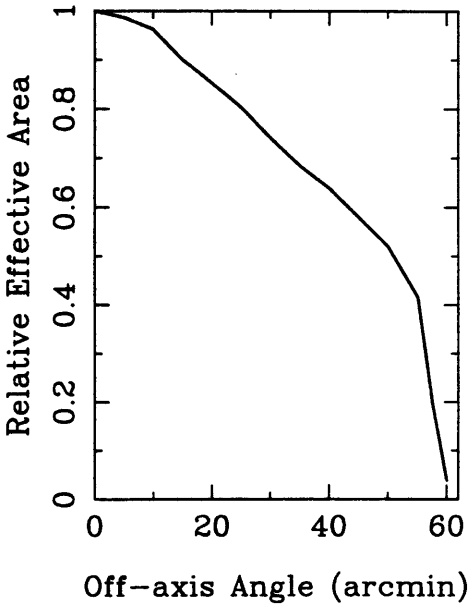

Figure 2.3: The PSPC effective area against off-axis angle for a nominal photon energy of 0.5keV.

so that each new bin has the same oversampling of the spectral resolution. These Standard Analysis Software System (SASS) channels are shown in Table 2.2. Background correction for such contamination as high energy particles and solar scattered X-rays is performed on the data.[2] The observed detector response to an input spectrum is found by convolving the effective area and the detector response at the given off-axis angle.

The point spread function (PSF) of the PSPC is a superposition of terms arising from the detector response and the mirrors. The effect of this superposition results in the image-size of a point source increasing with off-axis angle. The extraction radius required to contain 95% of a source's counts[3] thus increases with off-axis angle. In this thesis the parameterisations derived by Georgantopoulos, Saxton and Pye (1992) are used, as implemented in the Starlink ASTERIX data analysis package.

[2]Onboard particle rejection is ≈99.8% efficient, however when the particle rate becomes greater than 170 counts per second rejection efficiency drops . Hence all time periods where this threshhold is exceeded were removed from PSPC data in this thesis.

[3]As was used for PSPC source extraction in this thesis.

Table 2.2: ROSAT SASS bins

SASS bin	E_{low}	E_{high}	PI bins	SASS bin	E_{low}	E_{high}	PI bins
1	0.07	0.09	7–8	18	0.84	0.91	84–90
2	0.09	0.11	9–10	19	0.91	0.99	91–98
3	0.11	0.14	11–13	20	0.99	1.07	99–106
4	0.14	0.17	14–16	21	1.07	1.15	107–114
5	0.17	0.20	17–19	22	1.15	1.23	115–122
6	0.20	0.24	20–23	23	1.23	1.32	123–131
7	0.24	0.28	24–27	24	1.32	1.41	132–140
8	0.28	0.32	28–31	25	1.41	1.50	141–149
9	0.32	0.37	32–36	26	1.50	1.60	150–159
10	0.37	0.42	37–41	27	1.60	1.70	160–169
11	0.42	0.47	42–46	28	1.70	1.80	170–179
12	0.47	0.52	47–51	29	1.80	1.91	180–190
13	0.52	0.58	52–57	30	1.91	2.02	191–201
14	0.58	0.64	58–63	31	2.02	2.13	202–212
15	0.64	0.70	64–69	32	2.13	2.24	213–223
16	0.70	0.77	70–76	33	2.24	2.36	224–235
17	0.77	0.84	77–83	34	2.36	2.48	236–247

2.3.1 Coronal Studies Using the PSPC

The soft X-ray all-sky survey performed using the ROSAT PSPC had a limiting flux of $\approx 2\times10^{-13}$erg cm^{-2} s^{-1} in the 0.1—2.0keV energy range and detected around 60000 X-ray sources (Schmitt, 1991). The results of the survey indicated that ≈25% of high galactic latitude sources were late-type stars and the emission presumably coronal in origin. This fraction increases to ≈50% at lower latitudes.

The sensitivity available using ROSAT is unprecedented compared to earlier missions. Previously stars were often chosen for X-ray observation on the basis of their optical behaviour. Such bias is not present in ROSAT data. The ability to observe large numbers of stellar sources is exploited in Chapters 3 and 4 of this thesis, where I look at the galactic plane and the Hyades star cluster using pointed PSPC observations.

2.4 The ASCA Mission

The Japanese X-ray astronomy satellite ASCA (formerly known as Astro-D) was launched from Kagoshima Space Center, Japan, on February 20, 1993. The satellite has a roughly circular orbit at an altitude of 500—600km, an inclination of 31.5 degrees and an orbital period of ≈95 minutes. Ground contact occurs in 10 of the 15 daily orbits.

ASCA consists of 4 large-area telescopes focussing X-rays from a wide energy range onto four instruments. Two of these are X-ray sensitive charge-coupled devices (CCD's) known as the Solid-State Imaging Spectrometers (SIS, the first X-ray CCD spectrometer used in orbit). The remaining two instruments are gas imaging scintillation proportional counters (GSPC's) filled with xenon and named the Gas-Imaging Spectrometers (GIS). Each SIS is based around 4, 420×422 pixel CCD chips arranged in a 2×2 square with a field of view of 22×22 arcminutes. The GIS has a field of view of 30×30 arcminutes and is used to complement the SIS, though above the xenon edge (≈5keV) the GIS has the greater detection efficiency. The GIS can observe much brighter sources than the SIS and in general has better temporal resolution but lower spectral resolution.

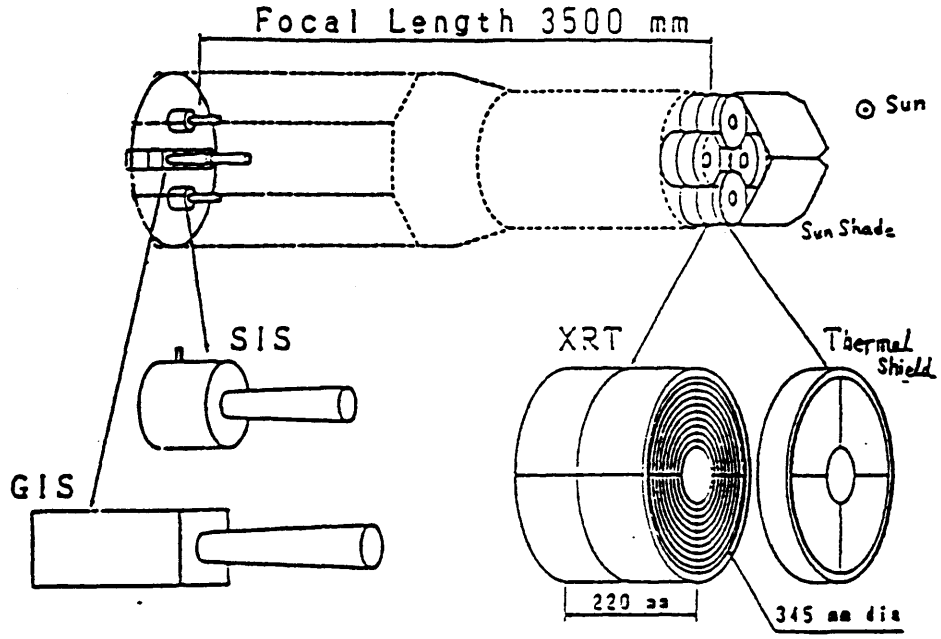

Figure 5.2b

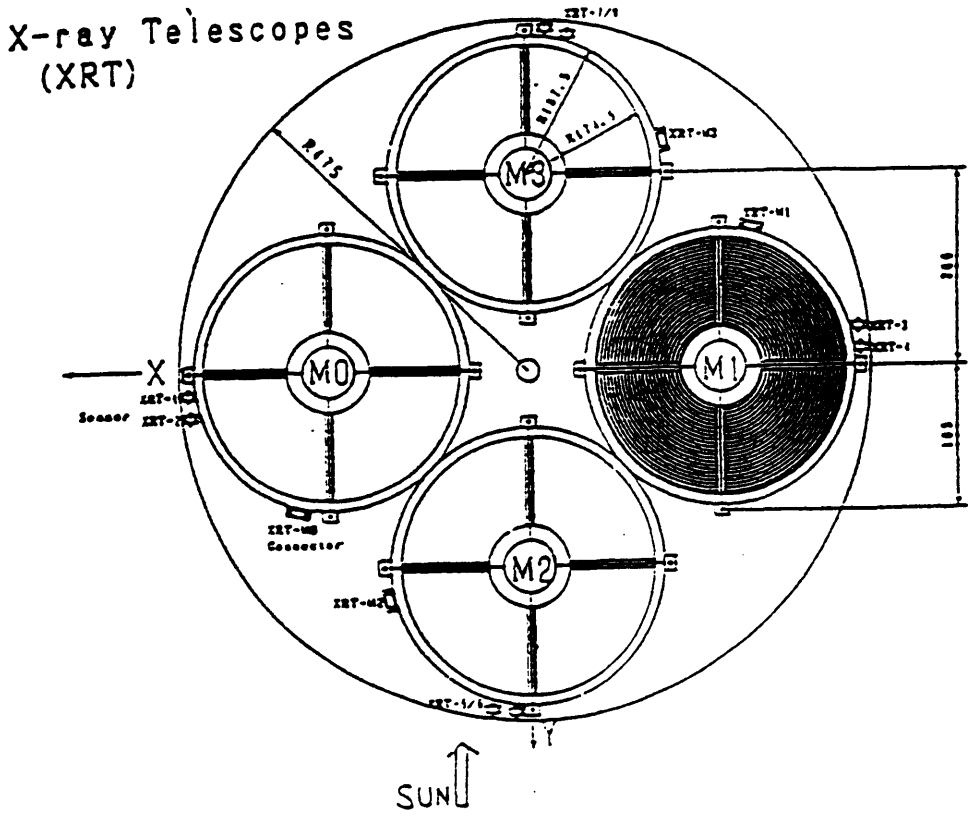

Figure 2.4: The ASCA satellite with main features shown.

ASCA has a broad pass band (operating between 0.5 and 12keV) and allows for the first time imaging combined with good spectral resolution (8% and 2% at 5.9keV for the GIS and SIS respectively) and a large effective area. The primary scientific purpose of the mission is the X-ray spectroscopy of astrophysical plasmas and as such it is an important new tool in the study of coronal emission. Indeed ASCA observations have already shown evidence for non-solar abundances in coronal sources (e.g. White 1996).

2.4.1 Observing With ASCA

The ASCA orbit imposes a viewing constraint based on the Sun angle making the observable region of the sky a belt of ±25 degrees wide along a great circle normal to the Sun vector. Another problem arises due to satellite transits through the South Atlantic Anomaly (SAA). High flux during a transition and induced radiation for a short while after removes 15—30 minutes of observing time per orbit for ≈9 orbits in a day. Geocoronal oxygen emission due to excitation by solar wind can contaminate an observation, hence it is advisable to exclude elevation angles of 10—20 degrees from the horizon. The result of these restictions usually yields 35—65ks of good data per day.

ASCA data reduction procedures are somewhat complex. A complete set of analysis instructions are given in 'ASCA an ABC guide' (Day *et al.* 1994). In Chapter 5 of this thesis I study the spectral and temporal behaviour of 3 W-UMa contact-binary systems using ASCA observations. When fitting the spectra I analyse simultaneously the data from SIS0 and GIS2 (the two best calibrated instruments).

2.5 X-ray Emission From Optically Thin Thermal Plasmas

The X-ray emission of a non-degenerate, late-type star comes from the very hot ($T>10^6K$) tenuous and highly ionised gas comprising its corona. Energetic collisions with free electrons strip gas atoms of nearly all their orbital electrons. The gas achieves a steady-state of statistical equilibrium with an ionisation balance, as determined by elemental recombination rates and electron collisions. Radiative and conductive energy loss is balanced

by energy input (by mechanisms not yet fully understood). Plasma electrons and ions fall into Maxwellian energy distributions with a common temperature (Mewe, 1991). Deviations from this model may arise from photo-ionisation, optical depth, high density, non-Maxwellian electron densities and transient ionisation (Raymond, 1988).

Observed X-ray emission results from collisional interactions between the ions and electrons. If a plasma has cosmic abundances ($\approx$90% hydrogen, $\approx$10% helium and $\approx$0.1% heavy elements) then the hydrogen and helium are fully ionised at typical coronal temperatures. It is only at higher temperatures ($T \geq 10^8$K) that the heavier elements approach full ionisation. Hence above $T \approx 10^8$K X-ray emission is almost fully bremsstrahlung continuum from H^+ and He^{++} whereas below this value line emission becomes significant and so emissivity becomes dependant on atomic abundances and ionisation state.

2.5.1 Spectral Models

Spectral models are constantly undergoing change as our knowledge of atomic physics improves. The updated models of several different groups were discussed at a recent plasma-codes workshop (Brickhouse *et al.* 1995). These models were:

- MFL (Monsignori Fossi and Landini, 1994).
- MEKA (Mewe, Gronenschild and van den Oord, 1985) with SPEX (Kaastra and Mewe, 1994) under development.
- RS (Raymond and Smith, 1977 and Raymond, 1988) with BRS (Brickhouse, Raymond and Smith, 1995) under development.
- Masai (Masai 1994).

All of these models work in a similar way. They are designed to model hot, optically thin plasmas. Given N_e, T_e and abundances the codes compute the power radiated in a given broad spectral range. The continuum emission processes include bremsstrahlung, radiative recombination and 2-photon emission. Line emission includes collisional excitation and satellite lines. Determining the population of a particular ionisation state, by

computing ionisation and recombination rates or assuming ionisation equilibrium populations, is the first step in calculating the line emission. Secondly a determination of the ion upper-level populations (from which line emission originates) must be made. The emission is proportional to that population times the radiative transition probability. In the 'coronal model' most of the population is in the ground state and statistical equilibrium is determined by a balance between collisional excitations from the ground-state to upper levels and subsequent radiative transitions down. Other factors such as upper level recombination and fine structure splitting are taken into account to different degrees in each of the models.

The most important aspect of the modelling is the completeness and accuracy of the atomic data. The accuracy is much improved today but still has some way to go (see Mason & Monsignori-Fossi, 1994). However a full understanding of the Fe L-shell has not yet been achieved and is a priority as it can contribute strongly to the 1keV X-ray spectrum. Also at this point there are still large uncertainties in the ionisation balance with the best recombination rates uncertain to the 30% level.

In Chapters 4 and 5 of this thesis I apply certain spectral models for an optically-thin thermal plasma to data obtained using ROSAT and ASCA. Two of the models, MEKA and RS, presume discrete plasma temperatures whilst CEMEKA is a continuous emission version of the MEKA model.

Figure 2.5 shows X-ray spectra calculated for a range of plasma temperatures using the RS model. The spectral shape can be seen to vary with temperature. This allows an estimation of plasma temperature to be made when energy resolution is low. Taking a simple isothermal plasma of temperature T and volume V the X-ray luminosity L_x in energy band $E \pm \Delta E/2$ is given by

$$L_X(T, \Delta E) = F(T, \Delta E)\epsilon \tag{2.1}$$

where $F(T, \Delta E)$ $(= F_C(T, \Delta E) + \Sigma_{\Delta E} F(T, E))$ is the total continuum plus line emissivity (radiated power per unit emission measure), and $\epsilon = \int n_e^2 dV \simeq n_e^2 V$ is the volume emission measure.

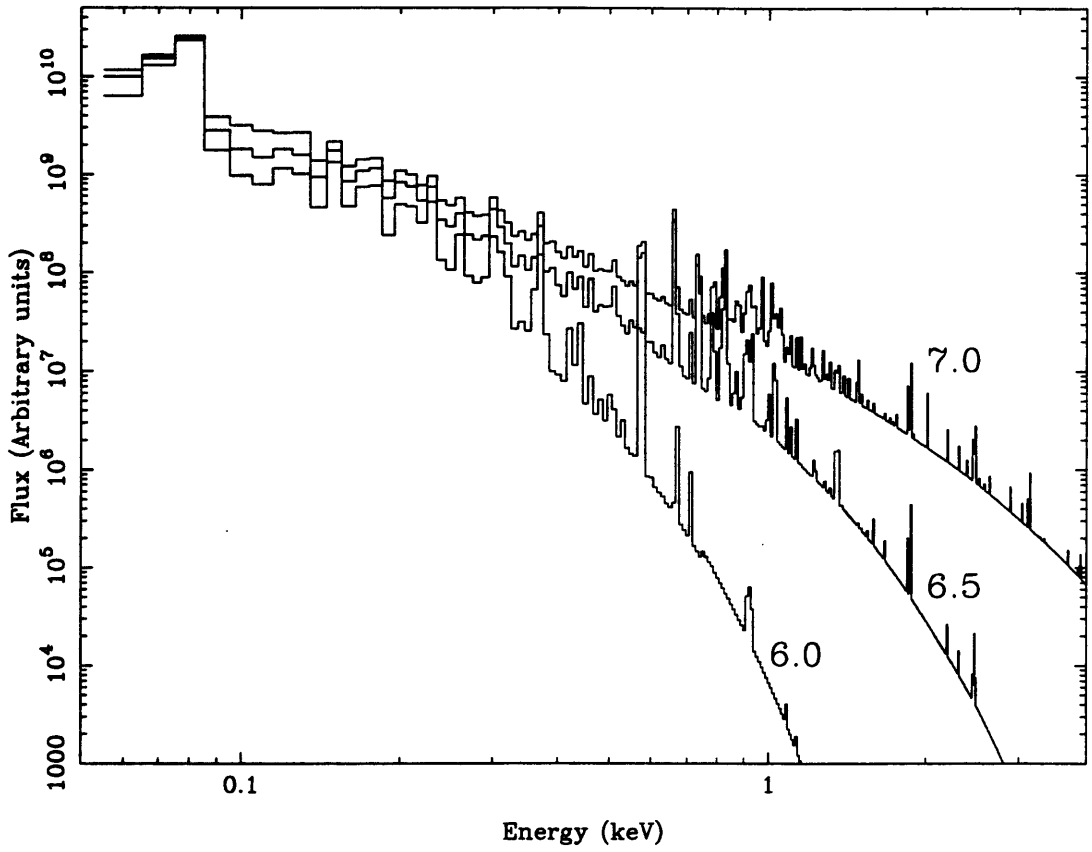

Figure 2.5: Spectral models calculated using Raymond & Smith (RS) code for temperatures T = $10^{6.0}$ K, $10^{6.5}$ K, $10^{7.0}$ K.

Where a plasma has a temperature distribution, emission from different parts of the plasma can be found by using the concept of the differential emission measure (see e.g. Pan & Jordan, 1995) $\phi(T) = d(\int n_e^2 dV)/dT$, and hence

$$L_X = \int F(T, \Delta E)\phi(T)dT. \tag{2.2}$$

2.6 The Local Interstellar Medium

Soft X-rays are attenuated when passing through the interstellar medium (ISM). This attenuation is a function of the number of atoms along the line of sight and the absorption cross-section of each atom. The effective cross section per hydrogen atom is given as

$$\sigma_{eff} = \Sigma \frac{n_i \sigma_i}{n_H} \tag{2.3}$$

where n_H is the volume number density of neutral hydrogen, and the density and absorption cross-section of element i are represented by n_i and σ_i respectively. The assumption of cosmic abundances and a value for the hydrogen column density along the line of sight allows the attenuation at a given energy to be found. The transmission (T) through the column is thus given by:

$$T = e^{-\sigma_{eff} N_H} \tag{2.4}$$

The local ISM consists of a warm, tenuous region known as the 'local bubble' with walls as close as 10pc in the direction of the galactic center and at the furthest ~100—200pc (Innes and Hartquist, 1984). X-ray background observations have shown evidence for the bubble being filled, at least partially, with gas of $T \approx 10^6$K and $n_e \approx 0.01 cm^{-3}$ (Snowden *et al.* 1990). Possible reasons for the existence of the cavity include a supernova event $\approx 10^5$ years ago[4] or a series of events over the past 10^7 years which repeatedly reheat the gas.

[4]Possibly resulting in the Geminga Gamma-ray Pulsar (Bignami, Caraveo and Mereghetti, 1993).

It is fortunate for X-ray astronomy that this cavity exists. Were it not present, leaving the ISM cold and dense, then stellar X-ray astronomy would be virtually impossible with emission being visible only from the nearest and brightest sources.

Chapter 3

A Third Quadrant Galactic Plane Deep Survey With ROSAT

3.1 Introduction

Flux-limited surveys are important both in the study of source populations and in the identification of individual interesting objects. In this chapter I will discuss a moderately deep soft X-ray (0.1–2 keV) survey of the Galactic Plane using pointed observations with the ROSAT Position Sensitive Proportional Counter (PSPC). The data consist of 9 fields each of $\approx$ 10 ks exposure, pointed at positions on or very close to the galactic plane ($|b| < 0.3°$) in the longitude range $180° \lesssim l \lesssim 280°$, a region often referred to as the Third Quadrant[1]. The survey reaches a factor > 10 lower in flux than previous 'galactic plane' surveys. I present the catalogue of X-ray sources and the number–flux relations which I compare with predictions of galactic (stellar) and extragalactic populations. I also discuss attempts at assigning optical counterparts based on inspection of digitised versions of sky-survey Schmidt plates, yielding magnitude estimates or limits for all the sources.

[1]Some workers, e.g. Paresce (1984), refer to this as 'Quadrant 4' or the 'Fourth Quadrant', while others, e.g. Frisch & York (1983) refer to it as 'Quadrant 3' or the 'Third Quadrant'. Here, I use the term 'Third Quadrant'.

3.2 Surveying the Galactic Plane

There have been two major galactic plane studies previously undertaken. The Einstein Galactic Plane Survey (EGPS; Hertz & Grindlay 1984, 1988) was a serendipitous source survey of Imaging Proportional Counter (IPC) fields at galactic latitudes $|b| < 15°$, covering a total area of 275 deg^2, and detecting 71 X-ray sources above a flux threshold of $\sim 2 \times 10^{-13}$ erg cm^{-2} s^{-1} in the energy band 0.15–4.5 keV. The median and 90 per cent coverage fluxes were $\approx 7 \times 10^{-13}$ and $\approx 2 \times 10^{-12}$ erg cm^{-2} s^{-1} respectively. The ROSAT Galactic Plane Survey (RGPS; Motch *et al.* 1991) utilises the ROSAT PSPC All-Sky Survey (RASS) data for $|b| < 20°$, with a typical limiting flux of a few times 10^{-13} erg cm^{-2} s^{-1}. Preliminary findings were presented based on 225 sources detected in an area of ≈ 200 deg^2 in the longitude range $108° < l < 155°$. These suggested that at least 50% of the X-ray sources were stellar in origin. More recently the RGPS has included a detailed study of a low-latitude area in Cygnus (Motch *et al.* 1996) centred at l =90°, b =0° with an area of 64.5deg^2. Of the 128 sources detected, 85% of those brighter than 0.03 PSPC ct s^{-1} were identified with active coronae. The number-flux relations obtained in the EGPS and RGPS are presented in Figures 3.1 and 3.2 respectively.

A further survey of the galactic plane was performed using the medium energy proportional conters on board EXOSAT with a 2—6keV erergy range (Warwick *et al.* 1988). This survey however only detected the brightest of sources, with no evidence of coronal emission (though some sources remain unidentified). Diffuse emission was detected, though no distinction could be made between what they called "hot spots" and individual discrete sources.

The present survey, whilst covering a much smaller area of sky ($\approx$ 2.5 deg^2, $180° \lesssim l \lesssim 280°$, $|b| < 0.3°$) than either the EGPS or RGPS, extends more than an order of magnitude deeper in flux, to $\sim 10^{-14}$ erg cm^{-2} s^{-1}, and has yielded 93 sources. Hence it complements well not only the EGPS and RGPS, but also ROSAT medium-sensitivity and deep surveys at high galactic latitudes (e.g. Hasinger *et al.* 1993; Branduardi *et al.* 1994; Boyle *et al.* 1995) and in other areas of the plane. The longitude range selected for our survey is relatively low in X-ray absorbing material out to distances of several hundred parsecs and presents fewer confusion problems than at other longitudes. The restriction in

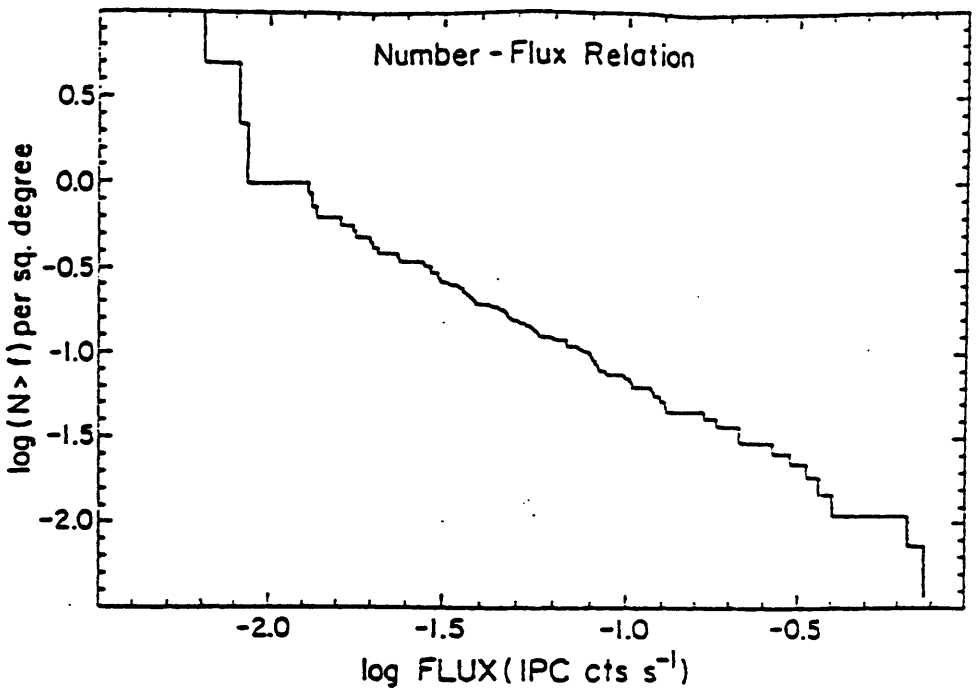

Figure 3.1: EGPS number-flux relation for low galactic latitude X-ray sources. Derived from observed fluxes of 71 sources with significance $>5\sigma$. Reproduced from Hertz and Grindlay 1984

Table 3.1: Observation log for the Third Quadrant Galactic Plane Survey.

FIELD	SEQ	RA	DEC	l	b	EXP(ks)	NOTES
1	900627	5 45 37.6	28 56 10.0	180.00	0.00	9.52	GAL PLANE 1
2	200084	6 15 15.0	17 43 41.0	193.10	0.32	9.41	TARGET=G104-27
3	900426	6 42 25.8	04 23 17.0	208.00	0.00	10.42	GAL PLANE 2
4	900628	7 02 32.3	-05 23 54.0	219.00	0.00	8.59	GAL PLANE 6
5	900380	7 18 29.0	-13 13 03.0	227.75	-0.13	18.68	TARGET=NGC2359
6	900428	7 23 18.9	-15 08 33.0	230.00	0.00	9.84	GAL PLANE 3
7	200049	7 24 40.1	-16 12 03.6	231.09	-0.21	8.66	TARGET=HD58343
8	900427	8 10 02.8	-33 16 56.0	251.00	0.00	10.80	GAL PLANE 4
9	400329	10 24 58.5	-57 47 00.5	284.39	-0.28	9.00	TARGET=1E102457

latitude essentially removes scale-height effects when attempting to interpret the spatial distribution of sources, since $|b| = 0.3°$ corresponds to a height of only 5 pc off the plane at a distance from the Sun of 1 kpc.

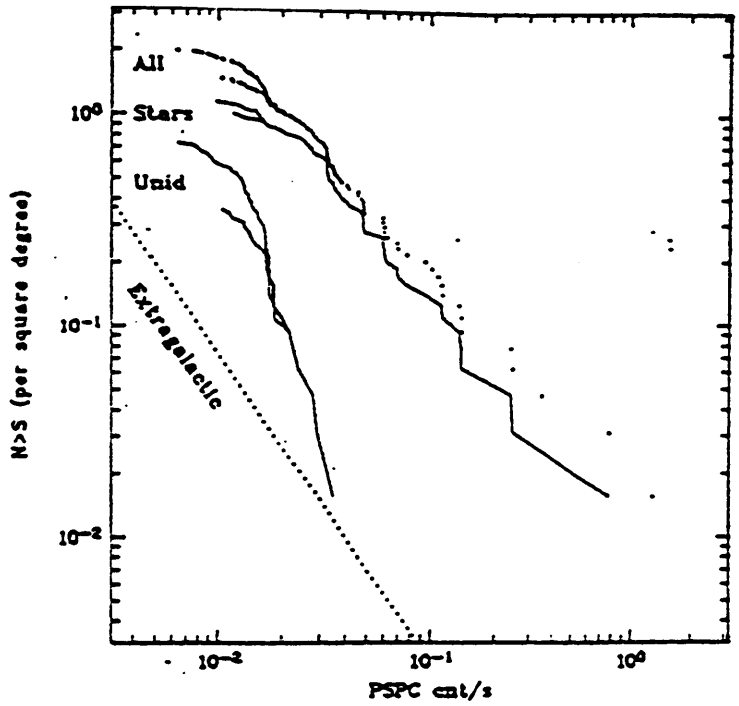

Figure 3.2: RGPS number-flux relations for sources with maximum likelihood $\geq$10 (lower curves) and ML $\geq$8 (upper curves). Relations are shown for the sample as a whole, those sources identified with stars and unidentified sources. The dashed line represents the expected extragalactic contribution. Reproduced from Motch *et al.* 1996.

3.3 Observations

3.3.1 Data selection

The survey used 9 ROSAT PSPC fields, each of $\approx$10ks exposure, to sample the galactic plane at longitudes from roughly 180° to 270° (the 'third quadrant'). A log of the observations is given in Table 3.1, while Figure 3.3 shows the distribution of the fields on the sky. Five of the pointings (numbers 1, 3, 4, 6 and 8) were specifically performed for this programme, while the remaining four datasets were obtained from the archive. These were the *only* archive datasets that fulfilled our criteria when the data selection for the project was made, in 1994 August. This remains true at 1995 November. The target objects for these latter pointings are noted in Table 3.1. All field positions were selected to avoid molecular clouds, strong ($\gtrsim$ 0.2 PSPC count s^{-1}) known X-ray sources, bright stars and SNRs, all of which might distort the survey. Each observation was required to have at least 8 ks exposure and to lie within 0.3° of the galactic plane. A reasonably uniform sampling in longitude was achieved for 180° $\lesssim l \lesssim$ 250°. The gap in the region

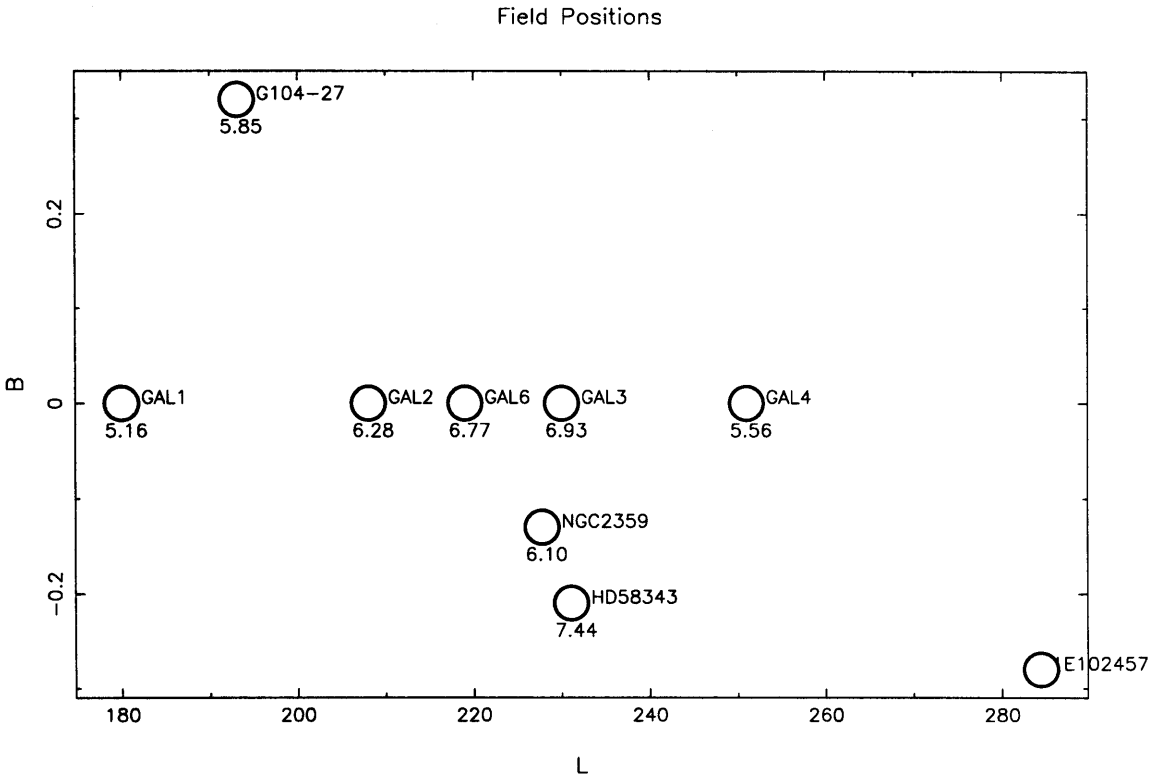

Figure 3.3: Location of the 9 PSPC fields used in the survey along the Galactic Plane. Shown with each field position is the value of the galactic n_H column number density in that direction (as $(n_H \times 10^{-21} cm^{-2})$ derived from the 21cm observations of Stark *et al.* (1992).

$260° \lesssim l \lesssim 270°$ is due to the Vela supernova remnant. In order to provide some sampling in this area, we included in our analysis field number 9, at $l \approx 284°$. The most heavily sampled region is around $l \approx 230°$, with fields 5, 6 and 7.

3.3.2 Source Searching

The point-spread function (PSF) of the PSPC widens with off-axis angle. Due to the increased background per source 'beam' at larger angles we get a lower sensitivity and a higher uncertainty in source position. The nature of this study ultimately requires correlation of the X-ray sources with optical sources, hence an accurate measurement of X-ray source position is very important. Due to this, the analysis was restricted to the inner 18 arcmin radius of all survey fields. This restriction also made background

and sensitivity-level calculations easier as there were no window support rings or ribs to account for. Those fields chosen from the archive had the central 3.5 arcmin radius removed from the analysis to prevent bias due to the central objects in these fields having been selected for their interesting nature[2]. Data intervals with poor aspect solutions or high anti-coincidence rates were also rejected (as discussed in Chapter 2).

Point source searches were carried out on the data. Three bands were defined, 0.1–0.4keV (PI channels 11—42), 0.4–2keV (channels 43—202) and 0.1–2keV (channels 11—202), designated 'soft', 'hard' and 'total' bands respectively. 256×256 pixel images were made in each band, with each pixel being 15×15arcsec^2. The data were analysed with the UK Starlink ASTERIX X-ray data-analysis software system and its point-source search algorithm PSS. Background levels were determined by first measuring the average count-rate in the central 18arcmin radius of an image. This was used for a preliminary PSS run. Detections made in this first run with a significance $>4.5\sigma$ were then removed and the resulting image smoothed using a 20×20 pixel^2 tophat function. This was used as the background model for a second PSS run where detections were accepted to be X-ray sources if they exceeded a significance of 4.5σ. In the total-band 93 sources were detected, however most of these (89) were detected in the hard-band and only 12 were detected in the soft-band (4 of which were detected in the soft-band only). As the hard-band detections overlap to such a large extent with the total-band and there are so few soft-band detections, this survey concentrates mainly on the hard-band data and considers the soft-band where appropriate. The hard-band detections and the hard-band upper limits on the four soft-only detections are shown in Table 3.2. Sources detected in the soft band are shown in Table 3.3. Also shown in Table 3.3 are the hardness ratios for each source, defined as HR= (H−S)/(H+S) where H is hard-band count-rate and S is soft-band count-rate.

[2]After completion of the analysis Field 9 was found not to have an on-axis target and that the two target sources had been erroneously included in the survey. Were this error to be corrected for the result would be a small (<1%) reduction in survey area and the removal of two sources from the high-flux end of the number-flux relation. This would not change the results of the survey in any significant way.

Table 3.2: Hard Detections and Upper-Limits.

RO	F	RA	DEC	l	b	SIG	C	δC	VMAG	log	N
		(h m s)	(d m s)	(deg)	(deg)		(10^{-3}ct s^{-1})	(10^{-3}ct s^{-1})		FX/FV	
01	1	05 44 40.27	+28 57 35.3	179.871	-0.164	4.914	1.986	0.694	17.25	-1.32	1
02	1	05 44 41.22	+28 47 41.3	180.014	-0.247	5.058	2.785	0.888	19.50	-0.27	1
03	1	05 44 41.37	+29 07 37.2	179.731	-0.073	7.003	3.845	0.987	15.18	-1.86	1
04	1	05 44 45.69	+28 55 06.3	179.917	-0.169	6.113	2.303	0.702	19.38	-0.40	1
05	1	05 44 57.62	+28 58 40.4	179.889	-0.101	12.177	5.258	0.101	17.06	-0.97	1
06	1	05 45 07.19	+29 09 31.5	179.753	0.023	99%	< 0.805		18.28	-1.30	1S
07	1	05 45 13.11	+28 43 33.5	180.133	-0.184	7.831	4.494	0.106	17.55	-0.84	1
08	1	05 45 22.97	+29 10 59.5	179.762	0.084	13.560	8.885	0.139	9.50	-3.77	1
09	1	05 45 27.27	+28 57 46.7	179.958	-0.016	5.293	1.574	0.579	13.24	-3.02	2
10	1	05 45 56.84	+29 07 56.7	179.869	0.163	7.162	3.655	0.938	8.91	-4.39	2
11	2	06 14 23.50	+17 44 29.5	192.988	0.144	4.753	1.690	0.627	13.02	-3.08	2
12	2	06 14 35.95	+17 49 10.0	192.943	0.225	6.320	1.429	0.470	15.30	-2.24	1
13	2	06 14 41.85	+17 34 09.5	193.174	0.126	10.121	4.926	0.974	14.20	-2.14	1
14	2	06 14 42.27	+17 43 32.2	193.037	0.202	7.281	2.085	0.584	12.57	-3.17	2
15	2	06 14 46.78	+17 36 48.3	193.144	0.164	5.223	1.530	0.533	18.41	-0.97	1
16	2	06 15 17.57	+17 39 29.4	193.163	0.293	5.235	1.479	0.507	9.94	-4.37	2
17	2	06 15 34.03	+17 37 55.2	193.218	0.338	5.013	1.067	0.425	12.63	-3.43	2
18	2	06 15 43.23	+17 53 44.3	193.003	0.496	5.877	1.870	0.608	14.42	-2.48	2
19	2	06 15 47.51	+17 52 34.1	193.028	0.501	4.840	1.156	0.453	17.25	-1.55	1
20	2	06 15 54.51	+17 34 59.6	193.299	0.386	6.075	2.247	0.674	15.40	-2.00	1
21	2	06 16 05.30	+17 37 27.6	193.284	0.444	9.782	4.211	0.877	11.85	-3.15	2
22	2	06 16 24.75	+17 39 57.4	193.284	0.532	99%	< 1.430		16.52	-1.76	1S
23	3	06 41 29.91	+04 19 56.9	207.944	-0.231	5.026	3.608	0.976	16.39	-1.41	1T
24	3	06 41 36.16	+04 28 55.4	207.822	-0.139	11.602	6.753	1.126	7.87	-4.54	3
25	3	06 41 36.24	+04 31 41.9	207.781	-0.117	7.135	3.331	0.802	13.52	-2.58	1
26	3	06 41 50.69	+04 20 08.5	207.980	-0.152	13.516	5.593	0.926	16.45	-1.19	1
27	3	06 41 59.31	+04 28 47.9	207.868	-0.054	8.992	3.162	0.727	15.44	-1.84	1
28	3	06 42 13.47	+04 09 31.9	208.181	-0.149	4.684	1.769	0.612	16.65	-1.61	1
29	3	06 42 45.14	+04 23 21.8	208.036	0.073	8.358	2.712	0.659	9.01	-4.48	2
30	3	06 42 45.30	+04 18 40.2	208.106	0.038	10.221	3.588	0.760	18.08	-0.73	1
31	3	06 43 00.59	+04 25 16.7	208.037	0.145	5.009	1.311	0.496	13.59	-2.96	1
32	3	06 43 11.50	+04 12 42.1	208.244	0.089	7.579	3.536	0.824	13.75	-2.47	1
33	4	07 01 21.23	-05 26 42.4	218.906	-0.283	7.337	4.516	1.083	14.03	-2.25	1
34	4	07 01 22.42	-05 24 51.6	218.881	-0.264	11.291	6.984	1.248	15.44	-1.49	1
35	4	07 01 25.01	-05 22 22.0	218.849	-0.236	6.081	2.929	0.846	10.24	-3.95	1

Table 3.2: – *continued*

RO	F	RA (h m s)	DEC (d m s)	l (deg)	b (deg)	SIG	C (10^{-3}ct s^{-1})	δC (10^{-3}ct s^{-1})	VMAG	log FX/FV	N
36	4	07 01 52.48	-05 25 51.0	218.953	-0.161	33.554	23.249	1.967	12.23	-2.26	2
37	4	07 01 58.50	-05 36 18.7	219.119	-0.219	14.637	10.562	1.515	18.41	-0.13	1
38	4	07 02 05.87	-05 33 22.5	219.090	-0.169	6.135	2.107	0.655	16.50	-1.59	1
39	4	07 02 30.16	-05 10 40.5	218.799	0.093	6.099	2.529	0.769	17.29	-1.20	1
40	4	07 02 51.91	-05 14 16.5	218.894	0.145	13.609	6.653	1.112	19.28	0.01	1
41	4	07 03 07.17	-05 35 19.7	219.235	0.041	12.546	8.211	1.332	13.39	-2.24	1
42	4	07 03 24.52	-05 27 29.2	219.152	0.165	5.286	2.513	0.802	10.30	-3.99	1
43	5	07 17 30.72	-13 05 23.1	227.527	-0.278	6.963	2.323	0.527	12.76	-3.05	2
44	5	07 17 32.64	-13 20 28.0	227.752	-0.388	7.461	2.560	0.544	12.48	-3.11	1
45	5	07 17 34.27	-13 17 47.2	227.716	-0.362	5.039	1.353	0.410	15.68	-2.11	1
46	5	07 17 41.39	-13 22 06.3	227.793	-0.370	5.563	1.816	0.488	16.65	-1.60	1
47	5	07 17 43.24	-13 25 23.3	227.846	-0.389	99%	< 0.518		15.50	0.68	1S
48	5	07 17 49.17	-13 15 14.4	227.707	-0.288	8.908	1.763	0.380	15.90	-1.91	1
49	5	07 18 05.63	-12 58 28.3	227.491	-0.099	5.965	1.821	0.466	12.00	-3.45	2
50	5	07 18 06.08	-13 18 37.5	227.789	-0.254	6.481	1.335	0.363	13.28	-3.08	2
51	5	07 18 08.13	-13 19 58.1	227.812	-0.257	4.761	1.005	0.336	10.89	-4.16	2
52	5	07 18 10.83	-13 22 38.5	227.857	-0.268	8.365	1.945	0.434	14.42	-2.46	1
53	5	07 18 12.13	-13 06 34.4	227.623	-0.138	5.311	0.981	0.315	15.40	-2.36	1
54	5	07 18 13.02	-13 27 04.1	227.926	-0.295	6.417	2.153	0.512	15.39	-2.03	1
55	5	07 18 13.29	-13 23 54.8	227.880	-0.269	23.129	8.529	0.827	16.75	-0.88	1
56	5	07 18 38.49	-13 01 15.7	227.594	-0.002	6.983	2.100	0.484	11.45	-3.61	2
57	5	07 18 44.34	-13 06 47.5	227.687	-0.025	8.840	2.261	0.467	17.50	-1.16	1
58	5	07 18 48.47	-12 57 23.4	227.556	0.063	6.061	1.867	0.479	14.33	-2.51	1
59	5	07 19 10.30	-13 14 56.1	227.856	0.004	14.549	3.699	0.544	9.20	-4.27	1
60	6	07 22 25.08	-15 10 59.3	229.933	-0.210	5.613	2.508	0.753	11.31	-3.59	1
61	6	07 22 29.87	-15 04 04.6	229.841	-0.138	7.157	3.699	0.908	15.90	-1.59	1
62	6	07 23 05.23	-15 17 46.1	230.109	-0.121	9.072	2.696	0.680	16.50	-1.48	1
63	6	07 23 07.04	-14 58 41.3	229.832	0.035	5.310	1.741	0.573	13.59	-2.84	2
64	6	07 23 14.56	-14 52 51.2	229.761	0.107	6.045	2.693	0.769	8.13	-4.83	3
65	6	07 23 31.02	-15 12 20.6	230.078	0.012	9.204	3.436	0.794	11.17	-3.51	2
66	6	07 23 33.20	-15 10 29.9	230.055	0.035	4.728	1.224	0.531	10.19	-4.35	2
67	7	07 23 40.72	-16 08 09.3	230.916	-0.392	6.850	3.561	0.901	16.00	-1.56	1
68	7	07 24 01.68	-16 11 40.7	231.008	-0.346	5.187	1.360	0.504	12.86	-3.24	2
69	6	07 24 02.69	-15 05 24.8	230.037	0.179	7.544	2.619	0.674	13.42	-2.73	2
70	6	07 24 03.44	-14 57 16.1	229.919	0.246	4.698	1.961	0.676	15.00	-2.22	1

Table 3.2: - *continued*

RO	F	RA (h m s)	DEC (d m s)	l (deg)	b (deg)	SIG	C (10^{-3}ct s^{-1})	δC (10^{-3}ct s^{-1})	VMAG	log FX/FV	N
71	6	07 24 08.21	-14 59 29.6	229.960	0.245	5.312	2.301	0.724	15.90	-1.79	1
72	7	07 25 18.36	-16 10 35.1	231.137	-0.067	13.797	6.966	1.101	16.87	-0.92	1
73	7	07 25 21.41	-15 56 36.0	230.938	0.053	7.489	4.757	1.050	19.80	0.07	1
74	8	08 09 24.01	-33 30 00.7	251.108	-0.232	5.919	5.424	1.694	12.82	-2.65	2
75	8	08 09 26.33	-33 20 15.2	250.976	-0.137	5.323	3.570	1.320	11.88	-3.21	2
76	8	08 09 26.95	-33 25 16.6	251.048	-0.180	6.339	4.732	1.474	16.50	-1.24	1
77	8	08 10 18.42	-33 06 10.3	250.879	0.143	4.988	2.425	1.011	15.60	-1.89	1
78	9	10 22 59.46	-57 42 41.6	284.128	-0.363	99%	< 4.085		15.90	-1.54	1
79	9	10 23 38.83	-57 58 00.1	284.339	-0.532	5.333	3.094	0.896	12.41	-3.06	2
80	9	10 23 43.65	-57 38 33.8	284.175	-0.252	6.401	3.418	0.888	9.09	-4.35	3
81	9	10 23 50.65	-57 57 44.3	284.359	-0.514	5.436	2.769	0.833	6.86	-5.33	3
82	9	10 23 59.78	-57 45 34.8	284.268	-0.332	27.617	33.671	2.581	15.60	-0.75	4
83	9	10 24 14.97	-57 39 46.8	284.245	-0.232	5.432	1.911	0.623	17.01	-1.43	1
84	9	10 24 47.19	-57 32 54.8	284.245	-0.097	4.803	2.137	0.722	14.64	-2.33	1
85	9	10 25 01.52	-57 54 24.9	284.462	-0.384	4.924	2.037	0.695	15.04	-2.19	1
86	9	10 25 35.09	-57 50 50.8	284.493	-0.294	9.766	3.245	0.711	15.32	-1.88	1
87	9	10 25 45.58	-57 35 30.9	284.378	-0.065	10.275	6.662	1.179	15.60	-1.45	1
88	9	10 25 52.33	-57 54 00.0	284.554	0.318	5.965	2.284	0.658	14.92	-2.19	1
89	9	10 25 54.37	-57 37 57.4	284.416	-0.089	8.537	3.644	0.828	12.75	-2.85	2
90	9	10 25 55.13	-57 48 52.3	284.514	-0.243	68.287	95.453	3.941	13.27	-1.23	2
91	9	10 26 03.40	-57 59 15.5	284.621	-0.380	27.257	29.346	2.351	13.88	-1.50	1
92	9	10 26 04.09	-57 46 38.6	284.511	-0.201	5.336	2.197	0.716	12.93	-3.00	2
93	9	10 26 11.14	-57 56 55.8	284.615	-0.338	12.579	8.676	1.335	15.90	-1.22	1

Notes: Columns are: source number, PSPC field number, RA, DEC (J2000), galactic latitude and longitude, significance of detection, count-rate, count-rate error (1σ, lower limit on visual magnitude (as discussed in section 3.5) and the log of the X-ray to optical flux ratio (discussed in section 3.6). The final column indicates the identification status of a source: 1=unidentified with possible optical counterpart on Schmidt plates, 2=possible counterpart in the HST Guide Star Catalogue (GSC), 3=possible counterpart detected in the GSC and SIMBAD database, 4=SIMBAD reference only with no GSC counterpart.

Table 3.3: Soft Detections.

RO	F	RA (h m s)	DEC (d m s)	l (deg)	b (deg)	SIG	C ($\times 10^{-3}$ct s^{-1})	δC ($\times 10^{-3}$ct s^{-1})	HRATIO
06	1	05 45 07.19	+29 09 31.5	179.75318	0.02296	5.153	4.569	1.223	<-0.640
16	2	06 15 17.57	+17 39 29.4	193.16395	0.29364	8.173	4.584	0.908	-0.512
21	2	06 16 05.30	+17 37 27.6	193.28400	0.44415	4.836	3.115	0.889	0.149
22	2	06 16 24.75	+17 39 57.4	193.28414	0.53188	6.259	5.458	1.205	<-0.690
24	3	06 41 36.16	+04 28 55.4	207.82292	-0.13909	8.738	7.096	1.232	-0.024
25	3	06 41 36.24	+04 31 41.9	207.78194	-0.11763	4.991	4.032	1.081	-0.095
36	4	07 01 52.48	-05 25 51.0	218.95326	-0.16154	19.754	6.124	1.188	0.583
47	5	07 17 43.24	-13 25 23.3	227.84553	-0.38908	5.077	2.320	0.605	<-0.397
67	7	07 23 40.72	-16 08 09.3	230.91691	-0.39249	7.621	5.810	1.180	-0.239
78	9	10 22 59.46	-57 42 41.6	284.12897	-0.36381	5.774	4.028	1.025	<0.006
91	9	10 26 03.40	-57 59 15.5	284.62120	-0.38046	7.417	4.381	0.981	0.740
93	9	10 26 11.14	-57 56 55.8	284.61527	-0.33847	9.754	7.271	1.251	0.088

Notes: Columns are: source number, PSPC field number, RA, DEC (J2000), galactic latitude and longitude, significance of detection, count-rate, count-rate error (1σ) and hardness ratio (where not detected in the hard-band this is the hardness ratio upper limit as shown).

3.4 The Number–Flux Relation.

The detection count-rate threshold is a function of position in each PSPC field since it depends on bachground level and vignetting. Each field has a similar yet different distribution of thresholds. Thus each source will have its own associated coverage fraction within the survey. Figure 3.4a shows the hard-band coverage correction curve for the survey. The curve takes into account the differences in survey area between our fields and those chosen from the public data archive. This difference in area arises from the fact that the archive fields had their central portions removed in order to eliminate bias due to the objects being studied in those pointed observations. It can be seen that good coverage is achieved down to around 0.002 counts per second, with $\approx$ 90% of the survey area being above this threshold. Below 0.002 counts per second there is a sharp fall off in coverage but we do still obtain some ($\approx$30%) coverage down to $\approx$0.001 counts per second. Figure 3.4c shows the soft-band coverage correction curve, where down to $\approx$ 0.004 ct s^{-1} we have 90% coverage. This drops to $\approx$80% at 0.003 ct s^{-1} and to <20% at 0.002ct s^{-1}.

From the coverage curves it is straightforward to calculate the hard and soft-band corrected number-flux relations. For each source-flux the percentage of the survey area covering that

flux was found. Integrating this distribution yielded the number-flux relation as shown in Figures 3.4b and 3.4d.

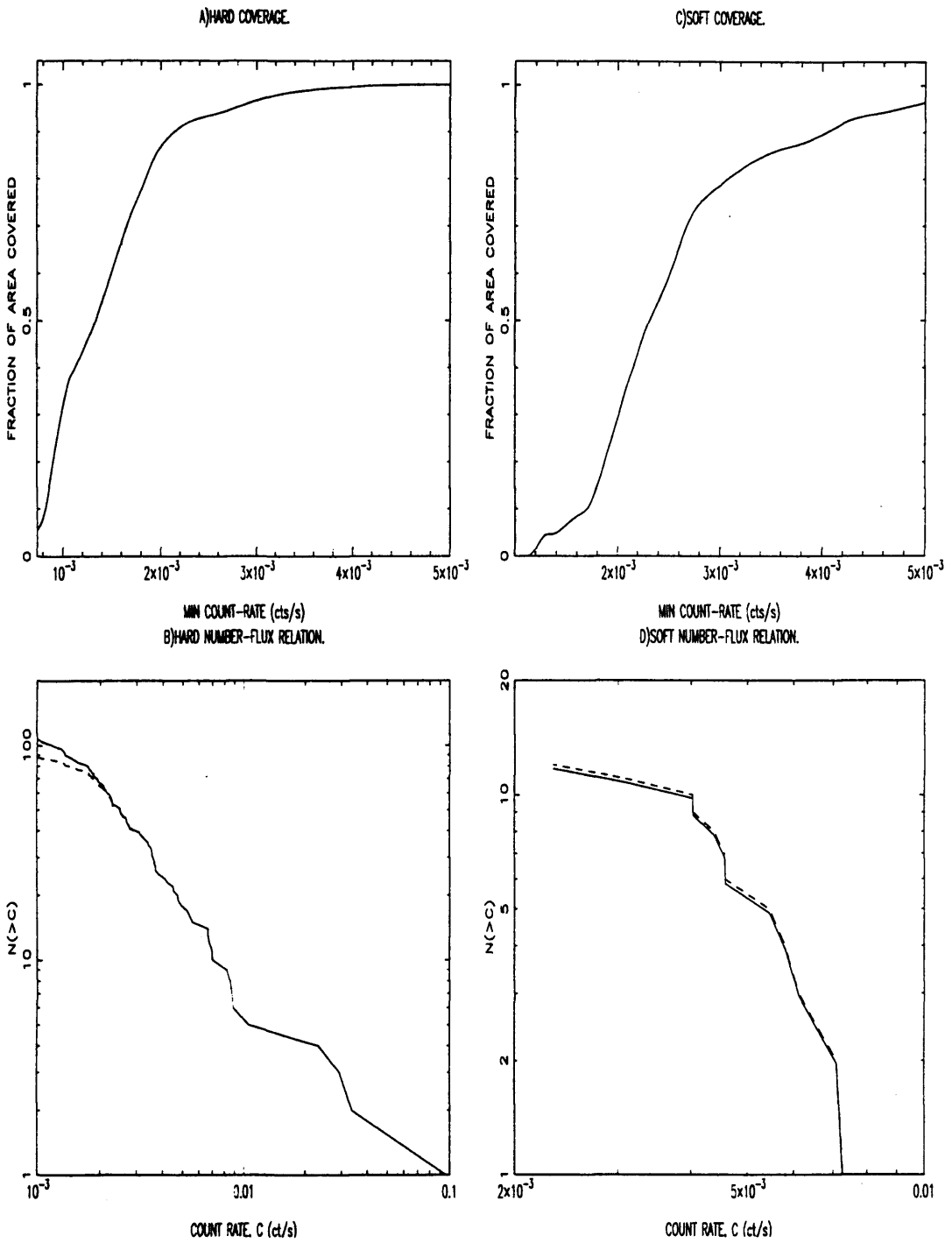

Figure 3.4: The coverage curves for the survey a)Hard-band, c)Soft-band. These take into account the differences in area between fields and different background levels. The number-flux relations are shown here in integral form, with both the raw-counts (dashed line) and coverage-corrected (solid line) b)Hard-band, derived from the 89 Hard sources detected in our 9 PSPC fields and d)Soft-band, derived from the 12 soft sources.

3.4.1 Calculating the Index and Normalisation

A power-law ($N(>S)=N_0S^{-\alpha}$) was fitted to the calculated number-flux relation for the hard-band only. Theoretically for a uniform, isotropic, distribution of sources, with no absorption, the value of α should be 1.5. Before fitting the power law, an estimate of the contribution to our source counts from extragalactic sources was removed. This required an assumption for the 'extra-galactic transmission factor' (EGTF) defined as $EGTF=C_a/C_u$, where C_a is the count-rate from an extragalactic source after absorption by the ISM of our own galaxy, and C_u is that count-rate if there were no galactic absorption. By considering a power-law spectrum with typical energy-index values (1—2) and n_H values (5×10^{21}—$10^{22}cm^{-2}$; cf. Table 3.6) the hard-band EGTF was found to lie in the range 0.2—0.3. The hard-band EGTF was thus nominally taken to be 30%, however analysis was also conducted using values of 20% and 0% (corresponding to zero extragalactic source contribution). The extra-galactic contributions were calculated using the ROSAT high-latitude source counts of Hasinger *et al.* (1993) and Branduardi-Raymont *et al.* (1994), both suitably attenuated by absorption in the galactic plane (see Table 3.4). Table 3.5 summarises the index and normalisation values found by fitting a power law model and using the different values for the extra-galactic transmission factor and the two sets of values for the high-latitude source counts.

Figures 3.5a to 3.5f show the 2-parameter, normalisation and index, fit of the model to the source counts, with regions of 68%, 90% and 99% confidence shown. Figures 3.6a and 3.6b show the single parameter fit for the index for both sets of high-latitude source counts, while Figures 3.6c and 3.6d show that of the normalisation[3]

Hence we see, for a 30% transmission factor and the Hasinger *et al.* source counts, the integral number-flux relation of the sources brighter than 0.002ct/s can be represented by a power law where at 90% confidence, the index $\alpha = 1.3\pm^{0.6}_{0.4}$ and the normalisation $N_0 = 21 \pm 5$ (N_0 = the number of sources per square degree above a countrate of 0.002ct

[3]The horizontal lines representing nominal, 68% and 90% confidence levels were derived using the work of Lampton, Margon and Bowyer (1976) on parameter estimation in X-ray astronomy. This shows that for one free parameter, the value of χ^2 at 68% confidence is equal to the minimum value plus one, and at 90% confidence it is equal to the minimum value plus 2.71.

Table 3.4: High-Latitude Source-Count Parameters.

	Branduardi-Raymont	Hasinger
Normalisation K	82.2	49.3
Break Flux	1.64	2.66
($\times 10^{-14}$ erg cm^{-2} s^{-1})		
index 1	1.78	1.94
index 2	2.64	2.72

Notes: Parameters derived by Hasinger *et al.* (1993) and Branduardi-Raymont *et al.* (1994) for a broken power-law model of high-latitude source counts.

Table 3.5: Index and normalisation values for the Galactic Plane source-counts after removal of an estimated extra-galactic contribution.

High-Latitude	Values at			Values at			Values at		
Source-count	EGTF=0.3			EGTF=0.2			EGTF=0.0		
Model	Best	68%	90%	Best	68%	90%	Best	68%	90%
	INDEX			INDEX			INDEX		
Hasinger	1.31	1.06 1.64	0.9 1.89	1.35	1.12 1.64	0.98 1.87	1.4	1.17 1.65	1.05 1.85
B-Raymont	1.33	1.08 1.66	0.93 1.9	1.34	1.13 1.66	1.0 1.88	1.39	1.17 1.66	1.05 1.85
	NORM			NORM			NORM		
Hasinger	20.62	17.21 23.94	15.1 26.2	23.1	19.76 26.46	17.52 28.66	25.73	22.28 28.9	20.0 31.1
B-Raymont	21.37	17.88 24.7	15.75 26.84	23.31	20.0 26.74	17.82 28.95	25.72	22.23 28.95	20.06 31.15

Notes: Index and normalisation parameters calculated using high-latitude source counts of Hasinger *et al.* (1993) and Branduardi-Raymont *et al.* (1994). The best-fit value, 68% and 90% values are shown for extra-galactic transmission factors of 0.3, 0.2 and 0.0.

s^{-1}). Changing the extra-galactic transmission factor is seen to change the results for the index only slightly ($\approx$5% change in index value for a 30% change in EGTF), whilst the normalisation simply scales upwards as the transmission factor decreases

3.5 Optical searches

In order to understand the X-ray sky it is important to identify as many of the sources detected as possible. At the very least an estimated magnitude is required in order to

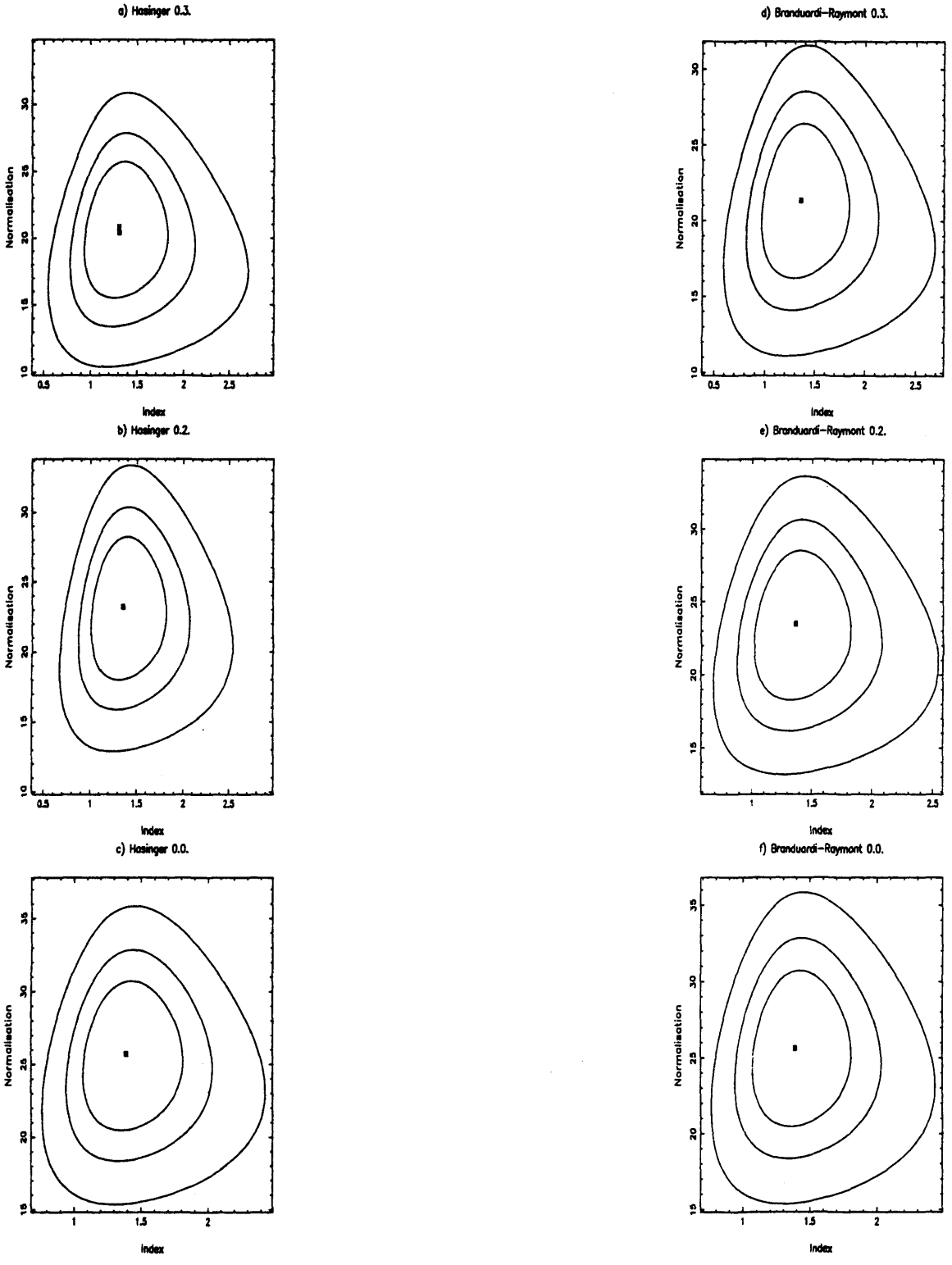

Figure 3.5: 2-parameter, normalisation and index, fit of the power-law model to the hard-band source counts, using 30%, 20% and 0% as the extra-galactic transmission factor and the high-latitude source counts of Hasinger *et al.* (1993) in Figures 3.5a to 3.5c and Branduardi-Raymont *et al.* (1994) in Figures 3.5d to 3.5f. Regions of 68%, 90% and 99% confidence are shown.

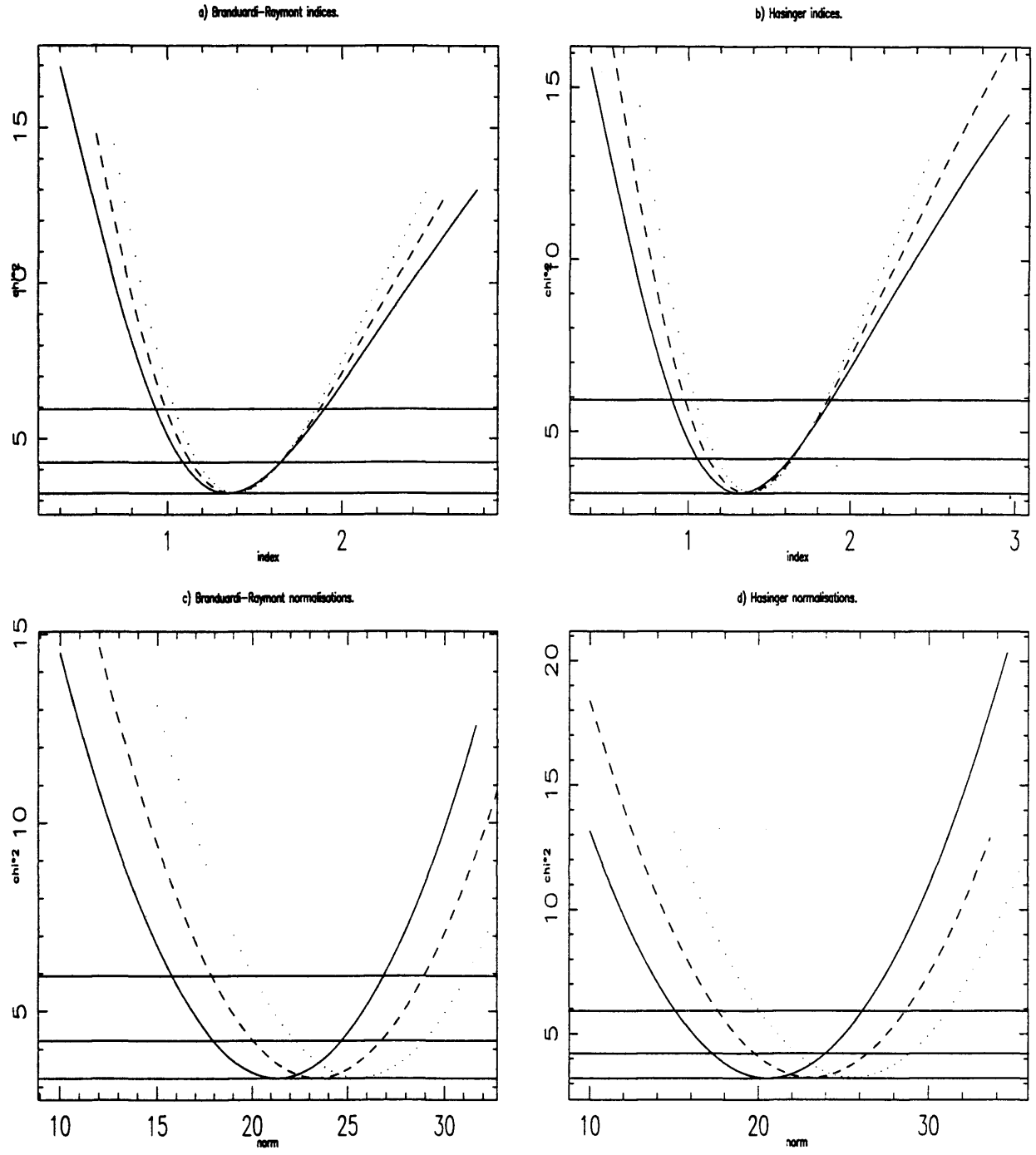

Figure 3.6: Figures (a) and b) show the single-parameter fit for the index using both sets of high latitude source counts. Figures c) and d) show that of the normalisation. The horizontal lines indicate the nominal, 68% and 90% parameter values. As in Figure 3.5, 3 EGTF values are used, solid curve indicates EGTF of 30%, dashed indicates 20% and dotted 0%.

calculate the X-ray to optical flux ratio. The identification scheme comprised firstly of a positional coincidence search of the SIMBAD database and the HST Guide Star Catalogue (GSC). This was followed by an analysis of sky-survey plates from the Palomar Observatory Sky Survey (POSS), UK Schmidt and ESO Schmidt. Digital scans of these plates were provided by J. Pilkington (RGO) using the PDS machine at RGO Cambridge. Figure 3.7 shows the separation between X-ray position and optical position of sources in the Hyades Star Cluster (from the survey discussed in Chapter 4). This shows that the majority of our galactic plane X-ray sources would be expected to lie within $\approx$0.3 arcmin, or $\approx$20arcsec, of their optical positions. This figure was used in the identification process to determine which objects should be considered as potential optical counterparts of our X-ray sources. If no candidates were present in the 20arcsec ring, this was extended to 30arcsec.

Only a small number of our sources (4) had a likely match in the SIMBAD catalogue. However a substantial fraction ($\approx$33%) had a possible match in the GSC. The majority of the sources however remained unidentified. Thus an attempt at a magnitude estimate for possible candidates was made using the Schmidt survey plates. Each sky area was scanned in two different bands. For the POSS plates these were O (blue) and E (red). Twenty of the 93 sources required the use of the ESO B and UKS J plates. UKS J is redder than ESO B but not as red as POSS E. However for the purposes of our rough magnitude estimation this makes little difference. All objects, down to the plate limit, lying within 20arcsec (30 arcsec if no sources within 20arcsec) of our X-ray source position were recorded (see Figure 3.9). This resulted in, on average, two or three potential candidates per X-ray source. It is possible to obtain an estimate of stellar magnitudes by direct measurement of the image size on the plate[4]. This was done for all likely candidates using the E and J scans. The brightest candidate in each error box thus gives us a lower limit for the magnitude. Only one source had no possible optical counterpart within 30arcsec of the X-ray position. An error on the magnitude can be derived from the accuracy of the measurement of the image radius. One image pixel was possible, for smaller objects (less than 16th magitude) this translates to an error of $\pm$1 magnitude. Brighter sources are measured to a greater accuracy, with a pixel error the equivalent of $\pm$0.5 magnitudes. Plate-to-plate calibration

[4]For examples of this technique see Humphreys *et al.* (1991) and King & Raff (1977).

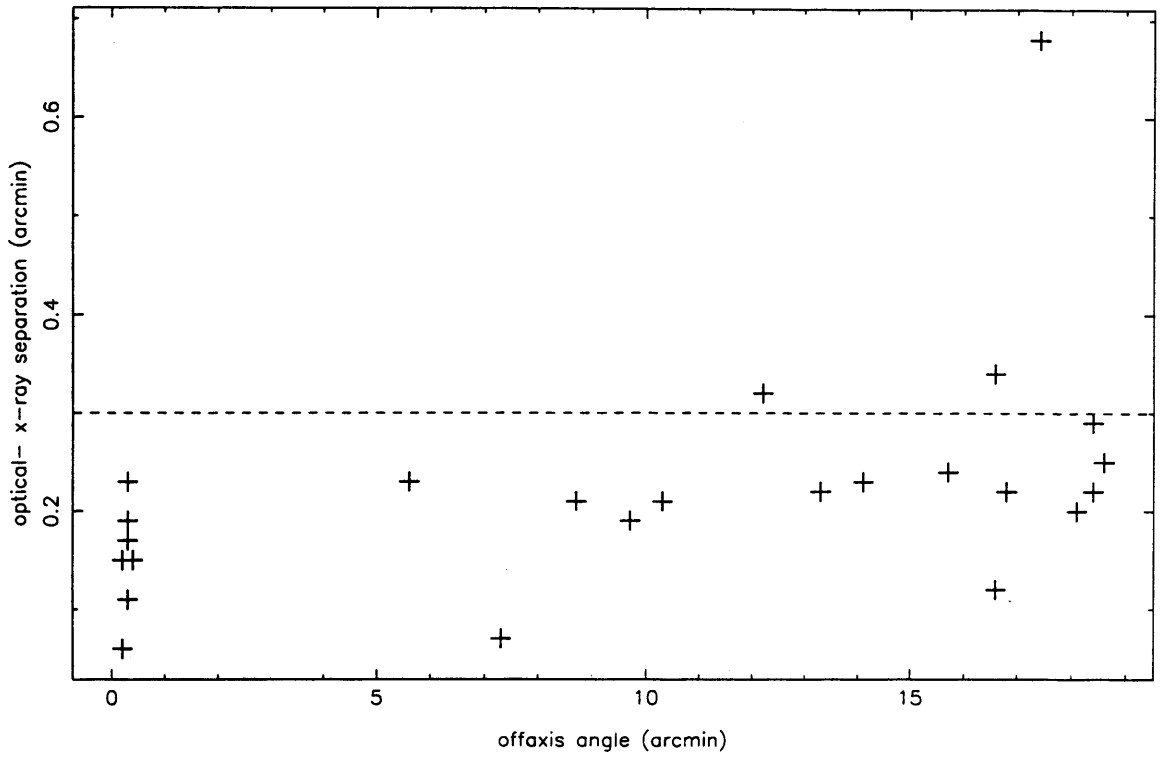

Figure 3.7: Comparison of the X-ray positions of PSPC detected Hyads and their known optical positions as a function of off-axis angle. The dashed line lies at a separation of 0.3arcmin, or ≈20arcsec. It should be noted that the point with a large optical - X-ray separation is not a cause for concern. This star lay on the inner ring of the PSPC in such a position that the wobbling motion of ROSAT made accurate position determination tricky.

errors can also lead to magnitudes estimates being out by ±1 magnitude.

Measured magnitude values of sources identified in the GSC were compared with their known GSC values, see Figure 3.8. This showed a tendency to under-estimate source magnitude by approximately 0.75 magnitudes. All values were corrected for this. There were no source magnitude estimates which, when accounting for systematic errors of ±1 magnitude, did not agree with the magnitude of its possible GSC counterpart (where such correlations existed). A summary of candidate counterparts and numbers of sources found in each field is given in Table 3.6.

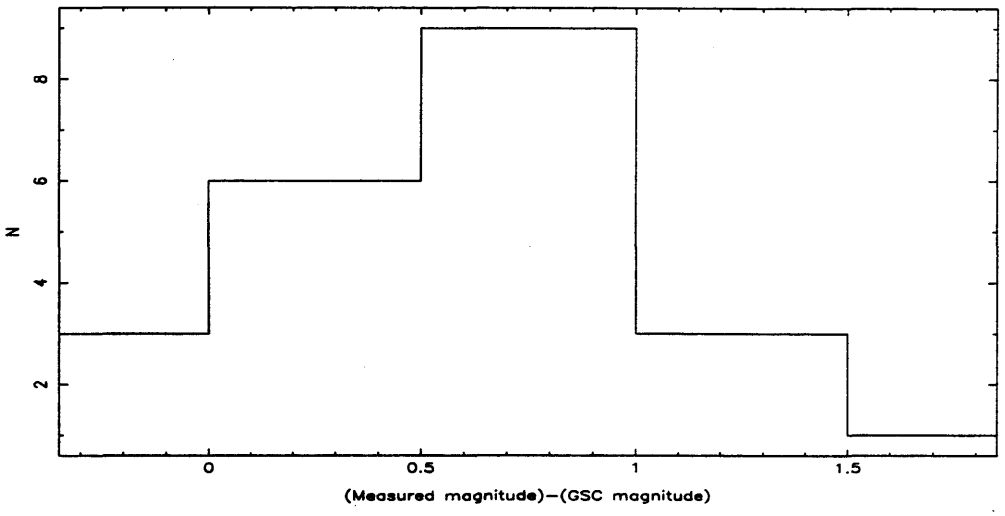

Figure 3.8: Histogram of the difference between my measured magnitude and GSC magnitude. The peak of the distribution shows that the method used here to obtain a source magnitude underestimates the magnitude by ≈0.75 magnitudes.

Table 3.6: Summary of survey results: Numbers of sources per field.

Field	l	b	Name	n_H	T	S	H	Total	Optical
	deg	deg		($\times 10^{21} cm^{-2}$)					1 2 3 4
1	180.00	0.00	GAL1	5.15e21	7	1	9 (8 8.17)	10	2 4 3 1
2	193.10	0.32	G104-27	5.84e21	7	3	11 (4 4.00)	12	1 5 5 1
3	208.00	0.00	GAL2	6.27e21	9	2	9 (7 7.00)	10	0 5 5 0
4	219.00	0.00	GAL6	6.77e21	9	1	10 (10 10.05)	10	1 3 5 1
5	227.75	-0.13	NGC2359	6.10e21	10	1	16 (7 7.00)	17	0 6 6 5
6	230.00	0.00	GAL3	6.92e21	5	0	10 (7 7.01)	10	0 5 2 3
7	231.09	-0.21	HD58343	7.43e21	3	1	4 (3 3.00)	4	0 2 1 1
8	251.00	0.00	GAL4	5.56e21	3	0	4 (4 5.29)	4	0 2 1 1
9	284.39	-0.28	1E102457	—	11	3	16 (15 15.60)	16	1 4 3 8
TOTALS					64	12 (13.66)	89 (65 67.12)	93	

Notes: The columns indicate; field number, galactic longitude and latitude, field name, hydrogen column(from Stark *et al.* (1992) 21cm measurements), number of sources detected in the total, soft and hard bands(the two numbers in parenthesis are the number of sources, observed and coverage corrected respectively, with $\geq$0.002ct s−1) and total number of sources observed per field. The final column indicates the number of sources in a field with 1, 2, 3 or $\geq$4 possible optical counterparts within 30 arcsec of the X-ray position.

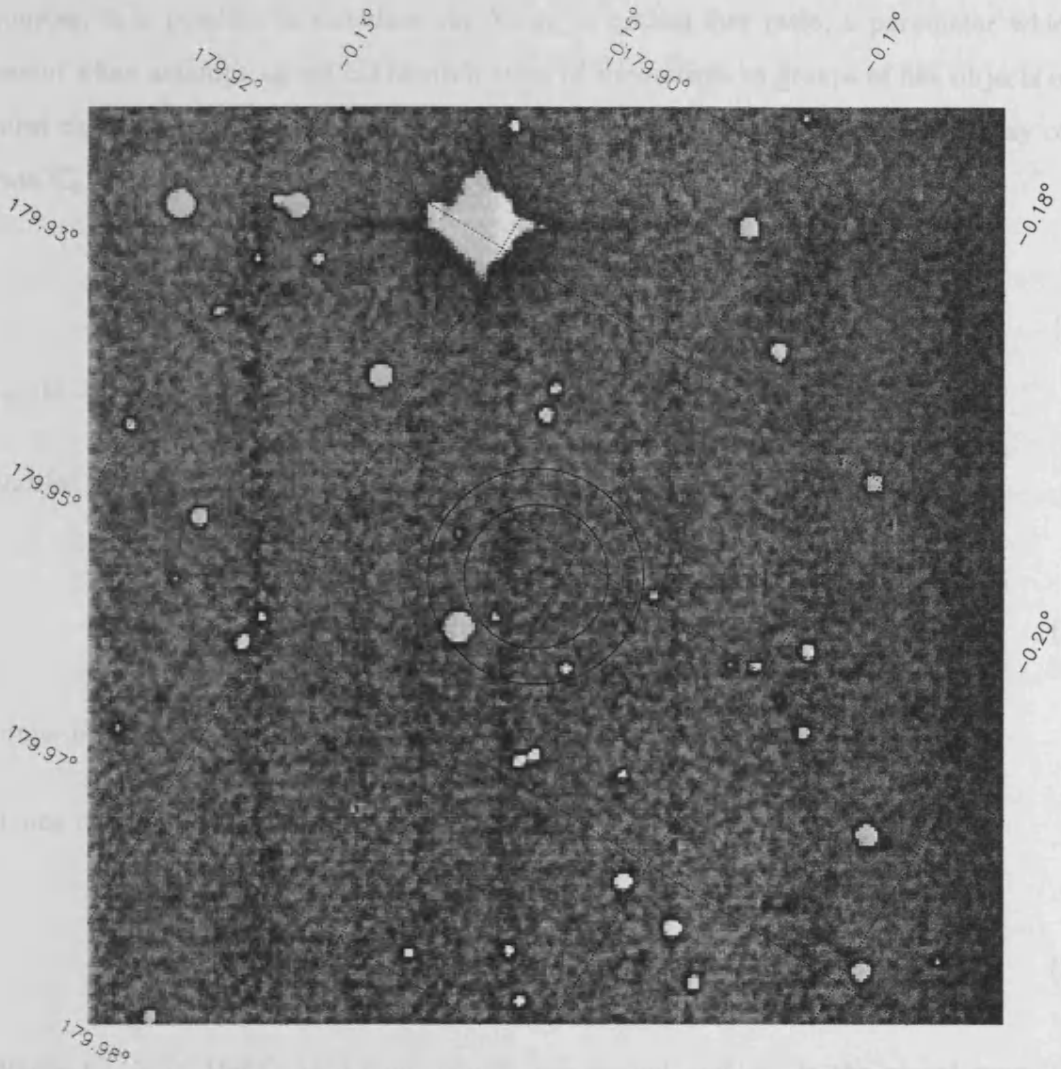

Figure 3.9: Example of POSS plate image centred on one of the X-ray detections. The circles indicate radii of 20 and 30 arcsec. All optical objects (above the plate limit of $m_v \approx 20$) within these regions were recorded, the brightest being used as a lower-limit estimate for the magnitude. The image is centred at the position of X-ray source number 4. The grid shows galactic co-ordinates with North being up and East, left.

3.6 The X-ray to Optical Flux Ratio

Having made an estimate of the optical magnitude (or its lower limit) for each of the sources, it is possible to calculate the X-ray to optical flux ratio, a parameter which is useful when attempting optical identification of the sources as groups of like objects often form characteristic distributions of ratios (Gioia *et al.* 1990). To convert the X-ray count rate C_x, of a source, into a flux f_x, we assume, for the PSPC hard-band:-

$$f_x = 1.0 \times 10^{-11} C_x \tag{3.1}$$

(units — erg $cm^{-2}s^{-1}$)

and for the optical (V-band) flux:-

$$\log f_v = -0.4 m_v - 8.43 \tag{3.2}$$

(units of f_v — erg cm^{-2} s^{-1} $Å^{-1}$, see Astrophysical Quantities, Allen 1973)

Hence the logarithm of the flux ratio is given as :-

$$\log\left(\frac{f_x}{f_v}\right) = \log(C_x) + 0.4 m_v - 5.52 \tag{3.3}$$

Where C_x is in PSPC hard-band counts per second and m_v is the visual magnitude estimate.

Figure 3.10 shows the distribution of $\log(f_x/f_v)$ for sources above 0.002 and 0.001 ct s^{-1}. Also shown are the respective cumulative plots, indicating the increasing number of sources with decreasing x-ray to optical ratio. These can be compared with the results from the WGACAT sources detected in the fields available from the ROSAT public data archive, currently numbering approximately 50000 sources (White *et al.* 1995). All available and useful pointed PSPC observations from Feb 1991 to March 1994 are used in the catalogue, covering $\approx$10% of the sky. However unlike the all-sky survey the coverage can be quite

good with long exposure times (typically a minimum of 5ks as compared to ≈500s in the RASS). In WGACAT, all sources detected had their hardness ratio calculated and had been correlated with the major optical, radio, X-ray and IR catalogues. All optically identified sources also had their X-ray to optical flux ratio calculated. Figure 3.11 shows the X-ray to optical ratio for a number of different types of object (X-ray binaries, CV, White Dwarfs and clusters) taken from the WGACAT. Figure 3.12 shows the $\log(f_x/f_v)$ for AGN, RSCVn and stars, divided into late-type(F-M), early-type(O-A). Figure 3.13 shows separately stars of types F, G K and M. Below a ratio of -2 our sources would appear to be almost purely stellar in origin. Unfortunately our optical flux estimates may only be upper limits to the true flux as it is possible that a dimmer source should have been chosen from inside the error circle. Hence the ratios calculated are, for many sources, only lower limits. Thus accurate measurements could only move the peak of our distribution to the right. Summarised below are some observations and conclusions found in comparing our ratio distribution to those in the WGACAT.

- The RS CVn, M-star and secondary K-star peaks lie in the the same region as the peak of our distribution.
- The galactic plane observations are consistent with being mainly late-type stars and RS CVn's with some CV's.
- The galactic plane observations of sources with $\log(f_x/f_v) \geq 0$ are consistent with being extra-galactic objects (e.g. AGN) or X-ray binaries.
- The galactic plane observations are inconsistent with being mainly early type stars (though some are likely to be present). F, G and early-type stars will account for $<50\%$ of the sources.
- Whilst the galactic plane observations are consistent with white dwarfs, only a few are likely to be observed due to the soft nature of their X-ray spectra.
- Whilst not placing strong constraints on the allowed source populations, these results are consistent with those from the number-flux modelling, presented in the next section.

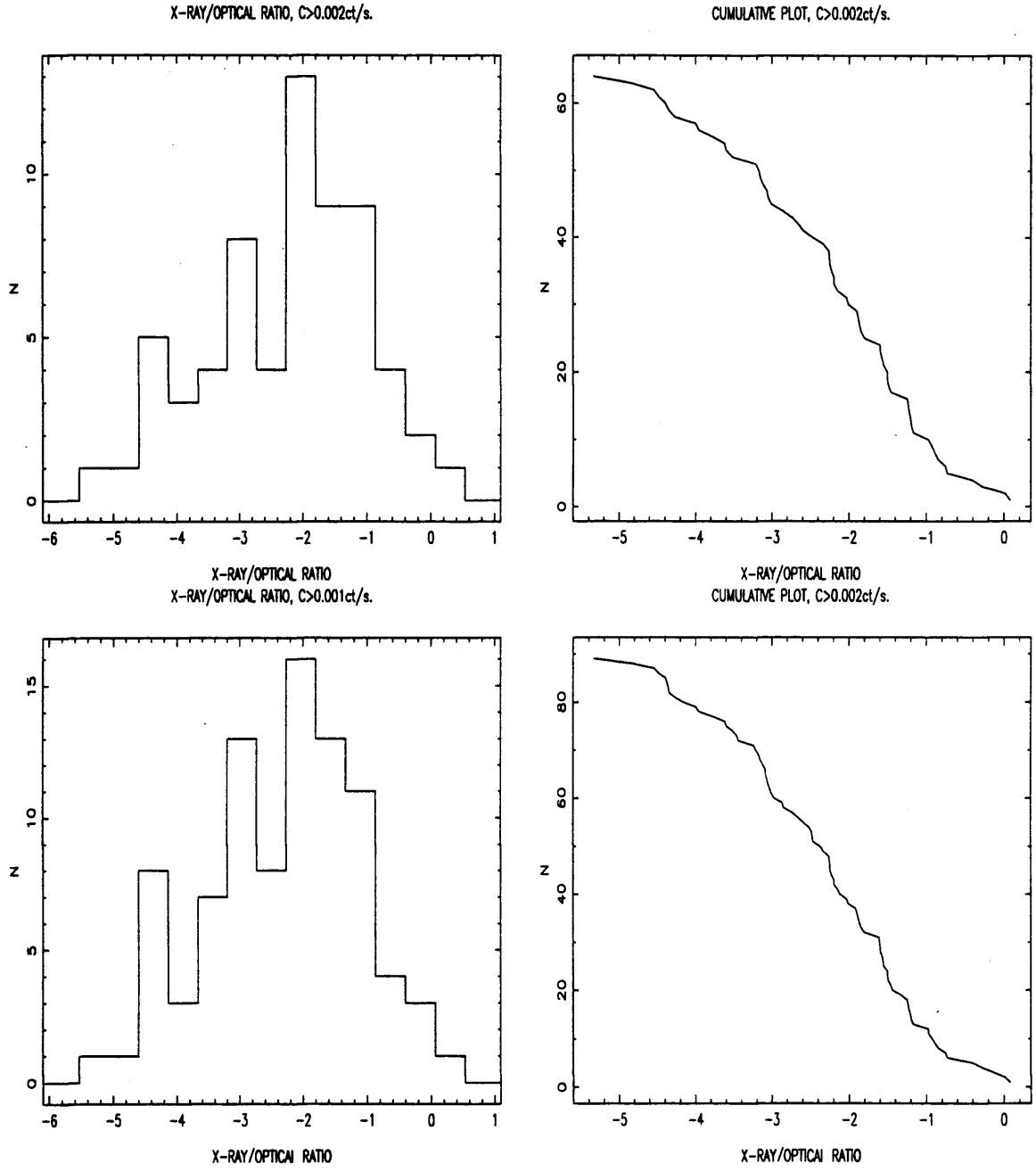

Figure 3.10: Histograms of the log of X-ray to optical flux-ratio of the galactic plane sources with associated cumulative plots. Values are lower limits (see main text). Top figure shows sources with $\geq$0.002 ct s^{-1}, bottom figure shows sources with $\geq$0.001 ct s^{-1}.

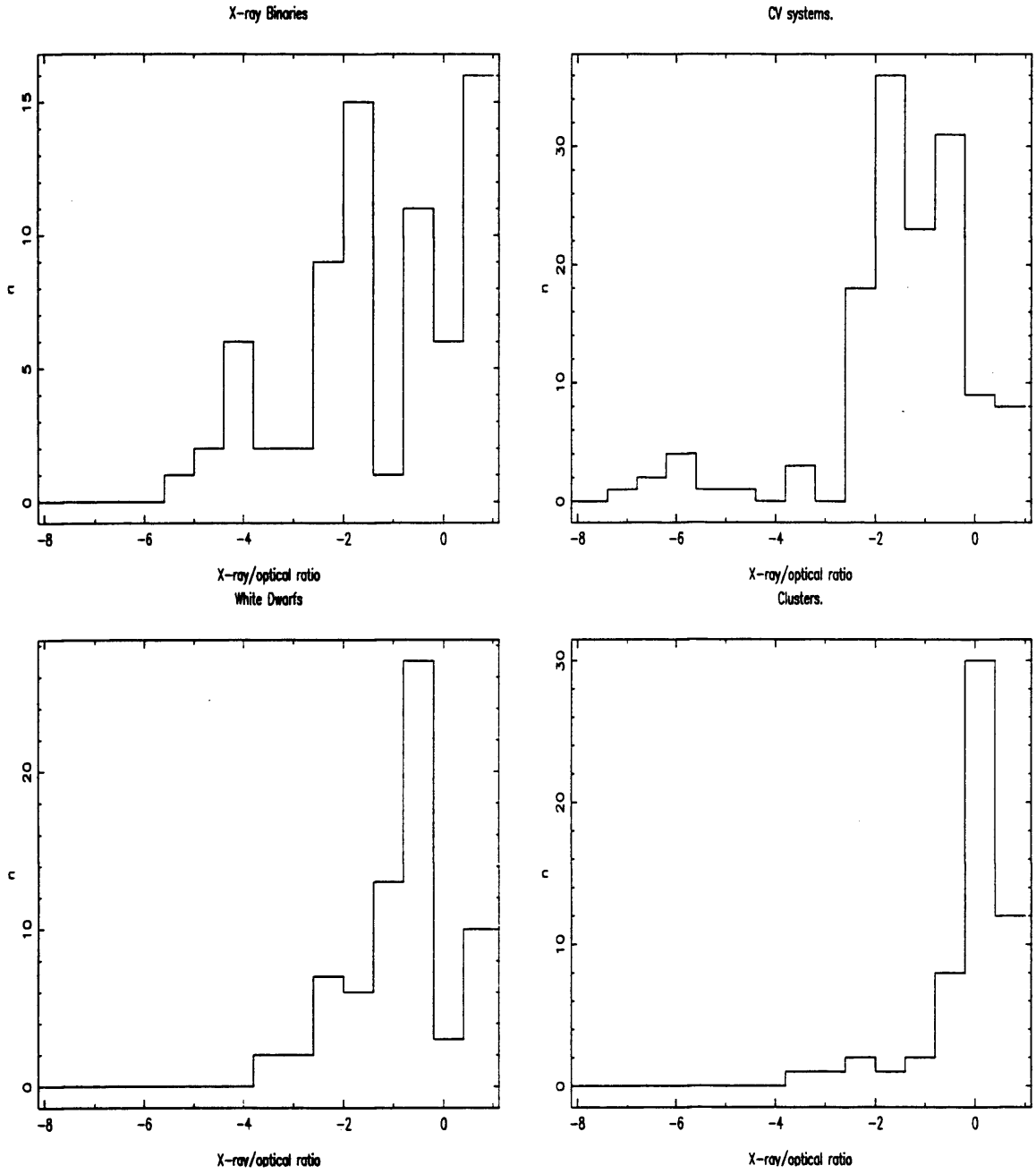

Figure 3.11: Histogram of the X-ray to optical flux-ratio for a number of different types of object (X-ray binaries, CV, White Dwarfs and clusters), from WGACAT.

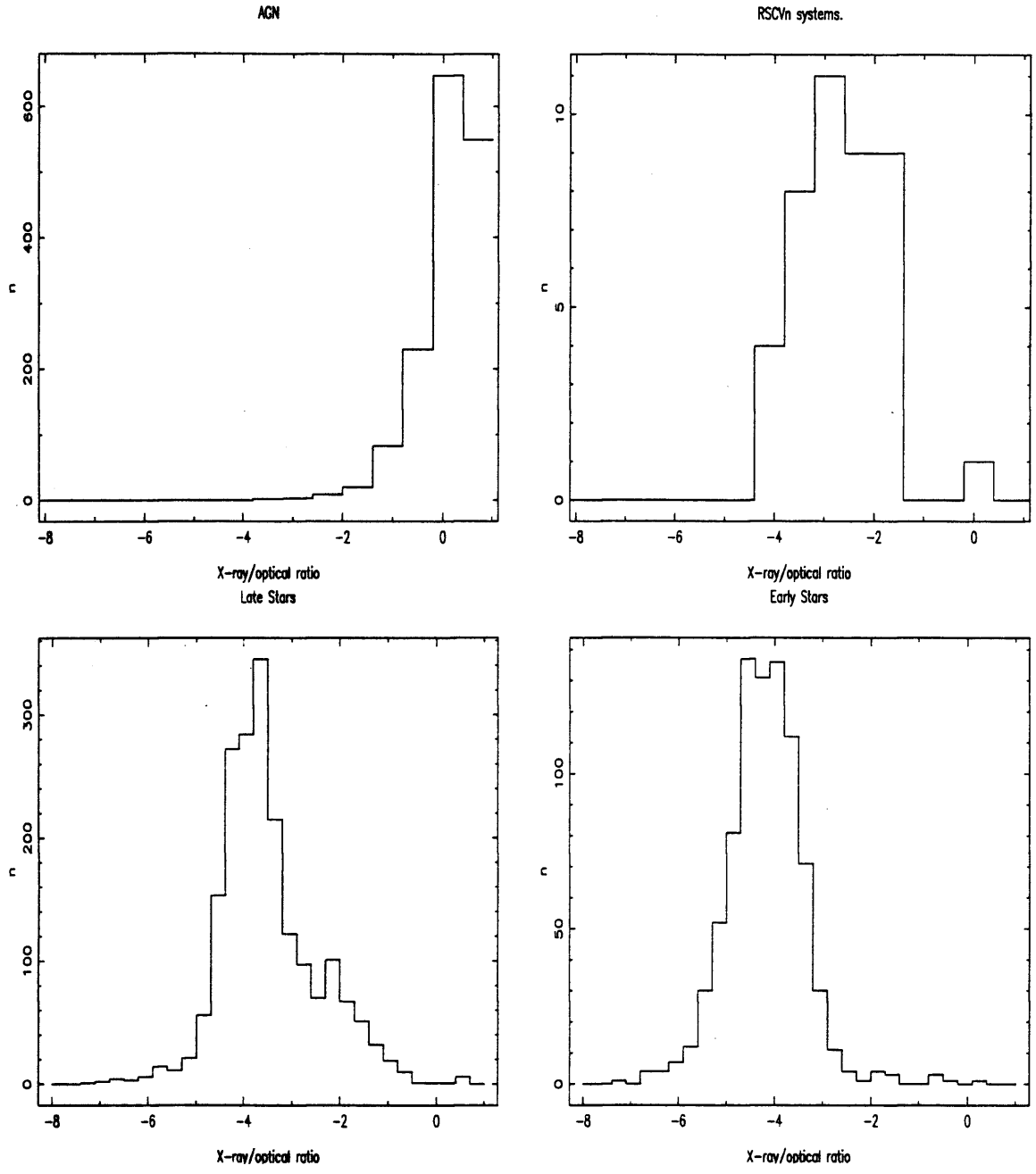

Figure 3.12: Histogram of the X-ray to optical flux-ratio for AGN, RSCVn, early type stars and late type stars from WGACAT.

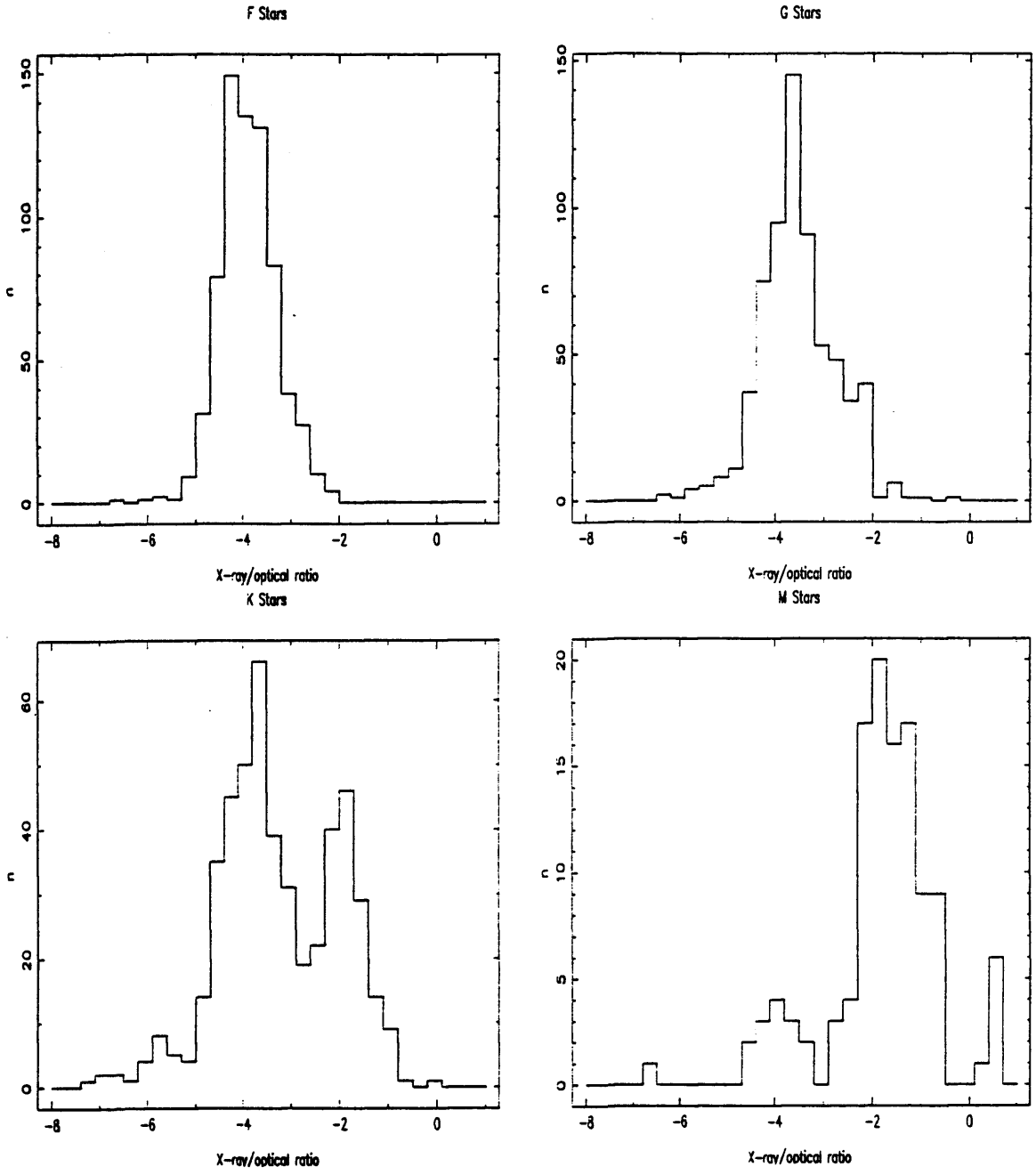

Figure 3.13: Histogram of the X-ray to optical flux-ratio of normal stars (F, G, K and M types) from WGACAT.

3.6.1 The Bimodal Nature of the X-ray to Optical Ratio Distribution in K-Stars

It is interesting to note that in Figure 3.13 we can see two distinct peaks in the distribution of the X-ray to optical flux ratio (this behaviour is mirrored to a lesser extent in G and M stars). The range of optical fluxes involved is small, hence this behaviour must be due to variations in X-ray activity. This would suggest that the peak with the less negative ratio is more active than the other peak. The question is, is there a set of middle range K-stars missing? The problem is that the answer to this question has not yet been established. A recent paper by Sterzik and Schmitt (1997) discusses a survey of cool stars within 25pc of the Sun. They find evidence for such a bimodal nature and suggest it could be due to two distinct populations of K-star, one young, the other older, raising interesting questions about our understanding of galactic star formation. The fact that this bimodal nature is visible in such a volume limited sample at least suggests that there is no selection effect present in the WGACAT data.

3.7 Source Count Modelling

We have taken published galactic stellar X-ray luminosity functions (A, F, G stars - Kashyap *et al.* 1992, K, M stars - Barbera *et al.* 1993 and Fleming *et al.* 1989 , RSCVn stars Favata *et al.* 1995 and Kashyap *et al.* 1992) derived from Einstein and ROSAT studies (see Appendix A), and used them to model source populations and their expected contributions to our measured (coverage-corrected) integral number-flux relation. The contribution from extragalactic sources has already been calculated in the process of finding the index and normalisation of the number-flux relation (Section 3.4.1). Where necessary, Einstein IPC count rates were converted to ROSAT PSPC count rates in our hard band using a Raymond-Smith hot X-ray emitting plasma model, assuming a nominal temperature of $\approx 5\times10^6$K. Results were also found using temperatures of $\approx 3\times10^6$K and $\approx 1\times10^7$K as exact source temperatures are not known. A local bubble model (2 region, with volume number density N=0.05cm^{-3} for 0<d$\leq$100pc; N=0.3cm^{-3} for d>100pc) of the ISM was assumed (Warwick *et al.* 1993). Space densities assumed for each population are shown in Table

Table 3.7: Assumed Space Densities of Stellar Objects

TYPE	DENSITYpc^{-3}
dA	0.0005
dF	0.0025
dG	0.006
dK	0.01
dM-early	0.025
dM-late	0.04
RSCVn	0.00005

3.7 (Kashyap *et al.* 1992, Favata *et al.* 1995). The modelling was done using the program SCOUNT2, courtesy of J.P. Pye. For a given minimum source count rate C_{min} and a luminosity L_i, the program computes the maximum distance $d_{max,i}$ to which sources can be detected, and allows for the effects of ISM absorption. If the volume number density of sources at L_i is n_i, then the total number of detectable sources (per 4π steradians) above C_{min} is given by:

$$N(> C_{min}) = (4/3)\pi \sum_i d^3_{max,i} n_i \tag{3.4}$$

Figure 3.14a shows the predicted individual contributions to our source counts from stellar (dF, dG, dK, early dM (0—4), late dM (5—9) and RSCVn) and extra-galactic sources. For each stellar type there have been a number of different luminosity functions derived over the course of many studies. The luminosity functions used here for modelling purposes are the most recent in the literature (up to June 1996) and are indicated on the figure by a letter in parenthesis refering to the paper from which the luminosity function was obtained. F indicates Fleming *et al.*, K Kashyap *et al.*, Fa Favata *et al.* and B Barbera *et al.*. It is clear that the major contribution to the source counts appears to come from RSCVn systems, a minimum of ≈27% and a maximum of ≈35% contributions at countrates >0.002 PSPC ct s^{-1} (the poorly understood space density of RS CVn's introduces a large error here, see Favata *et al.* 1995), with the contribution from each of the classes F, G, K and early-M stars and extra-galactic sources being roughly equal (within range of ≈ 3%—8%). Summing the contributions from the stellar sources, as in Figure 3.14b, allows us to see the possible extent of the known source contributions. This summing was performed using four different models, each derived using different combinations of the available X-ray

luminosity functions. Taking into account the assumed range of source temperatures we obtain the limits of the stellar contribution to our measured source-counts at 0.002ct/s as being 38% and 56% with a nominal value of 50%. The extra-galactic contribution is ≈8%. That is, of the ≈25 sources per square degree at count rates >0.002 PSPC ct s^{-1} (≈41 at 0.001 PSPC ct s^{-1}), 10—14 can be expected to be stellar in origin.

A similar procedure was carried out on data in the soft band (0.1—0.4keV). Figure 3.15 shows the individual contributions of F, G, K, M and RSCVn stars to the soft source counts (with fewer permutations of luminosity functions as using differing functions had little effect in the soft band) as well as the summed stellar contribution. Here we see the RSCVn systems are far less important than they were in the hard band, instead F and early-M stars dominate. The total contribution at 0.002ct/s is ≈ 20% (2—3 sources, ≈1 per deg^2), a much lower figure than that obtained for the hard band. Much of the difference between the soft and hard contributions is due to absorption by the ISM, greatly reducing the volume of space within which sources are detectable in the soft-band. Indeed in the soft-band we see no extra-galactic contribution as all soft photons have been absorbed.

3.7.1 Other Models

It is useful to compare the modelling results of this survey with those of others conducted recently. One such survey extended the ROSAT Galactic Plane Survey (RGPS) using RASS observations of a low-latitude area in Cygnus (Motch *et al.* 1996). Using their Besancon model (Guillout *et al.* 1996) they predict 45.9 sources per deg^2 at 1×10^{-3} PSPC ct s^{-1} as compared to our ≈41. At fluxes greater than 0.03 PSPC ct s^{-1} they predict 85% of sources are identified with active coronae. The modelled stellar-contributions from this paper are shown in Figure 3.16.

G. Micela (Palermo Observatory) and F. Favata (ESTEC), used their model, XCOUNT, to predict the number of stellar sources in our survey region. In the PSPC hard-band, for the total area of 2.5deg^2, they predicted the log(N)-log(S) curves for main-sequence (F—M) stars, giants and RS CVn's. A large source of uncertainty exists due to the spatial density of RS CVn's being poorly defined. The full range of densities obtained from Favata

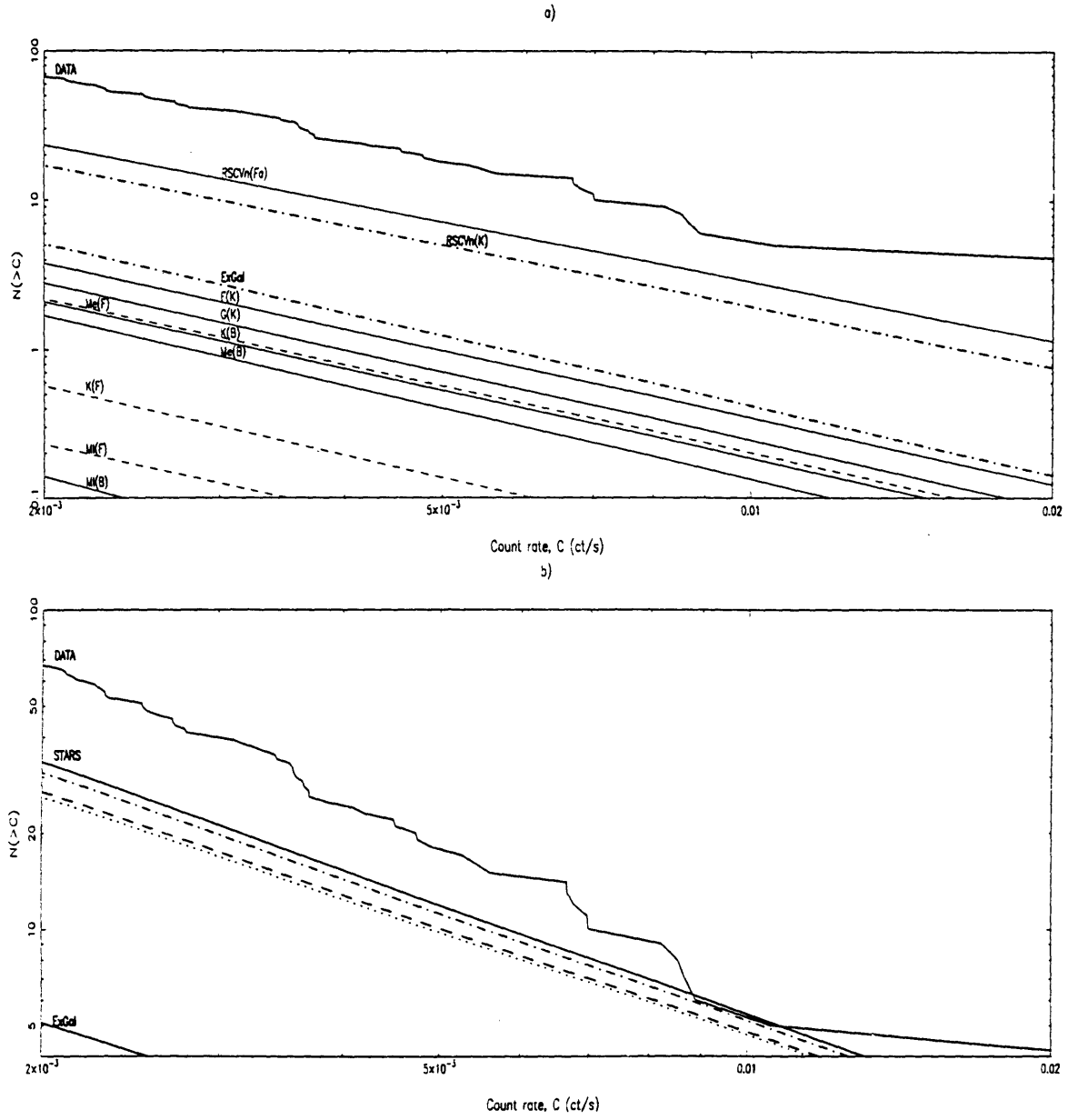

Figure 3.14: (a) Modelled individual stellar and extragalactic source contributions. The measured (coverage-corrected) curve is labelled DATA. Lines indicate calculated contributions from F, G, K and M (early and late) stars as well as RS CVn's and the extragalactic contributions. Different sources of luminosity functions have been used in the modelling, these are indicated by F for Fleming *et al.*, K Kashyap *et al.*, Fa Favata *et al.* and B Barbera *et al.* (b)Summed stellar contributions (with extragalactic also shown). The four curves below the DATA curve, labelled STARS, represent different model assumptions. From top down these are: T$\approx$1$\times$10^{7}K and high RS CVn contribution (luminosity function of Favata *et al.*); T$\approx$5$\times$10^{6}K and high RS CVn contribution; T$\approx$5$\times$10^{6}K and low RS CVn contribution (luminosity function of Kashyap *et al.*) ; T$\approx$3$\times$10^{6}K and low RS CVn contribution.

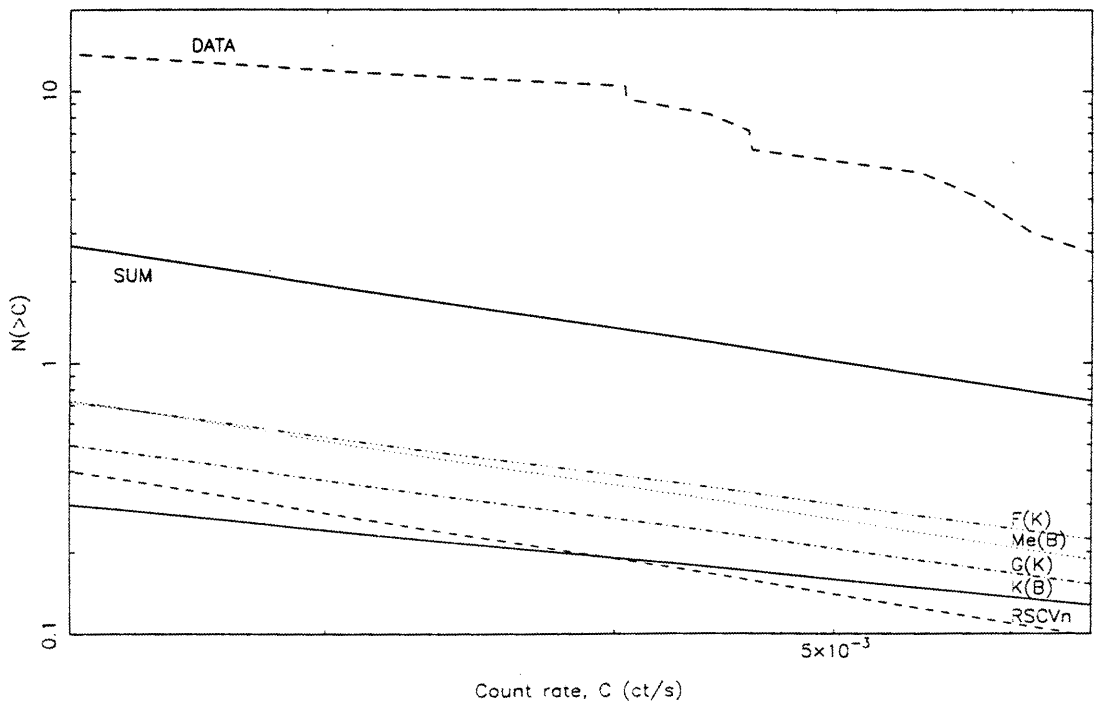

Figure 3.15: Modelled soft-band stellar contributions, individual and summed. Fewer permutations of luminosity functions are used as differing functions cause little overall change (see text). Nominal temperature T$\approx 5\times10^6$K used throughout.

et al. (1995), $(3.14 - 12.2) \times 10^{-5}$ pc^{-3}), was used for the modelling. Figure 3.17 shows the results of the Palermo model predictions compared to our observed number-flux relation for the soft and hard bands. In the hard band they predict 26—36 (10—14 per deg^2) stellar sources above 0.002ct s^{-1}, approximately 50% of our observed number of sources, but agreeing well with our prediction of 10—14 stellar sources per deg^2 above 0.002ct s^{-1}. In the soft-band the Palermo model predicts 2—3 stellar sources above 0.0023 ct s^{-1}, again in good agreement with our prediction.

It is interesting to note that both of these models (Besancon and XCOUNT) use combinations of age-dependant X-ray luminosity functions. Yet they still obtain roughly the same results as our model which includes no age dependancy. Also, considering the large contribution RS CVn systems appear to make in both the Palermo and our models, it is strange that they do not seem to be necessary in the Besancon model in order to account for all of the coronal emission.

3.8 Temporal Analysis

The ROSAT PSPC records the arrival time of every detected X-ray photon, allowing the creation of light-curves. Hard-band light-curves of all sources with a detection significance of $\geq 10\sigma$ were extracted (with 1ksec time bins) using circular regions with radii large enough to contain the individual source but no others nearby. As all sources were within the inner-ring the broadening of the PSF with increasing radius presented no problem. A background region was extracted from a nearby source-free area. Background subtraction was carried out using XRTSUB. This program calculates the expected particle count (as a function of PH channel) in a given background box using the formula of Snowdon *et al.* (1992). This is subtracted from the background counts which are then corrected to the source box position and normalised for the difference in area between the background region and source area. The resulting counts were then corrected for vignetting and scattering using XRTCORR. These programs are both in the ASTERIX software package.

This procedure resulted in 15 light curves. on which tests for variability were carried out by performing a χ^2 test on each curve to examine the null hypothesis of a constant count

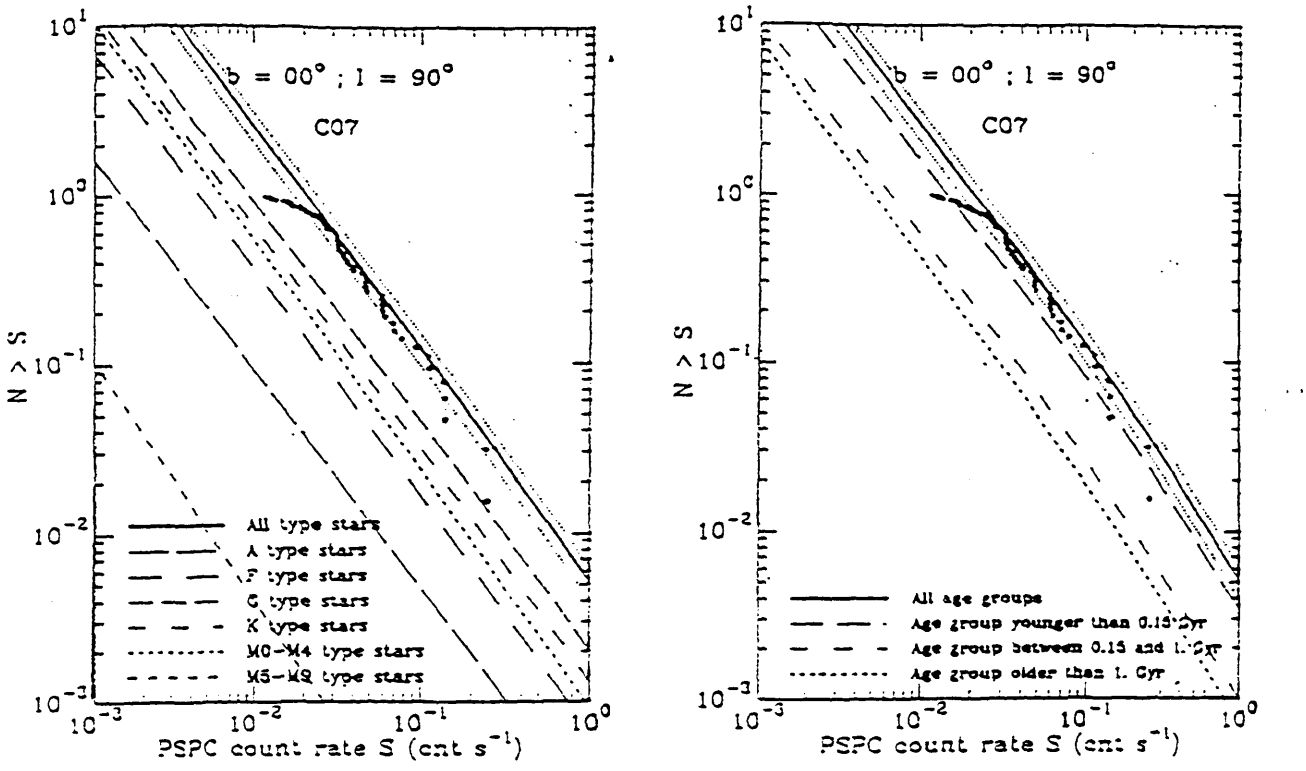

Figure 3.16: Theoretical logN(>S)-logS curves for all stellar coronae (thick line), assuming a constant stellar formation rate. N is the number of stars per square degree in the direction *l b* up to a given count rate in the PSPC band (0.1—2.4keV) as a function of count rate. (a) shown are the log(N)-log(S) curves computed separately for A, F, G, K and M type stars. (b) the range of summed stellar contributions in terms of age. In both figures the observed relation for all identified active coronae (giants excluded) is shown with asterisks. Reproduced from Motch *et al.* (1996).

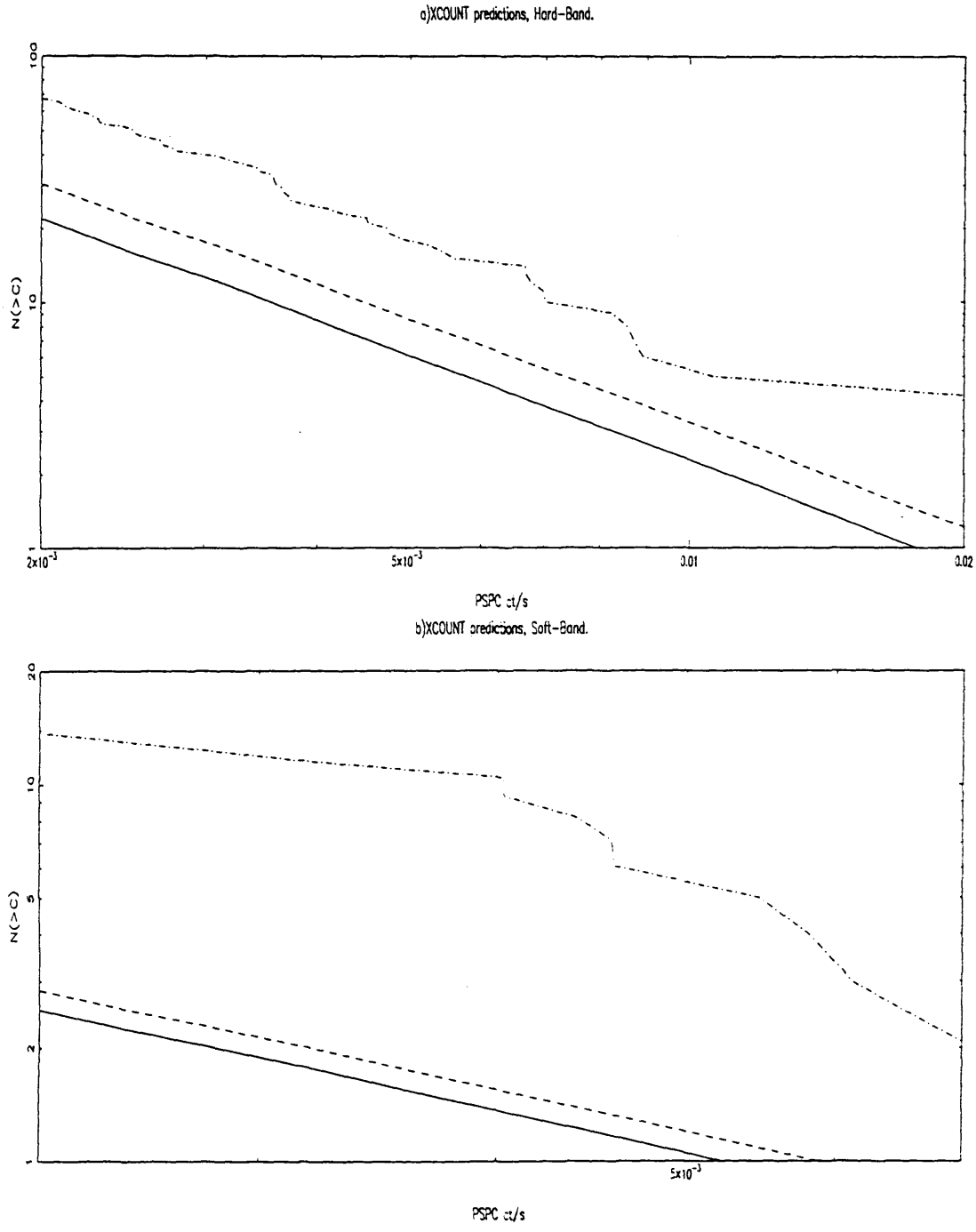

Figure 3.17: a) Hard-band number-flux relations as predicted by Micela *et al.* (private communication) in an area of 2.5deg^2. From top line down: Our measured log(N)-log(S), log(N)-log(S) for main-sequence stars, giants and RS CVn's (with high space density), and log(N)-log(S) for main-sequence stars, giants and RS CVn's (with low space density). b) Soft-band number-flux relations as predicted by Micela *et al.*. From top down lines ordered as in a).

rate. This test was accompanied with visual inspection. Of the 15 light curves only one showed any signs of variability, source 91, see Figure 3.18. This activity is clearly flare-like. As we are dealing with the inner ring there can be no problems with ribs and all time periods of high particle background and poor satellite aspect have been corrected for. Does this then give us any clues as to what the source could be? Source 91 has no potential counterpart in either the GSC or SIMBAD, though the optical counterpart, as identified from the Schmidt plate, of this source is the only object above the plate limit within the error circle and has the relatively bright magnitude of 13.88. Looking at the colours of the source in the two colour bands yields no further information. Source 91 is detected in the soft and hard bands and has a hardness ratio of 0.74 (possibly due to the variability). It is one of the brighter sources in the survey at 0.029ct s^{-1} and has a $\log(f_x/f_v)$ of -1.5. Looking at the WGACAT results (Figures 3.11 — 3.13) this would mean the source might be an M or K dwarf or possibly an RS CVn (assuming the value for the optical magnitude is correct). It could be a CV but the source is too hard and variable to be a white dwarf. If the optical candidate chosen were the wrong one then the optical magnitude of the X-ray source would have to be dimmer than 20th magnitude, implying perhaps either an extragalactic source or an X-ray binary.

Field 9, containing source 91, was the subject of a paper by Belloni and Mereghetti (1994). They too observed the variability of this source and suggest that it could be either a dM star, at a few hundred parsecs, or an RS CVn, at $\approx$2kpc. Using typical values of absolute magnitude we find either possibility would appear as a 14—16 magnitude object, which approximates well to our estimated magnitude for the possible optical counterpart.

3.9 Discussion

In modelling the source-count populations we have predicted that $\approx$50% of our sources should be coronal and $\approx$8% extra-galactic in origin. This model agrees well with observational results. The RGPS concluded at least 50% of its observed sources were coronal in origin (based upon optical identifications. Motch *et al.* 1991) whilst 10% were extra-galactic (again based on optical identification), with 40% remaining unidentified. M-stars

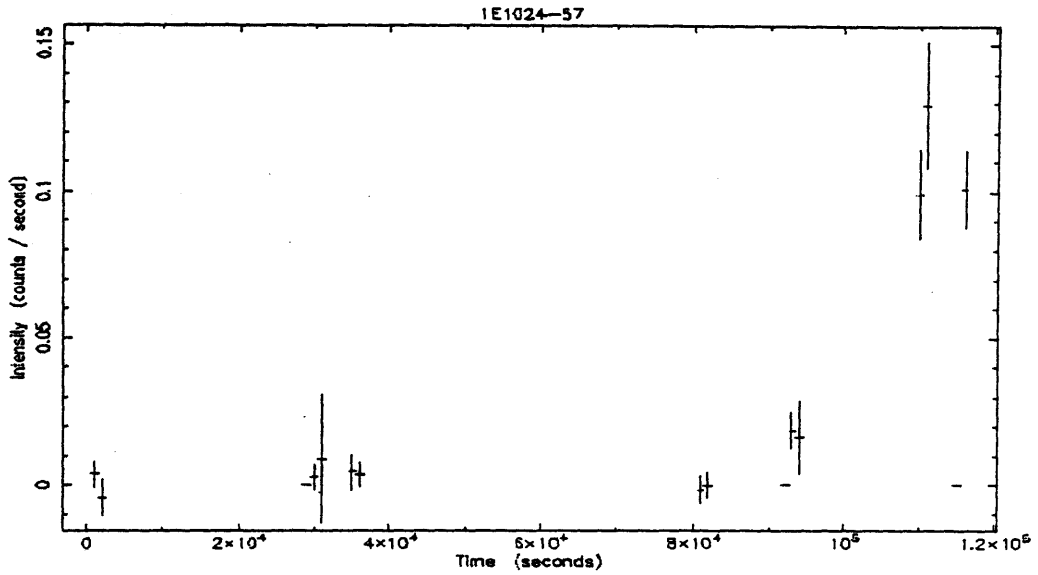

Figure 3.18: Hard-band light curve of galactic plane survey source 91. Flare-like activity is clearly visible.

accounted for a high proportion of their sources and they suggested that many of the unidentified sources were likely to be M-stars also. The EGPS provided similar results, though with a higher extra-galactic proportion, possibly due to their harder energy band. The EINSTEIN Medium Sensitivity Survey (EMSS; Gioia *et al.* 1990) was a survey at high latitudes. This found that 26% of the sources detected were coronal. This figure was later corroborated with ROSAT[5]. Approximately the same number of coronal sources was predicted in the modelling done by Guillout *et al.* (1996) at these higher latitudes.

What type of sources could comprise the unaccounted for populations when modelling the source-counts? Using a delta-function in SCOUNT as a best-guess, systems with poorly defined X-ray luminosity functions were modelled. In the hard-band CV's could account for from <1 to >30 sources (assuming L_x of 10^{30}—10^{31}erg s^{-1} and a space density of $6\times10^{-6}pc^{-3}$) (Hertz and Grindlay, 1984). Using distance and magnitude figures for the CV AM Her, using equation 3.3 we could expect a CV on the limit of our X-ray detection capability, 0.002ct s^{-1}, to have a visual magnitude of around 17. faint, but visible on our

[5]As far as the EXOSAT galactic plane survey is concerned. our large number of discrete. low luminosity, sources could possibly account for some proportion of their diffuse emission.

survey plates. The figures for White Dwarf Binaries suggest implausible contributions to the model (>100). Maoz and Grindlay (1995) postulate an extended galactic population of low-luminosity X-ray sources in a flattened, thick disk with a scale height of a few kpc. They suggest an X-ray luminosity of 10^{30}—10^{31} erg s^{-1} in the 0.5—2keV band and a number density of $3.2\times10^{-5}pc^{-3}$ in the solar vicinity. They also suggest these sources are faint CV's with low accretion rates, but include other possibilities such as subdwarfs, neutron stars and black holes. Putting their figures into SCOUNT we would expect to see in our survey area of $2.5deg^2$ at >0.002ct s^{-1}, $\approx$2 sources if their X-ray luminosity were 10^{30}erg s^{-1}, $\approx$10 at $10^{30.5}$erg s^{-1} and $\approx$30 sources at 10^{31}erg s^{-1}.

It is likely that many of the unidentified sources are actually late-type stars (if the optical magnitude estimates can be believed then this would agree with the X-ray to optical ratio measurements) and that we have underpredicted the stellar contribution. This could be a fault of the model or due to the fact that known luminosity functions do not hold in this deep survey. However it is almost certain that a number of the unidentified sources are in fact some combination of these other stellar systems. The efforts of Micela *et al.* towards optically identifying the X-ray sources should help determine the true galactic-plane populations. Meanwhile measurements at different latitudes are required to investigate how this population changes throughout the galaxy.

Chapter 4

The Hyades Open Star Cluster : An X-ray Variability Study

4.1 Introduction

In this chapter I will present an X-ray variability study of the Hyades open star cluster, using data from 13 pointed observations from the ROSAT PSPC. The data were obtained by Dr J.P. Pye in all cases but one where the PI was Dr R.A. Stern. This is a follow up study to the spectral survey work presented in the thesis by S.T. Hodgkin (1995).

As was discussed in Chapter 1, X-rays from stellar coronae originate in thermal continuum and line emission from optically thin plasmas (Rosner *et al.* 1978). Coronal models for cool (F—M) stars are based in general on solar observations and suggest that surface magnetic fields, generated by dynamo action in a differentially rotating star possessing a sub-photospheric convection zone, confine the coronal plasma. There is no complete theory as to how the plasma is heated to the temperatures ($\geq 10^6$K) required for X-ray emission. Possibilities include heating by DC currents, microflaring and magneto-hydrodynamic waves.

The age of a star is believed to be related to its level of X-ray emission. As activity is related to the magnetic dynamo effect in a star, rotation must be a significant part of

the equation (Walter and Bowyer 1981). Thus as a star grows older, magnetic braking causes it to spin down and hence the X-ray emission decreases over time, though in binary systems the high angular momentum of the stellar orbits acts as a reservoir to maintain the stellar rotation rate. By studying stars of different ages it is possible to examine the relationship between X-ray luminosity (as a proxy of 'dynamo-activity'), rotation and age. Our Sun is $\approx 5\times10^9$ years old and has a relatively low X-ray luminosity. Younger co-eval clusters of stars, such as the Pleiades and the Hyades exhibit higher X-ray luminosities than the Sun and provide large statistical samples of co-evolving stars.

Apart from the highly extended U Ma co-moving (kinematic) group the Hyades is the nearest open cluster to our Sun, at a distance of $\approx$ 45 parsecs. As we are dealing with an open cluster all of the members must have formed at roughly the same time and thus have the same age ($\approx 7\times10^8$ years). It provides an excellent stellar sample for the study of activity and dynamo action for several reasons. The detection of low-luminosity X-ray sources is possible not only due to the proximity to our Sun but also to the low hydrogen-column density in the direction of the cluster (the Hyades is within the 'local-bubble', cf Chapter 2). This low column also allows the measurement of X-ray photons below the PSPC carbon edge ($\approx$0.5keV). The Hyades forms a large stellar sample containing over 400 known members over a 40 degree diameter of sky. However roughly 50% of the members lie in a core of $\approx$4 degree radius. Finally there is a large amount of optical data on the Hyades, as it has been used to derive many astronomical properties (such as the mass-luminosity relationship and location of the main sequence on the H-R diagram).

I will first summarise the previous X-ray studies of the Hyades before moving on to discuss the variability study performed using ROSAT PSPC pointed observations. I will present the light curves for the variable stars, perform time-resolved spectroscopy on the flaring stars, discuss long-term variability and finally attempt to model the X-ray flares.

4.2 Previous X-ray Observations of the Hyades

In 1980 a survey of a region close to the cluster centre was performed using the Einstein IPC (Stern *et al.* 1981, Micela *et al.* 1988). This resulted in 66 cluster member detections

and showed that X-ray emission was a common property of F—G type stars. It allowed the determination of X-ray luminosity functions and showed that the average Hyades G-dwarf was $\approx$ 50—100 times more active ($L_x \approx 10^{29}$ erg s^{-1}) than our Sun. It was shown, comparing luminosity functions of the Galactic Young Disk, Old Disk, the Pleiades and the Hyades that there was a definite decrease in X-ray luminosity with age. Later follow up observations using the Einstein IPC (Stern, Antiochos and Harnden 1986) allowed the fitting of two-temperature optically thin plasma models and hydrostatic-loop models for some of the brighter sources. Also a large X-ray flare on VB22 was reported (Stern, Underwood and Antiochos 1983). Further observations using the EXOSAT LE were made by Westergaard *et al.* (1985) allowing the measurement of 'average' coronal temperatures and line-of-sight column density ($n_H \approx 1—2\times10^{19}$cm^{-2}).

Between July 1990 and January 1991, ROSAT was used to perform an all sky survey. This allowed a study to be made of the complete Hyades cluster, preliminary results of which were published by Stern *et al.* (1992) and updated in Stern *et al.* (1995). In the survey a typical exposure was 500 seconds. 187 cluster members were detected down to a limiting X-ray luminosity of $L_x \approx 1—2\times10^{28}$ erg s^{-1}. A comparison of ROSAT and Einstein observations of the four Hyades K0 giants indicated some X-ray variability, possibly due to stellar activity cycles on the scale of $\approx$10 years. Of the four, two increased by $\approx$ 1.5—2 times in flux whilst the ROSAT upper limit for another was $\approx$ 3 times below the Einstein detection. Comparing the other stars detected in both the ROSAT all-sky survey and the Einstein survey showed a general lack of significant (a factor >2) long-term X-ray variability.

4.3 ROSAT Pointed Observations

The thirteen PSPC pointings performed for this survey were all chosen to lie within the densely populated central region of the Hyades. In several cases the fields overlapped, providing a second look at some stars. Table 4.1 lists the observations and Figure 4.1 shows a merged image of the PSPC fields.

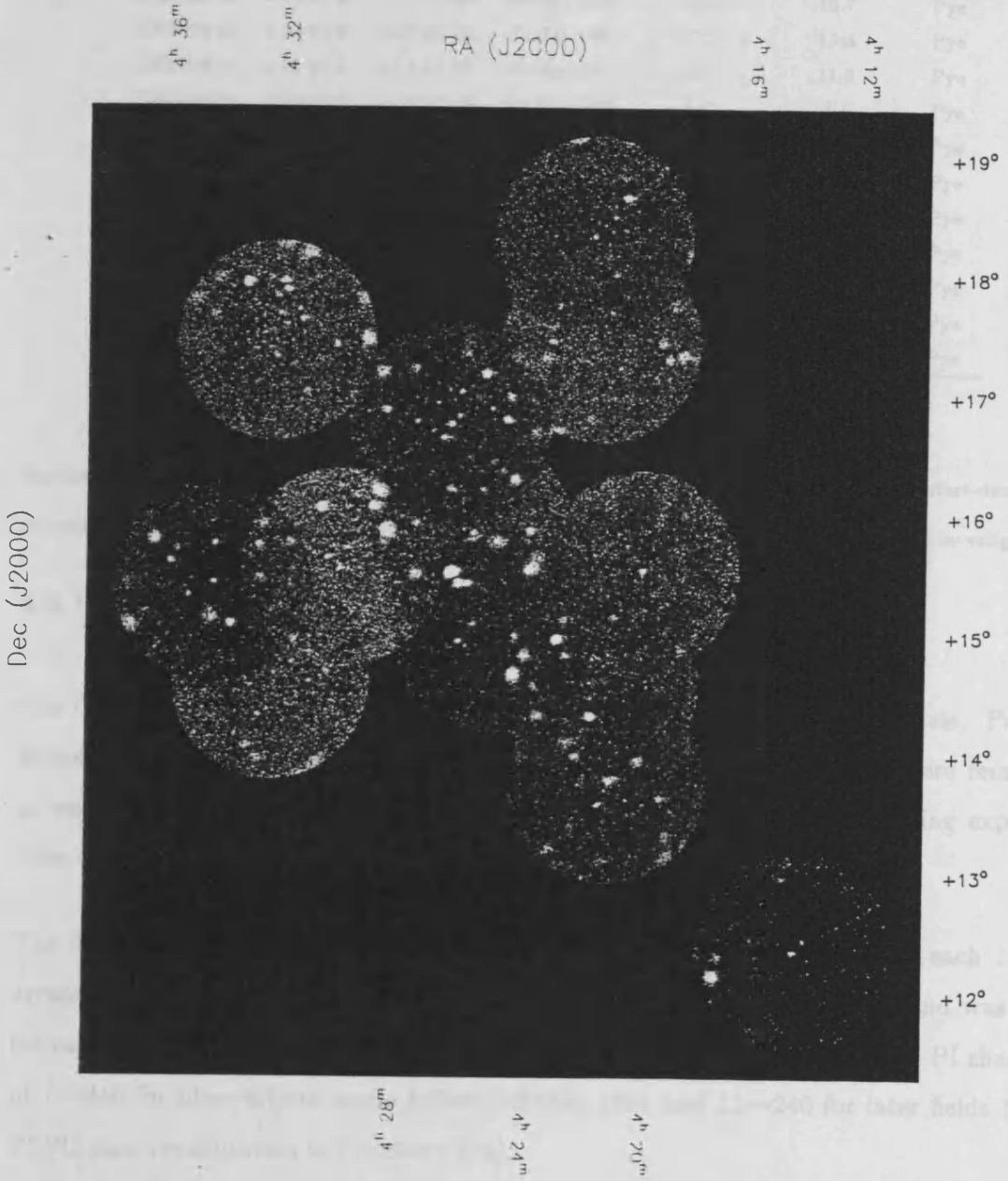

Figure 4.1: Merged image of the 13 PSPC fields used in the survey.

Table 4.1: ROSAT pointings

SEQ ID	α (h m s)	δ (d m s)	Start Date	T_{obs}(ksec)	T_{clean} (ksec)	PI
US200020	4 24 50.4	+15 06 00	27-Feb-1991	39.5	32.1	Stern
UK200441	4 21 12.0	+14 42 00	24-Feb-1991	15.1	8.0	Pye
UK200442	4 21 12.0	+17 31 48	24-Feb-1991	20.2	16.7	Pye
UK200443	4 32 31.2	+17 31 48	07-Mar-1991	20.3	15.4	Pye
UK200444	4 32 31.2	+14 42 00	06-Mar-1991	14.7	11.8	Pye
UK200775	4 19 48.0	+15 37 48	22-Feb-1993	4.0	3.4	Pye
UK200776	4 20 52.7	+13 51 36	30-Aug-1991	23.2	22.7	Pye
UK200777	4 25 36.0	+15 56 24	30-Aug-1991	16.5	15.8	Pye
UK201368	4 30 07.1	+15 38 24	10-Sep-1992	16.2	13.7	Pye
UK201369	4 26 24.0	+16 51 00	24-Feb-1993	15.2	13.2	Pye
UK201370	4 21 31.2	+18 25 12	23-Feb-1993	13.4	11.7	Pye
UK201747	4 34 34.9	+15 30 16	01-Sep-1993	19.2	18.7	Pye
UK201748	4 14 26.9	+12 26 08	15-Aug-1993	16.8	15.7	Pye

Notes: Columns are; ID of pointed PSPC observation, right ascension and declination (J2000), start-date of the observation, full exposure time of the observation, exposure time after data cleaning, and principal investigator.

4.3.1 Detection of Hyades Members

The data from each field were 'cleaned' before they were used in the analysis. Periods where aspect errors would affect co-ordinate conversion (detector to sky) were removed, as were periods of high background (X-ray or particle related). The resulting exposure time was therefore reduced in each field.

The data for each field were binned into a sky image of 512 × 512 pixels each 15×15 arcsec^2, centred at the pointing direction. The standard TOTAL energy band was used for each dataset, corresponding to a photon energy range of 0.1—2.4keV and PI channels of 7—240 for observations made before October 1991 and 11—240 for later fields (after PSPC gain recalibration in October 1991).

The point source detection program PSS (Allan, Ponman and Jeffries 1993) was used to find maxima in the field exceeding a threshold level set at 3.0σ (probability 0.001 that Poisson noise is responsible for the detection) (Pye *et al.* 1994). In this way $\approx$ 1000 source detections were made, the positions of which were cross-correlated against a Hyades star

Table 4.2: Summary of PSPC Hyades detections.

	Spectral Type					
Class	A	F	G	K	M	Total
Main Sequence—Detected	4	13	19	16	25	77
Main Sequence—Catalogued	8	13	19	25	39	104
Giants—Detected	0	0	0	3	0	3
Giants—Catalogued	0	0	0	3	0	3
Total Detected	4	13	19	19	25	80
Total Catalogued	8	13	19	28	39	107
Fraction Detected	0.50	1.00	1.00	0.68	0.64	0.75

Notes: Sources are divided into spectral type. Shown are the numbers detected in the pointed observations and those catalogued to lie within these regions. The fraction of the catalogued stars detected is also shown.

catalogue. This catalogue contains $\approx$ 450 stars with m_v<16 and was developed from the published literature by Stern *et al.* 1992. An estimated $\leq$10% of the stars are potential non-cluster members, as discussed in Stern *et al.* (1992).

In order to allow for catalogue and pointing inaccuracies a correlation radius of 1 arcminute was taken. The resulting source list was then further re-edited to remove sources where accurate PSS source identification was not possible. This included multiple Hyads associated with the same PSS detection, extra PSS detections in a field for any given Hyad and sources $\geq$ 50 arcmins off axis where the PSF of the PSPC is highly extended. This left 107 Hyads corresponding to 153 measurements of flux or upper limit on flux, with 80 positive, distinct Hyad detections in a total survey area of $\approx$18 degrees^2, corresponding to a detection rate of 75%. These detections are summarised by spectral type in Table 4.2. and are detailed in full in Appendix C. Fluxes were derived using a conversion factor of 1 PSPC count s^{-1}=6$\times$10^{-12} erg cm^{-2} s^{-1} = 1.45$\times$10^{30} erg s^{-1} (over the energy range 0.1—2.4keV).

4.4 Data Extraction and Analysis

The ROSAT PSPC records the arrival time of every detected X-ray photon, allowing the creation of light-curves. Light-curves of all identified sources were extracted using circular regions with variable radii, determined by the off-axis angle. The extraction radius was taken to be the greater of 4 arcmin and a radius encircling 95% of the source energy. Thus the further off-axis a source lies the larger the extraction radius is needed due to the broadening of the PSF with increasing radius. Using between 10 and 15 source-free background regions per field, each at the same off-axis angle (30 arcmin) and having the same radii (0.92 arcmin, the PSF radius at this off-axis angle for a mean energy of 0.2keV) the mean background counts were found. Background subtraction was carried out using XRTSUB. This program calculates the expected particle count (as a function of PH channel) in a given background box using the formula of Snowdon *et al.* 1992. This is subtracted from the background counts which are then corrected to the source position and normalised for the difference in area between the background region and source area. The resulting counts were then corrected for vignetting and scattering using XRTCORR. Both of these programs are part of the ASTERIX software package.

A similar method was used to extract PHA spectra. The Hyades survey results of spectral fits, hardness ratios and luminosity functions obtained from this data are described in Hodgkin (1995). The work presented here is a complementary study of variability.

4.4.1 Time Series Analysis

Tests for variability were carried out by binning source counts into 1 ksec bins. This bin size was chosen in order to both collect significant counts per bin and to counter effects caused by the 400 second periodic 'wobble' of the satellite. The light curves produced are shown in Appendix B. Those time bins with low exposure (and hence high errors) at the beginning and end of individual observing intervals were removed from the data. In order to determine whether the window support ribs caused any variability in sources lying on or near them, both variable and non-variable sources on and near ribs were compared. It appeared that the ribs were unlikely to cause significant variability as the near-rib variable

to constant source ratio was low (46 near-rib sources of which only 12 were variable).

A χ^2 test was performed on each light curve to examine the null hypothesis of a constant source count rate. This test was accompanied with visual inspection. For the 15—20 degrees of freedom present, a reduced χ^2 value of ≥ 2 was taken to represent a likely variable source ($< 1\%$ chance of a source being constant). Ultimately 17 sources were deemed variable (including one possible non-Hyad, H363), corresponding to 14 individual stars. The light curves for the 16 Hyad detections are shown in Figures 4.2 — 4.9. Table 4.3 lists the variable sources.

Table 4.3: Variable Sources.

Name	Field	RA	DEC	Bin	χ^2_ν	DOF	Spectral Type	Rise (10^4s)	Fall (10^4s)	Peak ct/s	Base ct/s
VB27	200442	4 19 07.6	17 31 29	0	3.13	22	G8V	?	12.0	0.11	0.01
VB30	200776	4 19 56.7	14 02 07	3	8.02	24	A9V	1.0	3.0	0.20	0.05
VB30	200441	4 19 56.7	14 02 07	3	2.82	11	A9V	0.3	1	0.18	0.02
VB40	200020	4 22 44.0	15 03 23	3	2.65	48	F9V	V	V	0.32	0.12
VB45	201369	4 23 24.9	16 46 39	3	2.49	15	F1III	5	3	0.14	0.01
VA288	200020	4 23 49.8	14 55 17	3	2.86	48	M3V	S	S	0.30	0.10
VB50	200441	4 24 11.7	14 45 30	3	12.38	11	G1V	0.3	1.10	1.0	0.35
VB50	200020	4 24 11.7	14 45 30	3	7.60	51	G1V	V	V	0.65	0.20
VA334	200777	4 24 48.6	15 52 26	3	7.70	19	M0V	1.4	2.2	0.34	0.14
VA351	201369	4 25 11.7	17 16 24	2	3.80	15	M2V	?	6	0.24	0.10
H363	200777	4 25 48.6	15 31 18	?	8.57	19	M1V	<0.1	0.1	0.25	0.05
VA383	200020	4 26 04.4	15 02 32	0	2.30	48	M1V	S	S	0.13	0.01
VB141	200777	4 26 20.7	15 37 06	3	9.00	19	A8V	1.0	1	1.10	0.80
VB141	200020	4 26 20.7	15 37 06	3	6.30	50	A8V	V	V	1.20	0.60
VB73	201369	4 28 47.7	17 17 09	0	3.30	13	G1V	1.0	6.0	0.20	0.07
VB190	201368	4 28 50.6	16 17 21	3	10.85	15	K8V	12.0	4	0.36	0.10
VB85	201368	4 30 46.5	16 08 56	3	3.80	15	F5V	5.0	7.0	0.30	0.16

Notes: Variable Hyad sources presented in order of Right Ascension. Columns show source name. pointed field number, Right Ascension and Declination (J2000), reduced χ^2 from the null hypothesis of a constant source, number of degrees of freedom (number of time bins in the light curve -1), spectral type, flare rise time, fall time (all times are approximations due to the nature of the time sampling), peak count-rate in the light curve and count-rate at quiescence. Where flare time parameters (peak time, count rate, flare-duration) are unknown an estimate is shown if extrapolation of part of a rise or decay is possible. A 'V' indicates random variability with no clear flare-like behaviour and an 'S' indicates a flare spike that lasts in total $\leq$1000seconds. Note that source H363 is a possible non-Hyad, however it is included in the analysis as it exhibits clear flare behaviour.

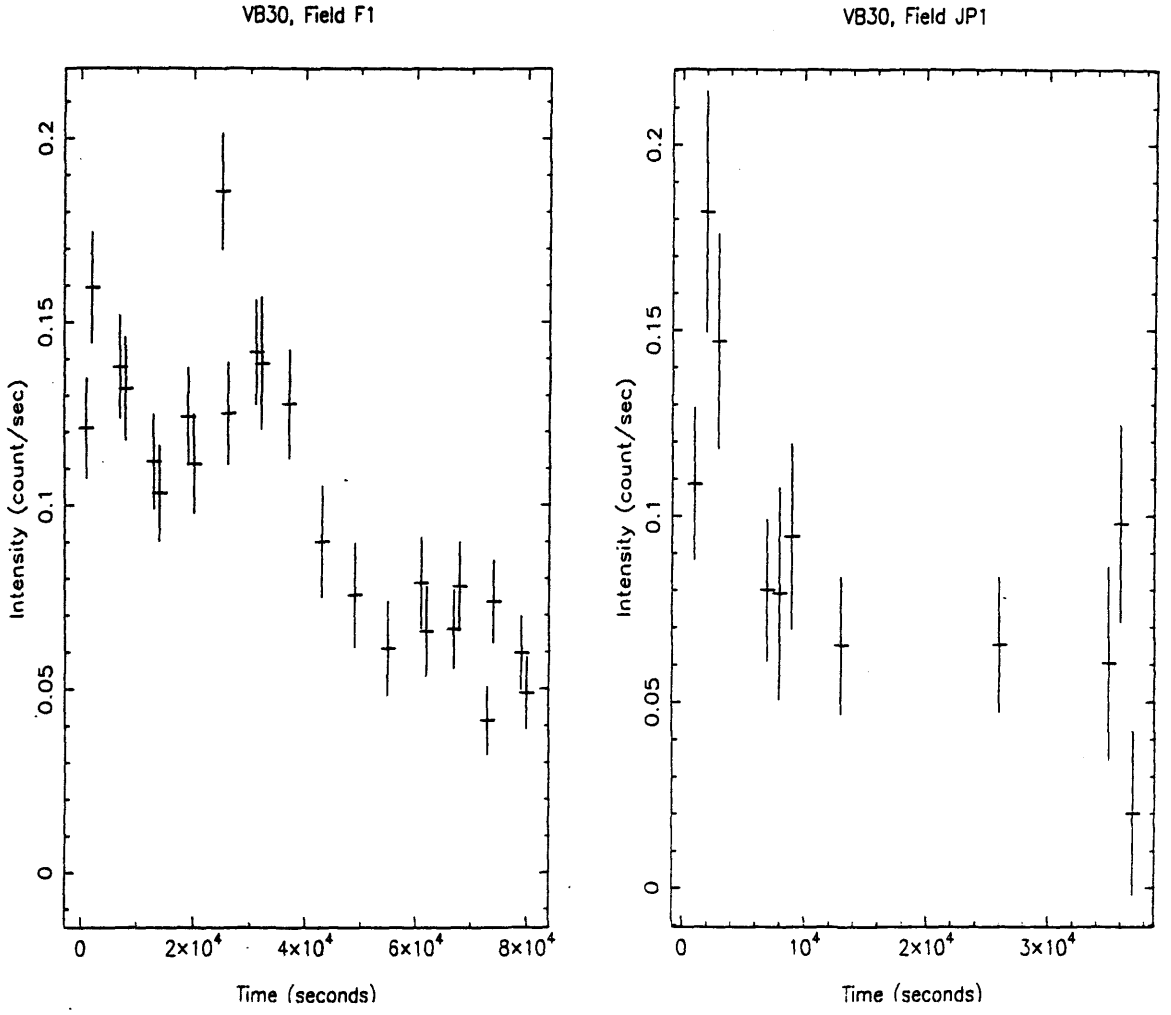

Figure 4.2: Hyad light curves found to be variable in the survey. VB30 (field 200776) and VB30 (field 200441). Note the different ranges and scales on both axes from plot to plot.

4.4.2 VB34.

VB34 (= HD 27483) is a triple system comprising a close binary system (period = 3.06 days) of two F6V stars with an inclination of 51 degrees, and a distant white dwarf companion. The X-ray light curve from field 200776 can be split into three distinct sections, see Figure 4.10. First we see a period with an almost constant count rate of $\approx$ 0.12 ct/s, followed by a period in which the mean count rate drops by over 30%. Finally the count rate returns to the original value. The duration of this 'dip' is between 6ksec and 17ksec. This behaviour is also exhibited in both the soft (0.1—0.4keV) and hard (0.4—2keV) bands. The flux during the quiescent periods is comparable with that found

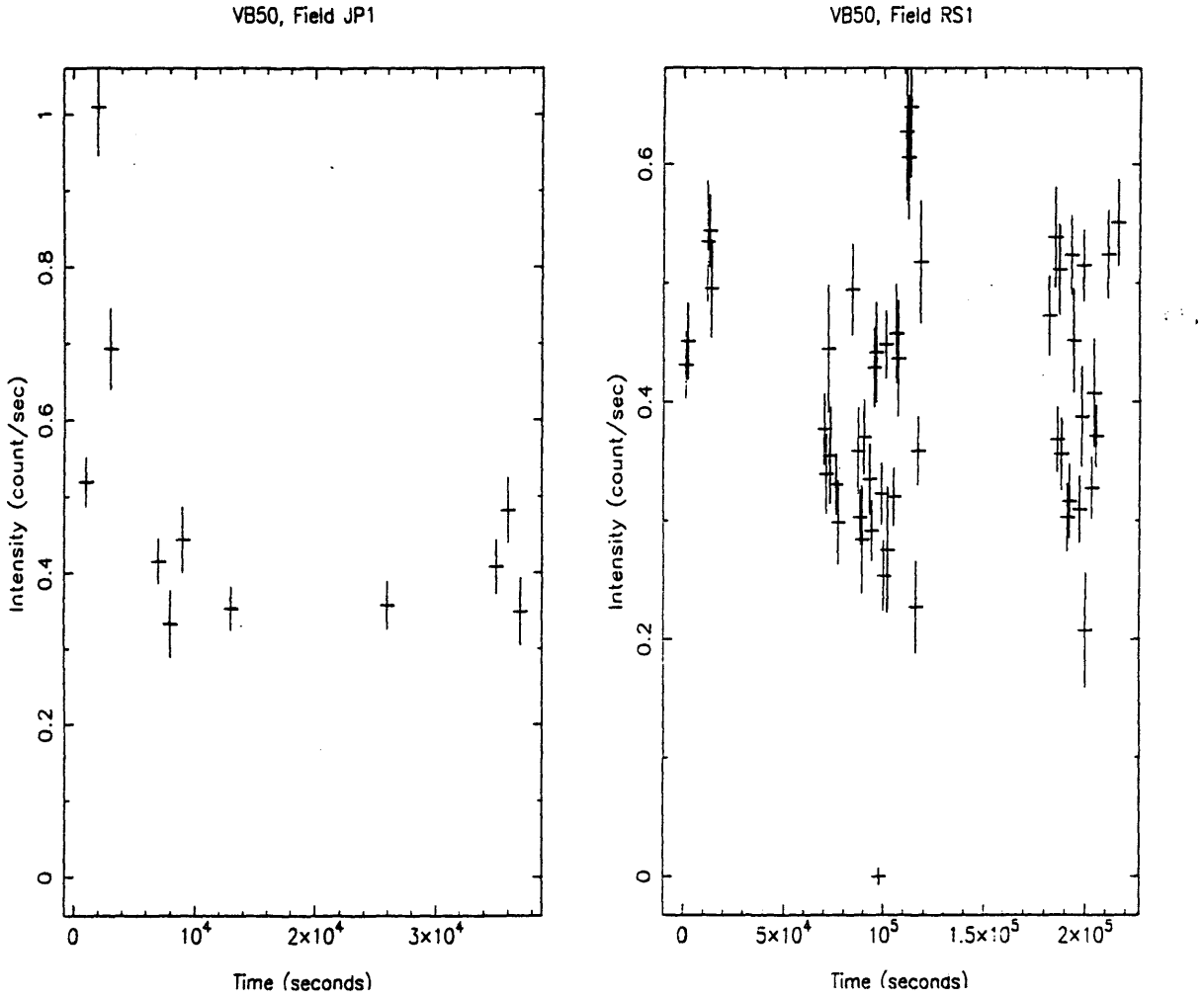

Figure 4.3: Hyad light curves found to be variable in the survey. VB50 (field 200441) and VB50 (field 200020). Note the different ranges and scales on both axes from plot to plot.

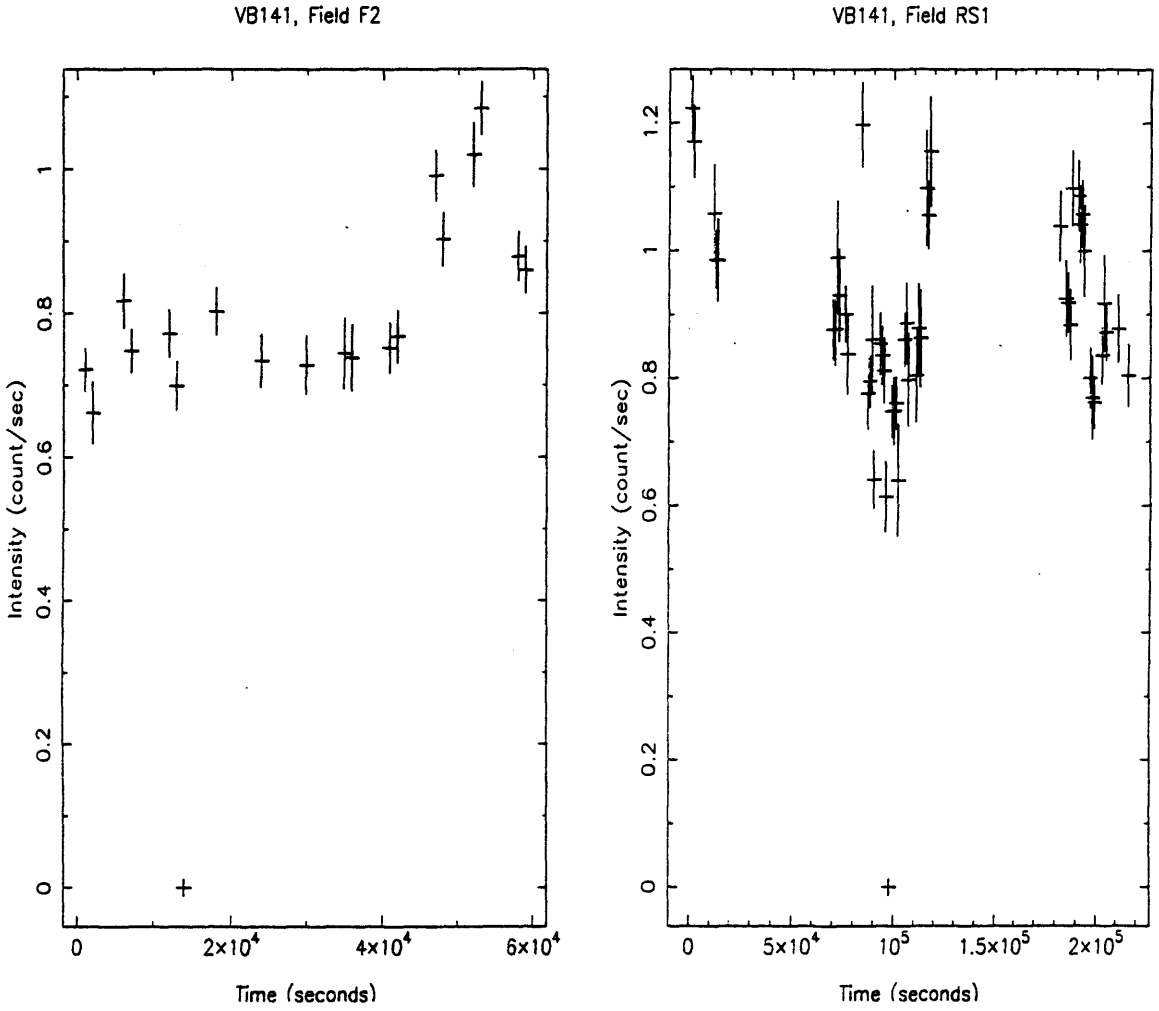

Figure 4.4: Hyad light curves found to be variable in the survey. VB141 (field 200777) and VB141 (field 200020). Note the different ranges and scales on both axes from plot to plot.

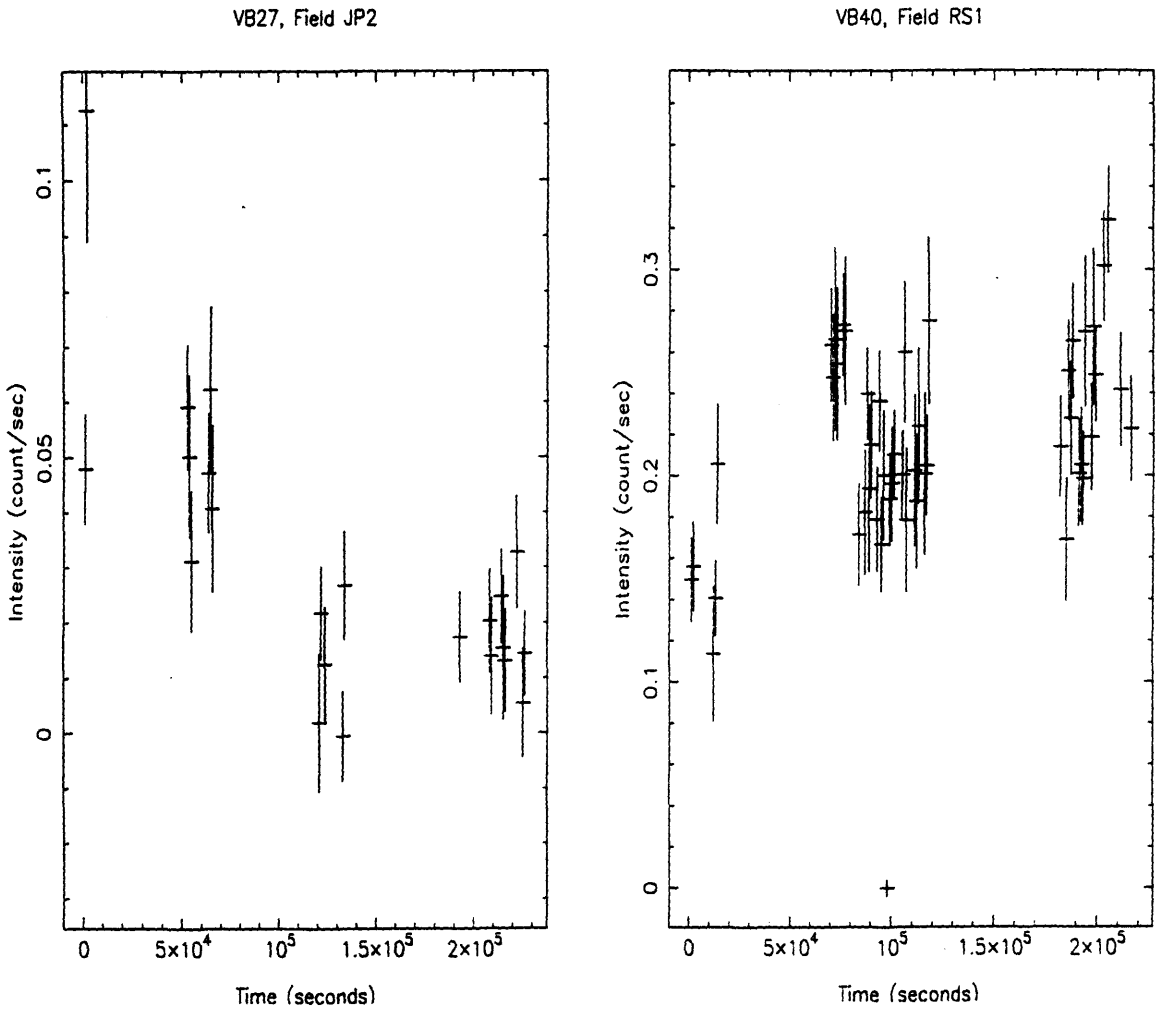

Figure 4.5: Hyad light curves found to be variable in the survey. VB27 (field 200442) and VB40 (field 200020). Note the different ranges and scales on both axes from plot to plot.

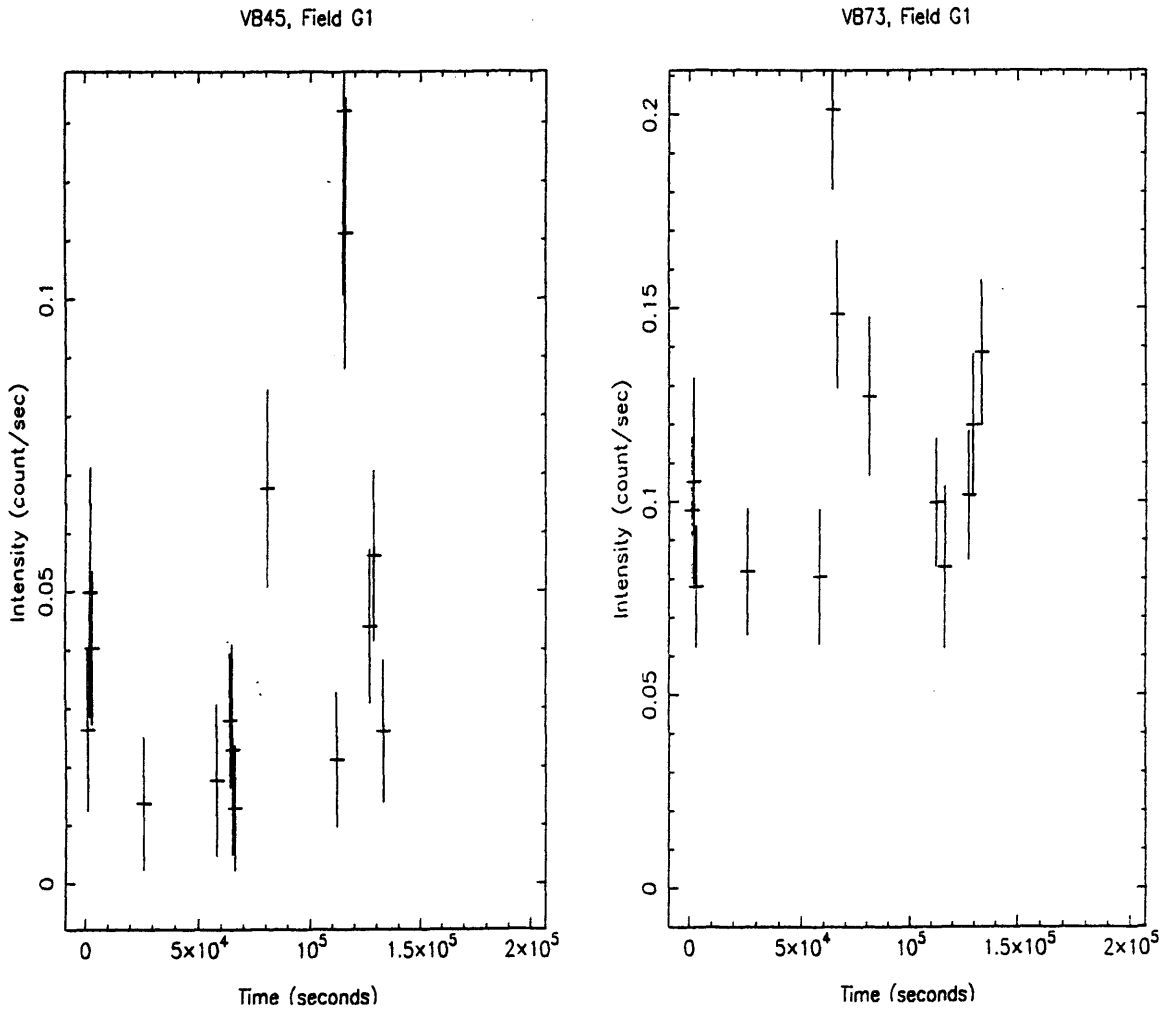

Figure 4.6: Hyad light curves found to be variable in the survey. VB45 (field 201369) and VB73 (field 201369). Note the different ranges and scales on both axes from plot to plot.

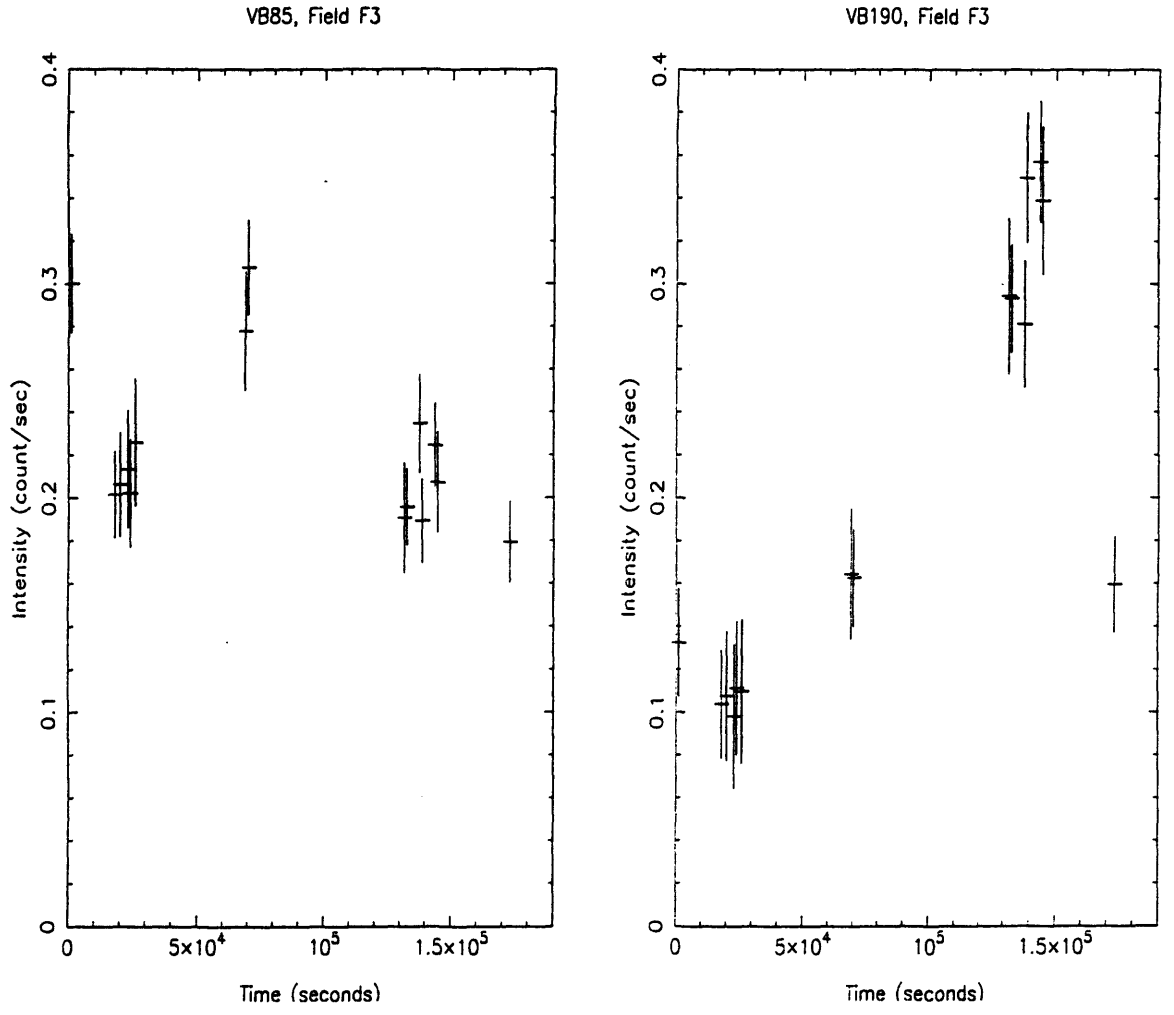

Figure 4.7: Hyad light curves found to be variable in the survey. VB85 (field 201368) and VB190 (field 201368). Note the different ranges and scales on both axes from plot to plot.

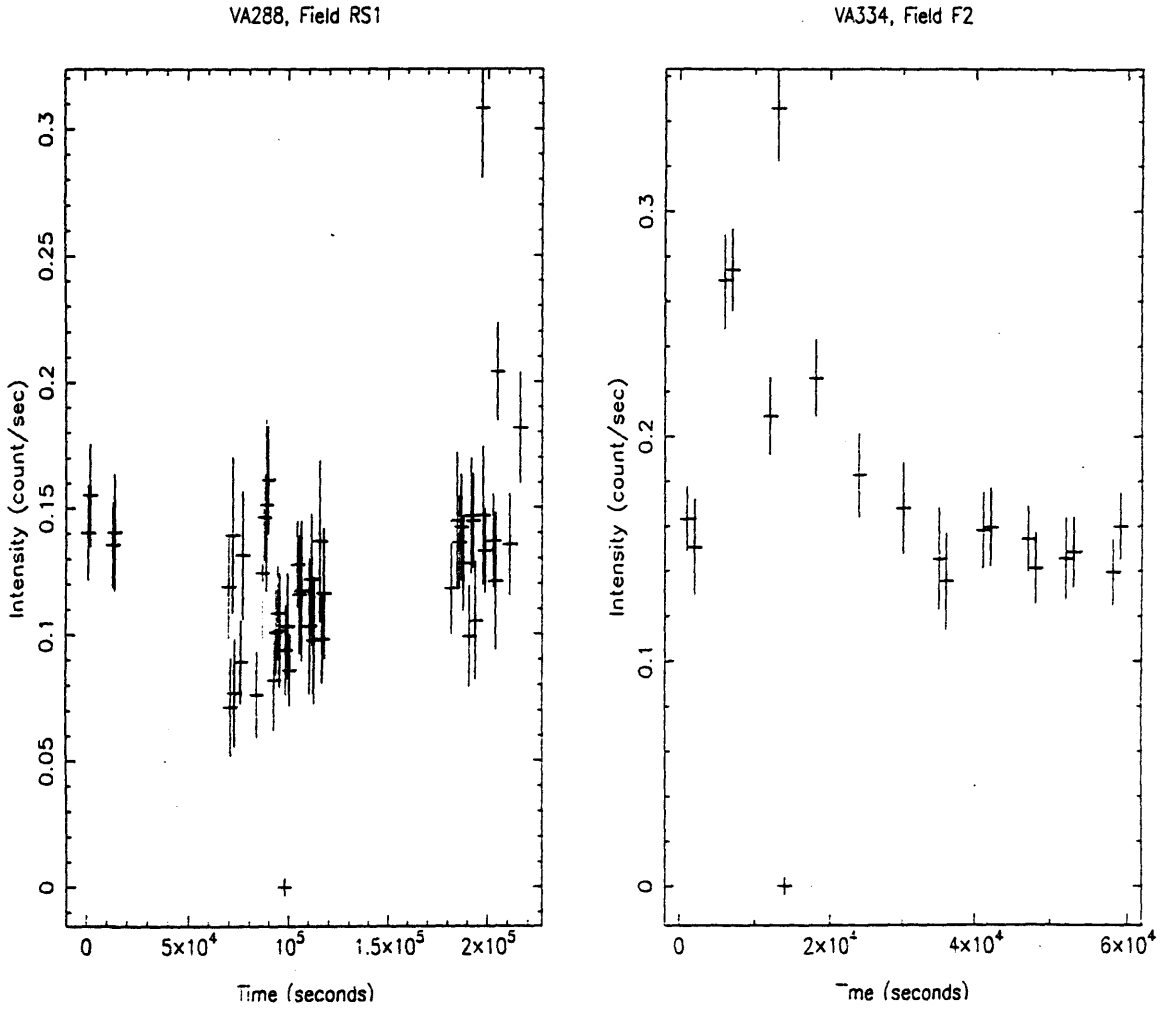

Figure 4.8: Hyad light curves found to be variable in the survey. VA288 (field 200020) and VA334 (field 200777). Note the different ranges and scales on both axes from plot to plot.

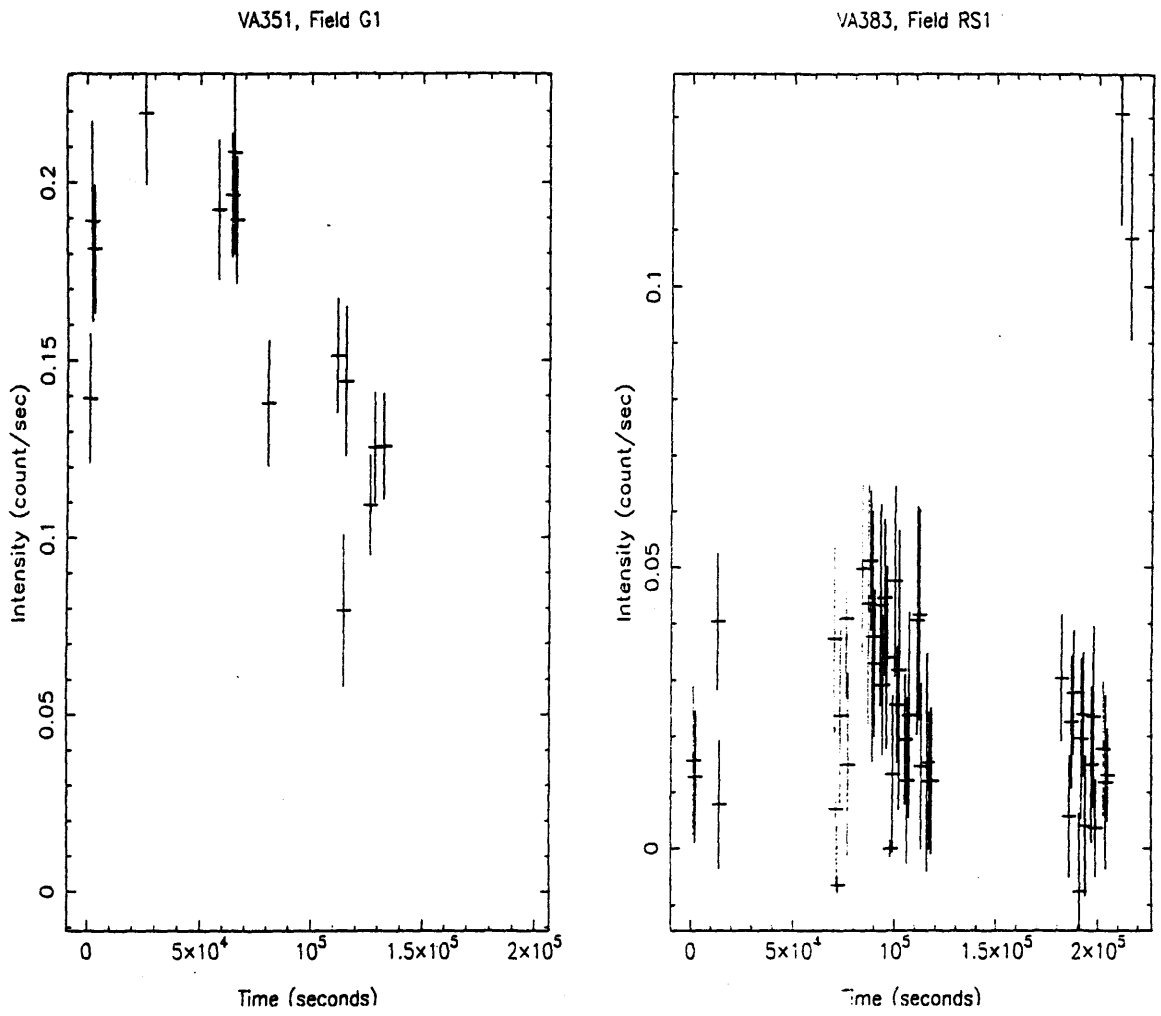

Figure 4.9: Hyad light curves found to be variable in the survey. VA351 (field 201369) and VA383 (field 200020). Note the different ranges and scales on both axes from plot to plot.

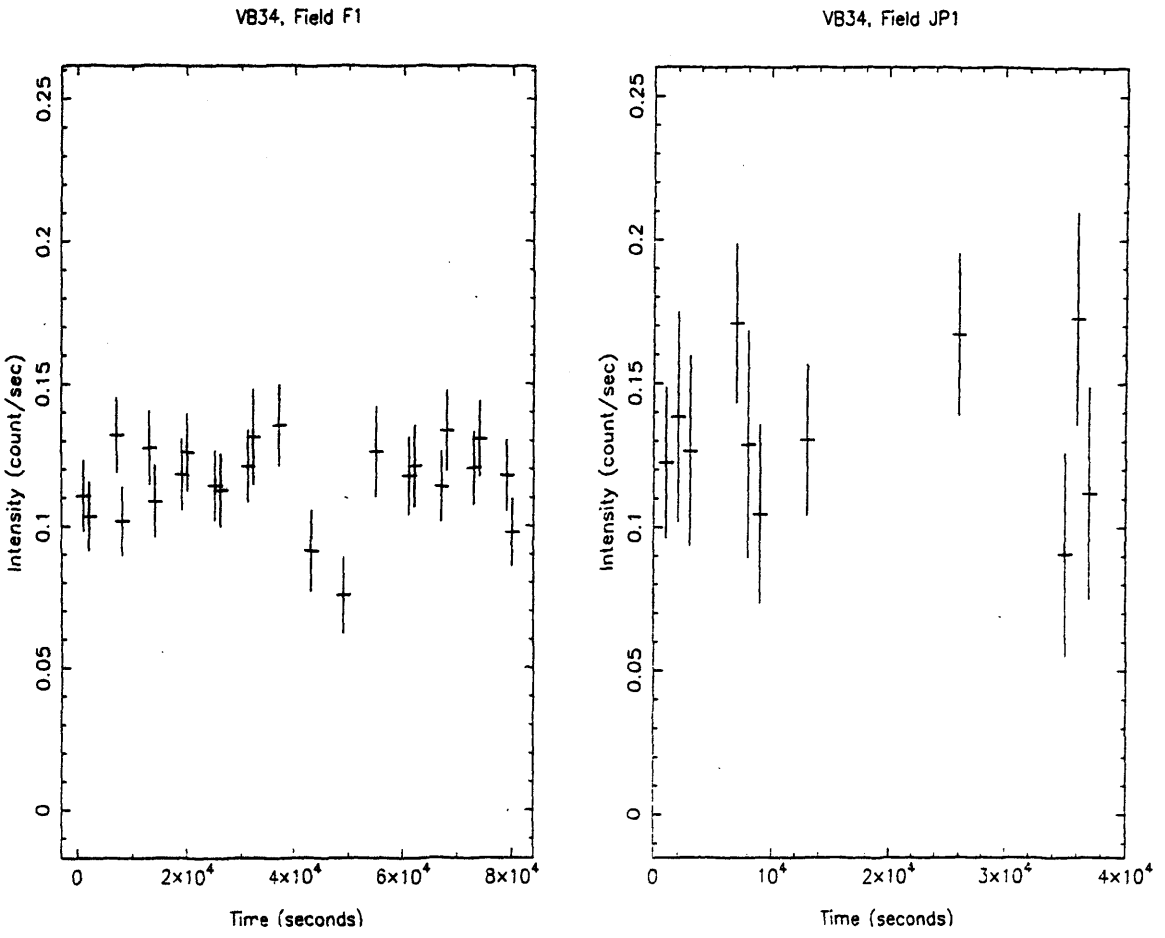

Figure 4.10: Light curves of VB34, left from field UK200776 and right from field UK200441. The first light curve clearly exhibits a 'dip' where the mean count rate drops by ≈30%.

in an EINSTEIN IPC observation of VB34, suggesting that we are not seeing a flare dropping to a lower count rate followed by another flare. This source was also observed in field UK200441 where it maintained a mean count rate of ≈ 0.12 ct/s throughout the observation. It is also unlikely that the dip in the lightcurve is due to some data dropout or other systematic problem as no similar dip is visible in any of the other lightcurves taken from the same PSPC field. Finally the system was the target of the PSPC field and hence on-axis and far from the window supports which can cause spurious variability in lightcurves. A simple 3-dimensional model of the close-binary system shows that no eclipse occurs between those two stars. It is possible that the dip arises from rotational modulation of an active region on one of the stars, though the detailed feasibility of this model has not been established.

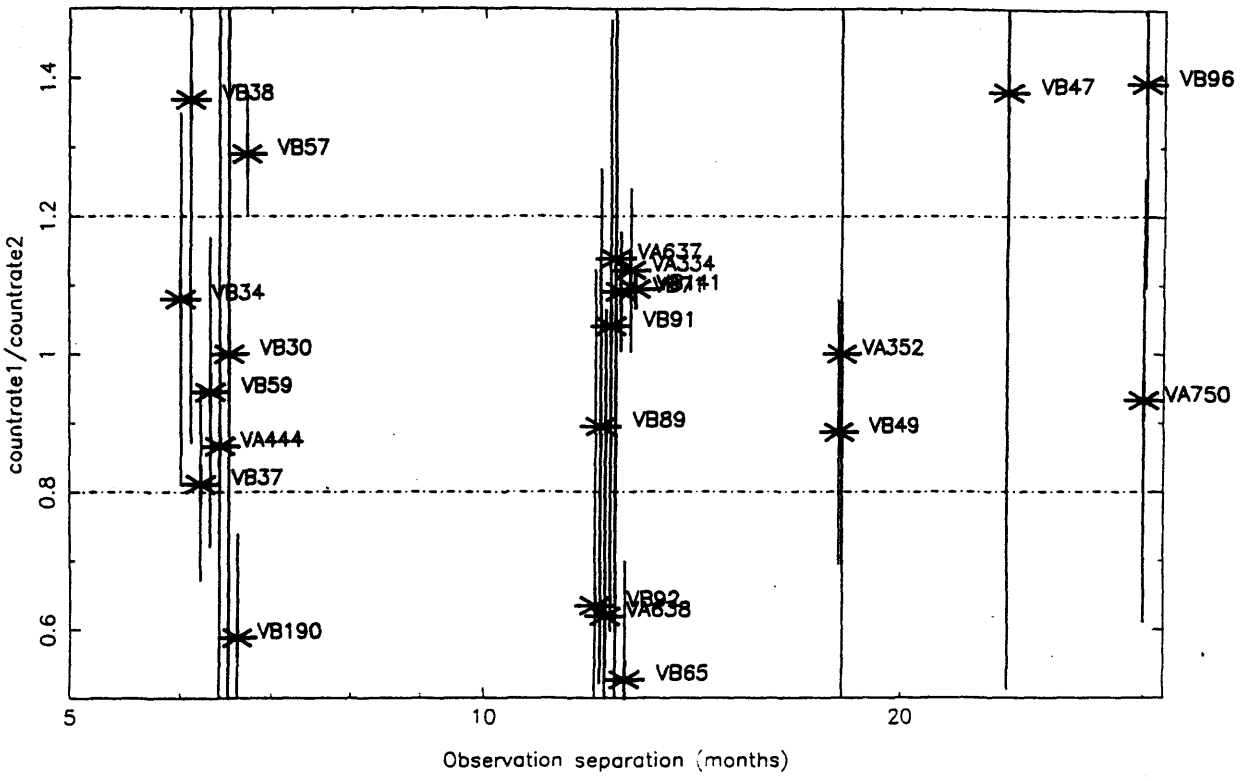

Figure 4.11: Ratio of count rates observed for a number of stars observed more than once in the survey against the time separation of observations. Count rate 1 refers to the earliest observation. Shown are lines indicating a change of 20% in flux. Minimum time separation in the sample was 6 months. Star names are shown.

4.4.3 Repeated Observations

Due to the way the fields overlap 41 stars were observed more than once, though only for 22 stars was the period between observations sizeable (>6 months). This enabled a comparison of the activity of stars to be made over a period of 6 months to two years. In order to remove short-term effects (those within a single observation) only the quiescent count rates are used for those observations where a flare occurs. Figure 4.11 compares the ratio of the PSS count rates for those stars viewed more than once to their time separation (shown in months). It is apparent that some stars do indeed undergo significant luminosity changes (>20%) over these timescales, namely VB57, VB65 and VB190. Of these three, only VB65 was observed whilst near a PSPC rib structure which may have resulted in flux differences between observations.

4.5 Long Term Variability

It is commonly known that the Sun has an activity cycle of 11 years. X-ray observations using *Yohkoh* have shown that the solar coronal luminosity can range between $\log L_x = 26$ and $\log L_x = 28$ (see review by Haisch etal 1996). One would expect that if the Sun is an average star then such luminosity changes should be visible in other stars too. A direct detection of a coronal activity cycle requires a long series of systematic X-ray observations as is available for the Sun. Unfortunately such data have not yet been obtained for other stars. Many people have tried to get around this problem. One method used was to consider regular stars with known rotation rates and examine their states of activity in order to look for any cyclic behaviour (Hemplemann etal 1996). They found some evidence for regular variations in stars correlated with their chromospheric emission. Further evidence of irregular variations was also found.

Similar logic can be applied to the four giants present in the Hyades. As they are of the same age, type and composition, it would be sensible to assume they would have the same levels of coronal activity. This is not the case, disparity exists. Robert Stern (private communication) has suggested that this may imply the giants are on different parts of their activity cycles.

However definitive evidence is sparse. The simple truth is that there is not sufficient data on which to draw any firm conclusions. One suggestion is that so little evidence of variability exists because of a "saturation" effect in the high X-ray emitters, or younger, more rapid rotators. That is to say, only on slower, older stars, such as the Sun, do variations become possible.

In order to search for long term variability in the Hyades, count rates obtained from the PSPC were compared with those from the Einstein IPC survey of the Hyades $\approx$10 years before the ROSAT observations (Micela *et al.* 1988). The ratio of PSPC count rate against IPC count rate for the Hyads observed in both surveys is shown in Figure 4.12. Comparing PSPC and IPC count rates is not trivial as the band passes of the two systems differ, with ROSAT being more sensitive at lower energies and the IPC at higher energies. Hence the relative count rates depend highly on the details of the incident spectrum. For softer

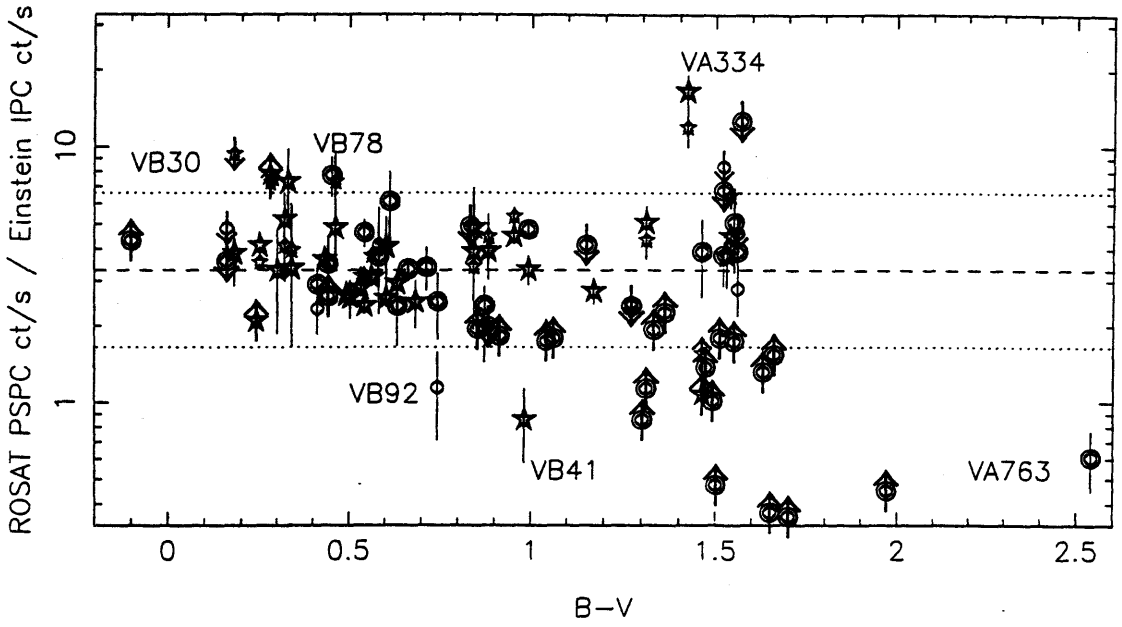

Figure 4.12: Ratio of count rates and count-rate limits for stars observed in the pointed PSPC and/or IPC surveys of the Hyades, against colour (B-V). A constant count rate ratio (see main text) between the two instruments is indicated (dashed line) as are lines (dotted) a factor of two above and below. Single stars are represented by star symbols, binaries by circles. Large symbols represent the best (most significant) PSPC detection or upper-limit of a star. Smaller symbols represent less significant PSPC detections and upper limits for those objects where a better detection exists. Stars exhibiting long term variability are named.

spectra with relatively little interstellar absorption column density, such as we see in the Hyads, the PSPC will record count rates approximately three times larger than the IPC. This theoretical count rate ratio (from the ROSAT Technical Manual) between the two instruments is indicated, taking into account the instrument responses and assuming a hydrogen column density of 10^{-19}cm^{-2} and coronal temperature of logT$\approx$6.5, as is a line a factor of two above and below. Shown are the PSPC/IPC survey best Hyad detections as well as the upper and lower limits of stars not detected in one survey or the other. This process is repeated for other pointed PSPC survey Hyad observations of lower significance with results being represented by the smaller symbols. Binaries are indicated by circles whilst single stars are represented by the star symbol. There were 45 positive detections in both the pointed PSPC and IPC survey, with 7 upper and 23 lower limits.

The majority of stars can be seen to lie close to the nominal ratio (within a factor of two). However a handful of stars varied noticeably, some appearing to change greatly in luminosity (factor $\geq$3) namely VA334, VB92, VB41 and VA763. For VA334 the high luminosity change can be explained as it appeared to flare in the PSPC observations. The apparent decrease in luminosity seen in the other three systems may be due to a flare during the IPC observation. Thus we are left with no clear evidence for long term variability. This result is similar to that obtained in the ROSAT All-Sky Survey (RASS) *vs* IPC study of long-term activity in Hyades stars (Stern *et al.* 1995). This compared RASS PSPC observations of the Hyades with the IPC observations used for comparison in our pointed survey. Limited (within a factor of two) variability was found over the 10 year time difference in observations. This lack of long-term variability would suggest that there is little or no cyclic activity apparent in the coronae of late-type stars of Hyades age, possibly implying that small scale magnetic field generation is more dominant than large-scale dynamo effects. As previously discussed however, there is as yet not enough information to come to any firm conclusions on this matter and studies such as this can only attempt to do what is possible with the sparse data available.

4.6 Time-Resolved Spectroscopy

In order to study the spectral behaviour of the Hyads as they undergo flaring, the PHA spectra of the 14 variable stars (three of which were found to be variable in more than one observation — see Section 4.5.1) were divided into clear 'flare' and 'post-flare' periods. For three of the stars no clear flare was visible, exhibiting instead 'random' variability possibly associated with many overlapping flares. A further two sources had only one time period (1ksec bin) where flaring occured, not containing enough counts for spectroscopic analysis. The remaining 12 sources were unfortunately not X-ray bright enough for high time resolution analysis, and due to the nature of the time-sampling (long periods without data) measuring accurate flare durations and maxima was not possible.

In order to decide what model to fit to the spectra (one or two temperature Raymond-Smith) a purely statistical argument was used. In the work by Hodgkin (Thesis 1996) in

fitting spectra to the Hyades, a single temperature fit was deemed acceptable if:

- $\chi^2_{\rm red} \leq 1.5$ (i.e the data is described by the model with confidence exceeding 3%), **and**
- If $\chi^2_{\rm red} > 1$ (probability that the model could reproduce the data with $\sim$ 50% confidence), an F test comparison with $\chi^2_{\rm red}$ for a two-temperature (2T) fit shows no significant improvement (at an arbitrary confidence level defined by the user – see below). The F test for additional terms is defined below

$$F = \frac{\chi^2(1T) - \chi^2(2T)}{N} \times \frac{1}{\chi^2_{red}(2T)} \tag{4.1}$$

The ratio is a measure of how much the additional terms have improved the value of the reduced chi-square. An improvement in the fit must be achieved to 99% confidence before a 2T fit is deemed to be required (where N is the number of additional terms).

In nearly all cases a two temperature Raymond-Smith model provided the better fit. In the few cases where this was not so a single temperature model was used. These models were fit to the spectra during quiescence and flaring (using XSPEC v8.5). For the brightest stars (VB50, VB30. VB141) an attempt was made to fit the model in both the rising and decay periods of the flare[1]. Table 4.4 summarises the results of this spectral fitting; where no value for high-temperature components is given, only a single temperature fit was required.

Figure 4.13 shows plots of the modelled temperatures. kT_1 against kT_2, and normalisations, K_1 against K_2, with 90% errors (as calculated in XSPEC) for all stars found to flare and requiring the fitting of a two-temperature model[2]. Figures 4.14 to 4.19 show the components for individual stars. Only the stars where a good two temperature fit in both flaring and quiescence are shown in this fashion. From these plots and Table 4.4 it is apparent that it is common for the temperature and normalisation of a star to

[1] All flares can be divided up into periods of increasing and decreasing flux. the sum of which comprises the whole event

[2] I use subscripts '1' and '2' to denote the low and high-temperature components respectively.

increase during flaring, in some cases with a high level of significance. However when considering the errors for the two parameters, temperature and normalisation, together, the confidence-contours are required. Figures 4.20 through to 4.27 show the 68% and 90% confidence χ^2 contours in (kT_1,kT_2) space and (K_1,K_2) space (K is the normalisation factor[3]) for flaring and quiescence. Four stars from the sample showed clear evidence of temperature variations during flaring (VB30, VB50, VB141 and the non-Hyad H363) and of these only two showed clear evidence of normalisation variations (VB50 and VB141). Two further stars (VA351 and VA334) showed an increase in K_2 during flaring but with no obvious associated temperature increase. All of the other variable sources, whilst having a clear best-fit increase in kT_2 and K_2 during flaring, had confidence contours overlapping to such an extent that no conclusions could be drawn.

Stars H363 and VB30 clearly show a best-fit kT_2 increase of $\approx$ 40% during flaring, with no overlap of confidence contours. For VB30 the flare rise and decay show no change in kT_2 and whilst the best-fit value of kT_1 does increase during flare decay, the considerable χ^2-contour overlap prohibits the drawing of conclusions from this. Both VB30 and H363 have poorly constrained normalisation contours.

VB50 shows an increase in kT_2 component at the 68% confidence level, however at the 90% level, contour overlap occurs. Attempts were made to fit the rise and fall of this flare. This was successful in that a good fit (reduced $\chi^2 \approx 1$) was obtained but the confidence contours were poorly constrained. VB141 exhibits no significant temperature change between flare rise and decay but clearly increases in kT_2 during flaring. However in the normalisation contours the flare-rise shows an increased K_2 over both quiescent and flare rise periods.

4.7 Flare Modelling

It has been known since the 1970's that the Sun is not unique in exhibiting flares. Studying stellar flares allows us to test for relationships between flaring and conditions such as a star's mass, age and rotation. parameters which obviously cannot be changed for the Sun. As compared to our Sun, most observed flares have been considerably more energetic,

[3]For a distance d=45pc the Emission measure EM=K$\times$1.1967d^2 in units of 10^{52}cm^{-3} with d in pc.

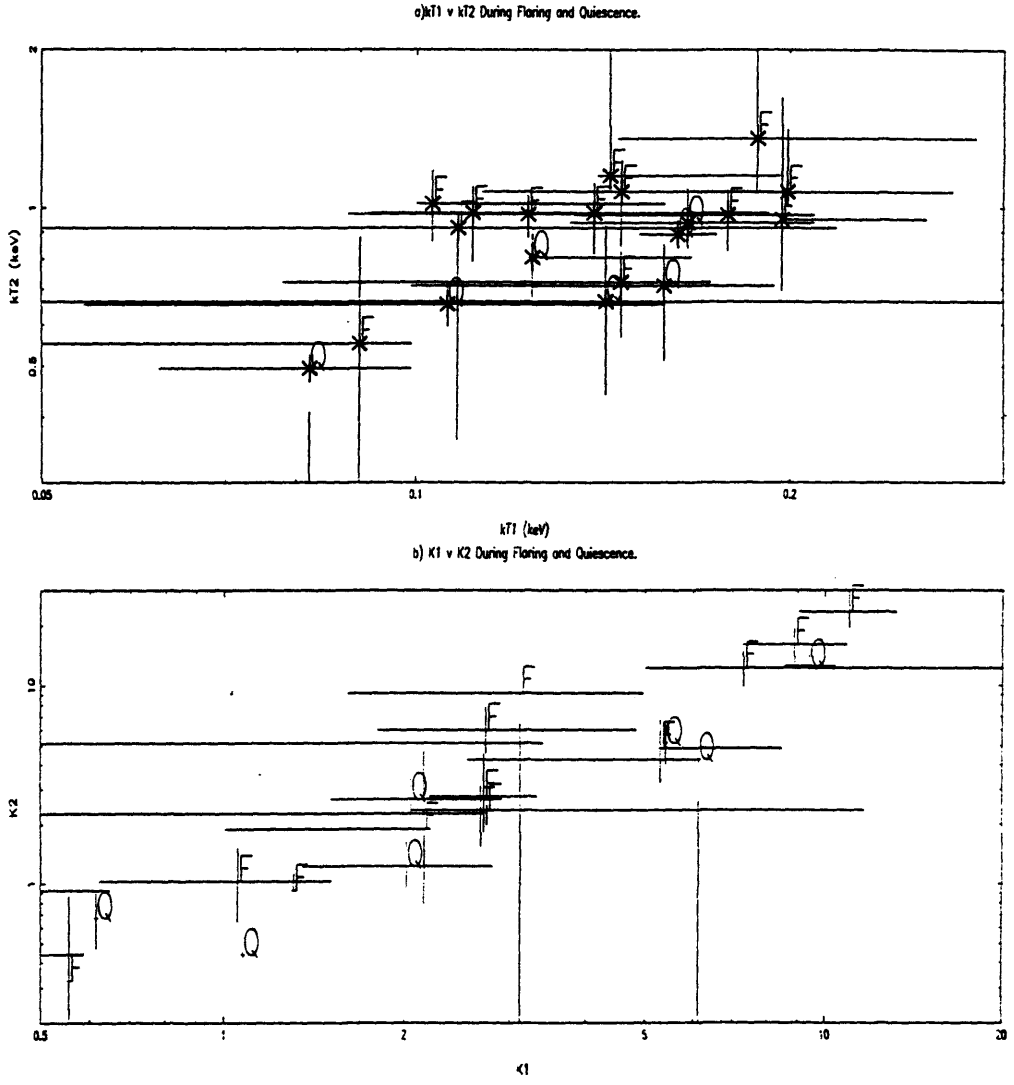

Figure 4.13: a)Plot of low and high temperature components (kT_1, kT_2) of the two-temperature Raymond-Smith model used to fit the flare stars. b) Plot of the normalisations K_1 and K_2 associated with the low and high temperature components of the model. The fits were time selected, this is represented on the plots by an F if the fit was done during a flare period or a Q if during quiescence.

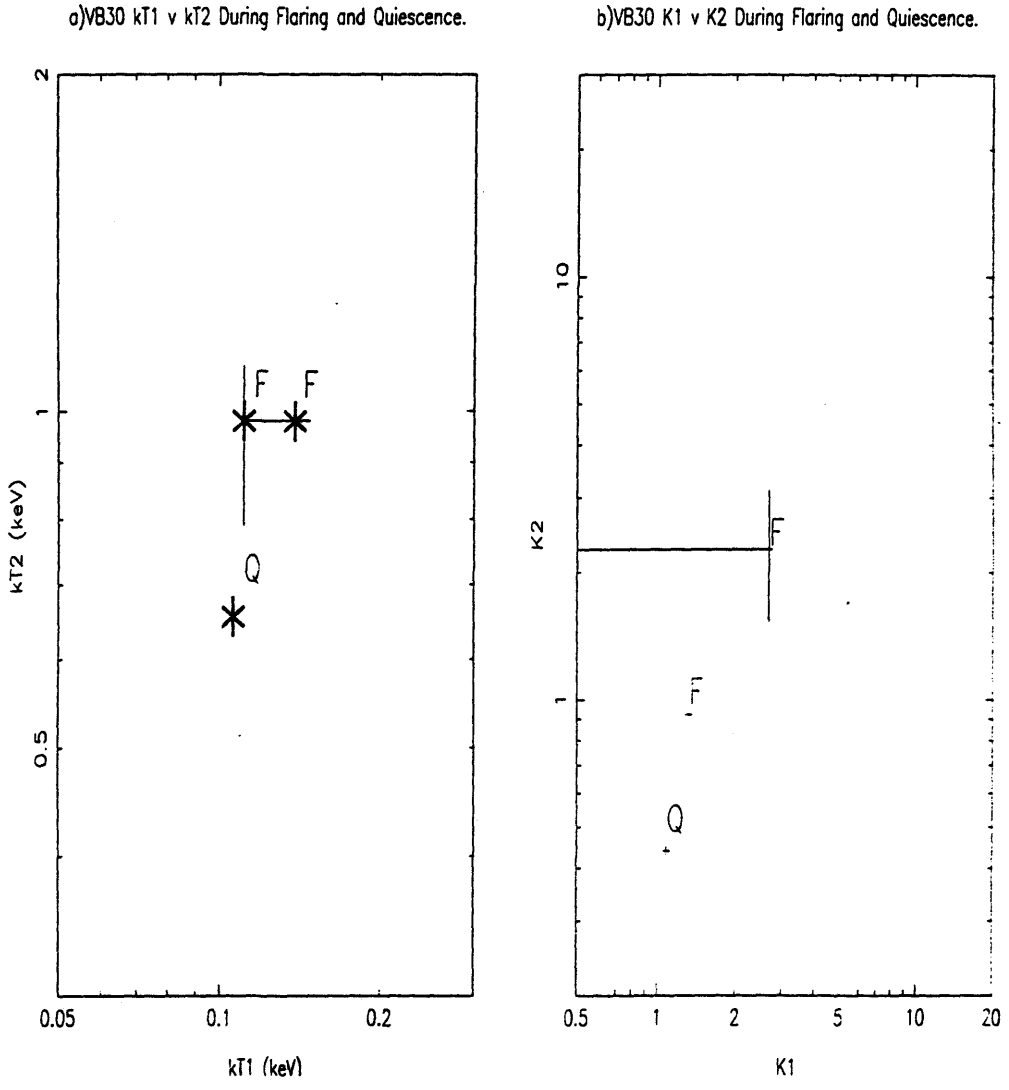

Figure 4.14: a)Plot of low and high temperature components (kT_1, kT_2) of the two-temperature Raymond-Smith model used to fit the spectra of VB30. b) Plot of the normalisations K_1 and K_2 associated with the low and high temperature components of the model. The fits were time selected, this is represented on the plots by an F if the fit was done during a flare period or a Q if during quiescence.

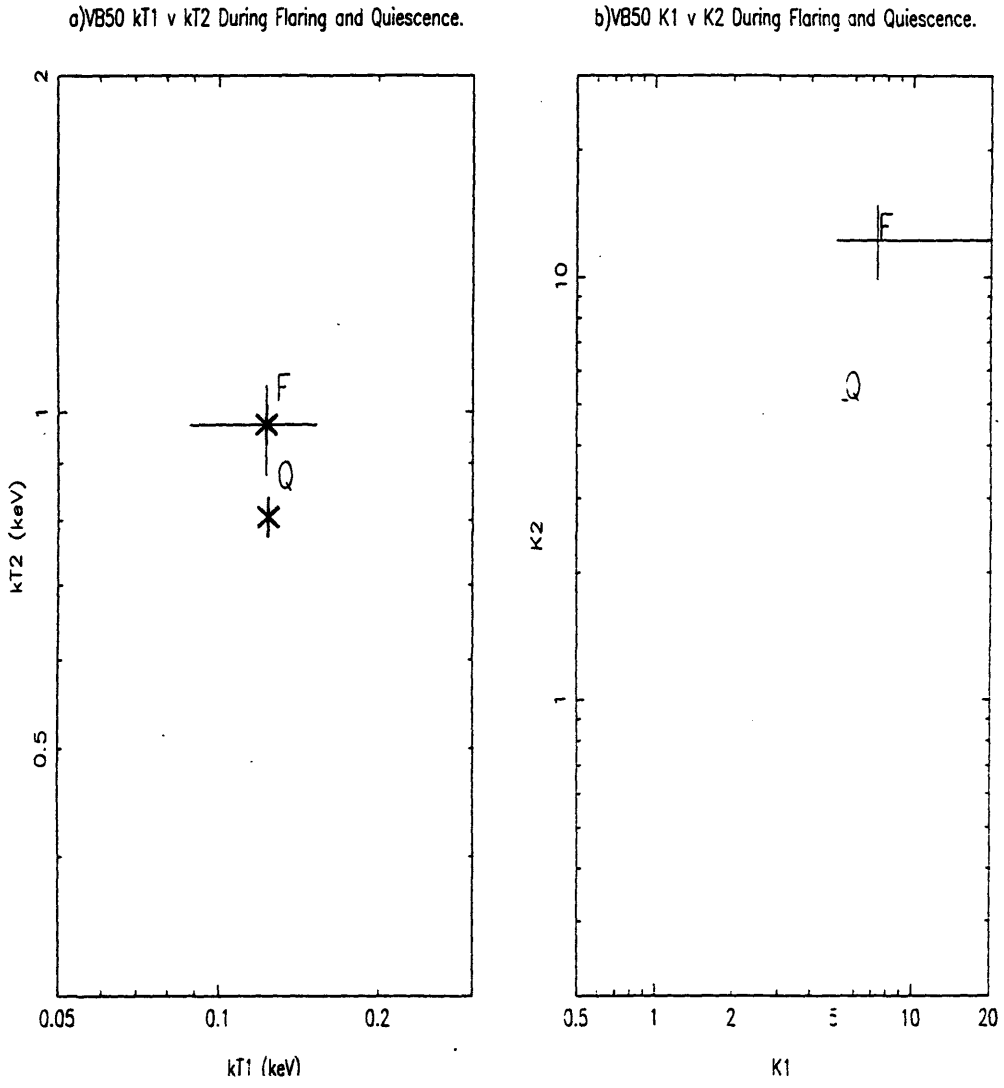

Figure 4.15: a)Plot of low and high temperature components (kT_1, kT_2) of the two-temperature Raymond-Smith model used to fit the spectra of VB50. b) Plot of the normalisations K_1 and K_2 associated with the low and high temperature components of the model. The fits were time selected, this is represented on the plots by an F if the fit was done during a flare period or a Q if during quiescence.

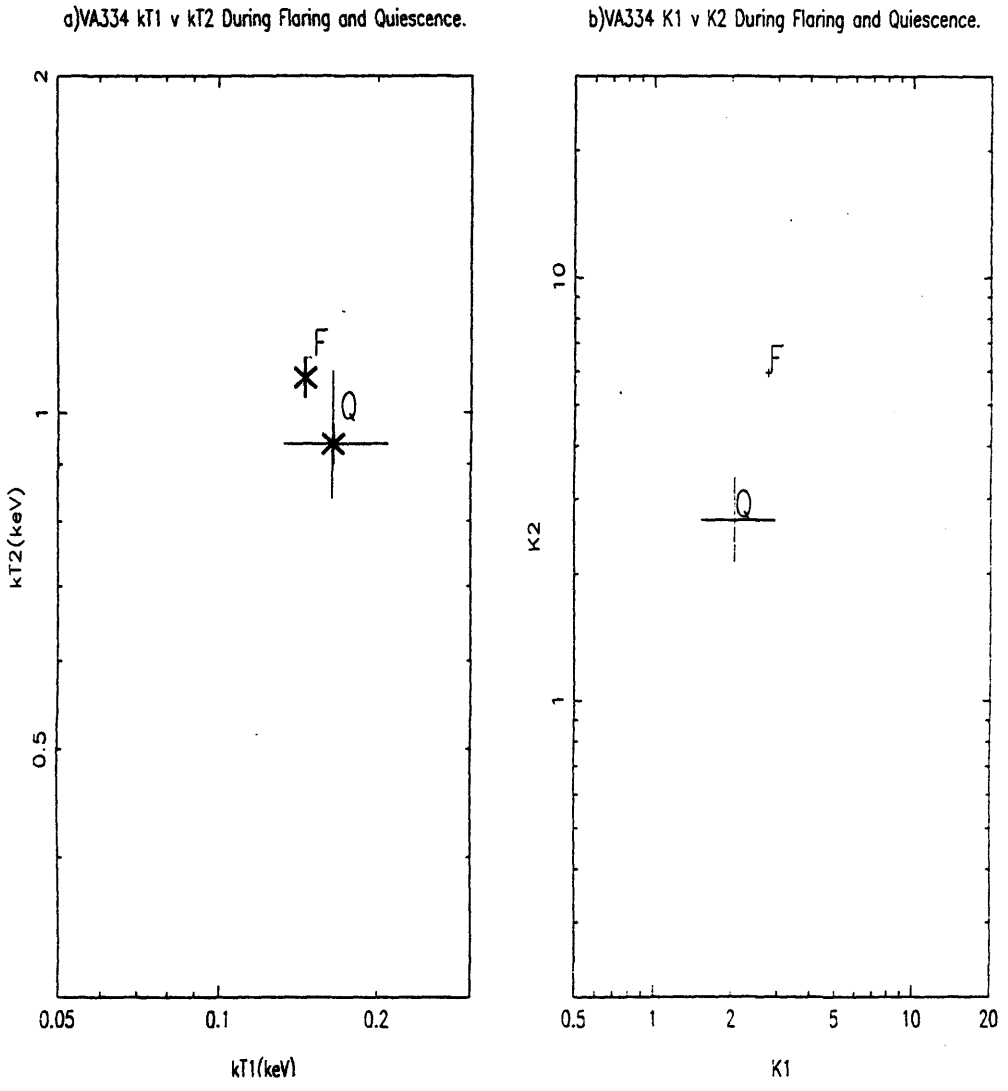

Figure 4.16: a)Plot of low and high temperature components (kT_1, kT_2) of the two-temperature Raymond-Smith model used to fit the spectra of VA334. b) Plot of the normalisations K_1 and K_2 associated with the low and high temperature components of the model. The fits were time selected, this is represented on the plots by an F if the fit was done during a flare period or a Q if during quiescence.

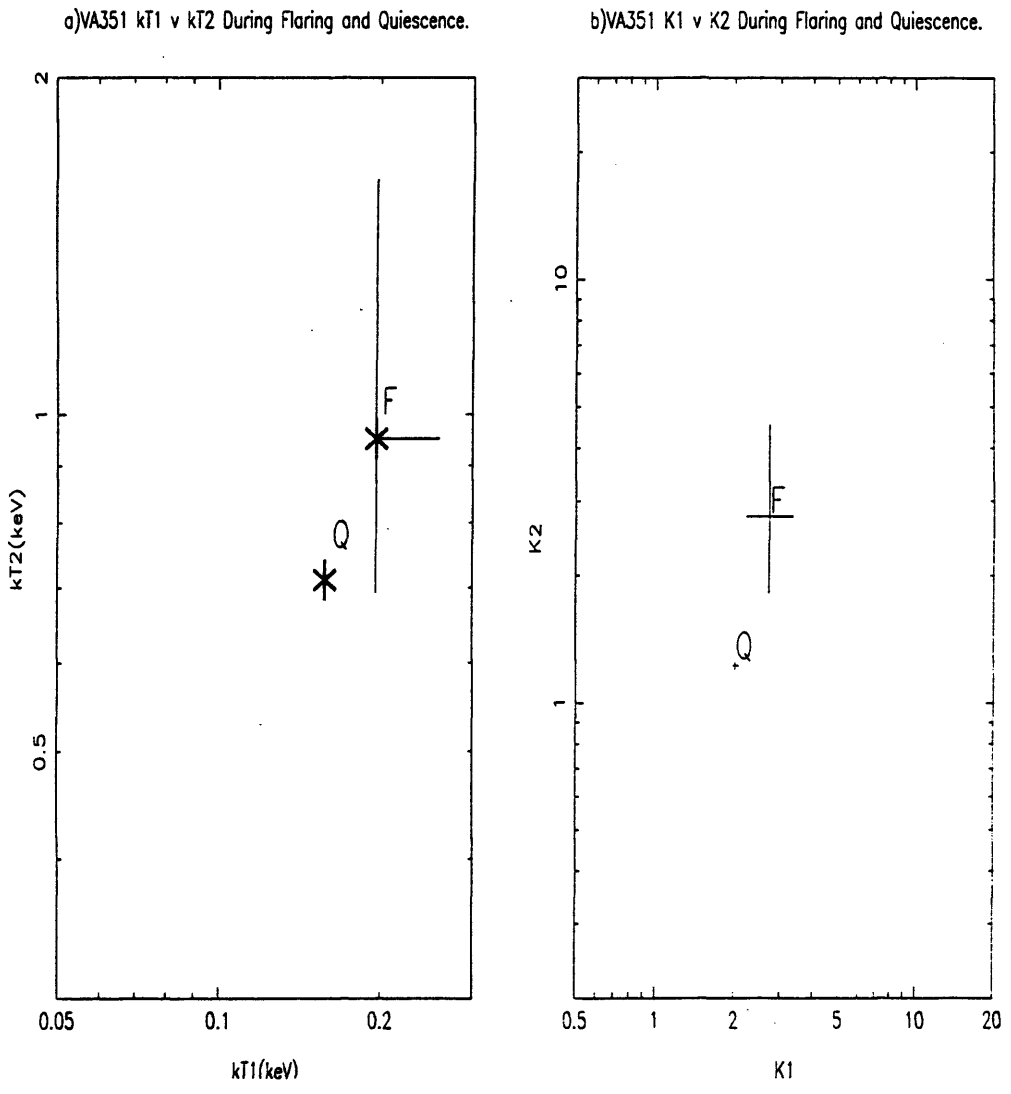

Figure 4.17: a)Plot of low and high temperature components (kT_1, kT_2) of the two-temperature Raymond-Smith model used to fit the spectra of VA351. b) Plot of the normalisations K_1 and K_2 associated with the low and high temperature components of the model. The fits were time selected, this is represented on the plots by an F if the fit was done during a flare period or a Q if during quiescence.

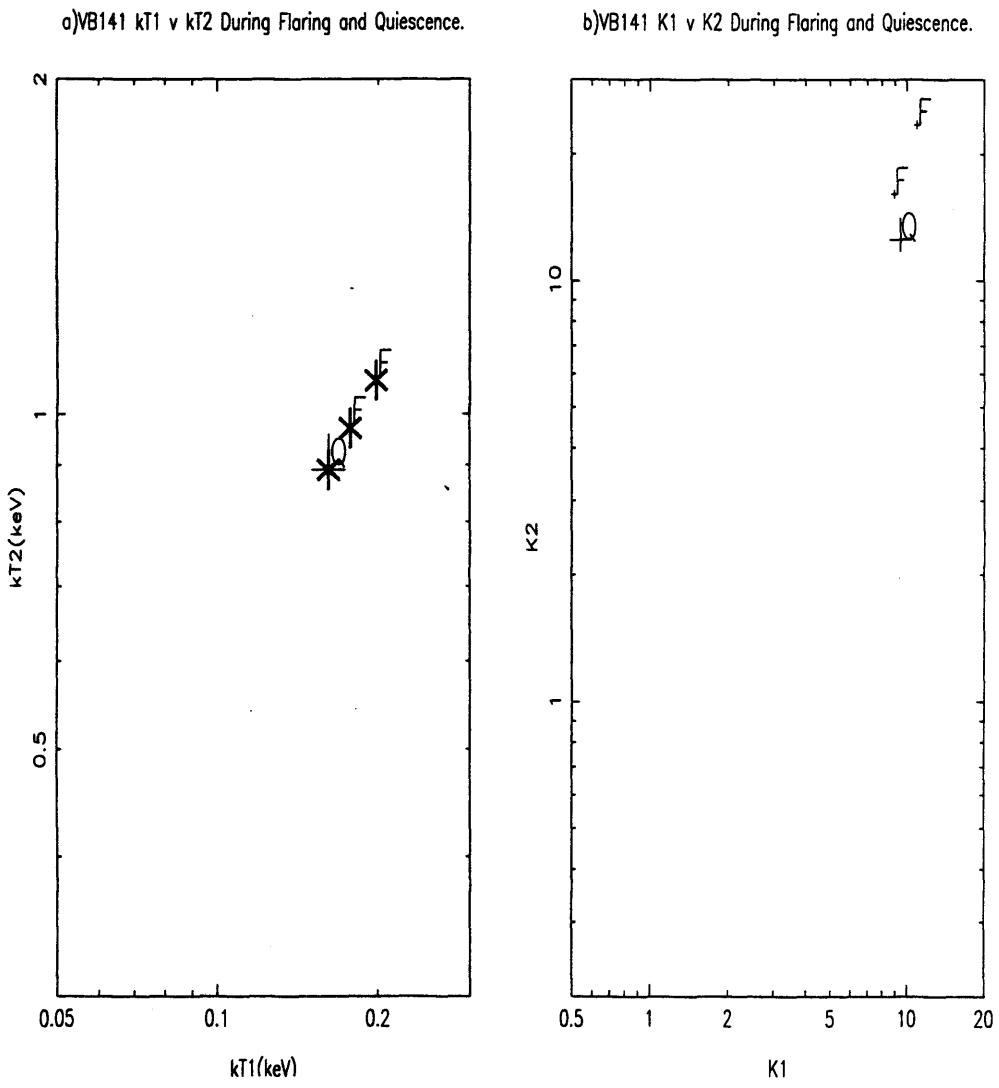

Figure 4.18: a)Plot of low and high temperature components (kT_1, kT_2) of the two-temperature Raymond-Smith model used to fit the spectra of VB141. b) Plot of the normalisations K_1 and K_2 associated with the low and high temperature components of the model. The fits were time selected, this is represented on the plots by an F if the fit was done during a flare period or a Q if during quiescence.

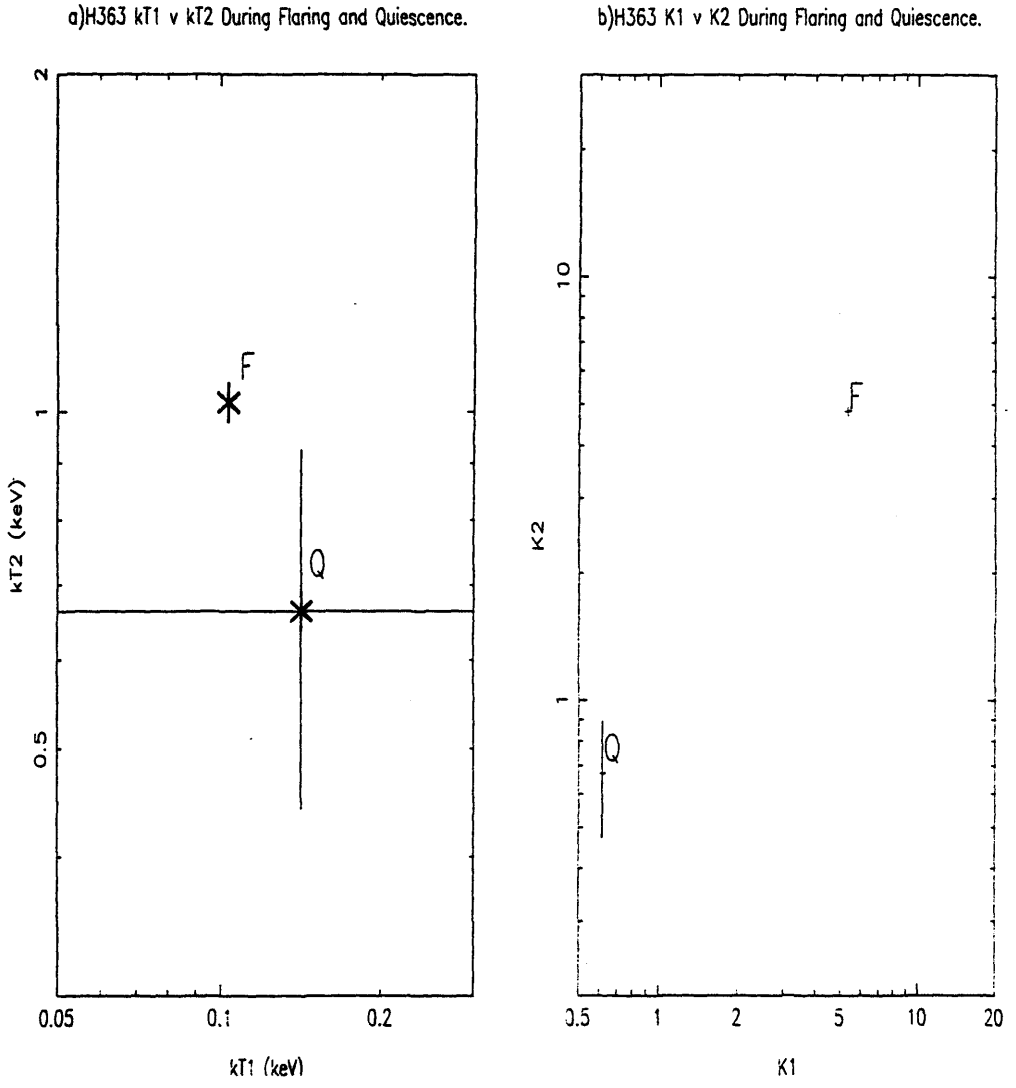

Figure 4.19: a)Plot of low and high temperature components (kT_1, kT_2) of the two-temperature Raymond-Smith model used to fit the spectra of H363. b) Plot of the normalisations K_1 and K_2 associated with the low and high temperature components of the model. The fits were time selected, this is represented on the plots by an F if the fit was done during a flare period or a Q if during quiescence.

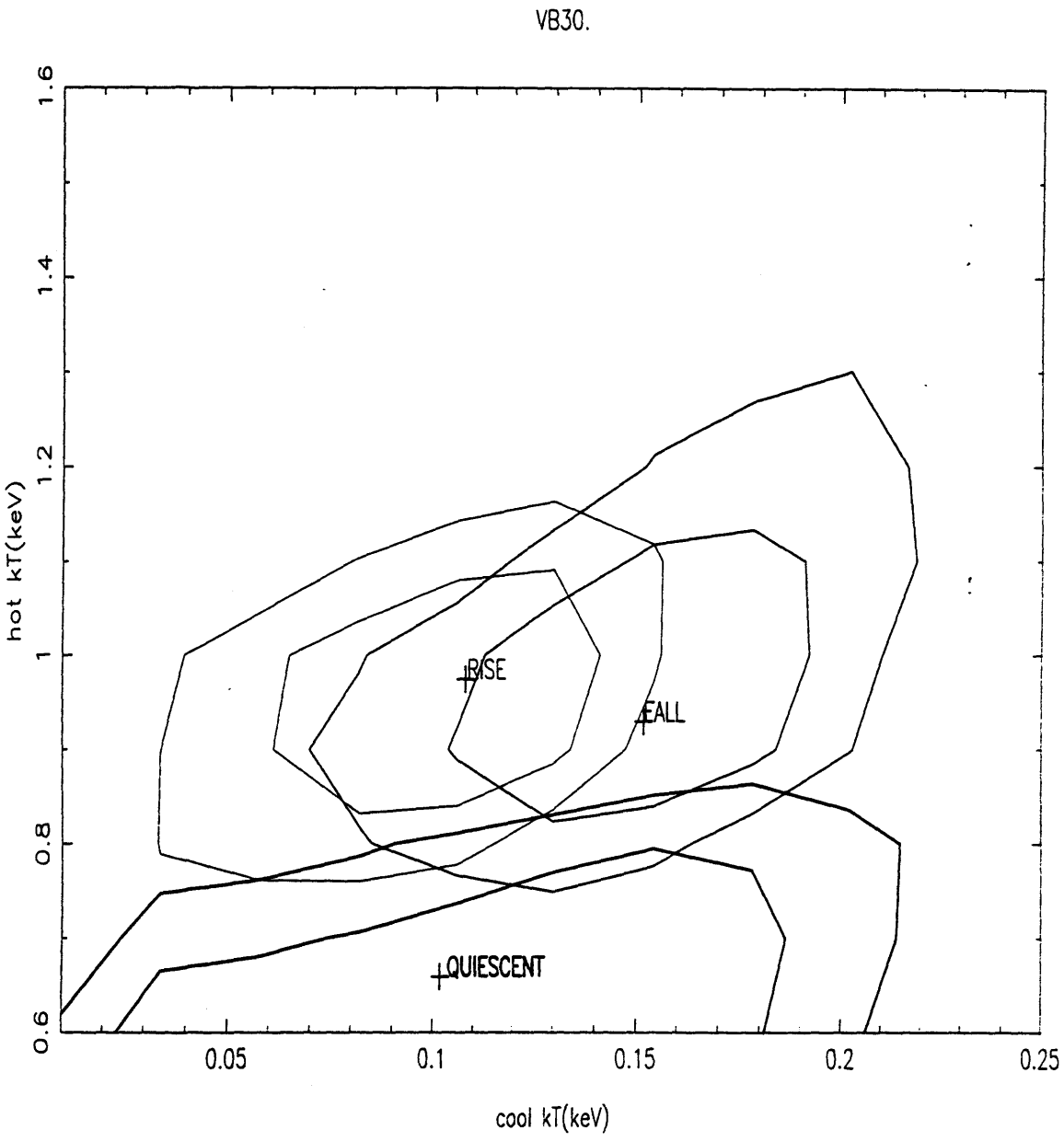

Figure 4.20: Two-parameter (kT_1,kT_2) temperature χ^2 confidence contours (68% and 90% levels) for VB30. Best-fit values are indicated by a cross.

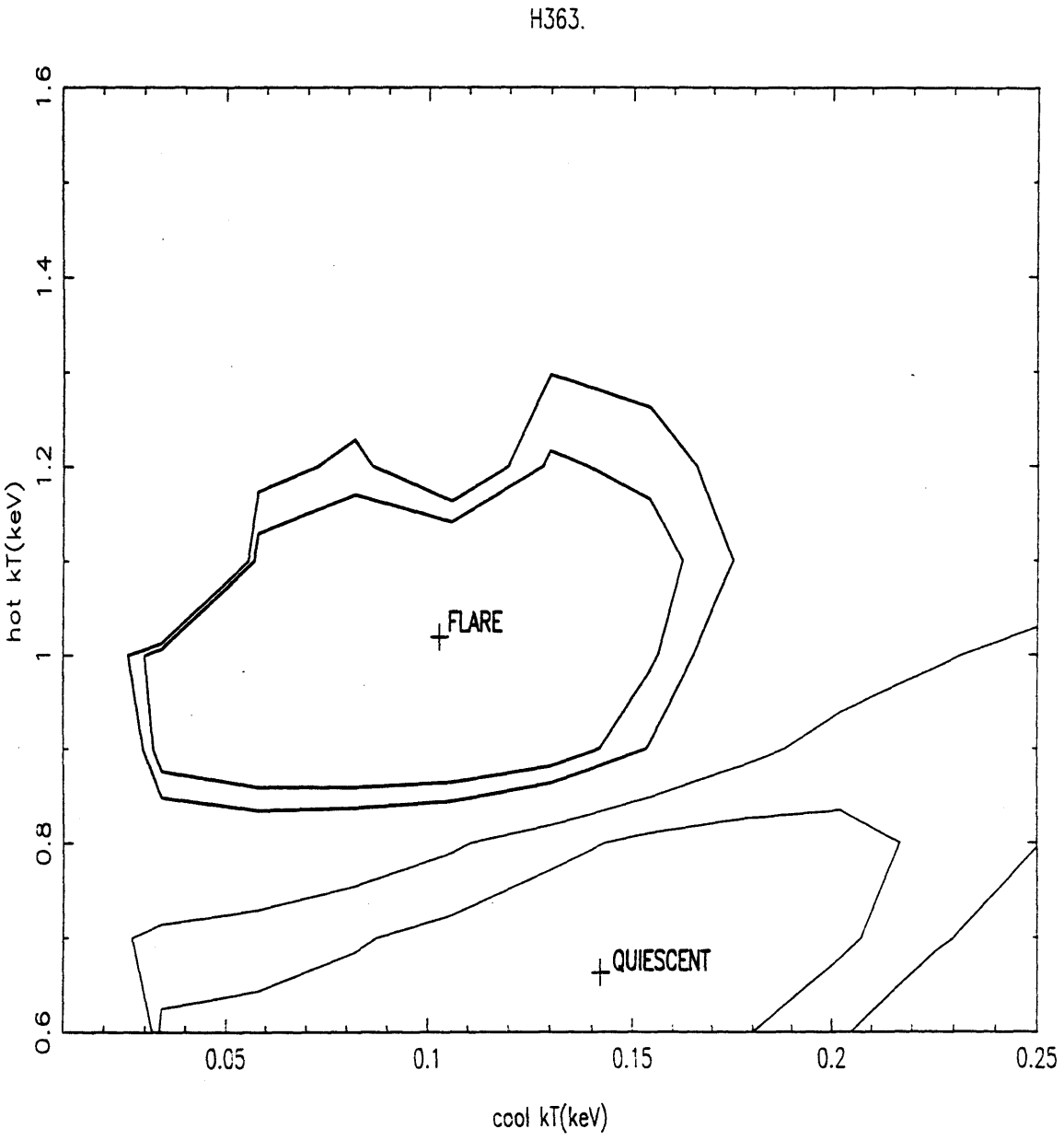

Figure 4.21: Two-parameter (kT_1,kT_2) temperature χ^2 confidence contours (68% and 90% levels) for H363. Best-fit values are indicated by a cross.

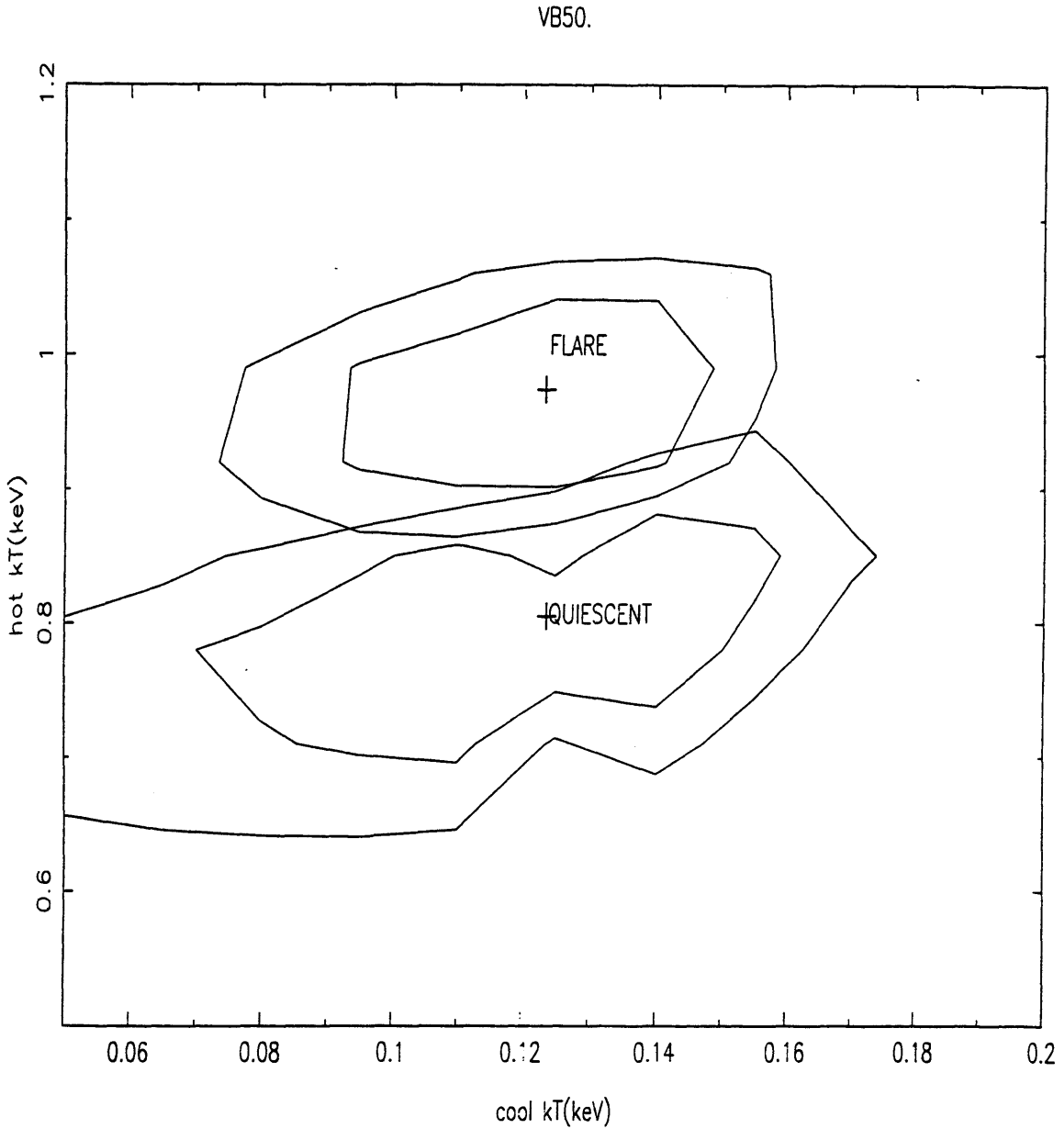

Figure 4.22: Two parameter (kT_1,kT_2) temperature χ^2 confidence contours (68% and 90% levels) for VB50. Best-fit values are indicated by a cross.

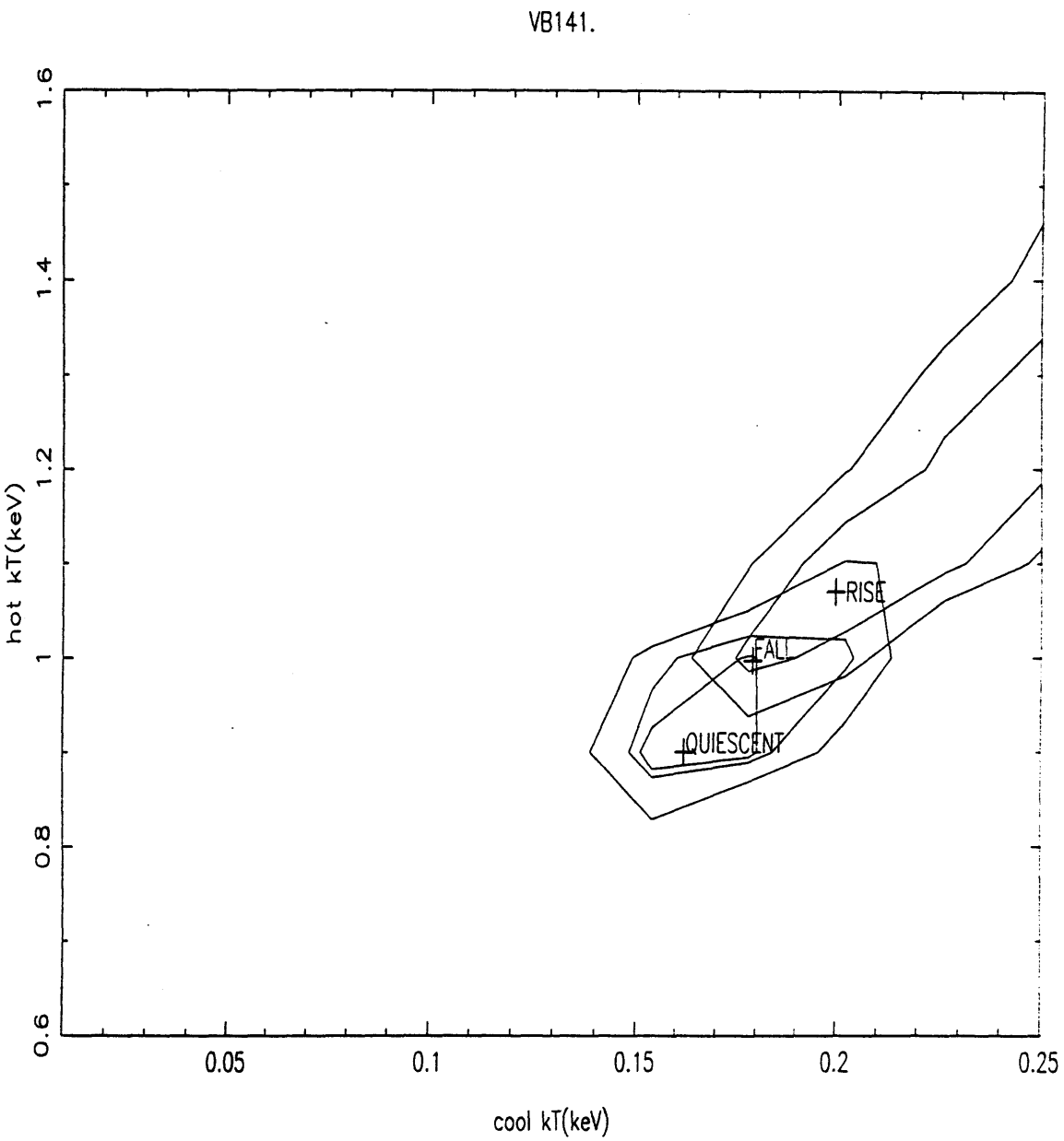

Figure 4.23: Two parameter (kT_1,kT_2) temperature χ^2 confidence contours (68% and 90% levels) for VB141. Best-fit values are indicated by a cross. For VB141 the 68% and 90% contours are small (due to the high number of counts in the quiescent spectrum), hence the 99%confidence parameter is shown as the hatched region.

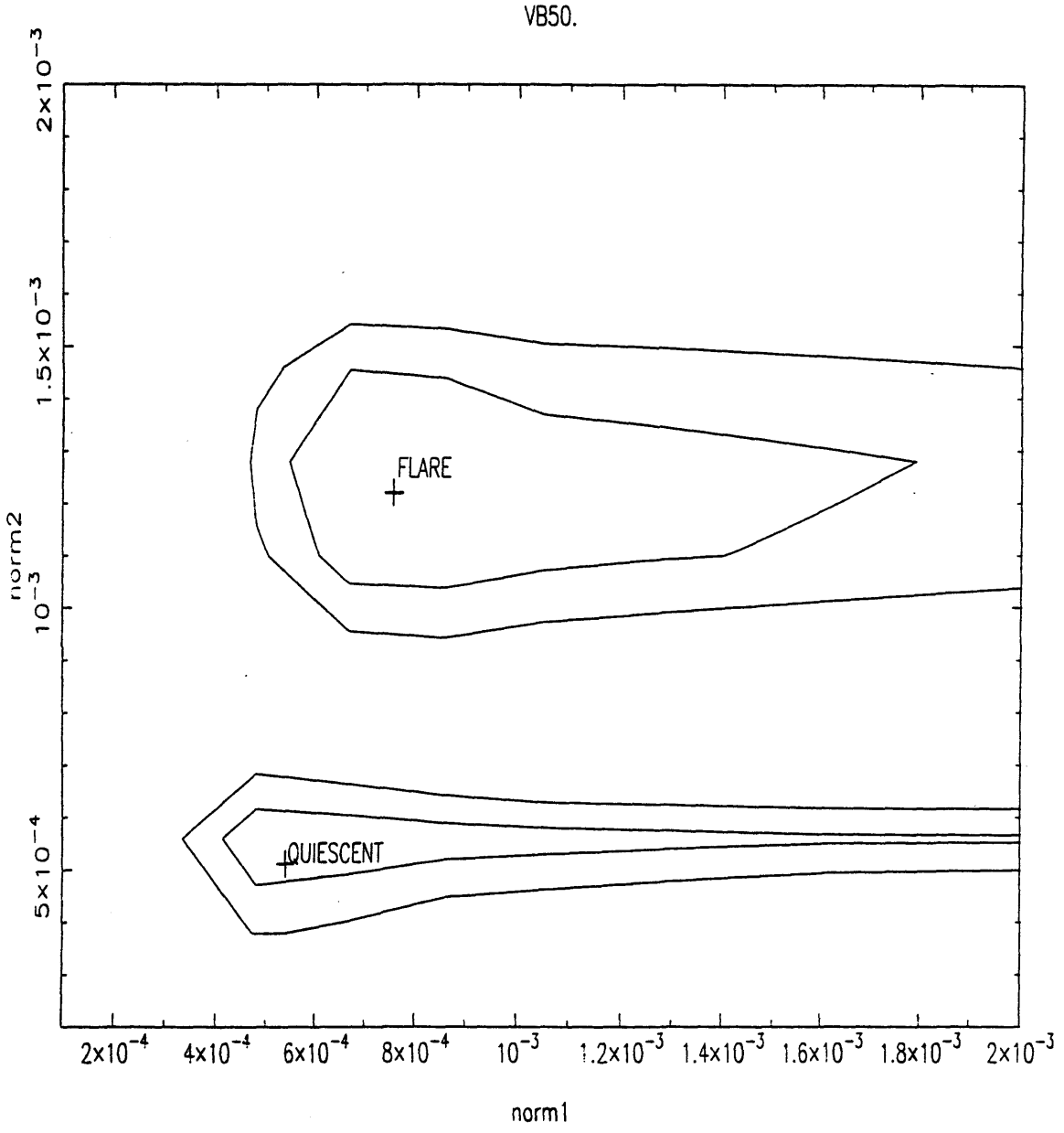

Figure 4.24: Two-parameter (K_1,K_2) normalisation χ^2 confidence contours (68% and 90% levels) for VB50. Best-fit values are indicated by a cross.

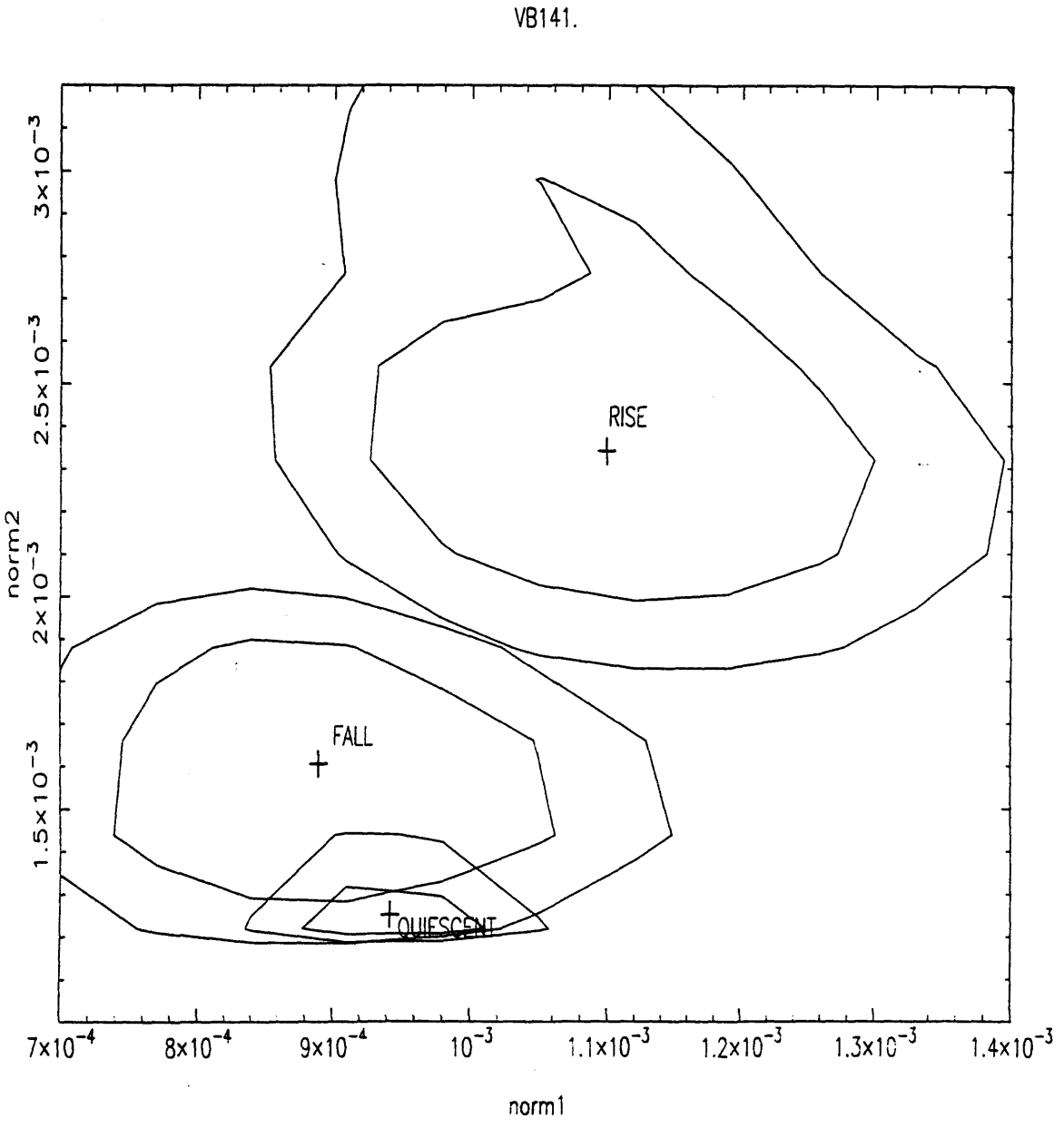

Figure 4.25: Two-parameter (K_1,K_2) normalisation χ^2 confidence contours (68% and 90% levels) for VB141. Best-fit values are indicated by a cross.

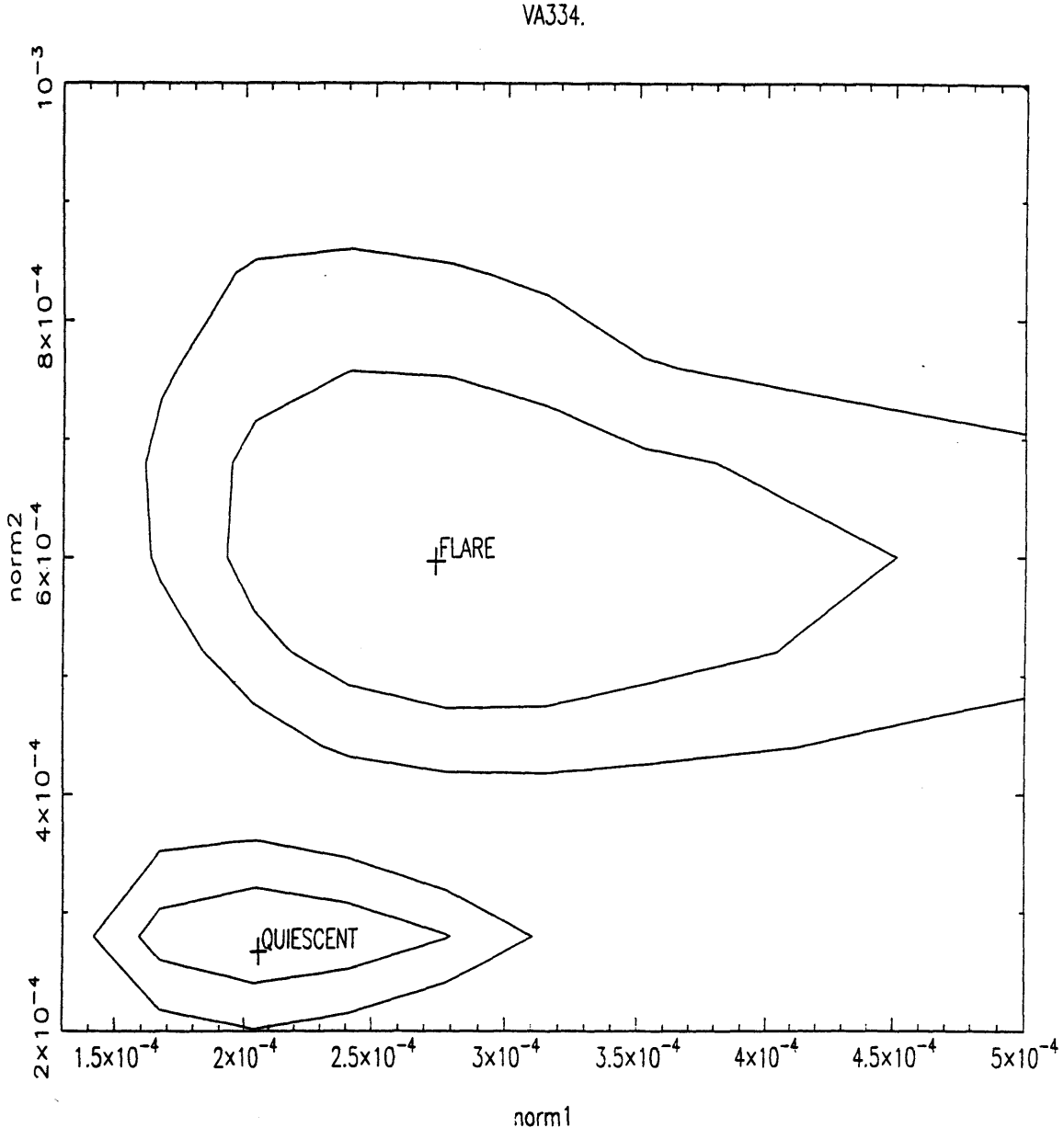

Figure 4.26: Two-parameter (K_1,K_2) normalisation contours χ^2 confidence (68% and 90% levels) for VA334. Best-fit values are indicated by a cross.

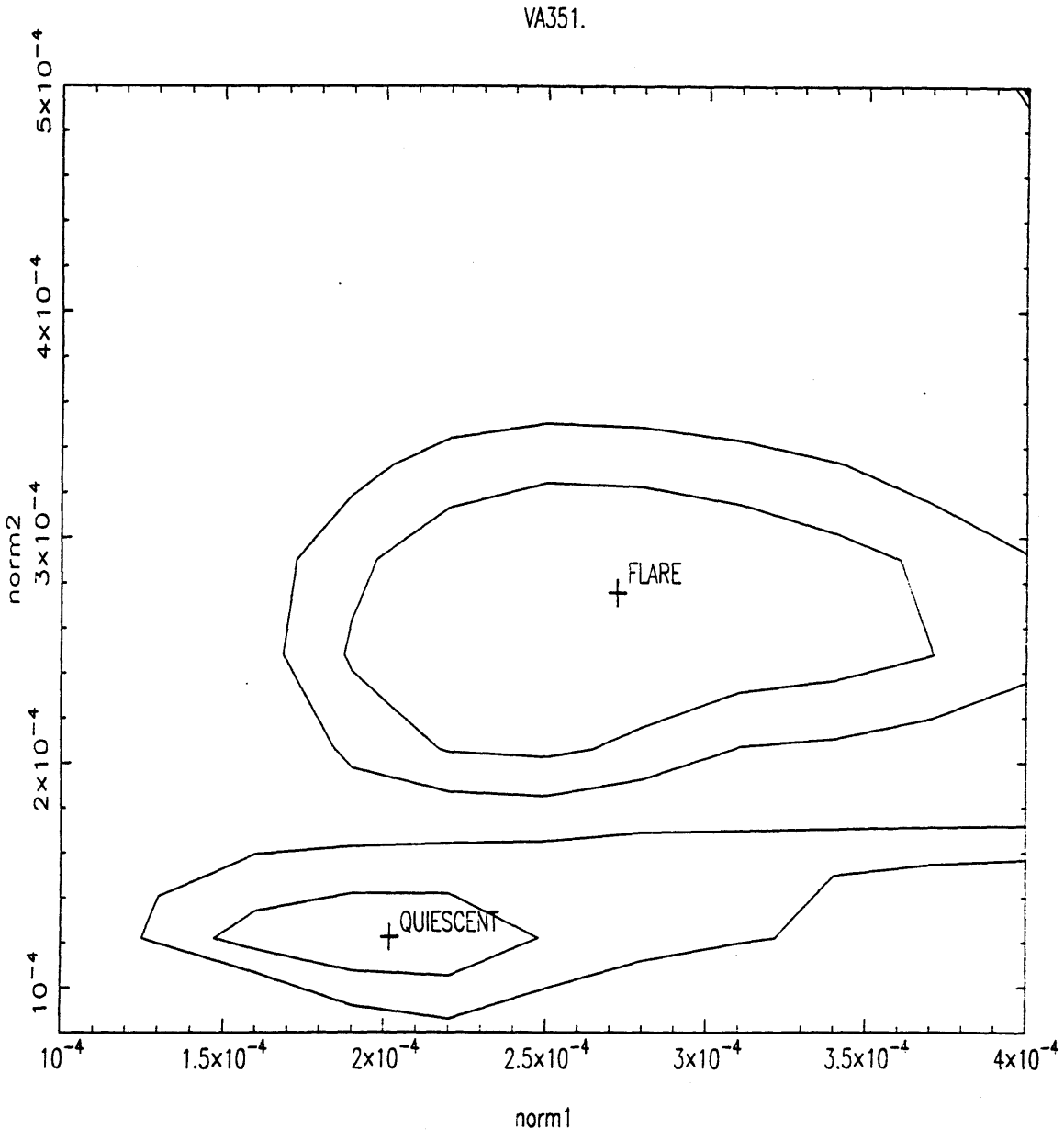

Figure 4.27: Two-parameter (K_1,K_2) normalisation contours χ^2 confidence (68% and 90% levels) for VA351. Best-fit values are indicated by a cross.

Table 4.4: Results of Time Resolved Spectral Fits.

Name	Act	χ^2_ν	χ^2	kT_1	δkT_1	kT_2	δkT_2	K_1	δK_1	K_2	δK_2
VB27	F	0.990	22.78	0.09	0.048 99	0.552	0.271 0.882	0.556	99 99	0.325	0.205 0.860
	Q	1.380	34.49	0.074	99 99	—	—	0.304	99 99	—	—
VB30	FR	1.046	24.06	0.111	0.109 0.148	0.980	0.789 1.098	2.684	2.717 99	2.264	1.529 3.119
	FD	1.064	24.48	0.139	0.0924 0.192	0.979	0.818 1.114	1.311	0.646 99	0.924	0.924 1.123
	Q	0.428	9.70	0.106	0.054 0.158	0.655	0.594 0.726	1.077	0.569 99	0.439	0.200 99
VB30	F	0.725	16.67	0.143	0.140 0.196	1.151	1.145 5.46	2.162	1.009 2.210	1.891	0.791 4.711
	Q	0.472	11.79	0.214	0.178 0.253	—	—	1.404	1.091 2.160	—	—
VB45	Q	0.571	14.29	0.325	0.234 0.518	—	—	1.127	0.711 1.666	—	—
	F	0.597	14.92	0.310	0.233 0.439	—	—	0.576	0.391 0.841	—	—
VB50	F	1.033	23.75	0.123	0.088 0.153	0.974	0.877 1.057	7.309	5.010 20.09	12.229	9.864 14.80
	Q	1.015	23.36	0.124	0.123 0.166	0.805	0.677 0.892	5.403	3.395 99	5.120	4.005 6.404
VA334	Q	1.206	27.74	0.165	0.133 0.209	0.938	0.838 1.089	2.057	1.515 2.905	2.675	2.133 3.377
	F	0.544	12.47	0.146	0.113 0.194	1.074	0.847 1.231	2.739	1.812 4.819	5.965	4.539 7.809
VA351	F	1.041	23.95	0.197	0.196 0.259	0.951	0.693 1.621	2.719	2.213 3.313	2.755	1.817 4.532
	Q	0.877	20.17	0.158	0.099 0.194	0.711	0.512 0.853	2.018	1.356 2.804	1.224	0.945 1.627
H363	Q	0.437	10.06	0.142	0.023 0.925	0.663	0.441 0.925	0.615	0.481 99	0.672	0.472 0.895
	F	1.141	26.24	0.103	0.100 0.158	1.019	0.865 1.178	5.296	5.292 8.443	4.821	3.216 6.711
VB141	Q	1.302	29.94	0.162	0.151 0.174	0.891	0.865 0.959	9.421	8.559 10.36	12.521	11.72 14.10
	FR	0.875	20.11	0.199	0.168 0.272	1.072	1.070 1.409	10.991	9.039 13.21	23.415	19.41 30.65
	FD	0.792	18.21	0.178	0.134 0.209	0.971	0.828 1.077	8.897	7.286 10.86	16.06	112.35 19.34
VB73	F	0.861	19.80	0.108	0.004 0.218	0.917	0.361 0.949	1.056	0.622 1.514	1.027	0.646 1.513
	Q	0.754	18.85	0.251	0.217 0.286	—	—	2.567	2.141 3.09	—	—
VB190	Q	0.937	23.43	0.268	0.224 0.329	—	—	2.607	2.046 3.447	—	—
	F	1.119	25.75	0.188	0.145 0.284	1.355	1.079 4.112	3.118	1.616 4.947	9.155	6.384 99
VB85	Q	0.759	17.48	0.082	0.062 99	0.495	0.409 99	6.124	2.552 6.125	4.228	2.609 99
	F	0.604	13.89	0.146	0.078 0.172	0.722	0.568 0.826	2.751	2.055 11.65	2.352	1.988 2.495

Notes: Columns are:Star name. state of activity(F=flare, FR=flare rise. FD=flare decay, Q=quiescent), reduced χ^2, χ^2, kT_1 (keV), error on kT_1 (keV, error value of 99 indicates no limit could be modelled).kT_2 (keV), error on kT_2 (keV), K_1, error on K_1 ($\times 10^4$), K_2, error on K_2 ($\times 10^4$).

because stellar distances and instrumental limitations allow only the detection of the most powerful events.

There are basically three models that have been commonly applied to the X-ray light-curves of stellar flares, the quasi-static cooling-loop model (van den Oord and Mewe 1989), the single-loop model (Reale *et al.* 1993) and the two-ribbon flare model (Kopp and Poletto 1984). Each of the models is based on different assumptions. The cooling-loop model assumes that the changing plasma conditions in a single loop give rise to the observed flare characteristics (rise, and subsequent decay by radiative cooling), the single-loop model is based on hydrodynamic simulations of compact stellar flares whilst the two-ribbon model assumes that different loops become activated over the course of the event.

4.7.1 The Quasi-static Cooling-Loop Model

In order to model the observed Hyades flares I applied the first of the above models (van den Oord, Mewe and Brinkman 1988). It is the simplest model which deals with only radiative energy loss and was chosen as the data is not good enough to support a more rigorous model. The model uses calculated values for free-free, free-bound, bound-bound and two-photon transitions in a plasma (Mewe *et al.* 1985). It ignores the flare rise and associated heating mechanisms and assumes that after the flare peak no additional heating occurs. Cooling is assumed to be quasi-static and completely radiative (mostly in the soft X-ray band) with no conductive losses of heat through the 'footpoints' of the loop back into the photosphere. In the quasi-static approximation it is assumed that scaling laws apply for the flaring plasma relating pressure, peak temperature, loop length and heating of the static loop.

The radiative cooling function is approximated by:

$$\Lambda(T) = 10^{-26.89} T^{\alpha} \mathrm{erg cm^3 s^{-1}} \qquad (4.2)$$

with α=−0.6. which applies between logT(K)≈6.7 and logT(K)≈7. With no heating the radiative energy loss per unit time is:

$$E_{rad} = \left(\frac{E_0}{(1 + (\frac{t}{3\tau}))^4} \right) \tag{4.3}$$

where E_0 is the radiated energy at the beginning of the decay phase, t is the time and τ is the radiative cooling time scale given by:

$$\tau = \left(\frac{3kT_0}{n_e \Lambda(T_0)} \right) \tag{4.4}$$

T_0 is the temperature at the start of the decay phase, n_e is the electron density, k is Boltzmann's constant and $\Lambda(T_0)$ is the emissivity or radiative cooling function. Temperature values taken for flare peak were the best-fit high-temperature components for the two-temperature Raymond-Smith model fit to the spectra during flaring.

Hence a set of theoretical flare decay curves was made for each flare event (see Figure 4.28 — 4.30). All flare models were arranged to start at the observed flare peak. The radiative cooling time scale τ was defined as the time required for a flare to drop to $\approx 1/e \times ((c_p) - (c_q))$ where c_p is the measured peak count rate and c_q is the measured quiescent count rate. This value was varied in an attempt to get a good fit. The only free-parameter in the model is τ. Using the best-fit flare models to the actual flares it was possible to establish physical parameters of the flare (volume, loop length, loop height). As the emission measure EM $\approx n_e{}^2 V$ and we have n_e from the value of τ previously calculated, the flare volume can be found. Assuming single loop geometry with aspect ratio α defined as the ratio of the loop diameter (2r) to the total loop length L we have:

$$V = \pi r^2 L = \left(\frac{\pi}{4} \right) \alpha^2 L^3 \tag{4.5}$$

Typically α=0.1 for solar loops. The approximate loop height is given by:

$$H = \left(\frac{L}{\pi} \right) \tag{4.6}$$

To compare the loop size to the pressure scale heights we use:

$$H_p = \left(\frac{kT_0}{\mu m_{Hg}}\right) \approx \left(\frac{3kT_0}{2m_{Hg}}\right) \tag{4.7}$$

where m_H is the hydrogen mass, g is the stellar surface gravity (assume log(g)$\approx$4) and the mean molecular weight of free coronal plasma particles is taken to be $\mu \approx \frac{2}{3}$.

The results of the model fits are presented in Table 4.5. Of the nine flares where it is possible to make a good estimate for the flare peak, four provide very good fits to the model, a further five fit well but with a possibility of multiple flare events extending the overall flare. The estimated flare-loop heights are mostly in the region of 1—2 solar radii ($R_{SUN} \approx 7 \times 10^{10}$cm), with the exception of VB190, which seems to exhibit large flare-height. As compared to the flares on the Hyads, the non-Hyad H363 has a much smaller, denser flare. The flare heights are generally less than the calculated pressure scale-heights, though most of the good flare fits (VB27, VB45 and VB190) have greater heights (by a factor of 30 in the case of VB190). The loop densities are mostly similar to those seen in our Sun ($n_e \approx 10^9 cm^{-3}$). Caillault *et al.* (1995) modelled a Pleiades flare, obtaining a density of $1.3 \times 10^{11} cm^{-3}$ (a value greater than that obtained for our Hyads) and a loop length of $\approx 3 \times 10^{11}$cm (comparable with our Hyad loop lengths).

Whilst these results seem believable in terms of their size (reasonable heights) and density (equivalent to solar), it is important to understand that these results are only estimates for the values of the physical parameters. This is a very simple model, the data do not justify a more complex one. In reality the results produced may not be strictly accurate, indeed it is highly likely that the single loops that we calculate the length of may in actual fact be a collection of smaller loops. Nevertheless, the model is commonly used and as such remains a powerful tool for the inter-comparing of similar surveys (eg the results of the Pleiades survey by Caillault *et al.*).

4.8 Flare Frequency

Most of the stellar X-ray flares reported prior to the launch of ROSAT (mainly from Einstein and EXOSAT observations) were from dK/dMe and RS CVn stars (Haisch 1983;

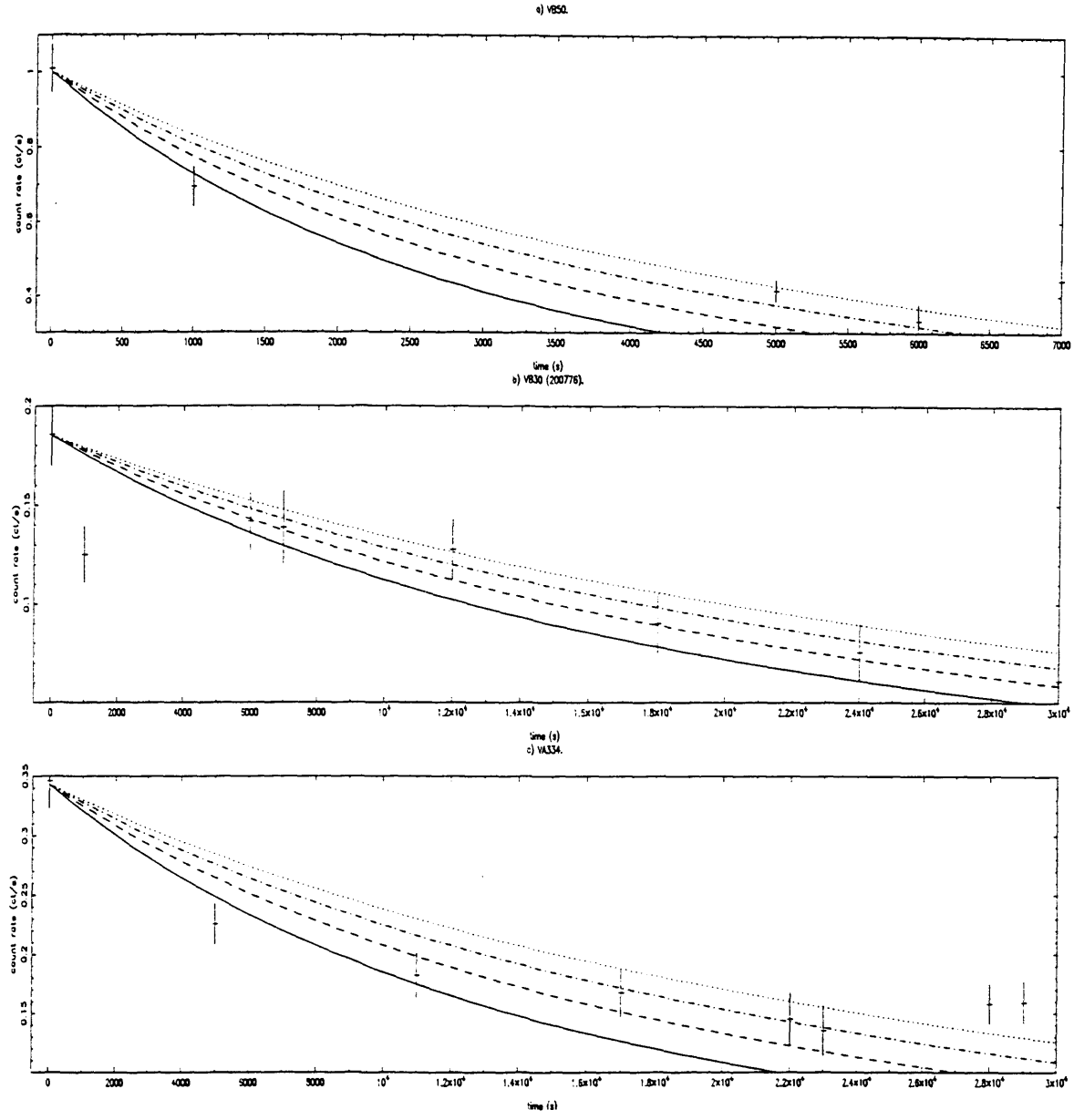

Figure 4.28: Modelled flare decay overlayed on observed flare. Each curve (solid, dashed, dash-dotted and dotted) represents a different value for the radiative cooling time (ranges are given in Table 4.5). Flares shown here are a) VB50, b) VB30 (field 200776) and c) VA334. For model results see Table 4.5.

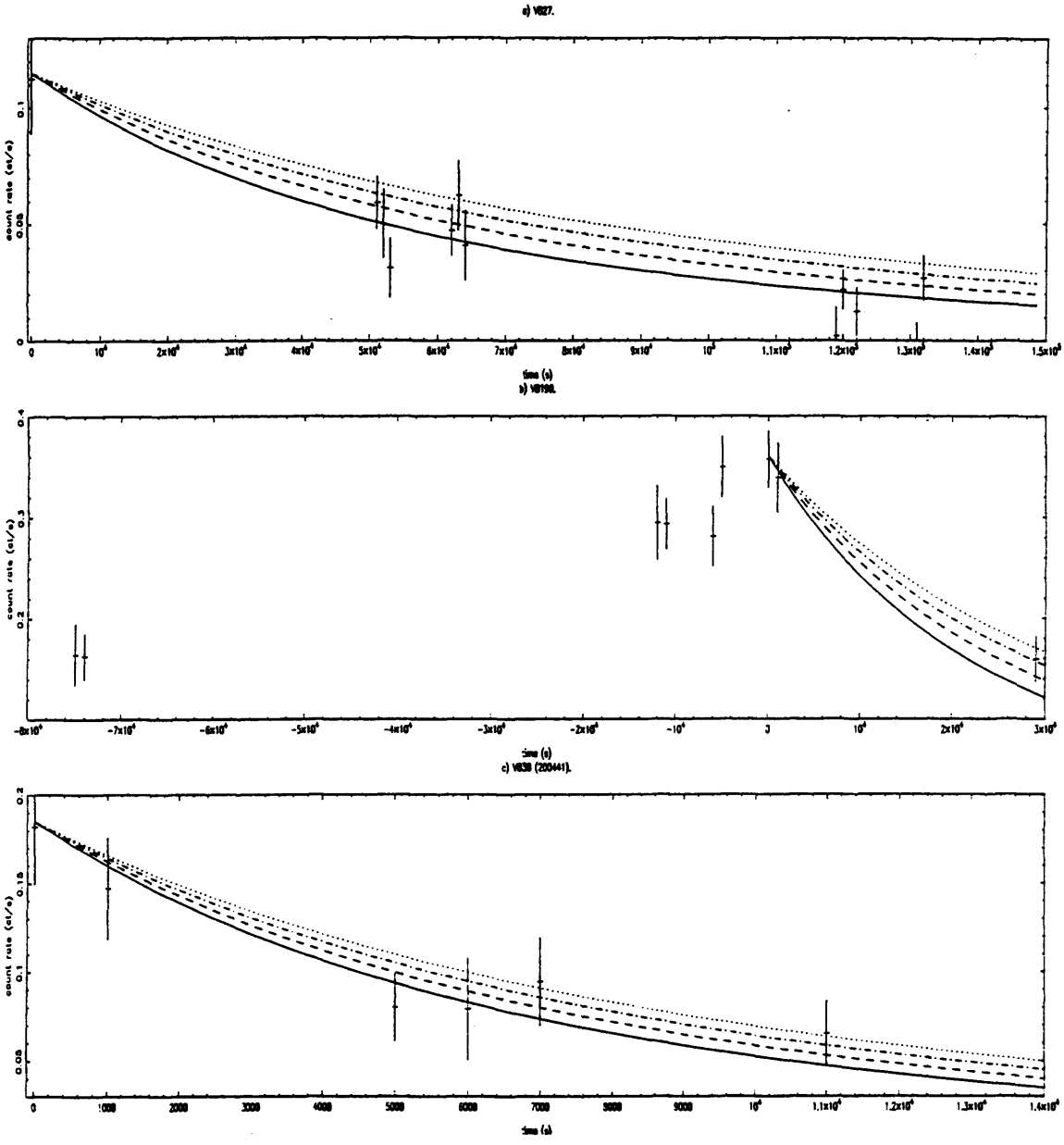

Figure 4.29: Modelled flare decay overlayed on observed flare. Each curve (solid, dashed, dash-dotted and dotted) represents a different value for the radiative cooling time (ranges are given in Table 4.5). Flares shown here are a) VB27, b) VB190 and c) VB30 (field 200441). For model results see Table 4.5.

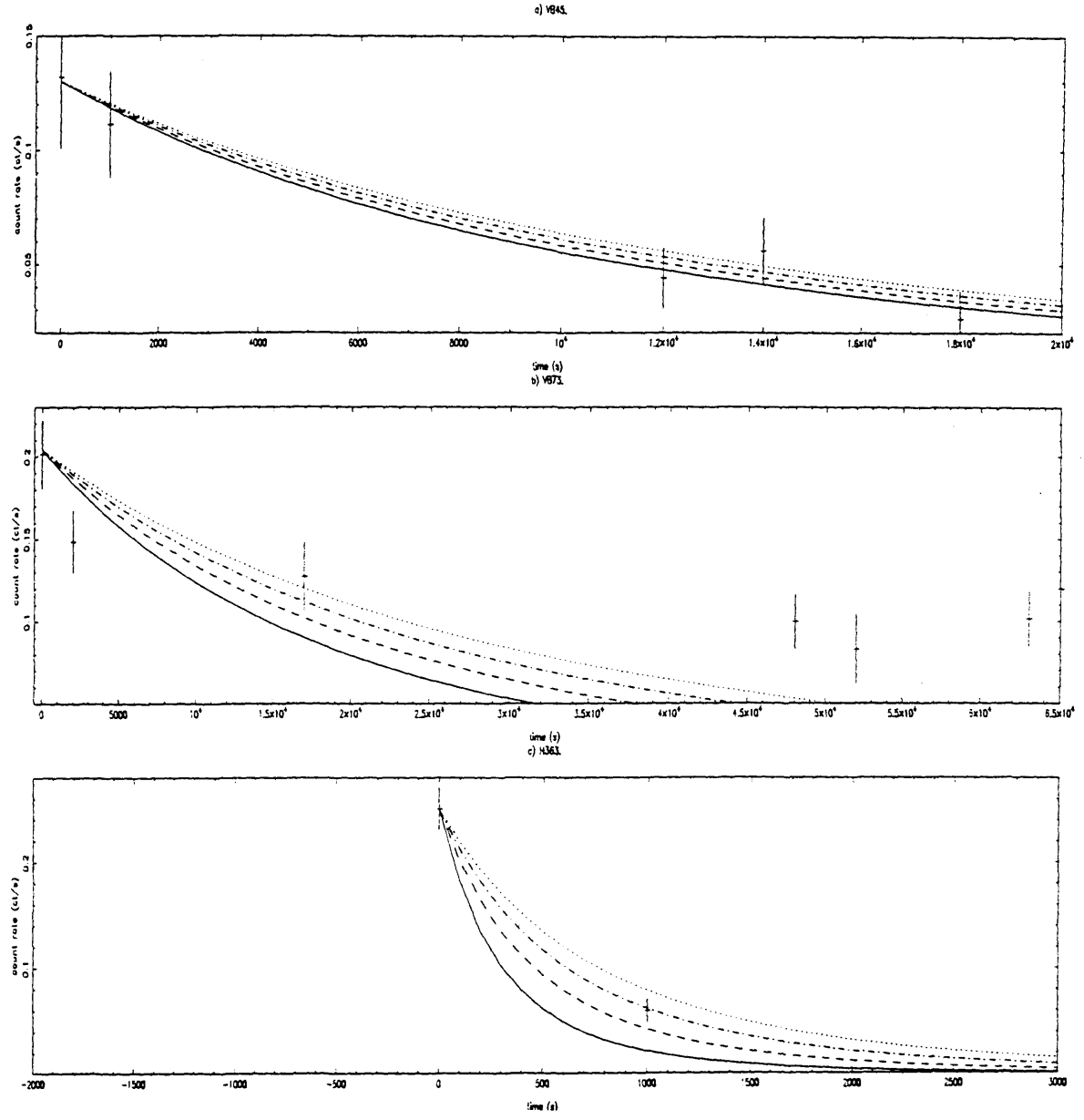

Figure 4.30: Modelled flare decay overlayed on observed flare. Each curve (solid, dashed, dash-dotted and dotted) represents a different value for the radiative cooling time (ranges are given in Table 4.5). Flares shown here are a) VB45. b) VB73 and c) H363. For model results see Table 4.5.

Table 4.5: Flare Modelling Results.

Name	τ	n_e	V	$L_{\alpha=0.1}$	H	H_P	Fit
	[ksec]	$10^{10}cm^{-3}$	$10^{31}cm^3$	$10^{11}cm$	$10^{11}cm$	$10^{11}cm$	
VB27	25—40	0.26—0.41	47.2—121	3.91—5.34	1.24—1.70	0.79	2
VB30 (200776)	25—40	0.64—1.02	21.5—55.1	3.00—4.11	0.96—1.31	1.4	1
VB30 (200441)	9—12	2.75—3.67	3.41—6.06	1.63—1.97	0.52—0.63	1.65	1
VB45	14—17	0.28—0.31	281—415	7.08—8.06	2.25—2.56	0.47	2
VB50	4— 7	3.60—6.30	7.4—22.8	2.10—3.06	0.67—0.98	1.40	1
VA334	20—35	0.84—1.48	66.3—203	4.37—6.35	1.39—2.02	1.54	1
H363	0.6—0.8	33.9—45.3	0.06—0.1	0.42—0.50	0.13—0.16	1.46	2
VB73	25—40	0.57—0.92	29.6—75.7	3.34—4.57	1.06—1.46	1.32	1
VB190	37—47	0.04—0.05	31300—50500	30.9—39.9	9.8—12.7	0.27	2

Notes:Columns are: star name, range of decay times used (decay time≈time taken for countrate to decrease by $1/e$ of (peak value)-(quiescent value)), range of loop densities, range of loop volumes, range of loop lengths (assuming α=0.1), range of loop heights, calculated pressure scale-height, an indication of goodness of fit, and notes. In the 'fit' column, the data points are compared (by eye) with the model decay. A 2 indicates a good model fit to the flare light-curve and a 1 represents a fit with only minimal deviation (possibly indicating multiple flare events).

Pallavicini *et al.* 1990). The ROSAT all-sky survey showed that X-ray flares are detectable on all categories of late-type stars (Schmitt 1994). This result agrees with the findings of the present Hyades survey; we see flares on dwarfs of types F, G, K and M. Despite the small flare sample and insensitivity to less powerful events, it is possible to estimate the Hyad flaring frequency. Of the total 80 stars detected, with a total of ≈21000ksec observing time, we see ≈300ksec of flaring activity (with peak $L_x > 10^{29}$erg s^{-1}), giving a frequency of ≈1%. Gagné *et al.* (1995) calculate the flaring frequency of the Pleiades (at peak $L_x > 10^{30}$erg s^{-1}) to be ≈1%. At this luminosity limit we would see a Hyades flare frequency of ≈0.3%. This difference in frequency (for the same absolute L_x threshold) is likely to be due to the comparatively lower Hyades activity levels, a consequence of the age difference between the Hyades and the Pleiades (≈600Myr and ≈70Myr respectively), or more fundamentally the generally lower rotation rates in the Hyades. Alternatively we can consider the flare frequency above some threshold defined by the *ratio* of flaring to quiescent L_x. Since the Pleiades stars have quiescent X-ray luminosities typically factors ~5—10 higher than the Hyads, the flaring frequencies in the two samples compared in

this manner are then similar, at ≈1%.

4.9 Summary

We have used 13 pointed PSPC observations of the Hyades cluster to obtain X-ray light curves for 80 stars (some of which were multiply observed in overlapping fields). Of these stars 14 were found to exhibit short-term variability (ranging from 10ksec—100ksec) mostly in the form of flare-like behaviour. The observations were compared with those of an Einstein IPC survey of the Hyades made ≈10 years earlier. There was little evidence for substantial long-term activity. This was also found to be the case with those stars observed more than once in the PSPC pointed survey, with time separations of 6 months to 2 years. The overall flare frequency was found to be ≈1% for flares of peak $L_x > 10^{29}$erg s^{-1}.

Using time-resolved spectroscopy, two-temperature models were applied to flaring and quiescent periods of several observed light curves. This revealed that during flare activity the high-temperature components (kT_2 and K_2) showed a marked increase over quiescence.

Finally, modelling of the flare decay, using a quasi-static cooling-loop model (van den Oord, Mewe and Brinkmann 1988), provided an estimate of the physical parameters associated with the flaring plasma. These have been compared with the results of Caillault *et al.* (1995).

Chapter 5

ASCA X-ray Spectral Survey of W UMa Systems

5.1 Introduction

In this chapter I will discuss the first results of an X-ray survey of W UMa systems, based on observations made using ASCA. Seven W UMa systems have been observed by ASCA during AO1—AO3: 44i Boo, VW Cep, XY Leo, SW Lac, W UMa, V566 Oph and ϵ CrA. The sample was chosen on the basis of relatively high X-ray fluxes and to represent a wide range of spectral types (from late-F to early K). Exposure times were $\approx$ 20ks for 5 of the systems and 40ks for V566 Oph and ϵ CrA. Principal investigators for these observations were Dr J.P. Pye of Leicester University and Prof. K. Makashima of Tokyo University. Results are presented here for the first three data sets received, namely the VW Cep, SW Lac and 44i Boo systems.

W UMa systems are eclipsing binaries showing continuous (optical) flux variability, with orbital periods between 5 and 18 hours. The components are as close as binary stars can be and therefore have the least angular momentum that such systems can possess (though this is still much more than a single star could possess). The component stars have the most rapid rotation rates of 'normal' (i.e. non-degenerate), late-type F—K stars

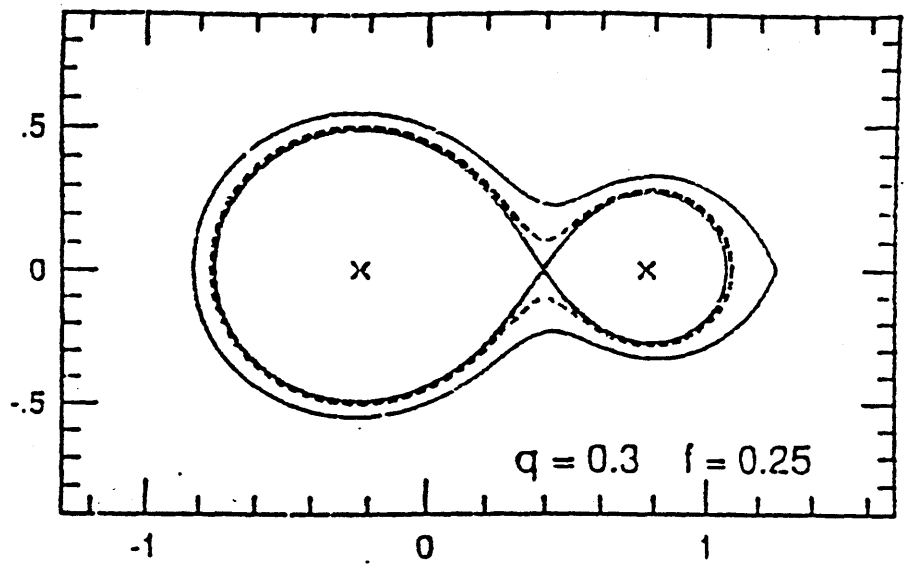

Figure 5.1: Roche geometry describes synchronously orbiting stars in the combined potential of their two point masses. The continuous lines show the two limiting equipotentials. An actual contact binary system fills an equipotential surface somewhere between these two limits (the broken line). The mass ratio of the system is defined as $q = M_2{:}M_1 \leq 1$ and the 'fill out parameter' f is the relative distance between the filled equipotential and the inner and outer critical potentials.

(in fact of any late-type stars, with the exception of the dM secondary components of cataclysmic variables) with equatorial velocities of typically $\sim 100 - 300$ km/s (Guinan and Giménez 1993). As such they are of great interest in the study of the relation between X-ray emission and rotation (see Chapter 1).

In order to account for the fact that the individual components of these systems have highly differing masses, yet almost identical surface temperatures, the contact model was derived (Lucy 1967). This postulates that the two component stars of the system are in contact via a common convective envelope (see figure 5.1). Tidal forces cause the component stars to rotate synchronously ($P_{rot} = P_{orb}$).

The contact model defines two sub-classes of contact binary. Binaries which conform to the model are known as A-type. Cooler systems (spectral types dF8/9 and later) do not obey the model as they display light curves where eclipses of the more massive component are the shallower of the two in any period (albeit by only a small percentage) rather than the deeper. Contact binaries that behave in this way are known as W-type systems.

Wang (1994) suggested that the reason the smaller component would be the hotter in these systems was due to 'thermal-relaxation-oscillation' (TRO) theory. This would mean the W-type phenomenon corresponds to the phase where the secondary component is contracting to its ZAMS radius, making it hotter by conversion of gravitational energy. This would explain why W-type systems are always found in a state of shallow contact. The secondary component of A-type systems is thought to be expanding. The TRO theory does not however explain why W-type systems have shorter periods than A-types.

Of the systems observed in our survey, 44i Boo, VW Cep, XY Leo, SW Lac and W UMa are W-type and V566 Oph and ϵ CrA are A-type.

W UMa systems are powerful X-ray emitters, though generally not as strong as RS CVn binaries. Approximately 120 W UMa systems have so far been catalogued. It is estimated that their frequency is around one W UMa system per one or two thousand of all dwarf stellar systems.

5.2 Previous X-ray Observations of Contact Binaries

Contact binaries were first detected in the X-ray band using HEAO1 (Carrol *et al.* 1980). An Einstein IPC survey was conducted of 17 W UMa systems (Cruddace and Dupree, 1984) in the spectral range 0.1—4.0keV. 44i Boo and VW Cep were also observed using the Solid State Spectrometer (SSS). Spectral fits were performed on these data, which required a two-temperature model with $T=6.5\times10^6$K and $T>3.5\times10^7$K. The sample stars were chosen for their proximity (closer than 100pc) and spread in periods and spectral type. An EXOSAT study of VW Cep, 44i Boo, W UMa and XY Leo (Vilhu and Heise, 1986) reported a phase dependance in the X-ray emission, though a later observation of VW Cep and XY Leo, again using EXOSAT (Vilhu, Caillault and Heise, 1988) showed no orbital modulation, though a flare was detected in VW Cep. A later, day long, Ginga observation of VW Cep (Tsuru *et al.* 1992) revealed no flaring or modulation.

5.3 The ROSAT PSPC X-ray Spectral Survey of W UMa Systems

Before the advent of ROSAT and ASCA X-ray spectral measurements were limited to two objects, VW Cep and 44i Boo. The work presented in this chapter follows on from a ROSAT PSPC survey (McGale *et al.*, 1996). The binaries studied in this survey were VW Cep, XY Leo, BV/BW Dra, SW Lac, W UMa, V839 Oph, AK Her and 44i Boo. The ROSAT High Resolution Imager (HRI) was used to resolve BV/BW Dra (separation $\approx$16 arcsec) and hence find the individual soft X-ray fluxes. Two-temperature models for an optically thin plasma adequately described the PSPC spectra. The values of the ratio of the 'hot' volume emission measure to the 'cool' volume emission measure and of the 'hot' temperature, were generally lower than those found in other types of active binary. The light curves were on the whole constant within $\approx$ 20% over each observation, with only VW Cep exhibiting a flare-like event. Comparing the ROSAT X-ray fluxes to those in the Einstein survey, most objects showed no long-term change in flux. SW Lac and V839 Oph were however brighter by $\approx$70% during the ROSAT observation.

5.4 ASCA Observations of W UMa Systems

The three W UMa systems to be discussed here are VW Cep, SW Lac and 44i Boo. All of these are w-type W UMa systems. These sources were observed by the ASCA satellite during AO1 and AO2 with relatively good phase-coverage (as compared with the ROSAT observations) being obtained. An observation log for the systems is shown in Table 5.1 whilst Table 5.2 summarises the relevant information for each system and Table 5.3 details the ephemerides of the systems.

Periods of data where the satellite's Earth angle was low enough to cause a significant oxygen edge contribution were removed, as were hot and flickering CCD pixels. From the cleaned data, pulse invariant (PI) spectra for each source, in each of the instruments (SIS0, SIS1, GIS2, GIS3) were extracted. Background spectra were obtained by averaging the spectra from a number of source-free regions near the target system. Also a light curve

Table 5.1: W UMa Systems — ASCA Observation Log.

System Name	Observation Date	Observation Duration (ksec)	ROR
VW Cep	5.11.93	24.7	21011000
SW Lac	8.7.94	18.3	22007000
44i Boo	10.5.94	14.0	21010000

Table 5.2: W UMa Systems Studied.

Name	RA(J2000)	DEC(J2000)	Sp.Type	Period	MassRatio	Distance (pc)
VW Cep	20h37m21.5s	47d39m15s	G8 K0	0.2678	0.5	23.2
SW Lac	22h53m41.3s	37d56m17s	G3 G3	0.3207	0.87	65.0
44i Boo	15h03m47.5s	47d39m15s	G2 G2	0.2678	0.5	12.2

Table 5.3: W UMa System Ephemerides.

System Name	Min.I HJD 2440000+	Period (days)	Observation Year
VW Cep	8521.6041	0.2783037	92±1
SW Lac	8833.0910	0.32071966	92
44i Boo	3604.844	0.26781696	91

Notes: Min.I HJD is the time of deepest optical, i.e. primary, minimum. References are: VW Cep, Guinan, private communication (quoted in McGale *et al.* 1996); SW Lac, Rong-Xian *et al.* (1992); 44i Boo. Burke *et al.* (1992).

Table 5.4: Fits to VW Cep in quiescence using normalisation ratios between the ASCA SIS0 and GIS2 instruments of 0.8, 0.9 and 1. Note that errors on temperature and normalisation are ≈5%.

Ratio	χ^2	$\chi^2_{reduced}$	T_{cool} (keV)	T_{hot}(keV)	Normalisation$_{cool}$ (10^{-3}	Normalisation$_{hot}$(10^{-3}
1	484.9	1.719	0.654	2.117	1.908	3.676
0.9	493.2	1.749	0.647	2.138	1.875	3.450
0.8	554.2	1.965	0.637	2.167	1.825	3.177

was generated for each system. Extraction of both spectra and time series was performed using the xselect program. Spectra were grouped so as to obtain a minimum of 15 counts per bin. XSPEC (Version 8.5) was then used to fit models to the data. The energy range chosen was 0.4—4.0 keV for SIS data and 0.7—4.0 keV for GIS data. Models used were Raymond-Smith (two, three and four temperatures), Mekal (two and three temperatures) and power-law continuous emission measure distribution (for details on spectral-models see Chapter 2). The MEKA model used was a recent update, MEKAL. This is essentially the same model as MEKA but includes the Fe L calculations of Liedahl (1995). Each model was applied both allowing the metal abundance to vary and then maintaining the abundance at solar levels. The fits were run for each instrument as well as the simultaneous combination of SIS0 and GIS2. with χ^2 minimisation being used to search for the best fitting spectral model, and to determine confidence ranges. When fitting SIS0 and GIS2 together the difference in normalisation between the two instruments had to be taken into consideration. The ratio is often taken to be ≈0.8 (Singh *et al.* 1996). Using values of 0.8, 0.9 and 1.0, the best fits arose in the case of a 1.0 ratio. An example using VW Cep in quiescence, with fits utilising the three different normalistion values is shown in Table 5.4.

It is clear that the systematic error introduced by not knowing the exact value of the normalisation ratio is <5%. The errors on any given fit parameter are usually around 5%. Due to this, rather than attempting to find a definitive value, the SIS0, GIS2 normalisation ratio has been taken to be 1 throughout.

In the case of a flare-like event. time-resolved spectra were taken during the event and then through the quiescent periods. Modelled 'cool' and 'hot' temperatures and volume

emission measures were compared in both states. If no difference was apparent then the data set was studied as a whole.

5.5 VW Cep

VW Cep is one of the nearest, brightest and best studied of the W UMa type contact binaries. As has already been shown VW Cep has been much observed in the X-ray band. The partially eclipsing nature of the system can account for periodic minor optical flux variations. However in the longer term it has been the subject of ongoing optical monitoring showing evidence of cyclic behaviour, with a period of $\approx$8—10 years. Starspot area coverage and locations have been derived from lightcurve modelling. During both the ROSAT and ASCA observations of VW Cep (June 1993 and November 1993 respectively) the star-spot area coverage was near its peak, hence implying that the observations were made near a peak of activity.

5.5.1 The ROSAT Data

The ROSAT PSPC observation (McGale *et al.* 1996) was performed in June 1992. The total accepted observation time after data-cleaning was $\approx$15.6ksec and the mean count rate of VW Cep was 1.532ct s^{-1}. A flare-like event lasting approximately 2—6 hours (see Figure 5.2) was detected. Hence for spectral analysis the data were split into flaring and quiescent time periods. XSPEC (version 8.5) was used to fit a two-temperature Raymond-Smith model to the data using solar abundances. This provided an adequate fit during both the active and quiescent periods (Figure 5.3). Table 5.5 shows the summary of the fitting. During flaring the X-ray flux was found to increase by a factor of two, the temperature of the hotter component rose by a factor of $\approx$1.5 and its volume emission measure by a factor of $\approx$5.

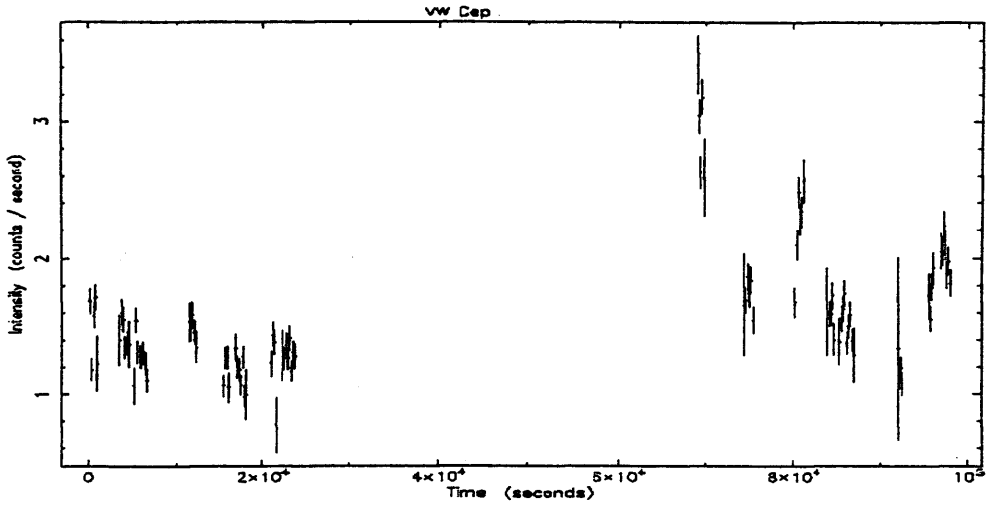

Figure 5.2: PSPC lightcurve of VW Cep (McGale *et al.* 1996). A flare (at 7×10^4s) is clearly visible lasting approximately 2—6 hours. The lightcurve is divisible into three distinct regions, pre-flare, flare and post-flare.

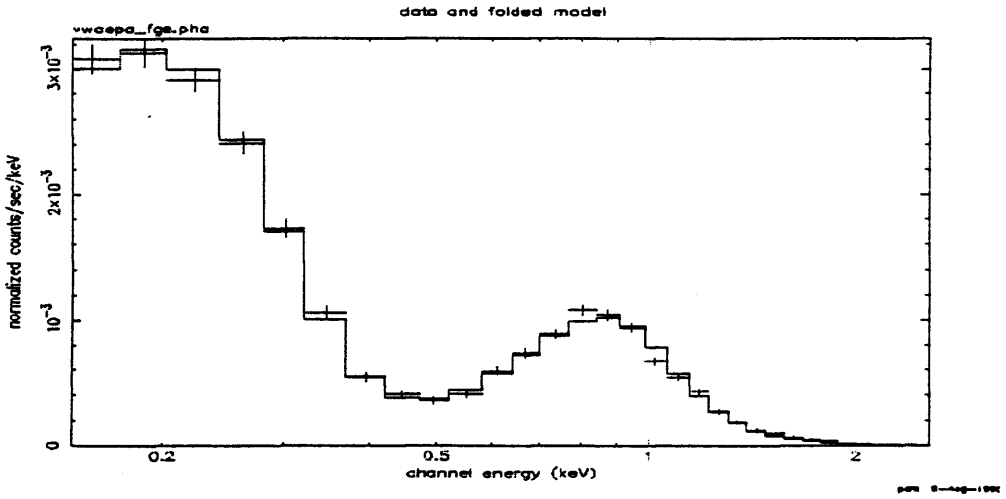

Figure 5.3: PSPC spectrum of VW Cep during the quiescent (pre-flare) period of the lightcurve (McGale *et al.* 1996).

Table 5.5: Summary of spectral fits to the ROSAT observations of VW Cep (McGale *et al.* 1996). A two-temperature, optically-thin, thermal model has been fitted to distinct sections of the light curve, pre-flare (A), flare (B) and post flare (C). Errors on VEM were not given, but were said to be $\leq 20\%$.

VW Cep	χ^2	$T_{cool}(10^6 K)$	90%	$T_{hot}(10^6 K)$	90%	$VEM_{cool}(10^{52} cm^{-3})$	$VEM_{hot}(10^{52} cm^{-3})$
A	1.64(26)	1.88	1.77—2.00	9.59	9.31—9.84	1.007	1.449
B	1.16(29)	2.78	2.33—3.11	15.6	13.20—19.20	1.676	6.941
C	1.77(25)	2.31	2.16—2.46	11.36	10.87—11.82	1.254	2.469

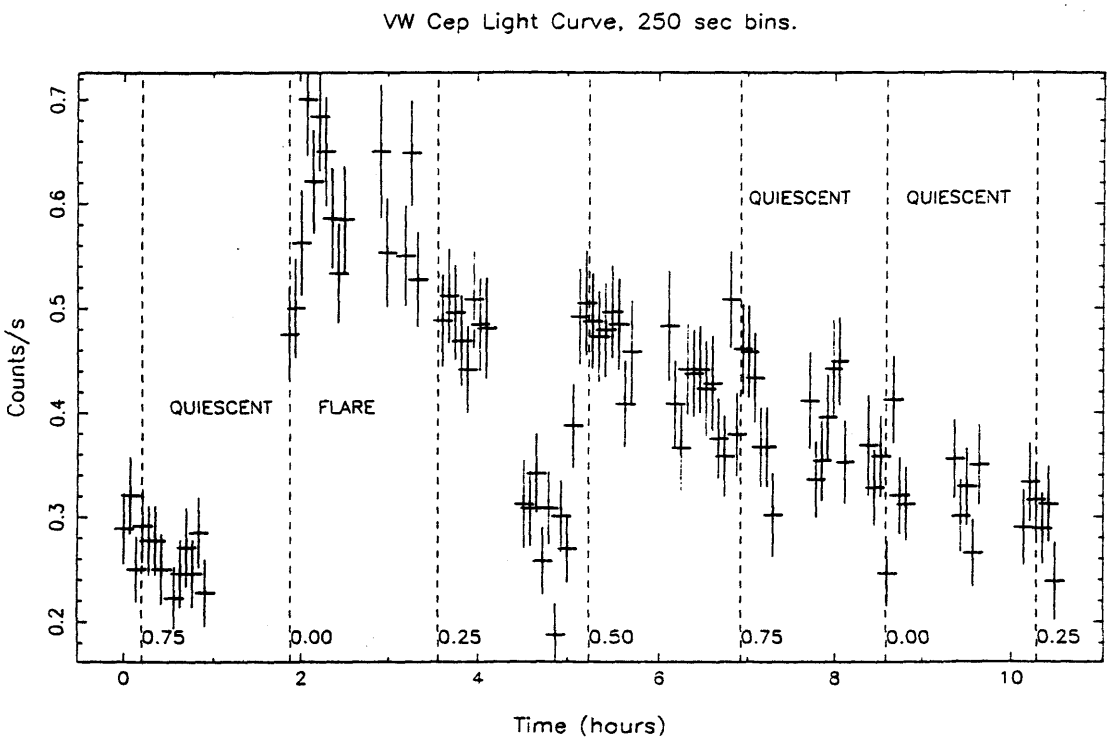

Figure 5.4: ASCA SIS0 lightcurve of VW Cep. Regions of quiescence, flare and post-flare (here also called quiescent, for spectral fitting, counts from these regions were added to the pre-flare counts) are shown, as are the orbital phases. Time binning is 250 seconds per bin.

5.5.2 Fitting the ASCA Data

Figure 5.4 shows the lightcurve from the ASCA (SIS0) observation of VW Cep. As was the case for the ROSAT time series, it is clear that a flare-like event occurs. The enhancement is not due to orbital or rotational eclipsing as we see much lower activity at the same phase in the next cycle, indicating a transient nature. During this flare the SIS0 countrate increases from $\approx$0.28 counts/s to $\approx$0.7 counts/s, an increase of a factor $\approx$2.5. It is uncertain whether the light curve contains one long flare (with a decay time of $\approx$8 hours) that is eclipsed (at a time of $\approx$4.5—5 hours) or two separate flares (with peaks at time $\approx$2.5 hours and 5.3 hours respectively). If there were two flares then it would appear that the second was smaller and had a slower decay. For the purposes of spectral fitting only the period marked as flare (between phases 0.0 and 0.25) was used to extract a flare spectrum. The post-dip region has been left out of the analysis at this time, and counts from the post-flare periods marked 'quiescent' in Figure 5.4 were added to the pre-flare 'quiescent' counts in order to achieve good statistics.

In order to see the behaviour of the flare more clearly, the method of time-resolved spectroscopy, as employed in Chapter 4, was applied to the VW Cep data. First attempts at dividing the light curve into flare-rise, flare-decay and 'post-dip' proved futile as insufficient counts were present to constrain the confidence contours. Thus a simple flare, quiescent division was made using the time intervals shown in Figure 5.4. Both MEKA (2 temperature) and R-S (3-temperature)[1] models were found to fit the spectra. The MEKA temperatures correspond roughly to the values of kT_2 and kT_3 in the R-S model (though this may be fortuitous). Since the models give comparable fits, only the former has been used (since it has fewer free parameters) to model the spectra of the contact binaries discussed herein. Application of a power-law continuous emission model (XSPEC model CEMEKAL) yielded no improvement over those shown due to poorly constrained upper temperatures.

Table 5.6 summarises the results of the Mewe-Kaastra model fits to the combined SIS0 and GIS2 data for quiescent and flaring periods. The two temperature model improves

[1] By performing a F-test, R-S 3T models were always found to be an improvement on 2T models with a confidence of $\geq$ 90%.

on the single temperature model in all cases (F-test confidence $\geq$99%). Figures 5.5 and 5.6 show the simultaneous fits to the SIS0 and GIS2 data of the two temperature MEKA model during quiescent and flaring periods using non-solar abundances (solar abundances are defined in Anders and Grevesse 1989). In allowing the abundance to vary a best fit value of $\approx$0.3 was found. The nature of this very low metal (elements heavier than Helium) abundance is discussed in Section 5.8.

It should be noted that in the spectrum of VW Cep there is a feature at $\approx$1keV that cannot be modelled using either of the plasma codes thus far discussed. This feature is likely to be due to the incomplete understanding of the Fe L-shell which contributes strongly to the 1keV spectrum. Solving this problem is a high priority for atomic physicists, work is currently underway at the Lawrence Livermore National Laboratory using their EBIT (electron beam ion trap) to generate L-shell emission. A wavelength survey of all Fe L-shell ions (Fe XVI to Fe XXIV) has recently been completed and experimental work is now focussed on measuring Fe L-shell emission line ratios (Liedahl, Osterheld and Goldstein, 1995).

Although the ASCA and ROSAT observations of VW Cep were not contemporaneous, an attempt was made to fit simultaneously the SIS0, GIS2 and PSPC data for quiescent periods, in order to investigate whether the spectra from the three instruments, covering different, albeit overlapping, energy ranges, could be mutually satisfied by a single 2-temperature model. Although the goodness of the fit ($\chi^2_\nu \approx 2.5$) was poor in a formal sense, it was sufficiently good[2] to indicate that there were no serious inconsistencies between the ASCA and ROSAT data.

[2]Especially as no re-normalisation of the data was performed to allow for flux changes between the two observing epochs.

Table 5.6: Summary of spectral fits to the combined SIS0 and GIS2 data for VW CEP for flaring and quiescent periods. Shown are the models (MEKA 1T and 2T), with abundance both variable and set at solar, reduced χ^2, temperatures and normalisations with 90% error ranges (note a 99 indicates Xspec did not calculate an error as $\chi^2\nu$ was greater than 2). The 2T fits are a significant improvement on the 1T fits (see main text).

Model	$\chi^2\nu$	χ^2	T_1 (keV)	T_2 (keV)	norm$_1$ ($\times10^3$)	norm$_2$ ($\times10^3$)	Abundance
Flaring							
Meka 1T	2.622	995.6	1.106	—	5.471	—	1.0
			99		99		
Meka 1T	1.691	640.9	1.037	—	20.42	—	0.12
			(1.005—1.066)		(19.10—21.81)		(0.10—0.14)
Meka 2T	1.375	519.5	0.727	2.259	2.142	6.091	1.0
			(0.692—0.762)	(2.079—2.479)	(1.956—2.324)	(5.757—6.421)	
Meka 2T	1.293	493.9	0.741	1.832	5.496	8.475	0.33
			(0.689—0.788)	(1.649—2.062)	(4.073—7.458)	(7.583—8.475)	(0.24—0.46)
Quiescent							
Meka 1T	6.332	1734.4	0.836	—	3.33	—	1.0
			99		99		
Meka 1T	2.14	584.9	0.862	—	17.01	—	0.098
			99		99		99
Meka 2T	1.706	464.1	0.662	2.144	1.867	3.753	1.0
			(0.643—0.681)	(2.029—2.311)	(1.787—1.961)	(3.602—3.906)	
Meka 2T	1.381	374.2	0.667	1.679	5.680	5.568	0.27
			(0.643—0.691)	(1.548—1.841)	(4.784—6.747)	(5.102—6.063)	(0.22—0.33)

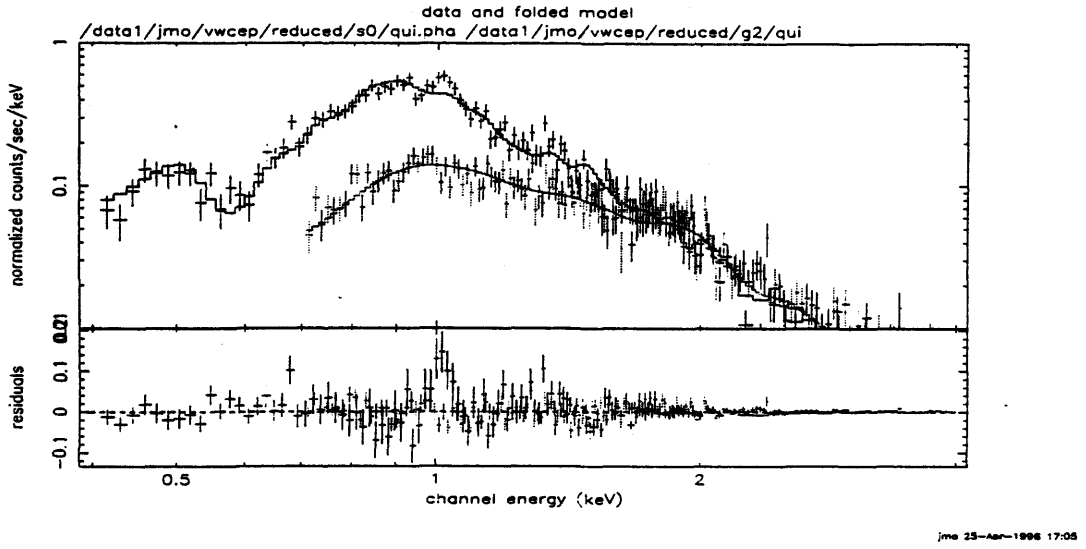

Figure 5.5: 2 temperature MEKA simultaneous fit to VW Cep SIS0 and GIS2 data during the quiescent period. Metal abundance is non-solar and a free parameter of the fit.

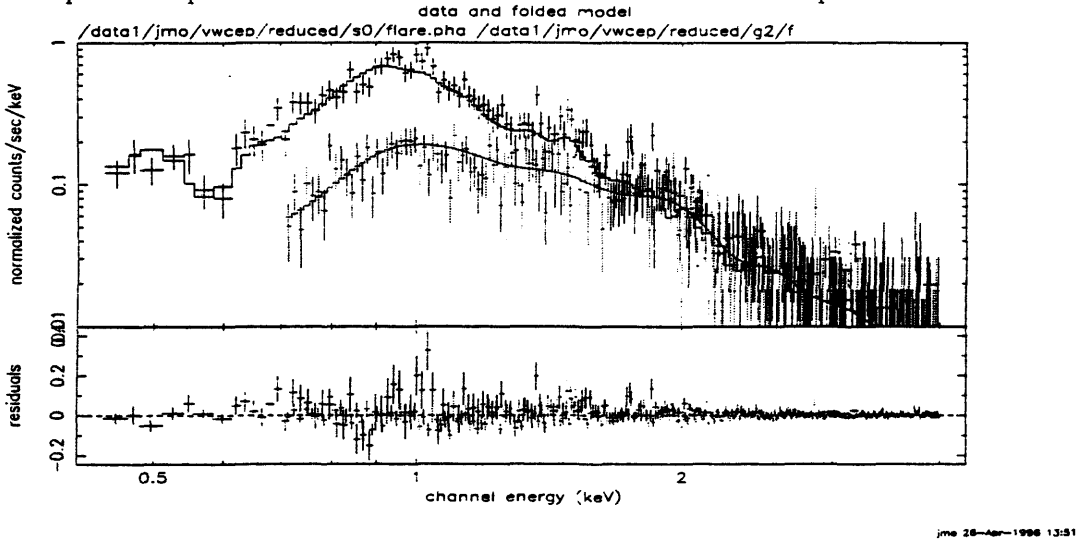

Figure 5.6: 2 temperature MEKA simultaneous fit to VW Cep SIS0 and GIS2 data during the flare period. Metal abundance is non-solar and a free parameter of the fit.

5.5.3 Spectral Behaviour During Flaring

It is clear from Table 5.4 that, whichever model is used (RS or MEKA), the best-fit high temperature increases during flaring, as does the associated best-fit volume emission measure (calculated from the normalisation). Figure 5.7 shows the confidence contours (68% and 90%) for kT_1 against kT_2 calculated using the 2-temperature, variable-abundance, MEKA model. It appears that whilst the best-fit high temperature may increase during flaring, in this system we cannot say that an actual increase occurs with any degree of confidence. However the cool temperature of this model does seem to increase during flaring (no contour overlap occurs at the 68% level and only little at the 90% level). The increase in the hot-component of the emission-measure during flaring is clear.

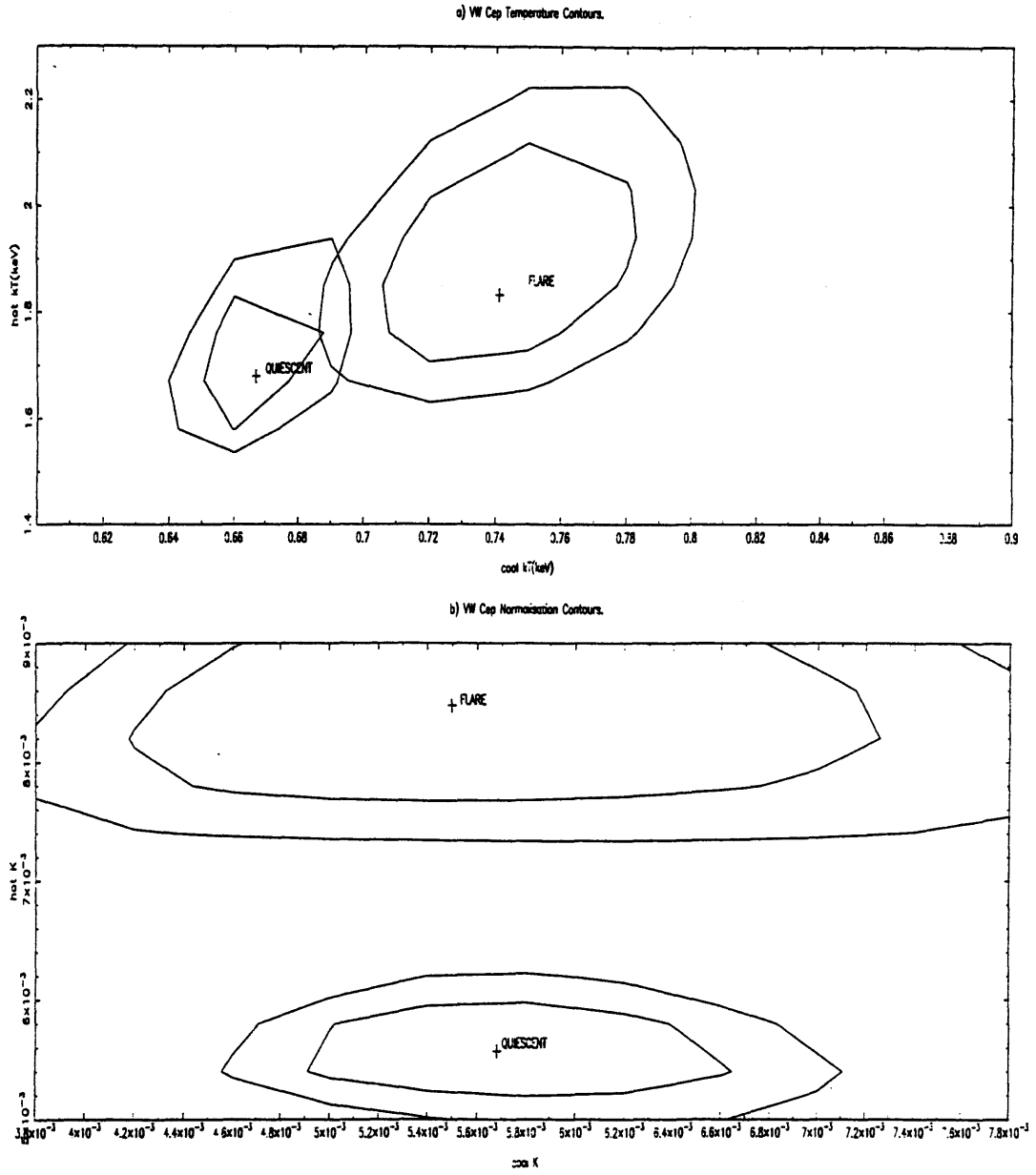

Figure 5.7: Confidence contours (68% and 90% shown) for kT_1 against kT_2 and K_1 against K_2 calculated using the 2-temperature, variable abundance, MEKA model. Flaring and quiescent periods are shown.

SPECIAL NOTE

THIS ITEM IS BOUND IN SUCH A MANNER AND WHILE EVERY EFFORT HAS BEEN MADE TO REPRODUCE THE CENTRES, FORCE WOULD RESULT IN DAMAGE

5.6 SW Lac

SW Lac, at 65pc, is the most distant of the three W UMa systems under cons tion. Like VW Cep it is a partially eclipsing system and though of similar spectra to 44i Boo, SW Lac has an extreme mass-ratio (almost unity). The PSPC spec indicated significant low-energy absorption, with a hydrogen-column value of $n_H \approx (1$ $6.5) \times 10^{20} cm^{-2}$ (McGale *et al.* 1996)[3]. Hence when fitting SW Lac ASCA spectra column was allowed to vary and compared with fits where the column was frozen at a value ($n_H = 1 \times 10^{19} cm^{-2}$). The results showed that the column had little impact on fits, due to the harder energy response of the ASCA instruments.

Figure 5.8 shows the MEKA 2-temperature simultaneous SIS0, GIS2 spectral fit, Figu 5.9 shows the SIS0 light curve. Little change in luminosity ($\lesssim 20\%$) is seen over the cour of the observation. Table 5.7 lists the fit parameters; it is interesting to note that again, fc the case where the abundance levels are allowed to vary, we obtain a value for the meta abundance less (by a factor of ≈ 3) than solar. Again an attempt was made to fit the PSP(spectrum along with those measured by the SIS0 and GIS2. The resulting fits (MEKA 2-temperature) yielded approximately the same results as seen in Table 5.7 for variable abundance. When using solar-abundances the cool-components of the fit were reduced to those values more commonly seen in PSPC-only fits ($kT_1 \approx 0.35 keV$, $K_1 \approx 0.6 \times 10^{-3}$).

[3] Consistent with the n_H contours of Paresce (1984).

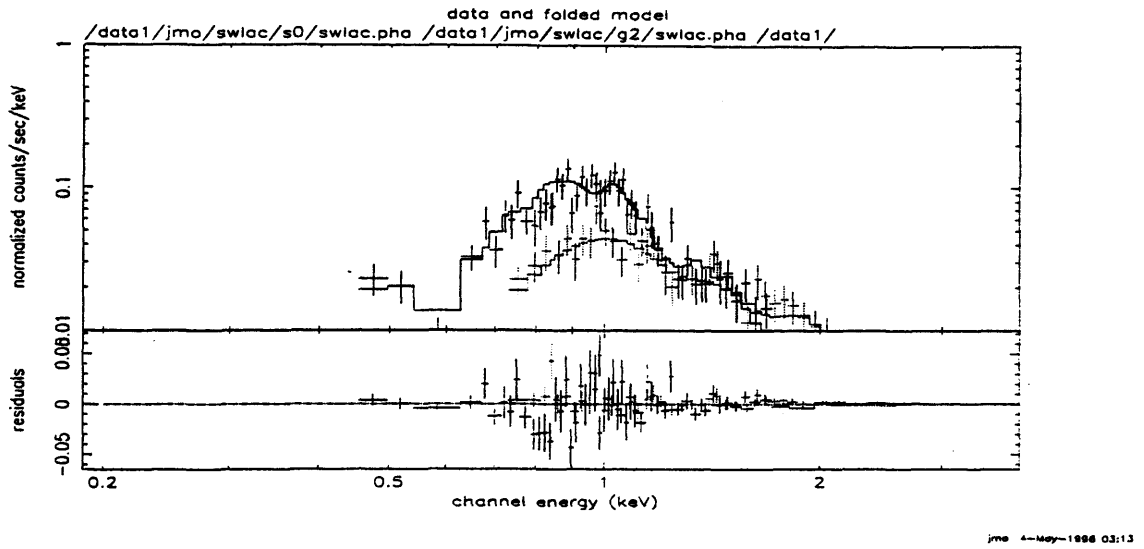

Figure 5.8: MEKA 2-temperature simultaneous spectral fit to SIS0 and GIS2 SW Lac data. Abundances were allowed to vary.

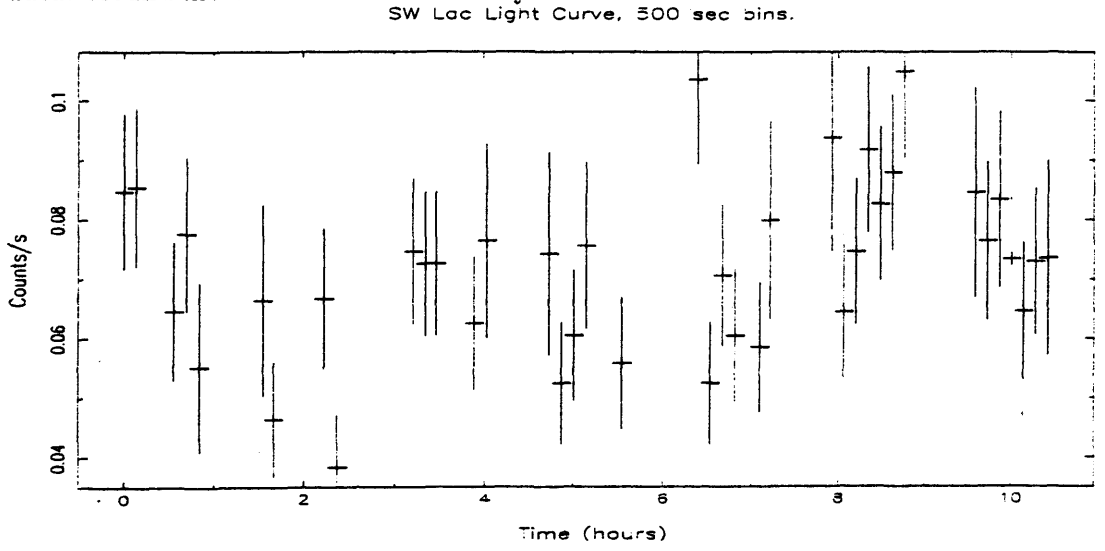

Figure 5.9: SW Lac light curve (SIS0 data). 500second time bins.

5.7 44i Boo

44i Boo is the nearest and one of the brightest W UMa systems in the survey. When observed with the ROSAT PSPC (a short observation covering only ≈10% of the orbital phase) the light curve appeared constant. Again a 2-temperature Raymond-Smith model adequately described the spectrum (McGale *et al.* 1996). 44i Boo has a F5V companion star with a separation of <3arcsec (Batten *et al.* 1978). Vilhu and Heise (1986) suggest that contribution from this star to the X-ray flux of 44i Boo is insignificant.

The light curve in the ASCA observations shows considerable variability as indicated in Figure 5.11. The flux enhancements are non-periodic, suggesting a flaring origin. Figure 5.10 shows the 2-temperature simultaneous flaring-interval, SIS0 and GIS2 MEKA model fit with variable metal abundances. Time resolved spectroscopy was performed on the data, with spectra from all flare intervals being combined into one spectrum and both quiescent spectra similarly combined. The results of the fits are given in Table 5.8. Unfortunately the 2-parameter temperature and normalisation contours overlap to such an extent that little can be said about the coronal behaviour during flaring, though we do see best-fit increases in the values of kT_2 and K_2 during flaring over quiescence. Again the best fits were achieved with non-solar abundances, in this case a value of ≈0.25—0.3 was obtained.

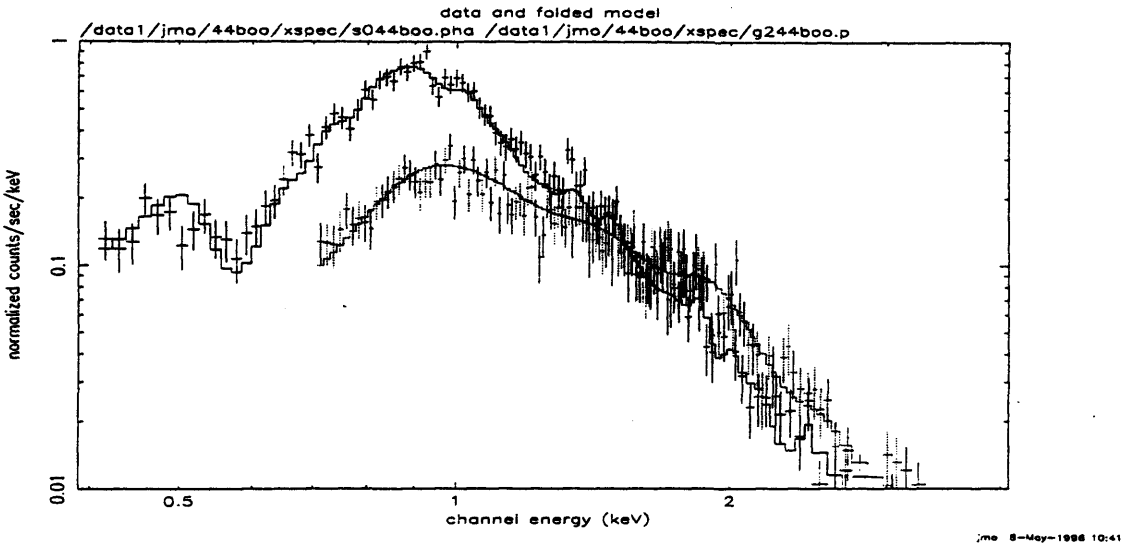

Figure 5.10: MEKA 2-temperature simultaneous spectral fit to S0 and G2 44i Boo 'flare' data. Abundances were allowed to vary.

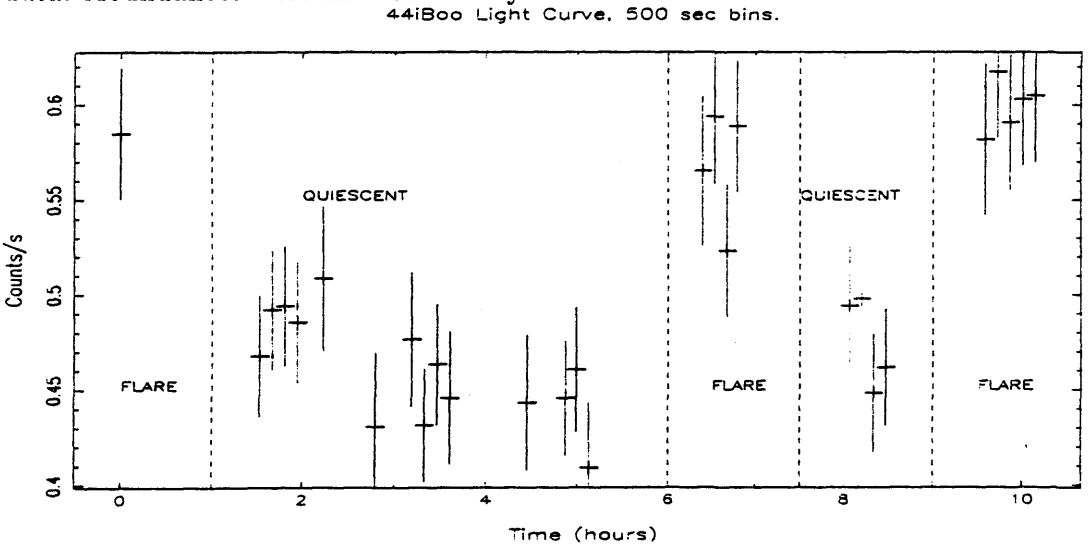

Figure 5.11: 44i Boo light curve (S0 data). Indicated are periods of flux-enhancement (here called flare) and lower flux (here called quiescent).

Table 5.7: Summary of spectral fits to the co-modelled SIS0 and GIS2 data for SW Lac. Shown are the models (Meka 1T and 2T), with abundance both variable and set at solar, reduced χ^2, temperatures and normalisations with 90% error ranges (99 indicates no error available in XSPEC). The F-test column shows the confidence of the 2T model being an improvement over the 1T model.

Model	$\chi^2\nu$	χ^2	T_1 (keV)	T_2 (keV)	norm$_1$ ($\times10^3$)	norm$_2$ ($\times10^3$)	Abundance	F-test %
Meka 1T	2.54	244.3	0.85	—	1.05	—	1.0	—
			99		99			
Meka 1T	1.67	156.1	0.826	—	4.38	—	0.15	—
			(0.792—0.861)		(3.82—4.96)		(0.12—0.19)	
Meka 2T	1.105	103.8	0.651	1.581	0.575	0.949	1.0	99.99
			(0.601—0.696)	(1.417—1.811)	(0.501—0.658)	(0.840—1.054)		
Meka 2T	1.066	99.14	0.636	1.311	1.279	1.538	0.37	98.5
			(0.604—0.691)	(1.136—1.472)	(0.801—1.474)	(1.329—1.710)	(0.28—0.79)	

5.8 Discussion

How do our ASCA results on contact binary systems compare with other binary types? Figures 5.12 a and b show the modelled temperatures and volume emission-measures using 2-temperature optically-thin plasma models for both our W UMa fits and a number of representative systems of other types (taken from the literature). Those systems marked by a star were observed with the ROSAT PSPC, whilst all others were ASCA observations. Note that for our flaring systems (VW Cep and 44i Boo) the best fit value of T_{HOT} increases during flaring but with considerable error-bar overlap. It seems that our observed W UMa's are comparable in terms of T_{HOT} with RS CVn and BY Dra systems. though AR Lac and the ALGOL systems seem to be hotter. T_{COOL} in the PSPC observations of W UMa, BY Dra and RS CVn systems appears to be much lower than the comparable values of all the other sources. The lower-temperature values of sources observed with the PSPC are likely to be a consequence of the softer reponse of that instrument as compared to those on board ASCA. A better parameter to use when comparing measurements made with different satellites is the volume emission measure (VEM). Figure 5.12b shows the similarity in VEM for most systems with the exceptions of 44i Boo (with very low VEM) and the RS CVn and ALGOL systems having much higher (factor $\approx$10) VEMs. Again for

Table 5.8: Summary of spectral fits to the co-modelled SIS0 and GIS2 data for 44iBoo. Shown are the models(Meka 1T and 2T), with abundance both variable and set at solar, reduced χ^2, temperatures and normalisations for flaring and quiescent periods with 90% error ranges (99 indicates no error available in XSPEC). The F-test column shows the confidence of the 2T model being an improvement over the 1T model.

Model	$\chi^2\nu$	χ^2	T_1 (keV)	T_2 (keV)	norm$_1$ ($\times 10^3$)	norm$_2$ ($\times 10^3$)	Abundance	F-test %
Flaring								
Meka 1T	2.97	574.9	0.853	—	5.902	—	1.0	—
			99		99			
Meka 1T	1.173	224.1	0.839	—	28.99	—	0.108	—
			(0.814—0.867)		(26.70—31.32)		(0.092—0.126)	
Meka 2T	1.117	213.3	0.679	1.917	3.489	5.571	1.0	99.99
			(0.651—0.708)	(1.758—2.120)	(3.213—3.771)	(5.147—5.989)		
Meka 2T	0.891	169.4	0.692	1.504	12.47	8.604	0.23	93.77
			(0.654—0.730)	(1.327—1.746)	(9.441—99)	(6.937—16.33)	(0.17—0.31)	
Quiescent								
Meka 1T	2.64	451.6	0.849	—	5.09	—	1.0	—
			99		99			
Meka 1T	1.17	198.2	0.812	—	23.66	—	0.122	—
			(0.784—0.841)		(21.43—25.97)		(0.102—0.146)	
Meka 2T	1.184	200.1	0.663	1.730	3.053	4.289	1.0	99.99
			(0.603—0.695)	(1.582—1.923)	(2.781—3.328)	(3.914—4.662)		
Meka 2T	1.003	168.5	0.663	1.357	10.02	7.186	0.25	99.99
			(0.615—0.707)	(1.188—1.569)	(7.386—99)	(5.702—7.186)	(0.18—0.35)	

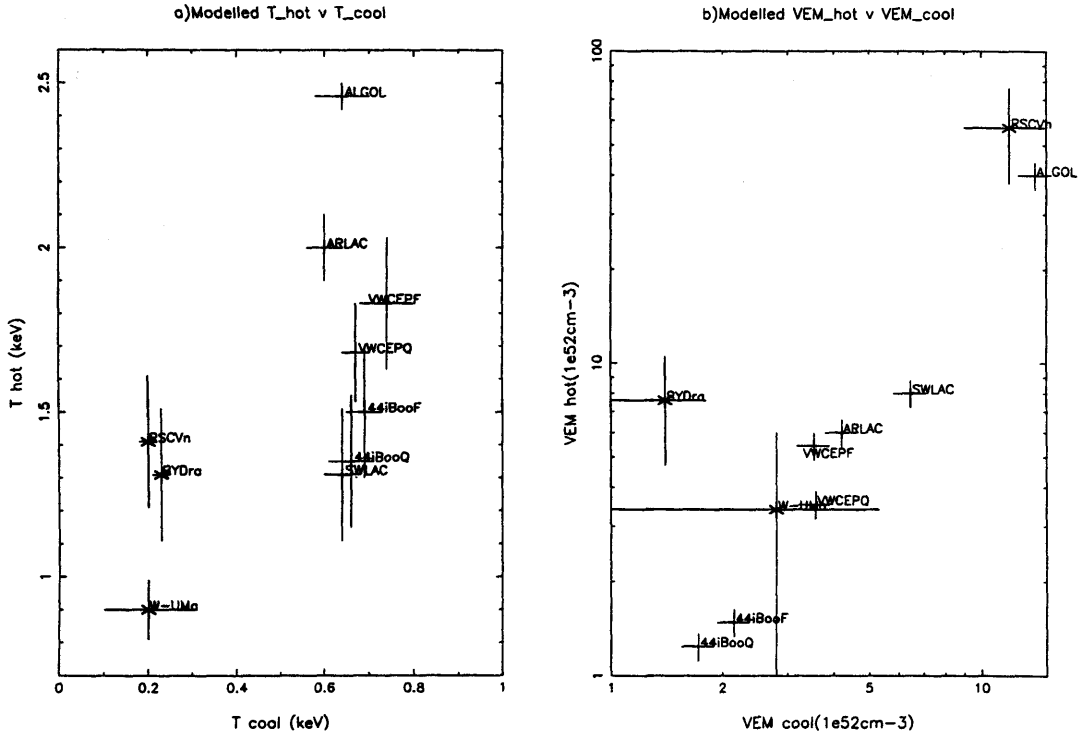

Figure 5.12: Modelled, hot and cool, temperature and volume emission-measure (VEM) components using 2-temperature optically thin plasma models for our survey W UMa systems and fits to other representative types of binary. The other systems (including references to their spectral modelling) are: RS CVn (Dempsey *et al.* 1993); BY Dra (Dempsey *et al.* 1994); Algol (Tsuru 1992) and AR Lac (Singh 1996). The modelling of the PSPC observations of W UMa systems was performed by McGale *et al.* (1996).

our systems during flaring we see increases in the best fit value of VEM_{HOT}.

5.8.1 Metal Abundances

Optical and UV measurements of abundances in W UMa systems have not, so far, been successful, due to the extreme rotational broadening of spectral lines (Rucinski 1995). Therefore, modelling the coronal X-ray emission of these stars provides a potentially important method of abundance determination. As presented earlier in this chapter, the derived metal abundance for the studied W UMa systems is $\approx$0.3 times the solar value. A Ginga LAC study of VW Cep (Tsuru *et al.* 1992) found an iron-K line upper-limit intensity that implied an iron abundance of $\leq$0.4 solar, or alternatively the presence of

non-thermal X-ray emission. Assuming the low iron abundance was reflected in the other metals, this result would seem to agree with the ASCA observation. However the Ginga observation showed a very hard spectrum with thermal emission up to 10keV. This does not agree with the ASCA observation where no such emission is present. This is not an energy range problem either (a common problem when dealing with the ROSAT PSPC) as ASCA is perfectly capable of observing in the 10keV range. This leads to the conclusion that there was probably something wrong with the Ginga observation, hence suggesting that we cannot consider the abundance result as corroboration.

Figure 5.13 shows the relative abundances for a range of metals as modelled from ASCA SIS spectra of Algol (White 1996). Again it is clear that the abundances involved are far from solar. White found that uncertainties in the plasma code models could not explain these under-abundances, nor could a complex temperature distribution, thus raising the prospect that these values are actually correct. Similar results were found in an ASCA AR Lac observation by Singh *et al.* (1996). It is expected that in Algol systems mass transfer between component stars will affect the surface chemical composition of the secondary. It may be possible that some kind of temporary coronal-composition change is occuring in our observation of VW Cep as we do see the best-fit value for the abundances undergoing an increase during flaring. Is there some 'dredging' process going on whereby flares increase the coronal metallicity or is it all simply a feature of the imperfect atomic physics?

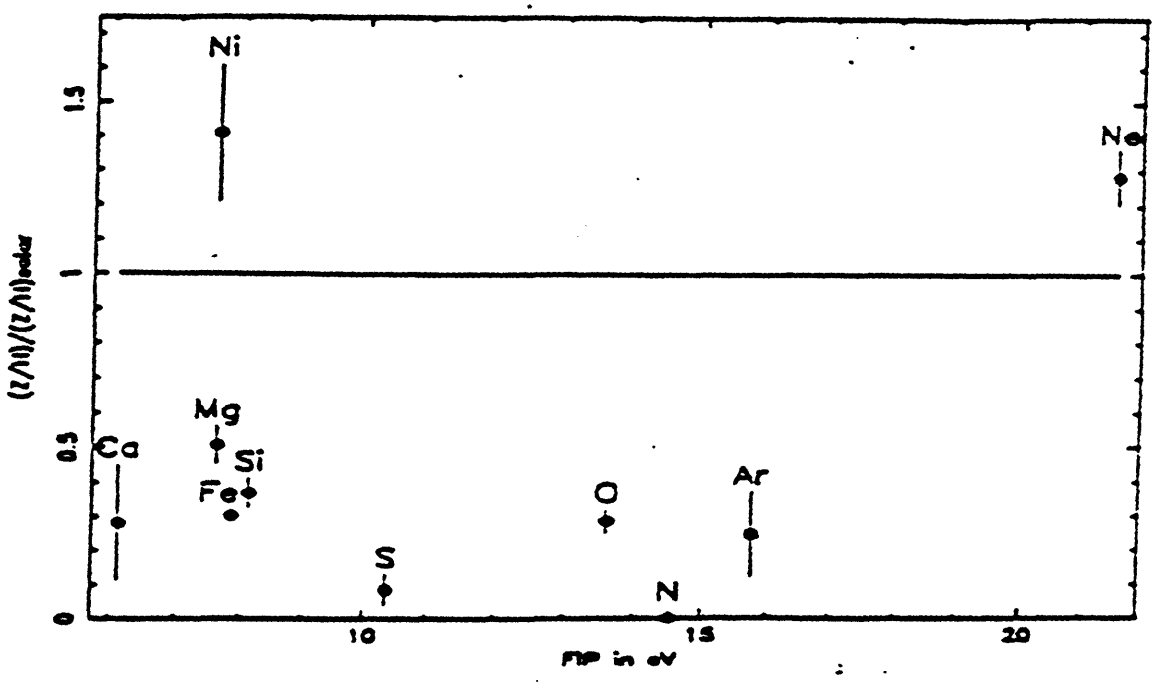

Figure 5.13: The coronal abundances relative to hydrogen against first-ionisation potential (FIP) for Algol, determined from 2-temperature fits to ASCA SIS spectra. Abundances are relative to the cosmic values of Anders and Grevesse (1989). Reproduced from White (1996).

Chapter 6

Concluding Remarks

6.1 Summary

Throughout this thesis I have been looking at X-ray emission from late-type stars, using observations made with the ROSAT and ASCA satellites. In Chapter 3 I described a deep soft X-ray survey of the Galactic Plane using pointed ROSAT PSPC observations. The survey yielded 93 sources, 89 in the 'hard' band (0.4—2.0keV) and 14 in the 'soft' band (0.1—0.4keV). Approximately 90% of the survey area in the hard-band was covered to a sensitivity of about 0.002ct s^{-1} ($\approx 2\times10^{-14}$erg cm^{-2} s^{-1}). Thus the survey extended deeper in flux by a factor of $\approx$10 over previous surveys (Einstein Galactic Plane Survey and the ROSAT all-sky survey). After removing the estimated contribution from extragalactic sources ($\approx$8%), the integral number-flux relation of sources brighter than 0.002ct s^{-1} can be represented by the power-law $N(>S)=N_oS^{-\alpha}$ where $\alpha = 1.3\pm^{0.6}_{0.4}$ and $N_o=N_{(>0.002)}=21\pm5$ sources per deg^2. My modelling of the number-flux relation in terms of stellar populations indicates that F, G, K and early-M dwarfs contribute roughly equally (within a factor of $\sim$2). A major contribution is predicted to come from RS CVn systems, though they are subject to a large degree of uncertainty as their space density and X-ray luminosity function are poorly known. The sum of the modelled stellar contributions accounts for between 38% and 56% of the observed sources, with a nominal value of 50%. Work for the future includes further investigations of the contributions from RS

CVn systems and a possible, so far unidentified, population. A collaborative programme is underway with F. Favata (ESTEC) and G. Micela (Palermo Observatory) towards optically identifying the X-ray sources, which would then enable direct comparisons with the source-population models. For example, if Maoz and Grindlay (1995) were correct in predicting an extended galactic population of low-luminosity X-ray sources, then they should be optically identified in this process.

In Chapter 4 I presented the third element in the analysis of a deep PSPC survey of the Hyades, comprising 13 overlapping pointings. The first two parts, X-ray luminosity functions of dK-dM stars, and a spectral study, were presented in Pye *et al.* (1994) and Hodgkin (1995) respectively. I have reported the temporal behaviour of the Hyads. From 107 light curves corresponding to 80 individual Hyads I found 14 variable sources (three of which were seen to vary in two separate observations). Of these stars 11 varied in a flare-like manner. In order to look for evidence of long-term flux variations I looked at stars observed more than once in overlapping fields. This showed little variation occurred over periods of 6—30 months. Similarly when comparing our PSPC observations with those made with the Einstein IPC $\approx$10 years earlier little variability (at levels $\geq$factor 2) was evident. This lack of long-term variability suggested that there is little or no cyclic activity evident in the coronae of stars of Hyades age.

For those stars with flare-like variability, time-resolved spectroscopy was performed for the flaring and quiescent periods. This revealed a tendancy for the high-temperature components (kT_2, K_2) to increase during flaring with little or no change in their low-temperature components. When plotted as two-parameter confidence contours, this evidence was clear for a number of stars, as flare and quiescent contours were well separated at the 90% level. However for most stars significant contour overlap occurred. Future work may involve co-adding spectra according to spectral type and rotational velocity (see Gagné *et al.*, 1995), thus reducing confidence contours around the best-fit parameters. However this would require optical measurements to determine periods or $v \sin i$ for many Hyads.

Finally in this chapter a quasi-static cooling loop model was used to estimate flare parameters (density, volume, height). On the basis of this model, it was found that most flare loops were in the region of $\approx 1 R_{SUN}$ in height with comparitive densities to those seen on

the Sun.

Finally Chapter 5 deals with the first three observations, using ASCA, in a survey of (so far) 7 W UMa systems. This survey continues the W UMa studies from ROSAT (McGale *et al.* 1995). Spectra of VW Cep, SW Lac and 44i Boo were modelled in XSPEC using Raymond-Smith and Mewe-Gronenschild models, and both discrete temperature components (2 and 3 temperature) and continuous emission measure distributions. Data from SIS0 and GIS2 fitted simultaneously as was SIS0, GIS2 and PSPC data. Values obtained for metal abundances were $\approx$0.3 of the expected solar values, and similar to ASCA results for the active binaries AR Lac and Algol (e.g. White 1996).

It only remains to look at how all of these results can lead to a greater understanding of stellar coronal astrophysics. The prediction from modelling in chapter 3 that a major contribution to the X-ray population comes from RSCVn systems is an important one. Indeed there has been some corroborative evidence that this may be so in a study by Kang *et al.* of the OGLE microlensing survey. The study found a larger than expected number of RSCVn's out of a sample of 2000 variable stars in the direction of the galactic bulge. Kang *et al.* show that by combining the high X-ray emission from RSCVn's with other types of variables , e.g. Algol or W-UMa type stars, it is possible to account for most, if not all, of the soft diffuse X-ray background as observed by ROSAT. In order to confirm this study, models such as our own that predict galactic populations are very important. For the same reason, studying the X-ray emission of such stars (as done in chapter 5) is important in identifying more distant sources.

The Galactic Plane survey contained, as one would expect, many coronal sources. Due to the flux-limited nature of the survey only the highly active sources in the fields would be observed. In contrast, the study of open clusters provides a well defined, co-eval sample with roughly similar luminosity limits.

Using data from the Hyades survey in chapter 4, in combination with X-ray and optical observations from other open clusters, of which ROSAT has so far observed $\approx$30 (e.g. αPer, the Pleiades, Praesepe), and for star-forming regions (such as Orion and ρ Ophiuchi) it may soon be possible to address more quantitively how mass, gravity, metallicity,

binarity, chromospheric activity and X-ray emission are linked, and hence to address the fundamental question of the relation between 'activity' and the stellar magnetic dynamo.

These relationships are by no means simple, indeed study of the young open cluster NGC 2516 (Jeffries *et al.* 1997) has shown that it does not obey the accepted rotation-activity-age paradigm. Jeffries *et al.* suggest a modification to the paradigm explaining their observations in terms of the different convection zone properties that late type stars of differing metallicities have at the same colour or mass. Indeed as spectral resolution increases it is becoming more and more apparent that not all stars have solar abundances (as I suggest in chapter 5). It is reasonable to assume that stars in the same open cluster will have the same metallicities. If therefore we are to fully understand the paradigm, we not only need to survey the activity of open clusters (as done in chapter 4) we must also develop more accurate spectral codes.

Yet another problem with the paradigm could lie in the phenomenon of super-saturation. ROSAT observations have shown that basically as stellar rotation decreases, so X-ray emission decreases. However above certain speeds no further increase in emission can be seen, such rapid rotators exhibit a plateau of saturated X-ray emission. However, some extremely fast rotators begin to show a decreasing level of X-ray emission. What is causing this is so far unknown, whether it is merely an error in rotation speeds or metallicities or whether we are looking at some new physics. Perhaps beyond a certain speed, coronal plasma is not efficiently confined by the stellar magnetic field.

For the future, multi-epoch comparisons of modelled photospheric star-spot areas and spatial distributions, with coronal activity levels (from contemporary X-ray measurements) will allow a better determination of the temperature and spatial structure of active regions. Study of ultra-fast rotators will be needed to understand the phenomenon of super-saturation. Further high spectral resolution observations and improved spectral models should also enable the metal abundance questions to be resolved. Work is in progress by several groups to revise the spectral codes, including improvements to the underlying atomic physics calculations (e.g. Dere *et al.* 1994). An immediate objective is to enlarge the sample by completing the analysis of the remaining W UMa observations.

6.2 Future Missions

As discussed, ASCA and EUVE observations have already begun to show evidence for non-solar abundances in active stars such as the contact binaries dealt with in this thesis, and Algol (e.g. Antunes *et al.* 1994). It is however still possible that the effect is not due to abundance anomalies, rather that the spectral models are deficient, either in their assumptions or atomic physics. Future missions will have improved capabilities for determining the properties of stellar coronae (temperature and density structure, energy balance, abundances). In particular, instruments capable of identifying individual spectral lines will allow independent coronal temperature and density measurements and will also help to confirm (or otherwise) the accuracy of the plasma models.

Below I conclude this thesis with a summary of some of the more important and eagerly awaited X-ray missions that should be launched in the near future.

- **JET-X.** The Joint European X-ray Telescope (JET-X) is designed to study X-ray emission in the band 0.15—10keV, using CCD detectors. It will have similar sensitivity and angular resolution to the ROSAT PSPC but with much better spectral resolution and high energy response (similar to the ASCA SIS but with better spatial resolution). The primary scientific goals of JET-X lie in cosmological and extra-galactic astronomy, however it will also be valuable for studying the spectral characteristics of stars in much more detail than previously achieved. JET-X is the core instrument in the scientific payload of the Russian Spectrum-X Gamma (SRG) project. However, given the current Russian economic climate, the launch of JET-X is uncertain.

- **XMM.** XMM is the second of four ESA 'cornerstone' missions and is due to be launched in August 1999 with an expected lifetime of 10 years. A highly eccentric orbit provides for 32 hours of continuous observation per orbit. It comprises of 3 mirror modules and three instruments, EPIC, RGS and OM. EPIC (the European

Photon Imaging Camera) is the main focal plane instrument providing CCD imaging and spectroscopy at the foci of the three mirrors. The CCD's provide high sensitivity (limiting sensitivity $\approx 2\times10^{-15}$erg cm^{-2} s^{-1}) over a 0.1—10keV bandwidth. Simulations show that clear resolution of individual stellar lines should be possible. The RGS (Reflection Grating Spectrometer) is used to produce high resolution dispersed spectra, whilst the OM (Optical Monitor) is an optical telescope sensitive down to 24^{th} magnitude (m_B). The OM will be used to monitor the optical flux from X-ray sources observed by EPIC and the RGS, and as an aid in source identification.

- **AXAF.** The Advanced X-ray Astrophysics Facility (AXAF) is due to be launched in spring 1999. It will have a bandwidth of 0.1—9.0keV, an angular resolution of 0.5arcsecs and be sensitive down to 10^{-16}erg cm^{-2} s^{-1}. This combination will enable AXAF to observe fainter and more crowded fields than was previously possible. This will be of great interest in stellar astronomy as more distant open clusters may be observed, thus allowing a wider range of stellar ages (and other parameters, e.g. metallicity) to be studied.

Appendix A

Cool Star Luminosity Functions

The following pages contain the luminosity functions used in Chapter 3. These are, in order of presentation:

- dK stars, Barbera *et al.* 1993 , from Einstein observations.
- Early dM (M0—M4) stars, Barbera *et al.* 1993 . from Einstein observations.
- Late dM (M0—M4) stars, Barbera *et al.* 1993 , from Einstein observations.
- dK stars, Fleming *et al.* 1995 . from ROSAT observations.
- Early dM (M0—M4) stars, Fleming *et al.* 1995 . from ROSAT observations.
- Late dM (M0—M4) stars, Fleming *et al.* 1995 . from ROSAT observations.
- dF stars, Kashyap *et al.* 1992 . from Einstein observations.
- dG stars, Kashyap *et al.* 1992 . from Einstein observations.
- dK stars, Kashyap *et al.* 1992 . from Einstein observations.
- RS CVn stars. Favata *et al.* 1995 . from Einstein observations.
- RS CVn stars. Kashyap *et al.* 1995 . from Einstein observations.

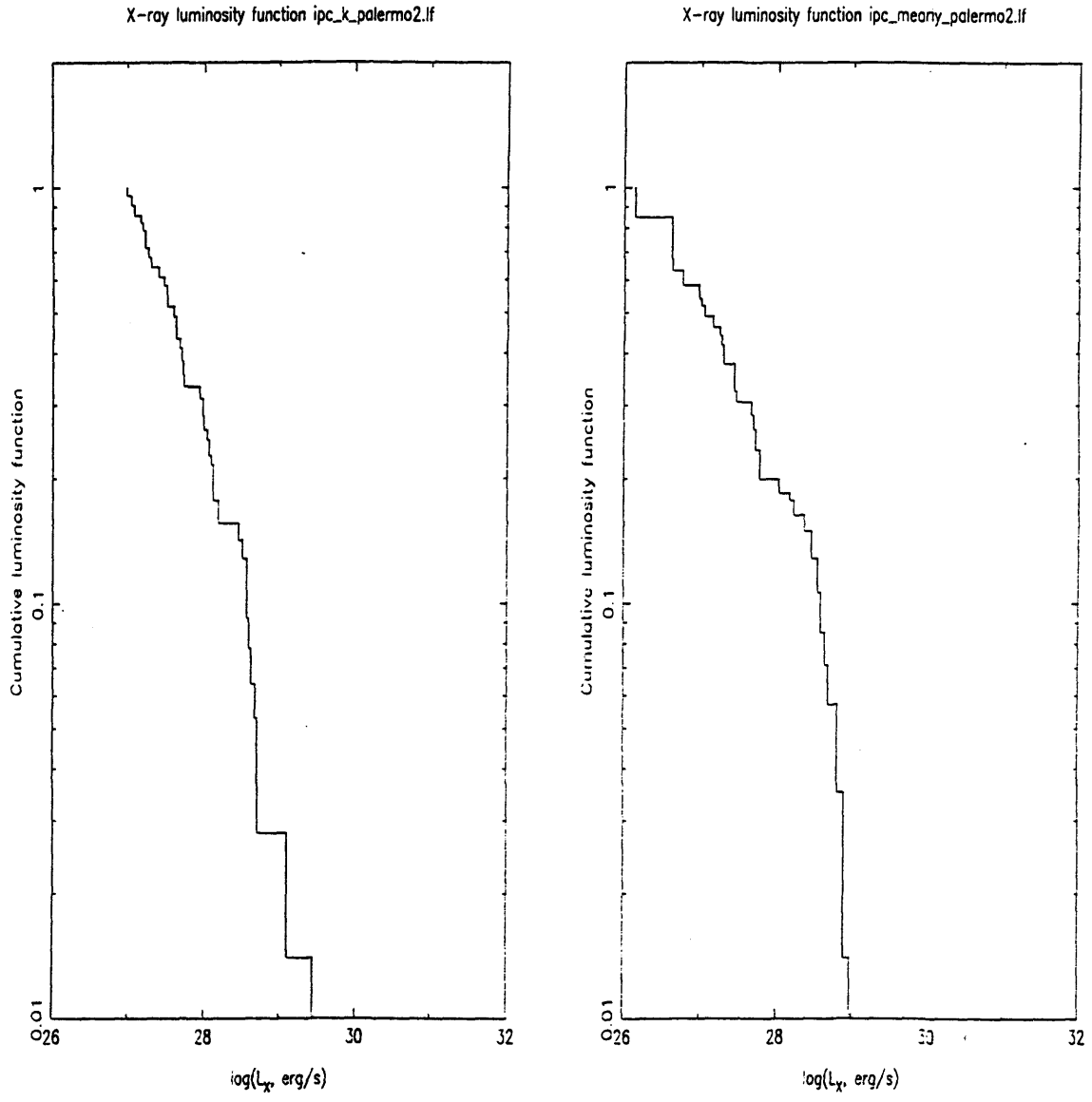

Figure A.1: Cumulative x-ray luminosity functions (differential form) vs $\log(L_x, \text{erg s}^{-1})$ (see main text). These are dK Barbera *et al.* and early dM Barbera *et al.*

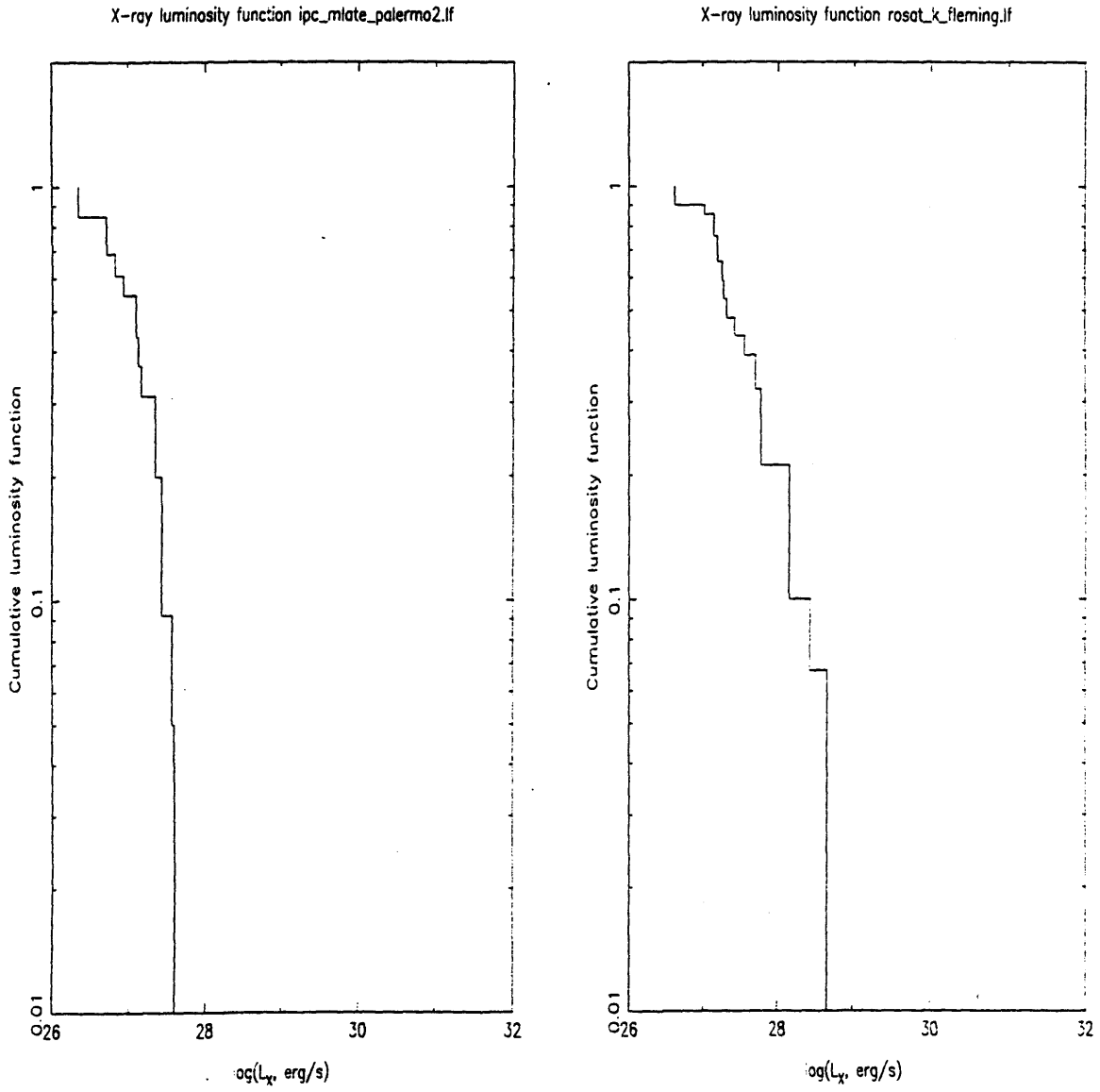

Figure A.2: Cumulative x-ray luminosity functions (see main text). These are late dM Barbera *et al.* and late dM Barbera *et al.*.

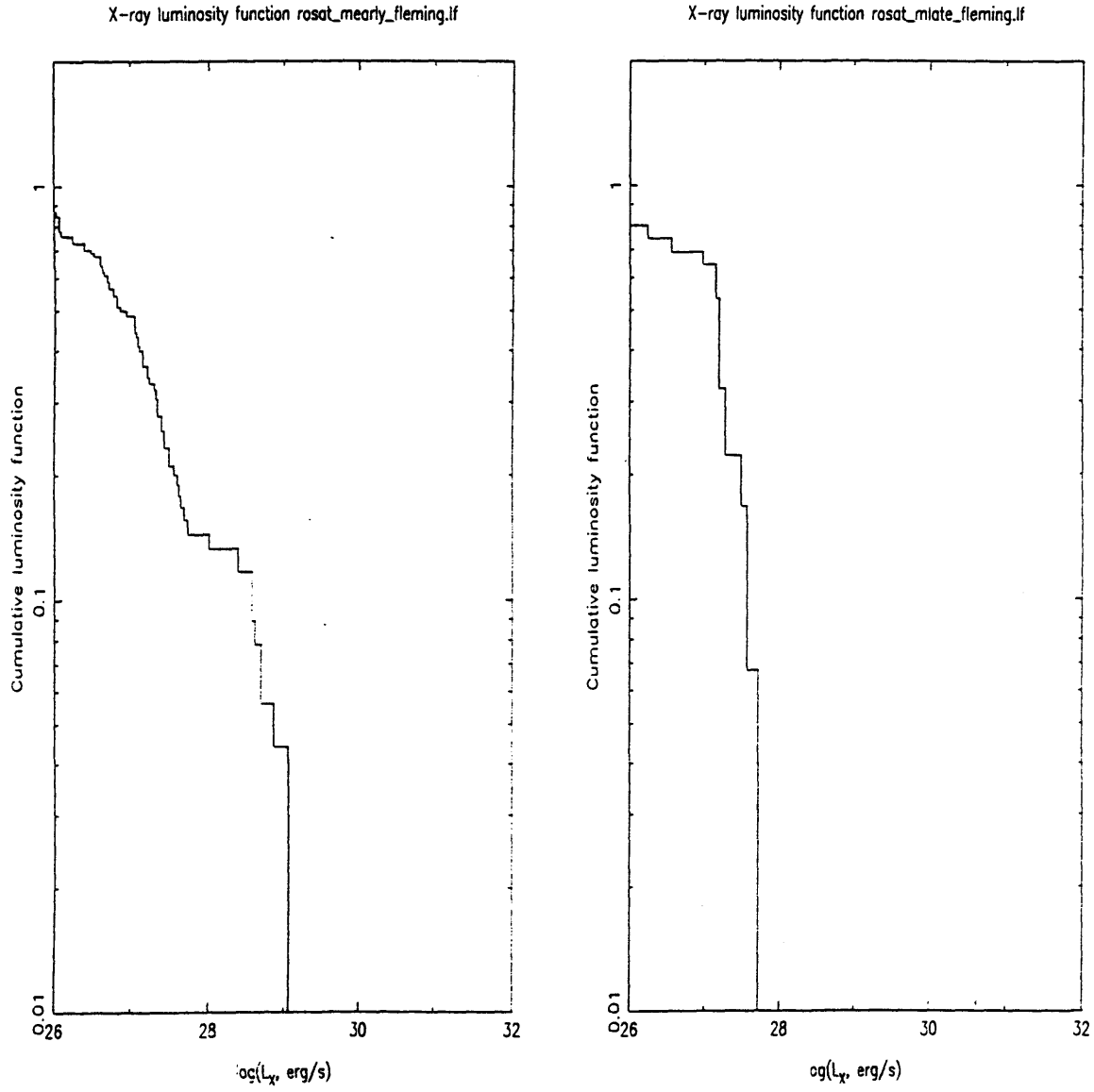

Figure A.3: Cumulative x-ray luminosity functions (see main text). These are early dM Fleming *et al.* and late dM Fleming *et al.*.

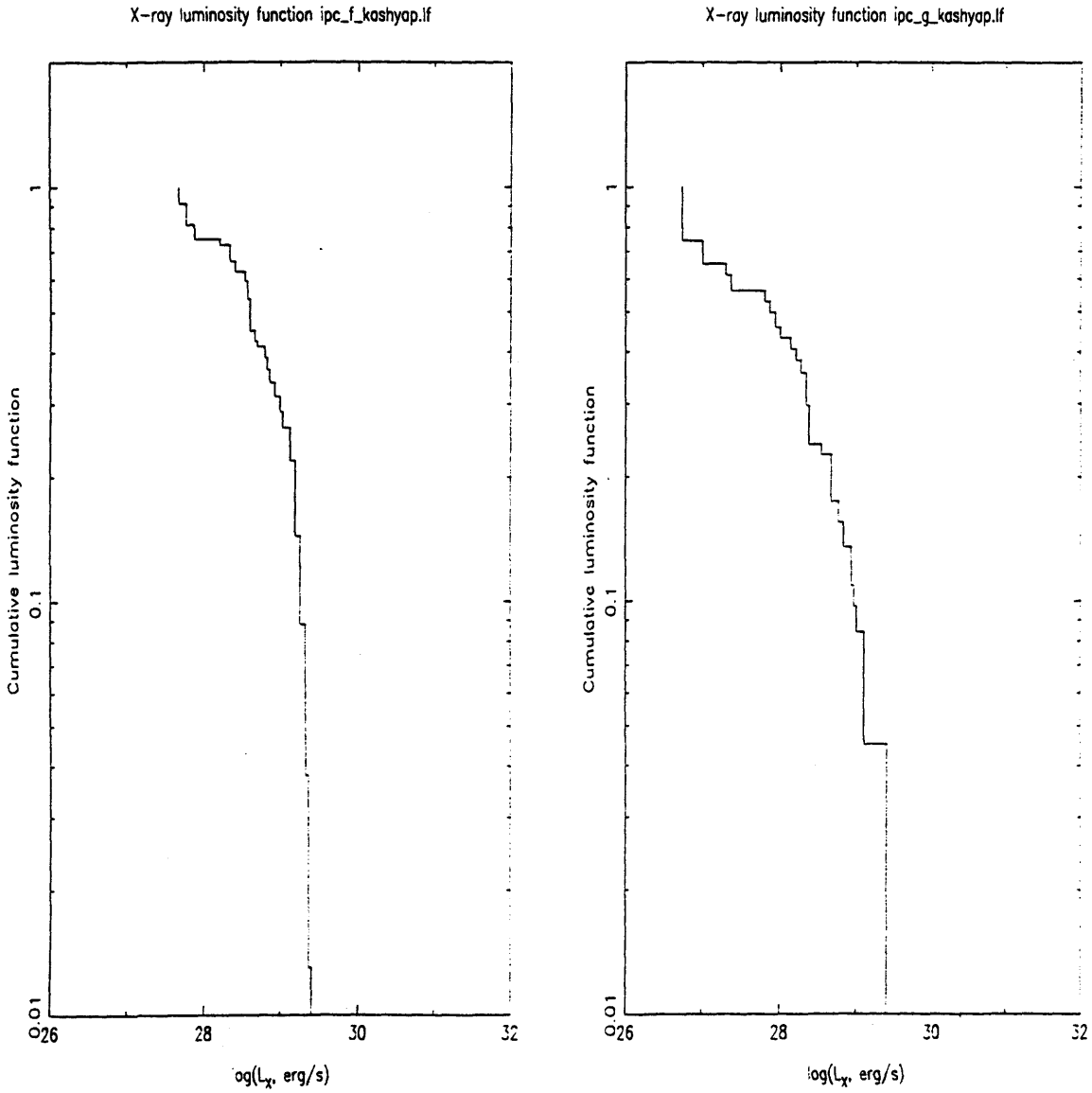

Figure A.4: Cumulative x-ray luminosity functions (see main text). These are dF Kashyap *et al.* and dG Kashyap *et al.*.

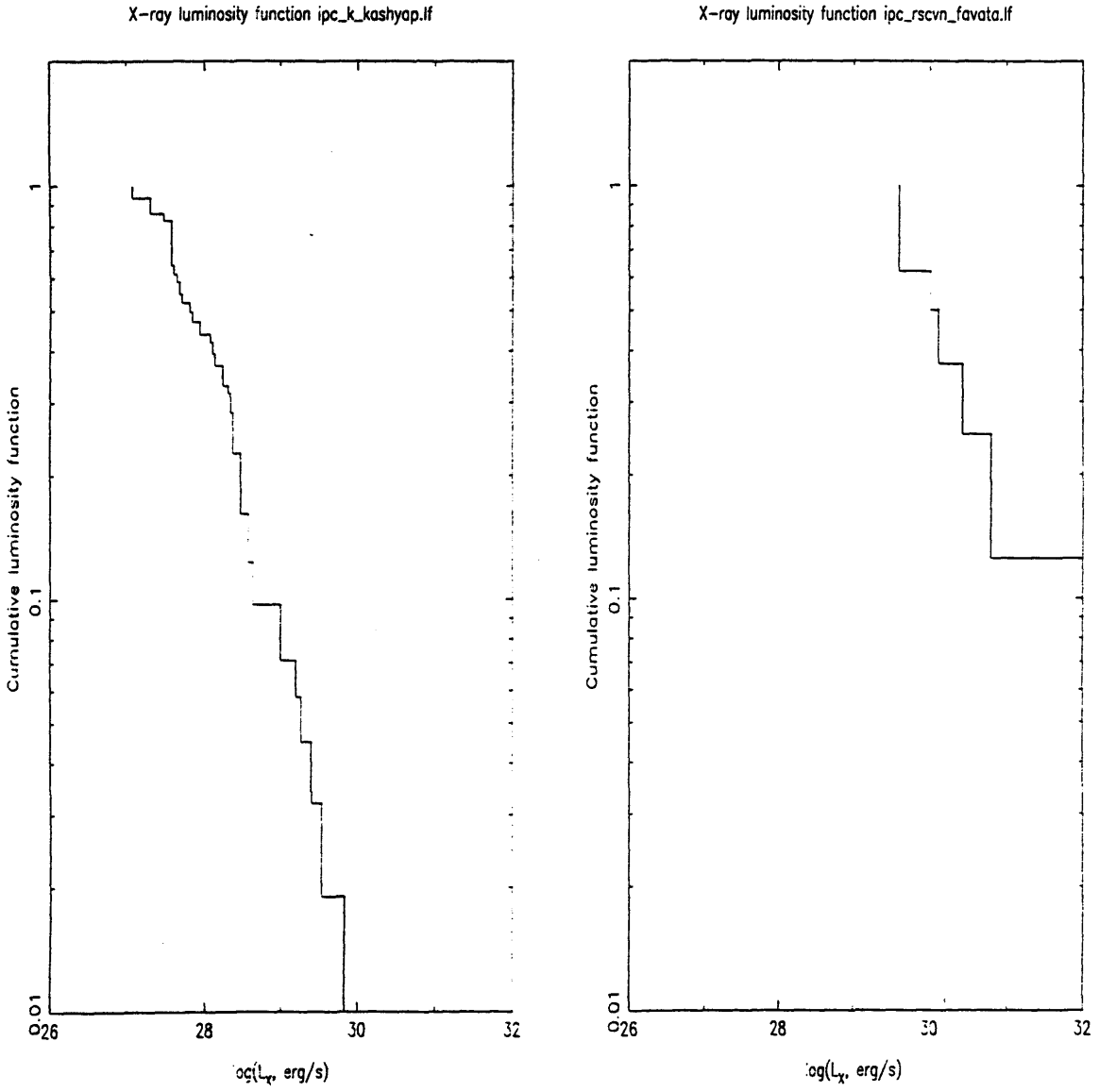

Figure A.5: Cumulative x-ray luminosity functions (see main text). These are dK Kashyap *et al.* and RS CVn Favata *et al.*.

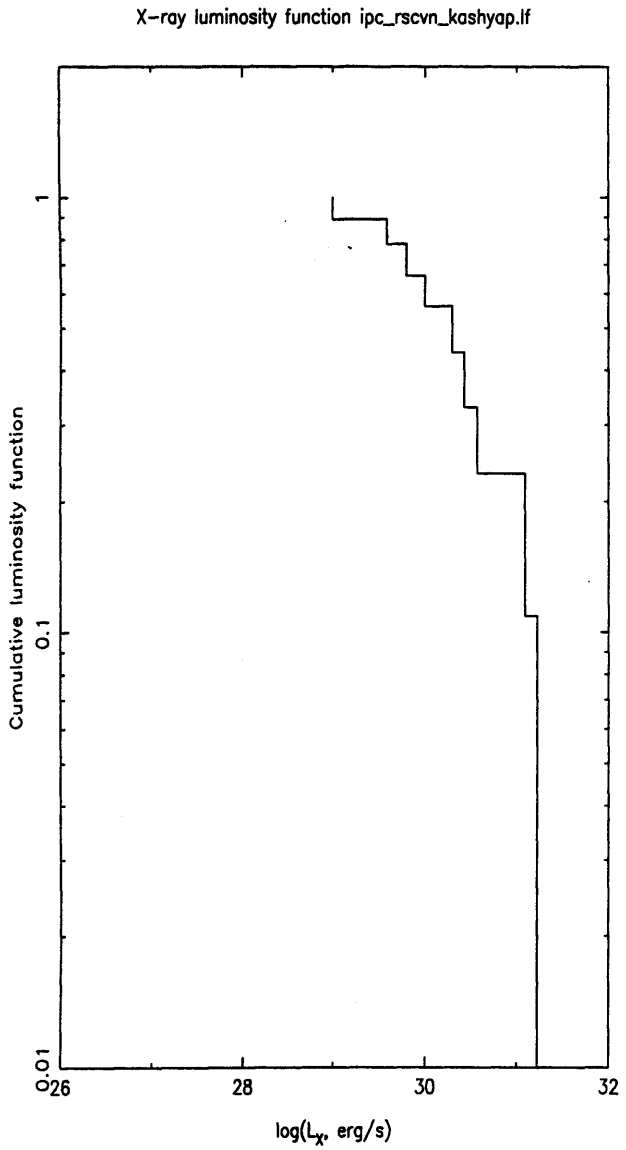

Figure A.6: Cumulative x-ray luminosity function (see main text) for RS CVn Kashyap *et al.*

Appendix B

Hyades PSPC Pointed Survey Light Curves

The following pages contain Hyades light curves observed using ROSAT and discussed in Chapter 4. They are presented, from top left, reading left to right, in RA order as shown in the tables in Appendix C. All light curves are binned into 1000 second time intervals. Note the different scales and ranges in both time and count rates from plot to plot.

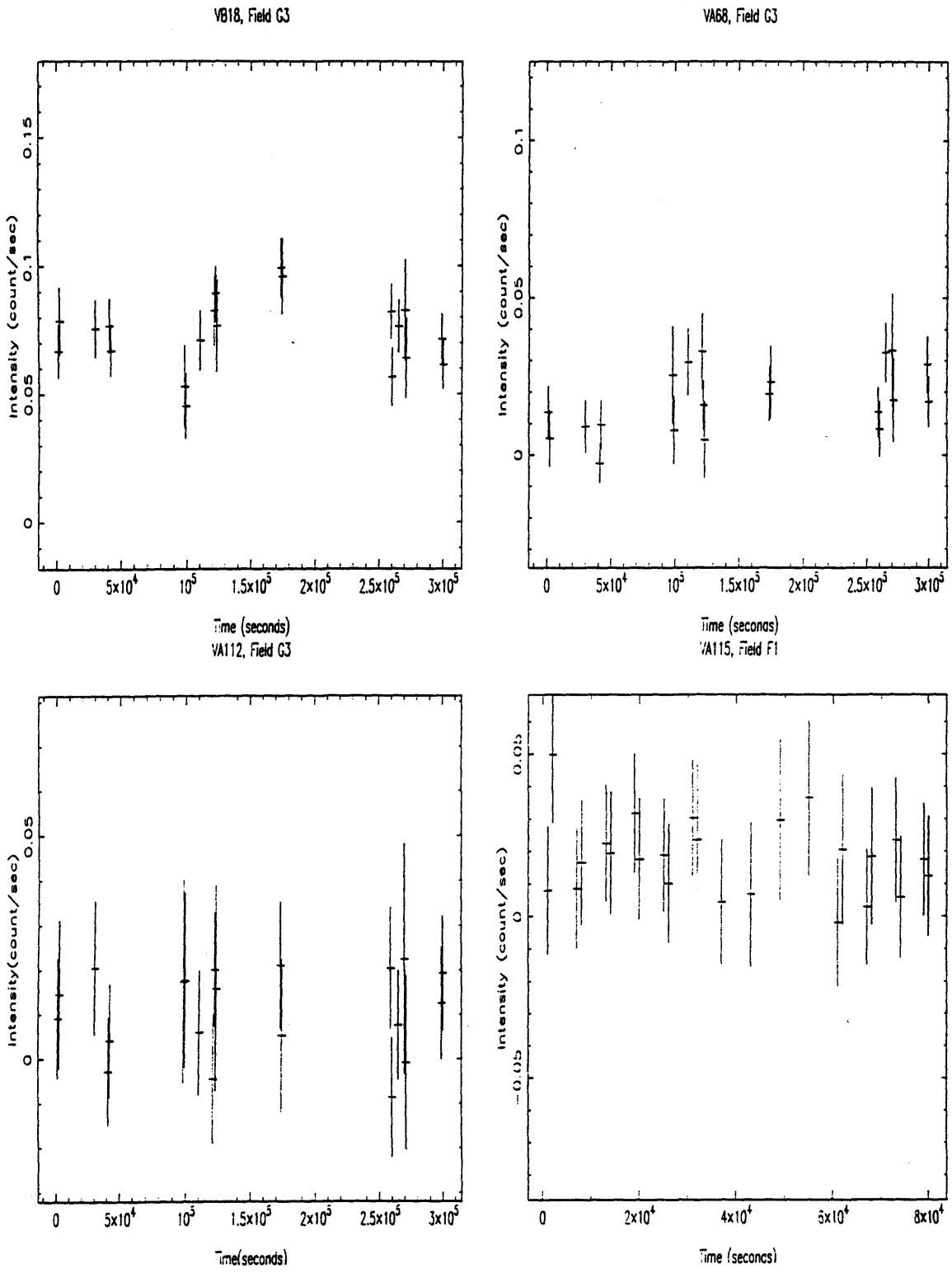

Figure B.1: Hyades PSPC pointed survey lightcurves (see main text).

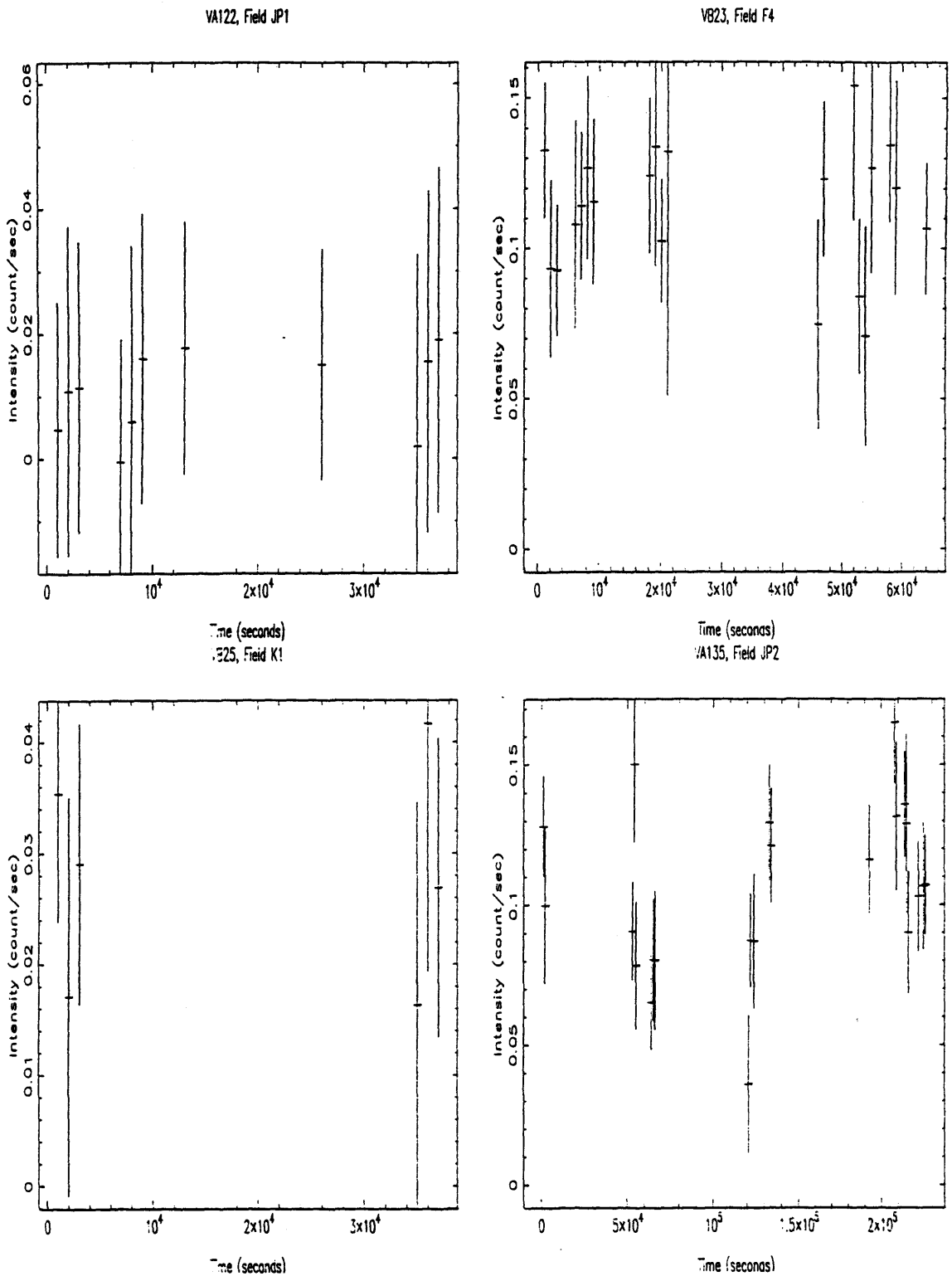

Figure B.2: Hyades PSPC pointed survey lightcurves (see main text).

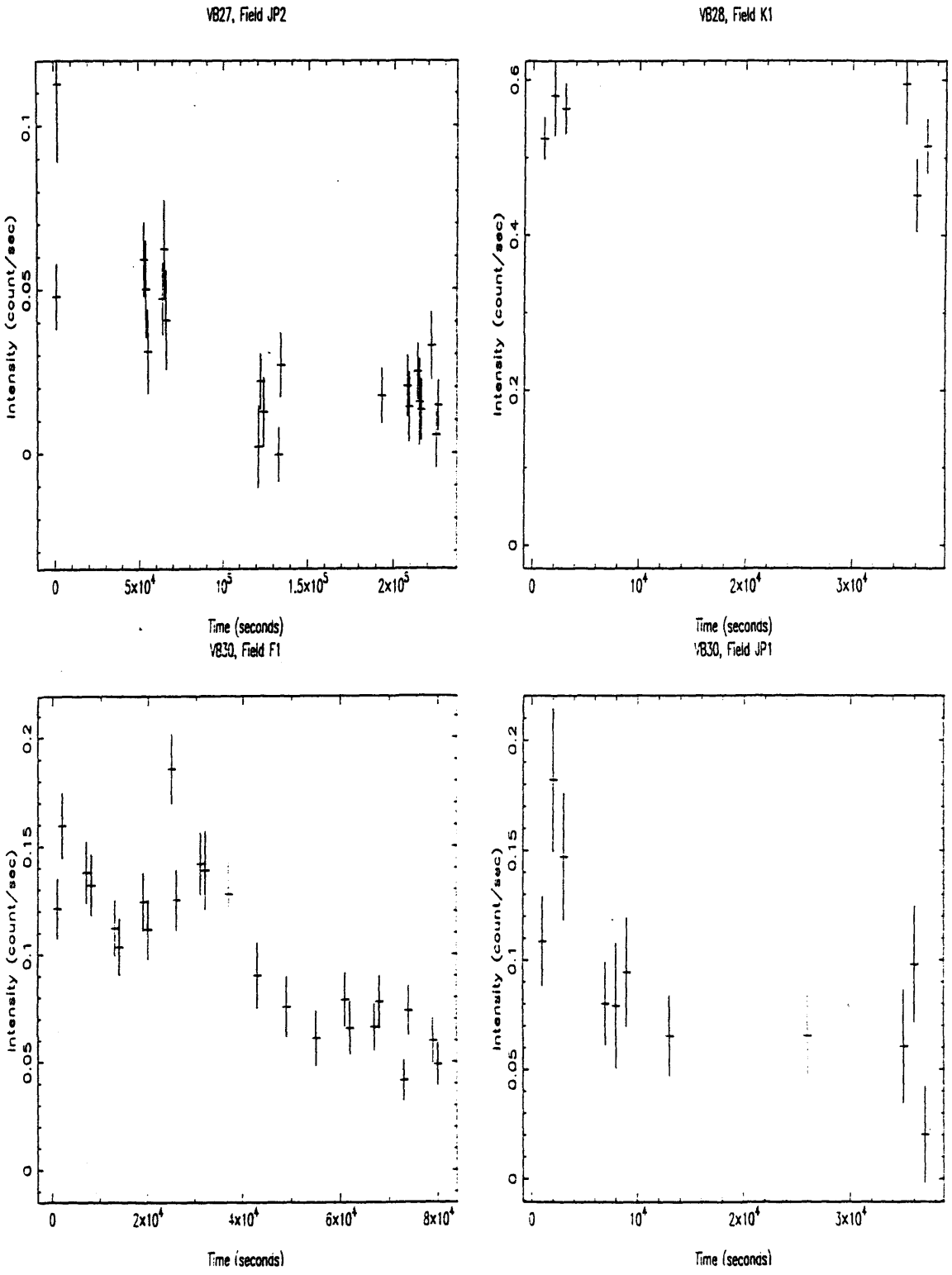

Figure B.3: Hyades PSPC pointed survey lightcurves (see main text).

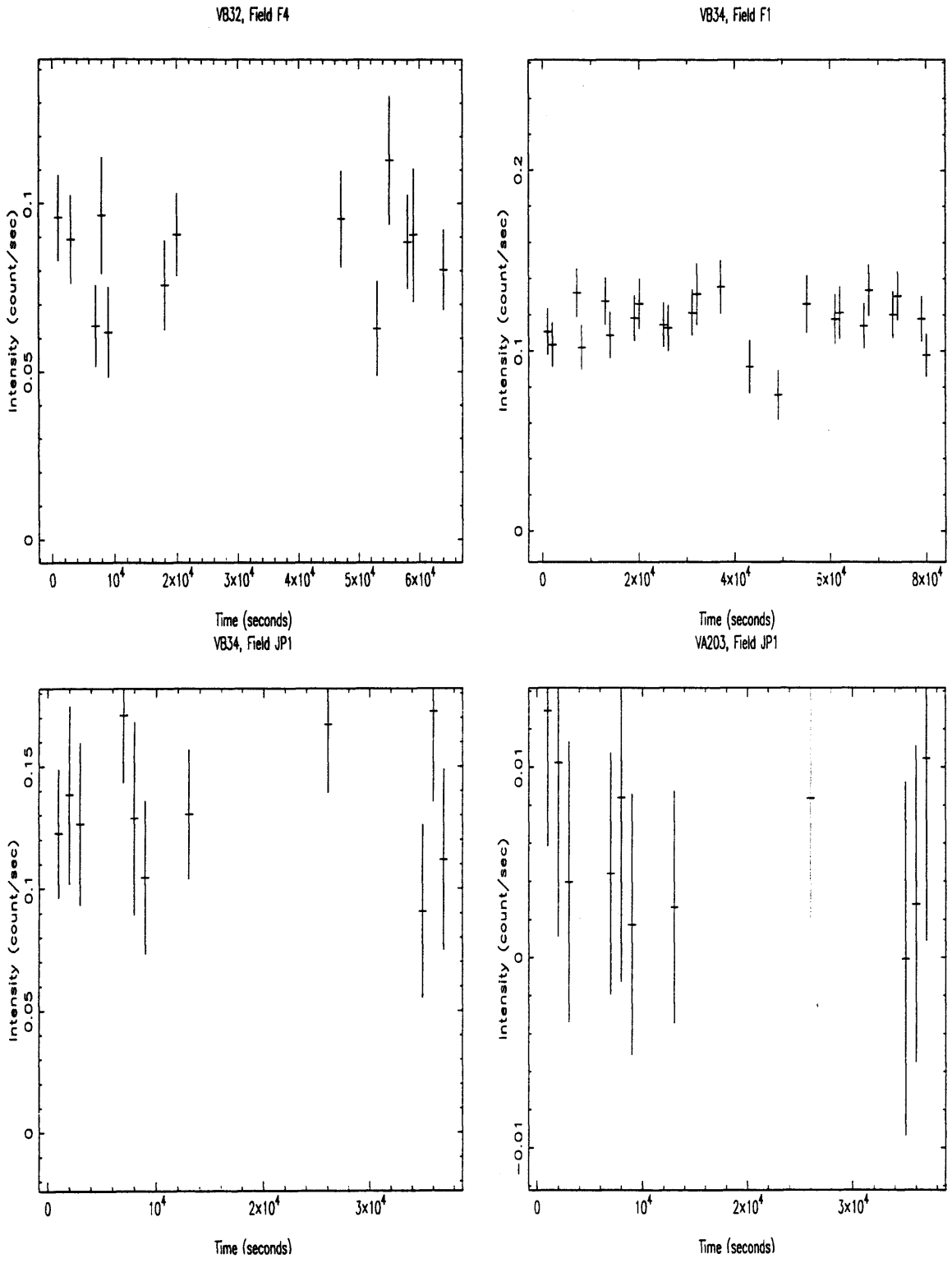

Figure B.4: Hyades PSPC pointed survey lightcurves (see main text).

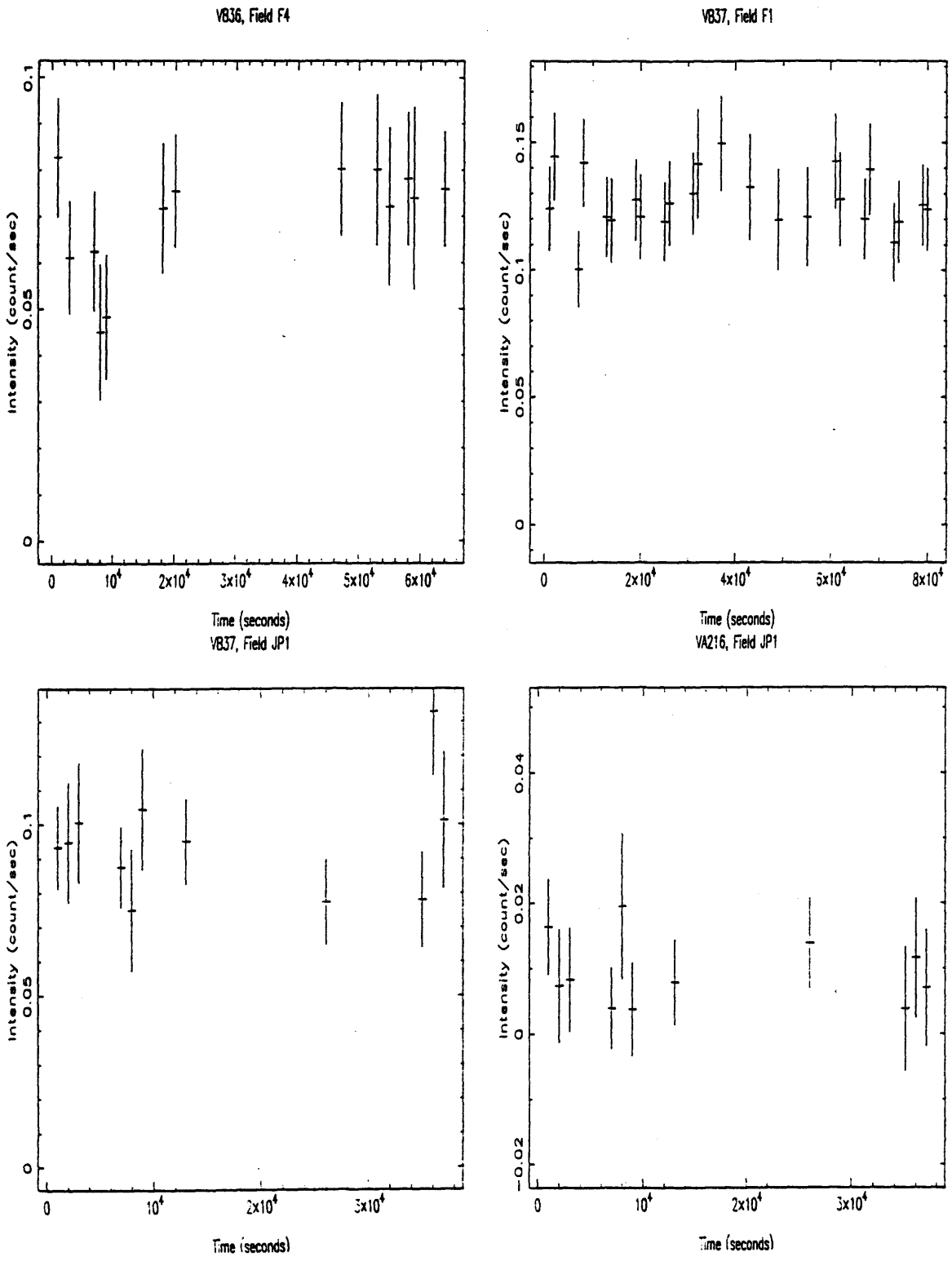

Figure B.5: Hyades PSPC pointed survey lightcurves (see main text).

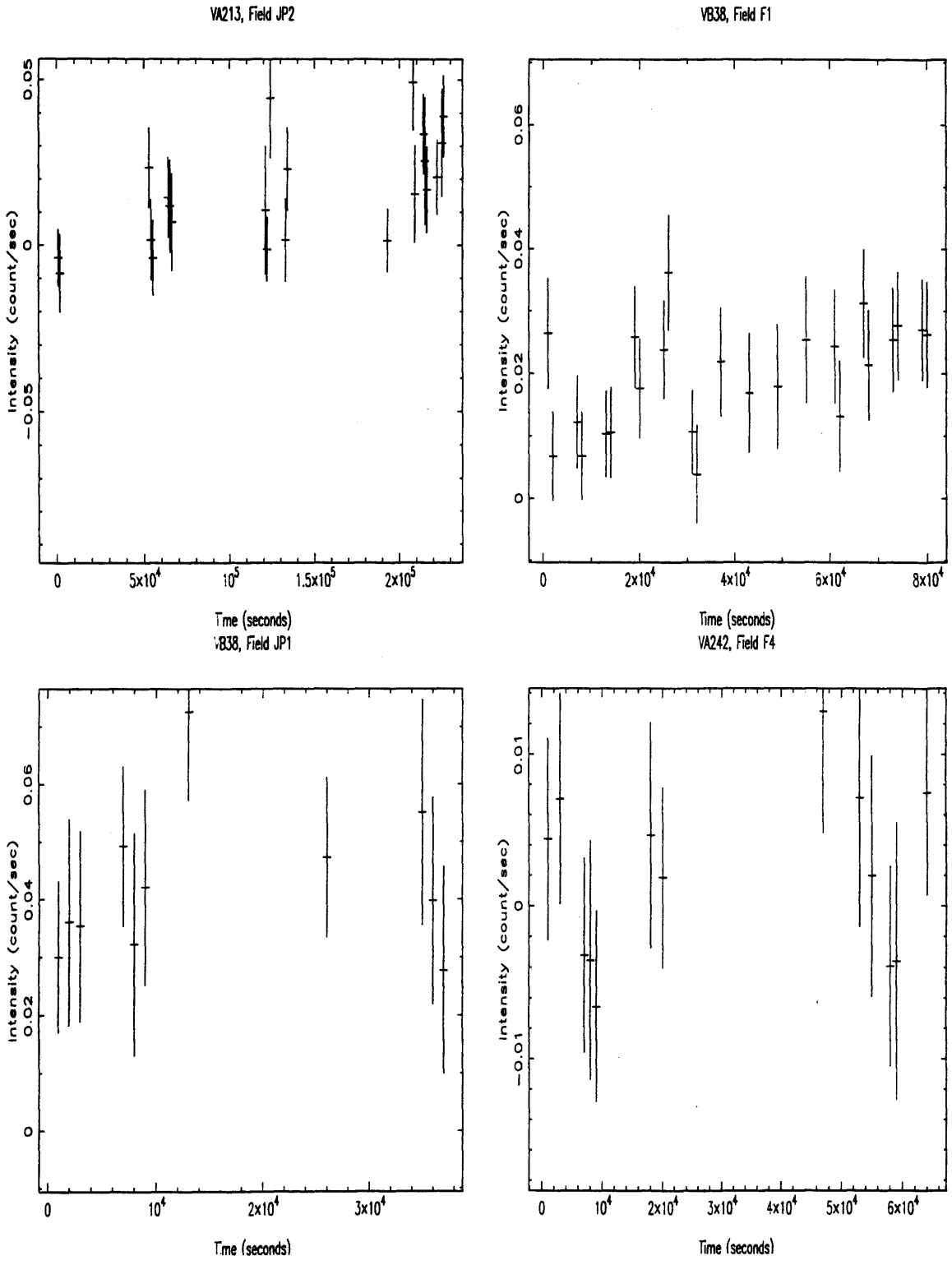

Figure B.6: Hyades PSPC pointed survey lightcurves (see main text).

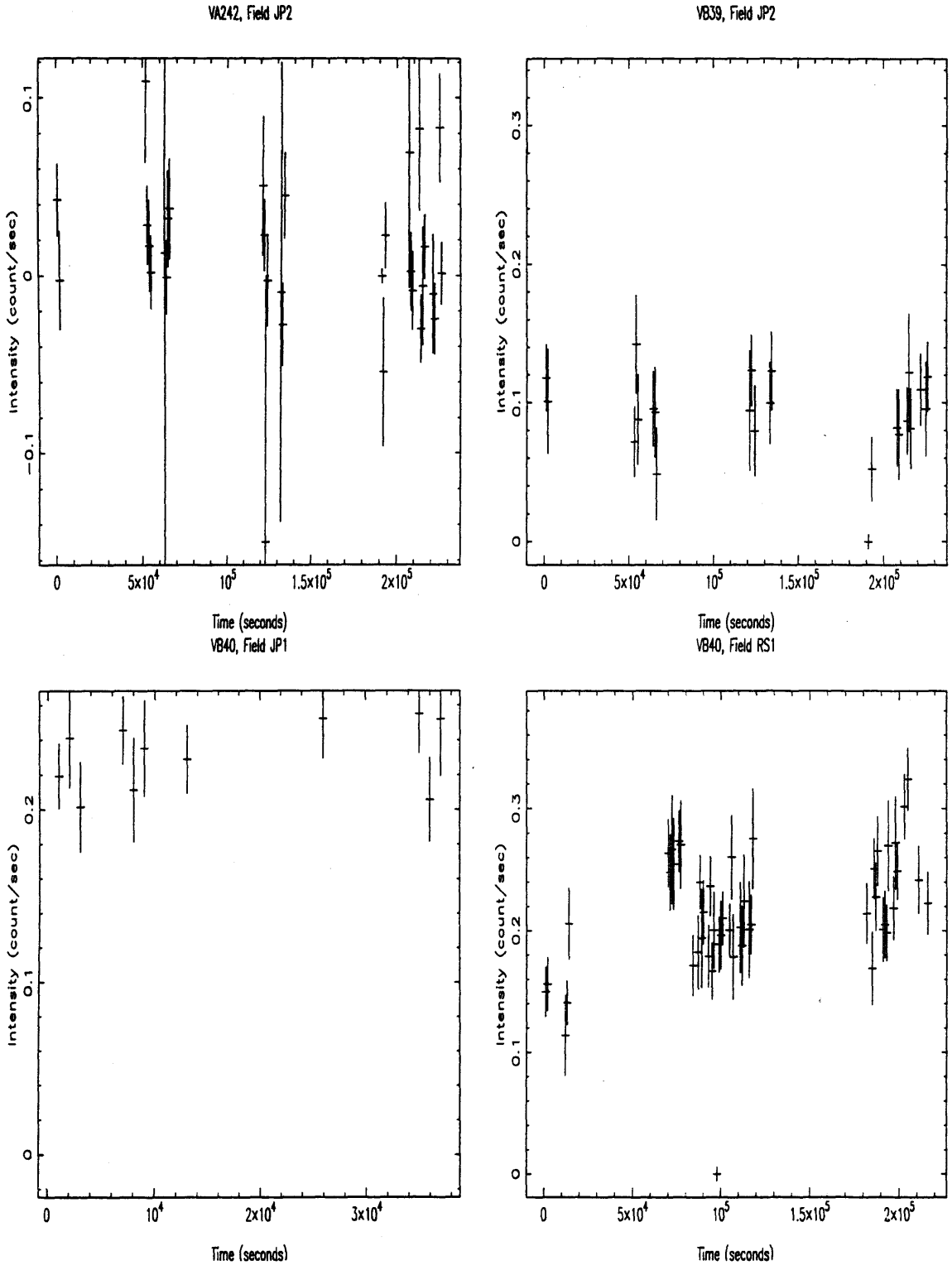

Figure B.7: Hyades PSPC pointed survey lightcurves (see main text).

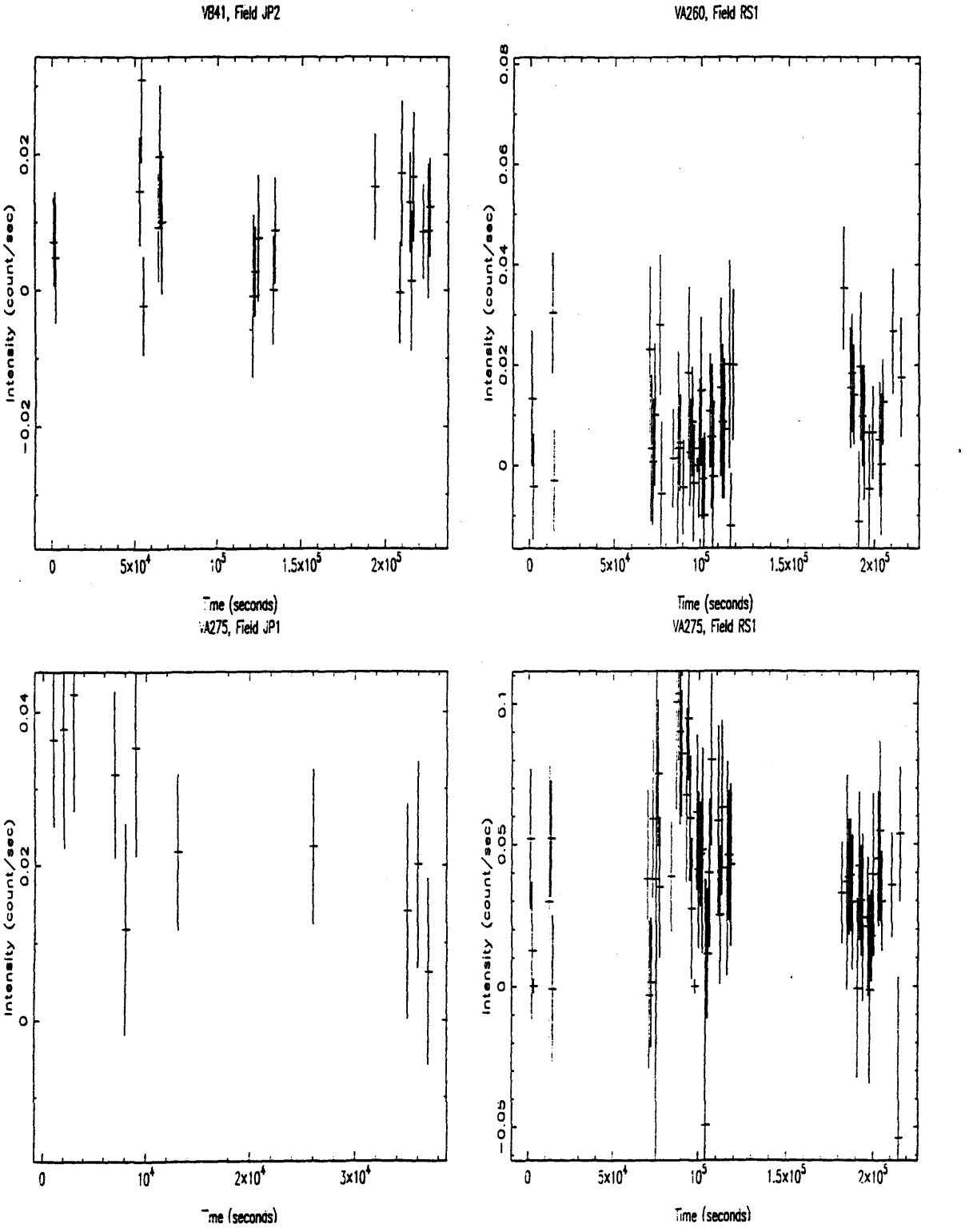

Figure B.3: Hyades PSPC pointed survey lightcurves (see main text).

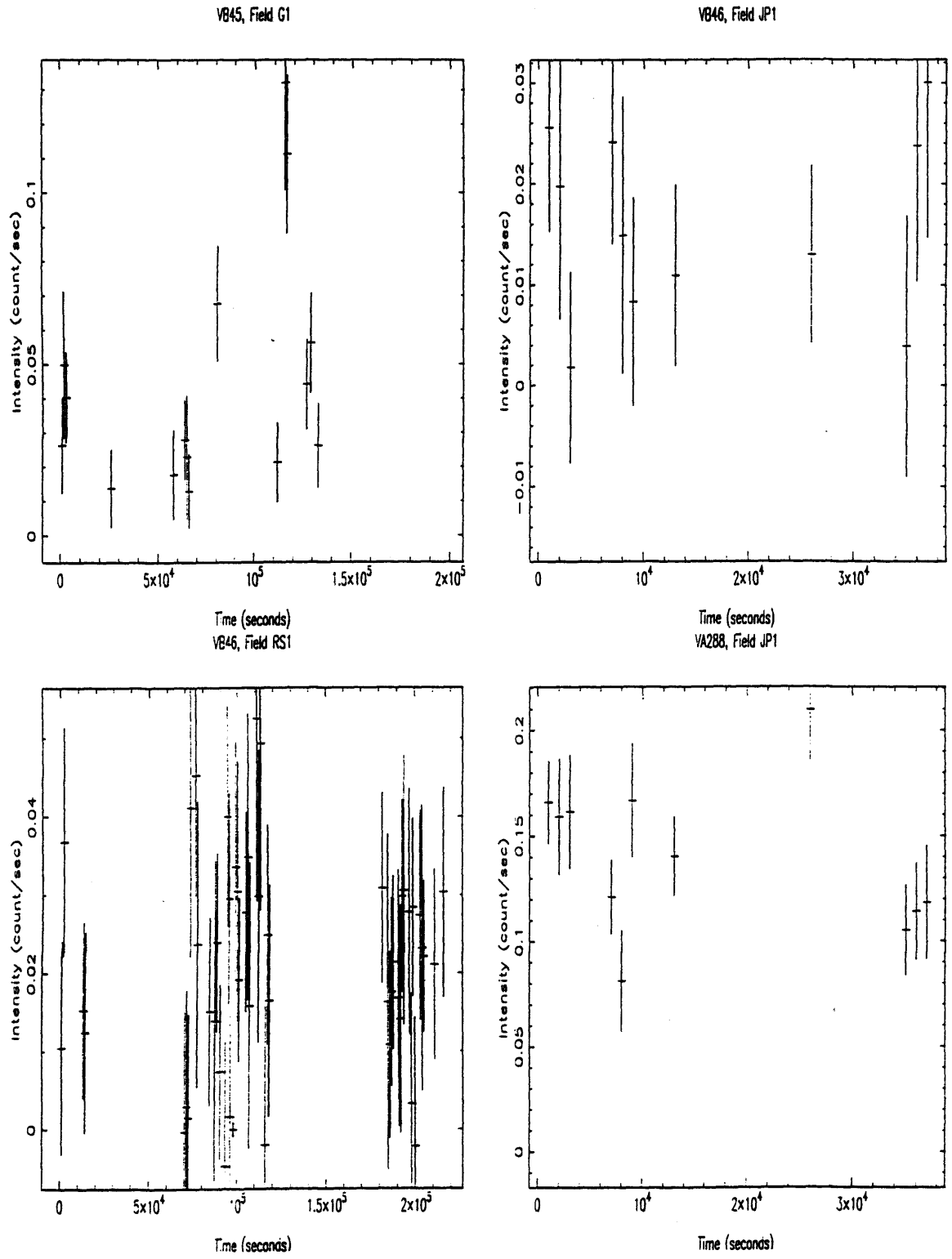

Figure B.9: Hyades PSPC pointed survey lightcurves (see main text).

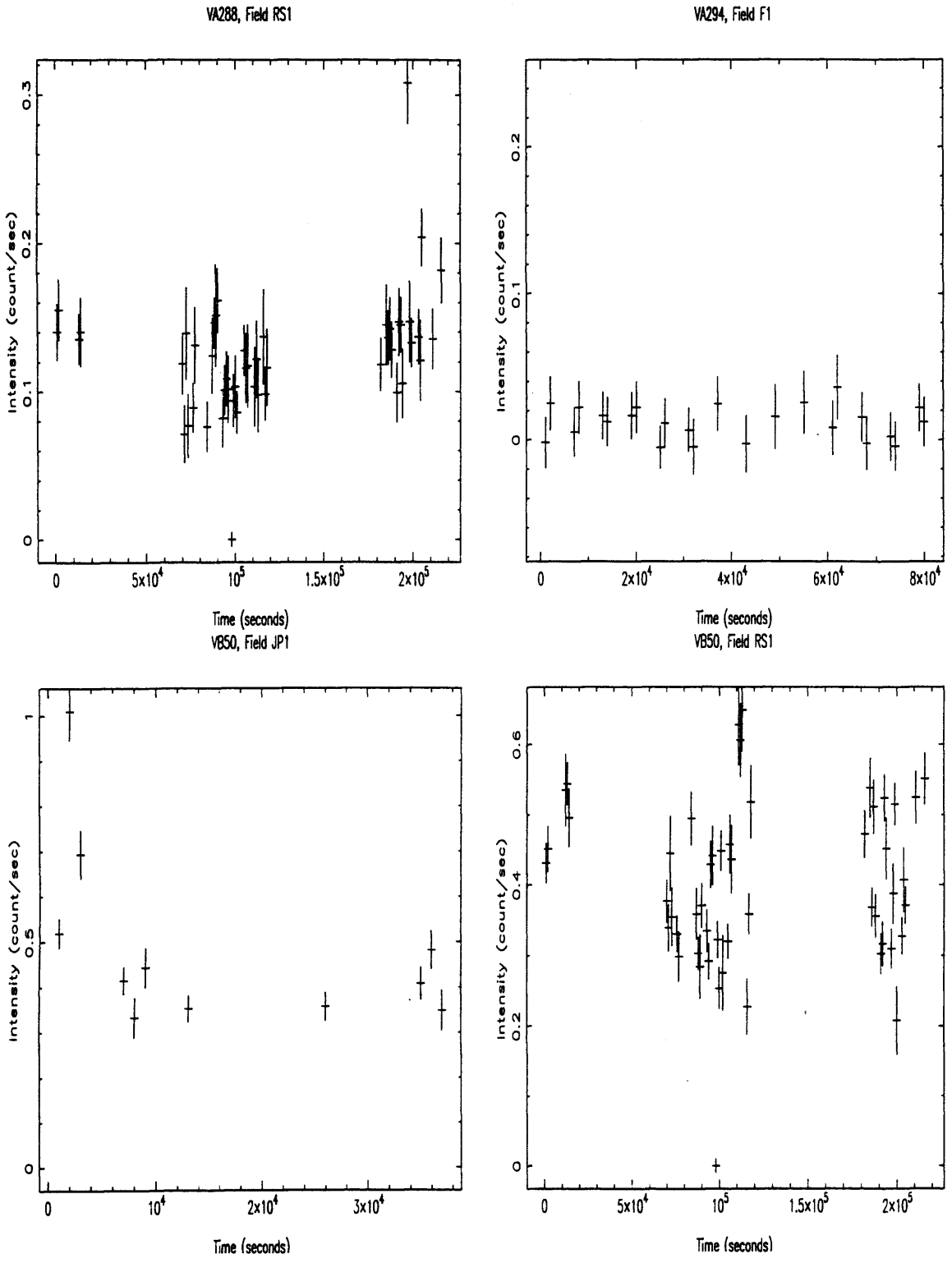

Figure B.10: Hyades PSPC pointed survey lightcurves (see main text).

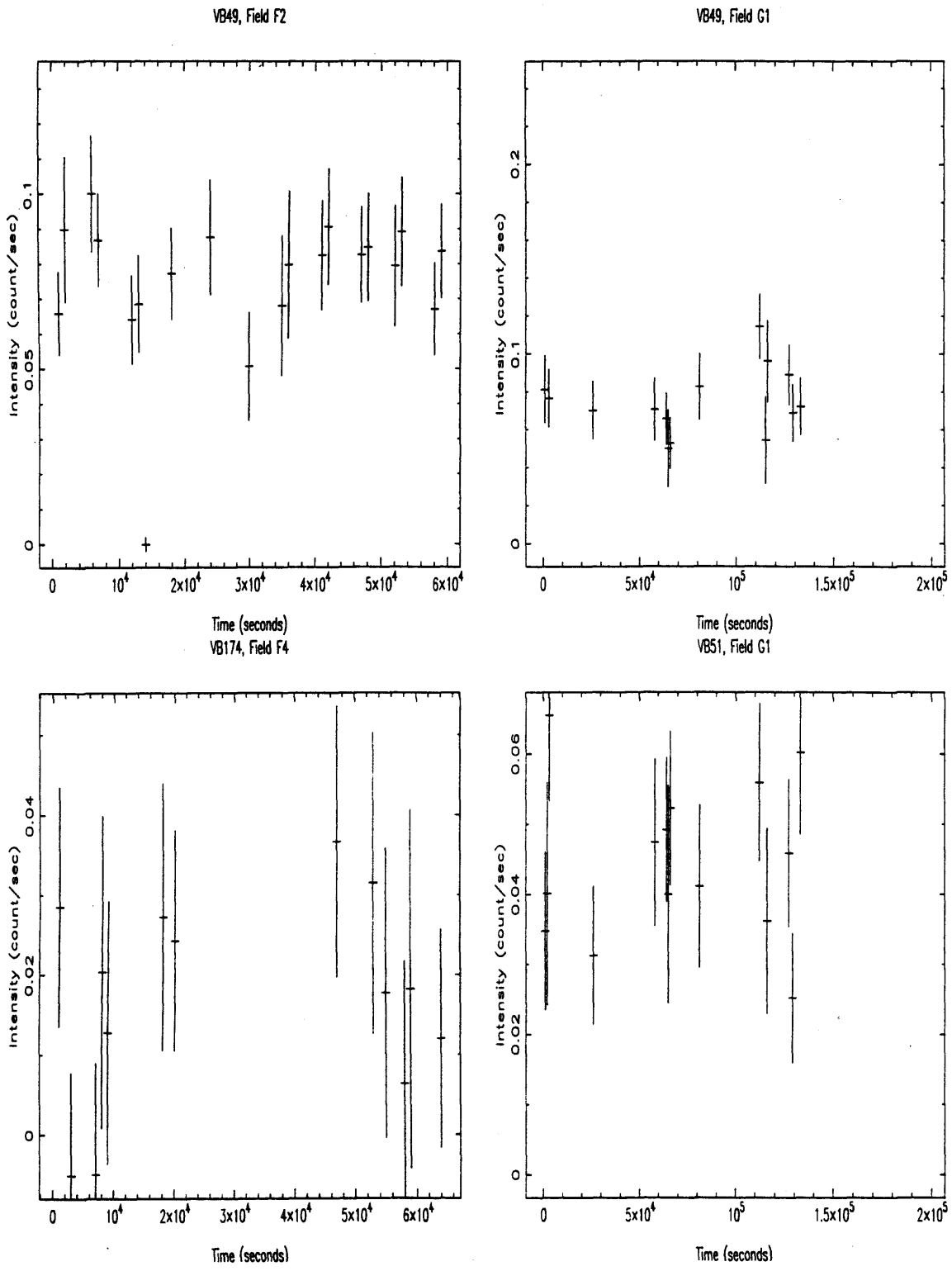

Figure B.11: Hyades PSPC pointed survey lightcurves (see main text).

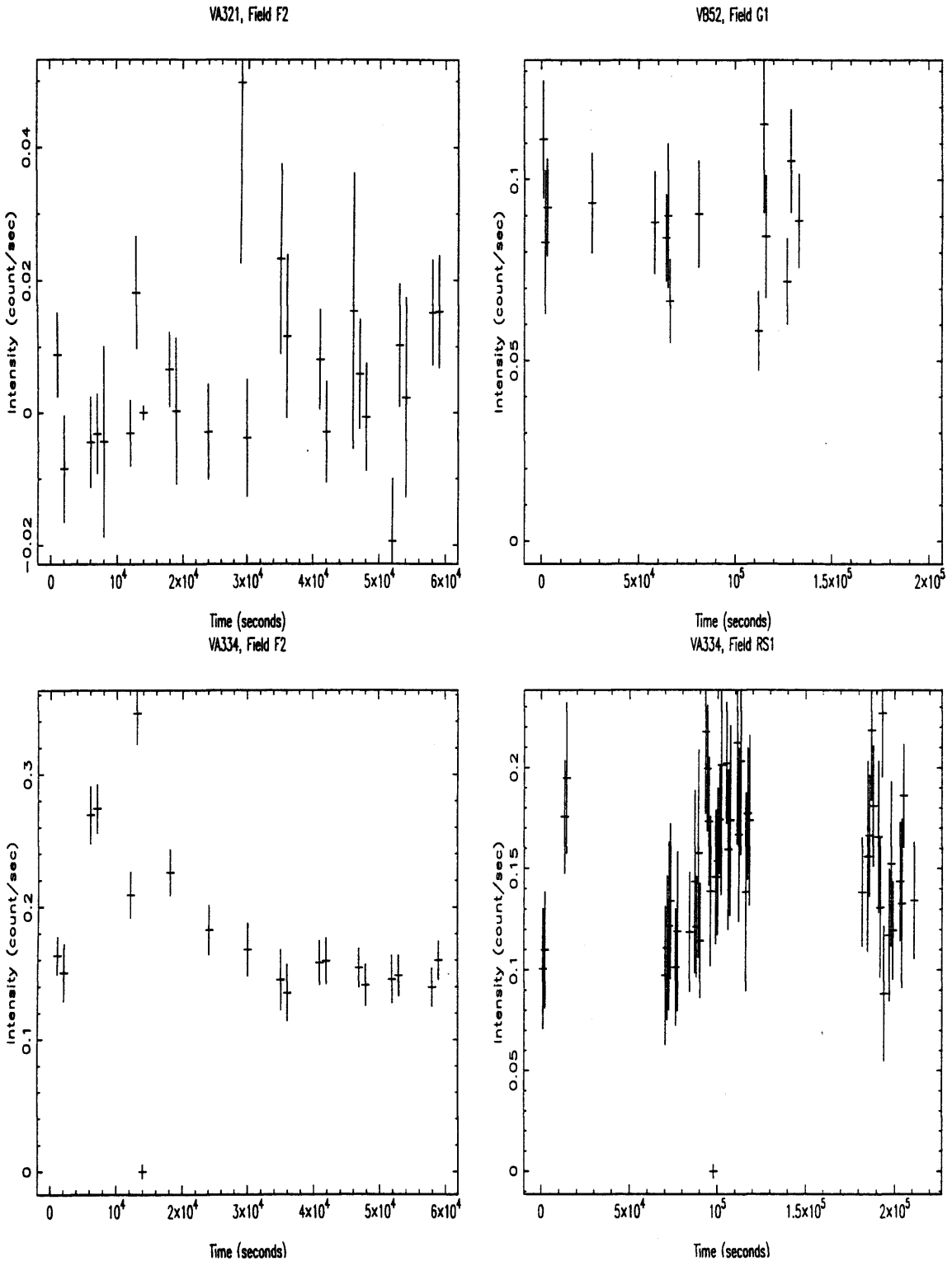

Figure B.12: Hyades PSPC pointed survey lightcurves (see main text).

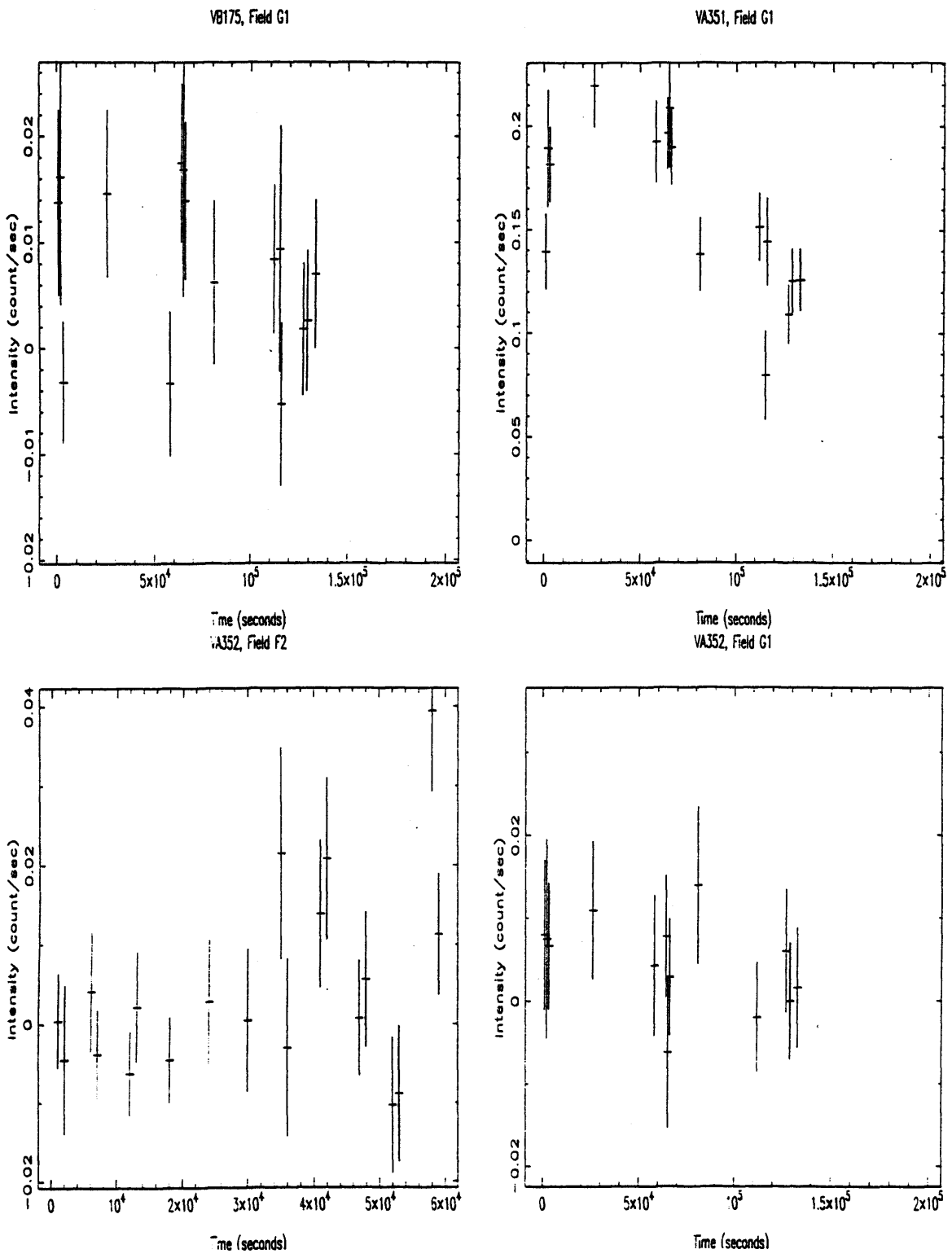

Figure B.13: Hyades PSPC pointed survey lightcurves (see main text).

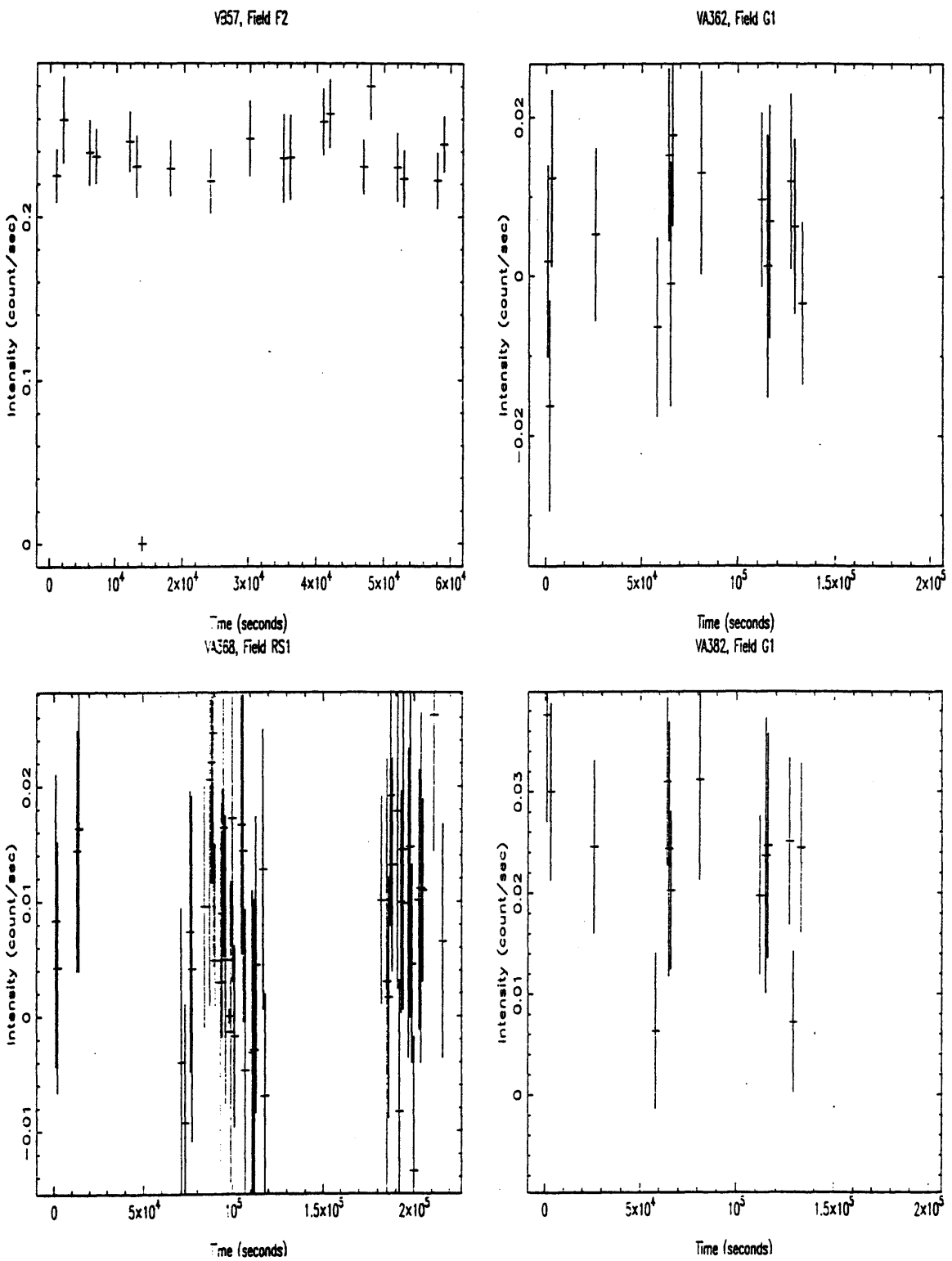

Figure B.14: Hyades PSPC pointed survey lightcurves (see main text).

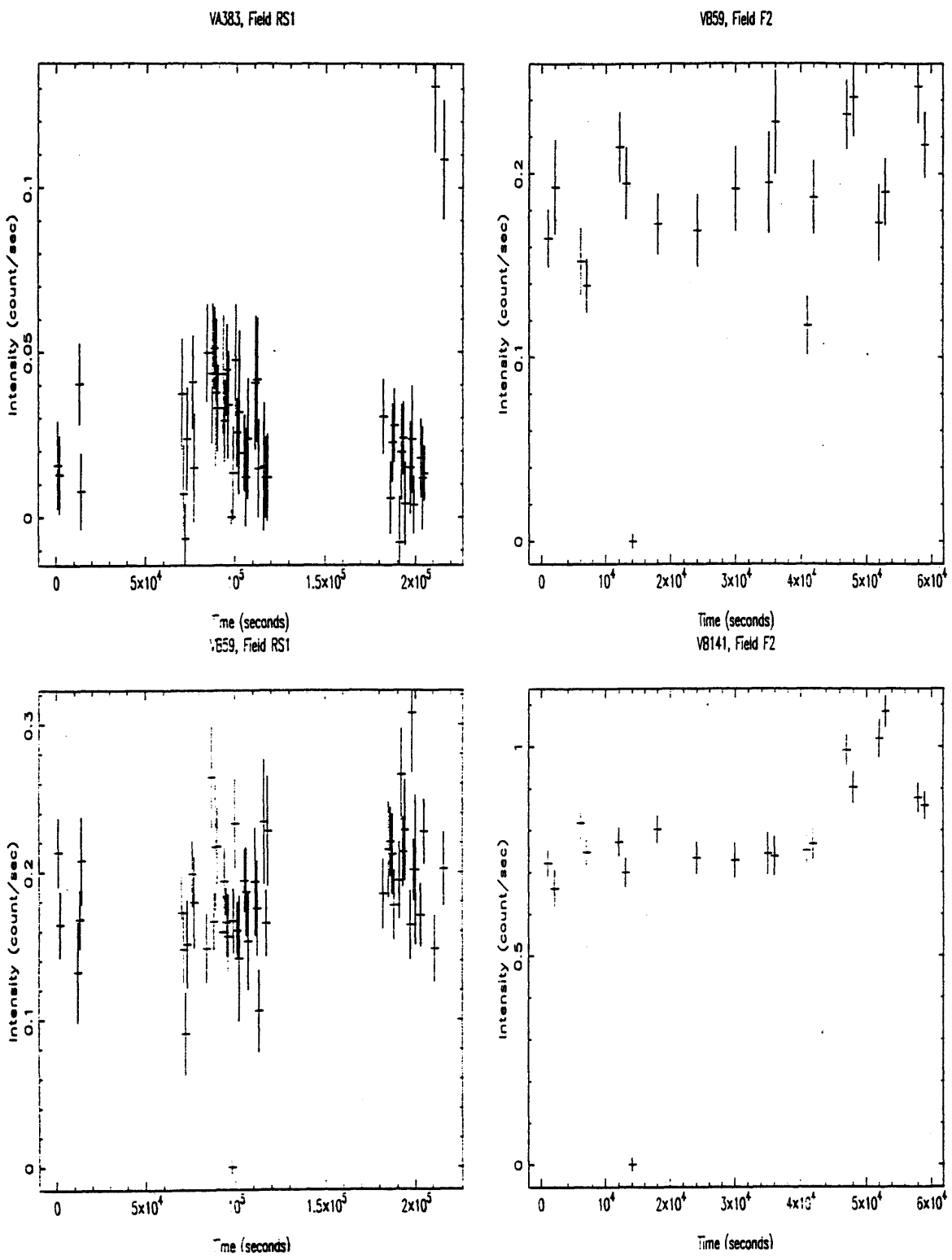

Figure B.15: Hyades PSPC pointed survey lightcurves (see main text).

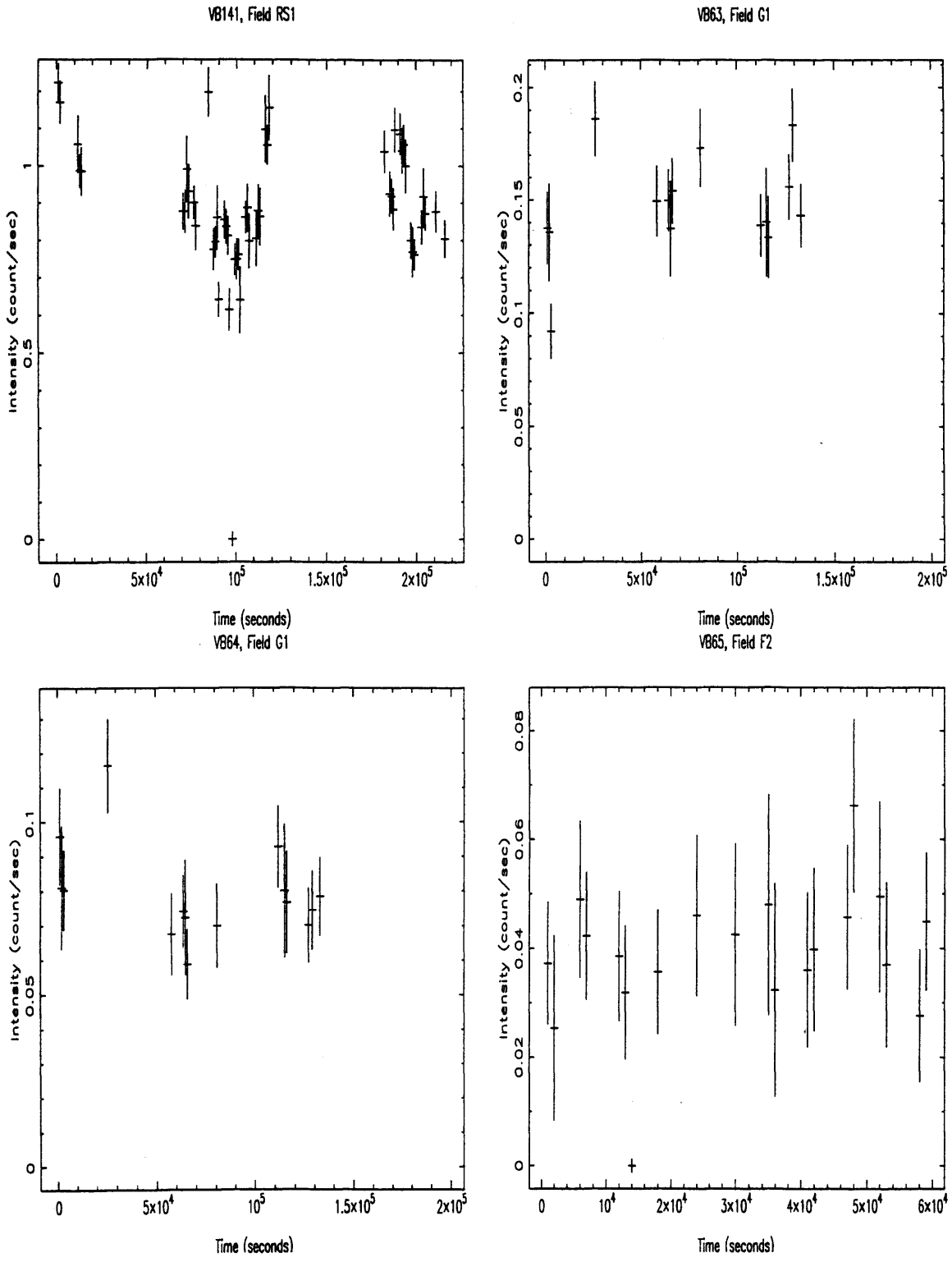

Figure B.16: Hyades PSPC pointed survey lightcurves (see main text).

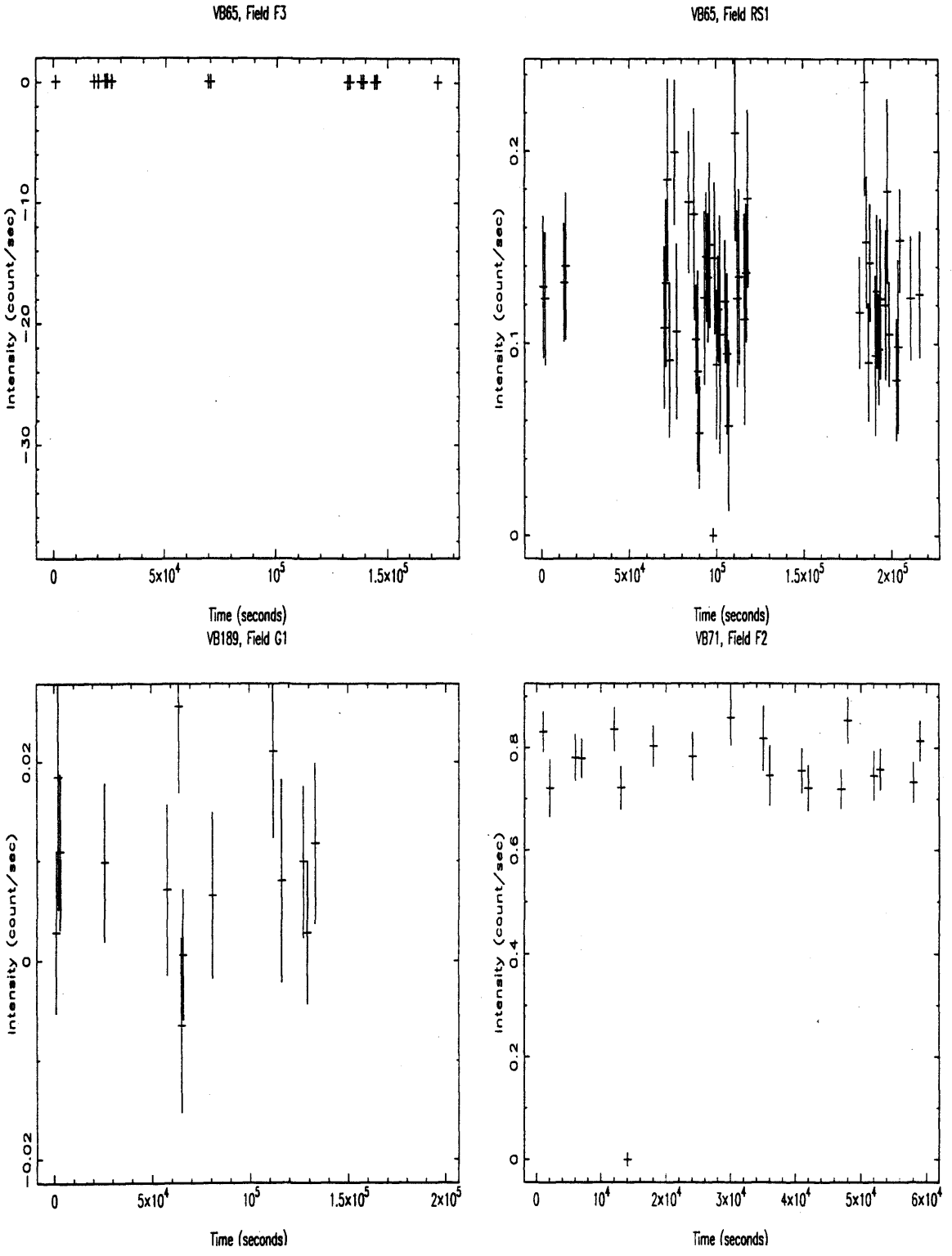

Figure B.17: Hyades PSPC pointed survey lightcurves (see main text).

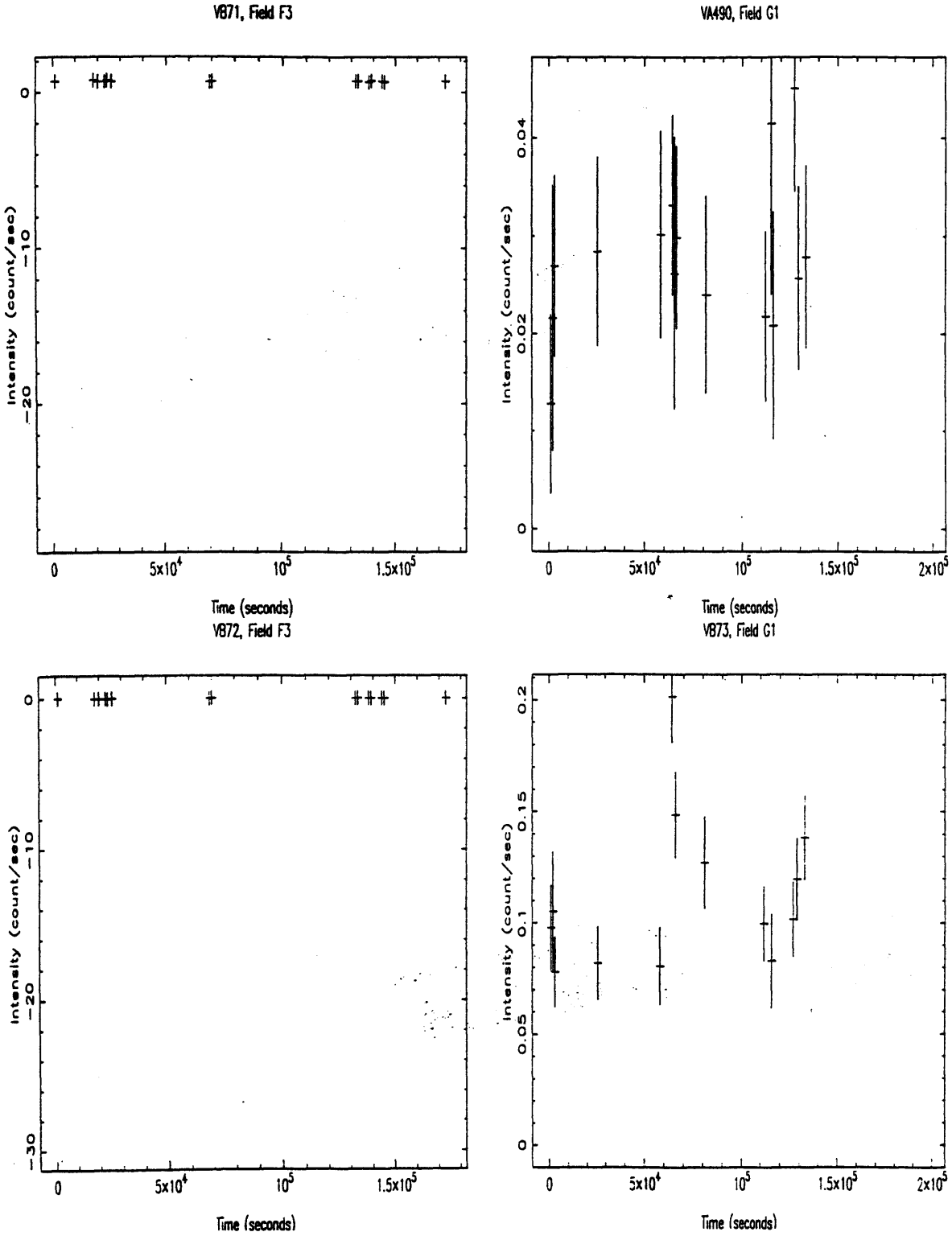

Figure B.18: Hyades PSPC pointed survey lightcurves (see main text).

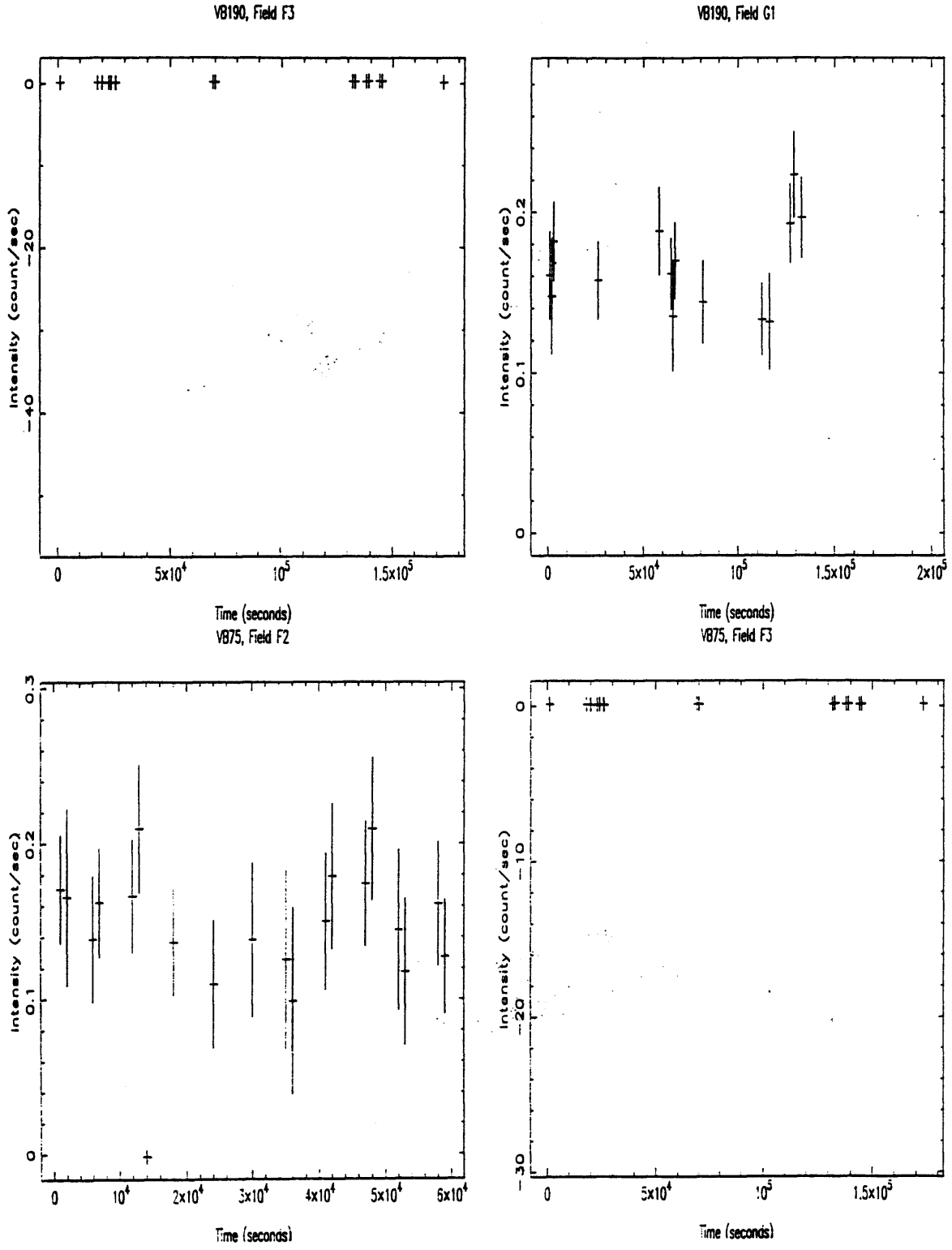

Figure B.19: Hyades PSPC pointed survey lightcurves (see main text).

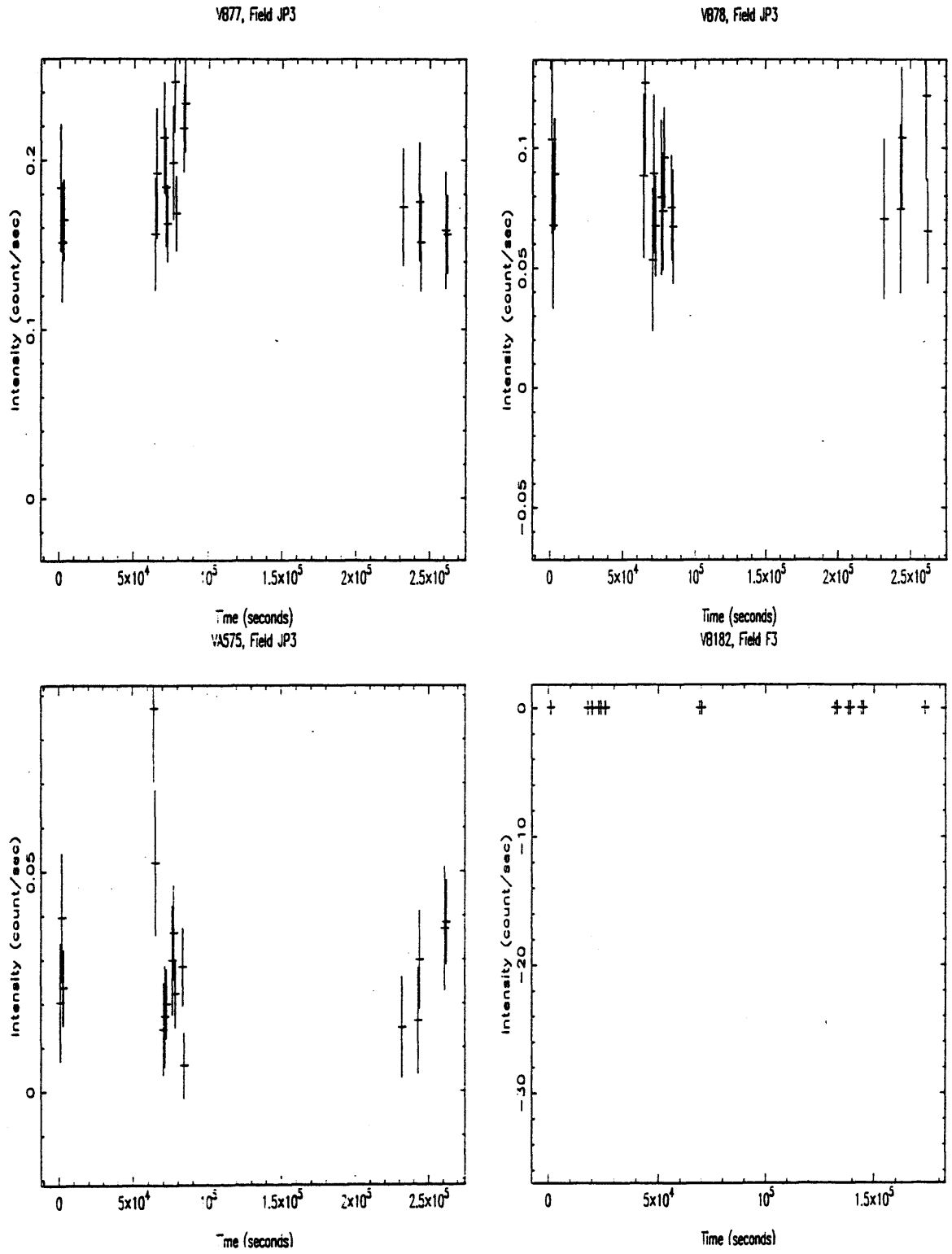

Figure B.20: Hyades PSPC pointed survey lightcurves (see main text).

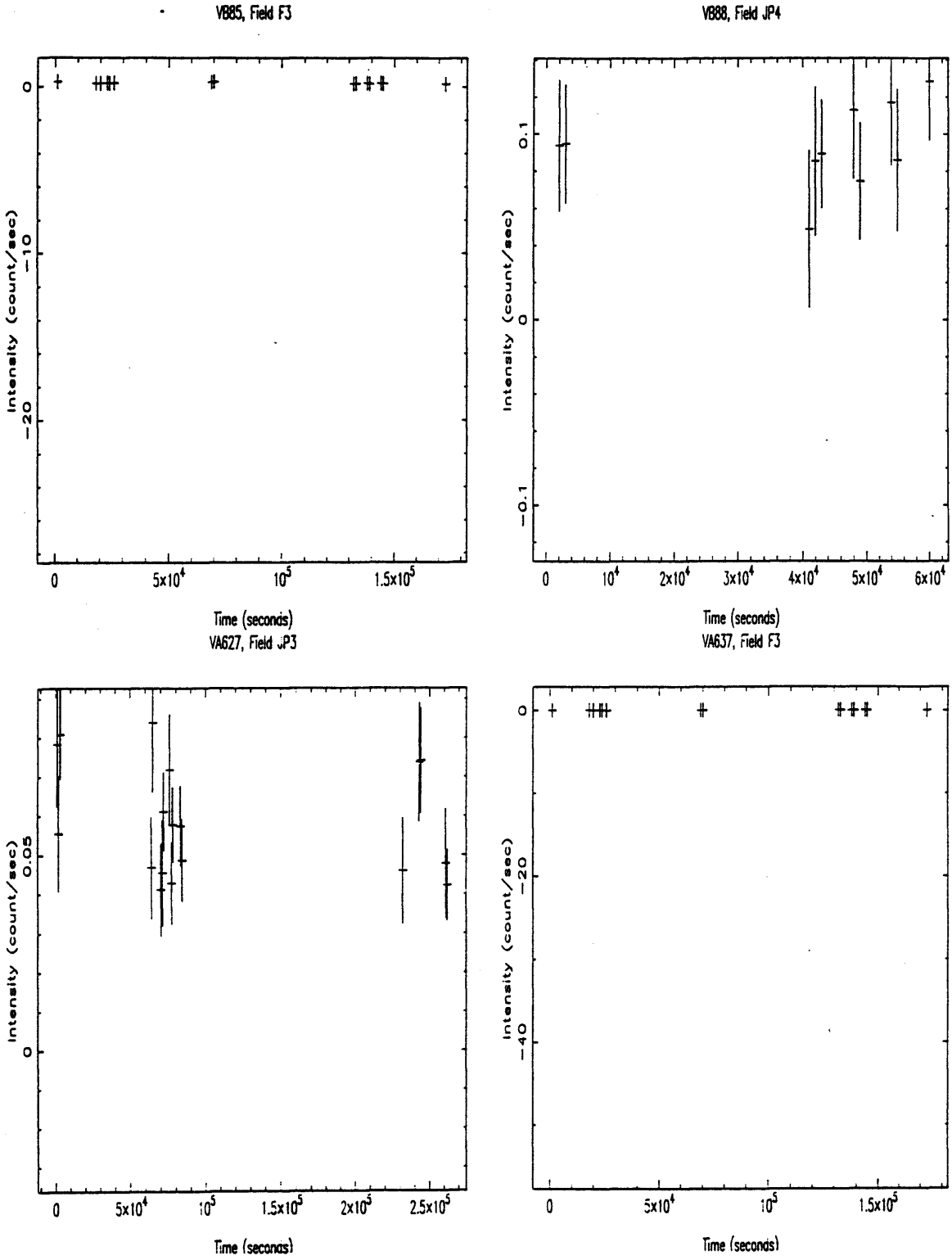

Figure B.21: Hyades PSPC pointed survey lightcurves (see main text).

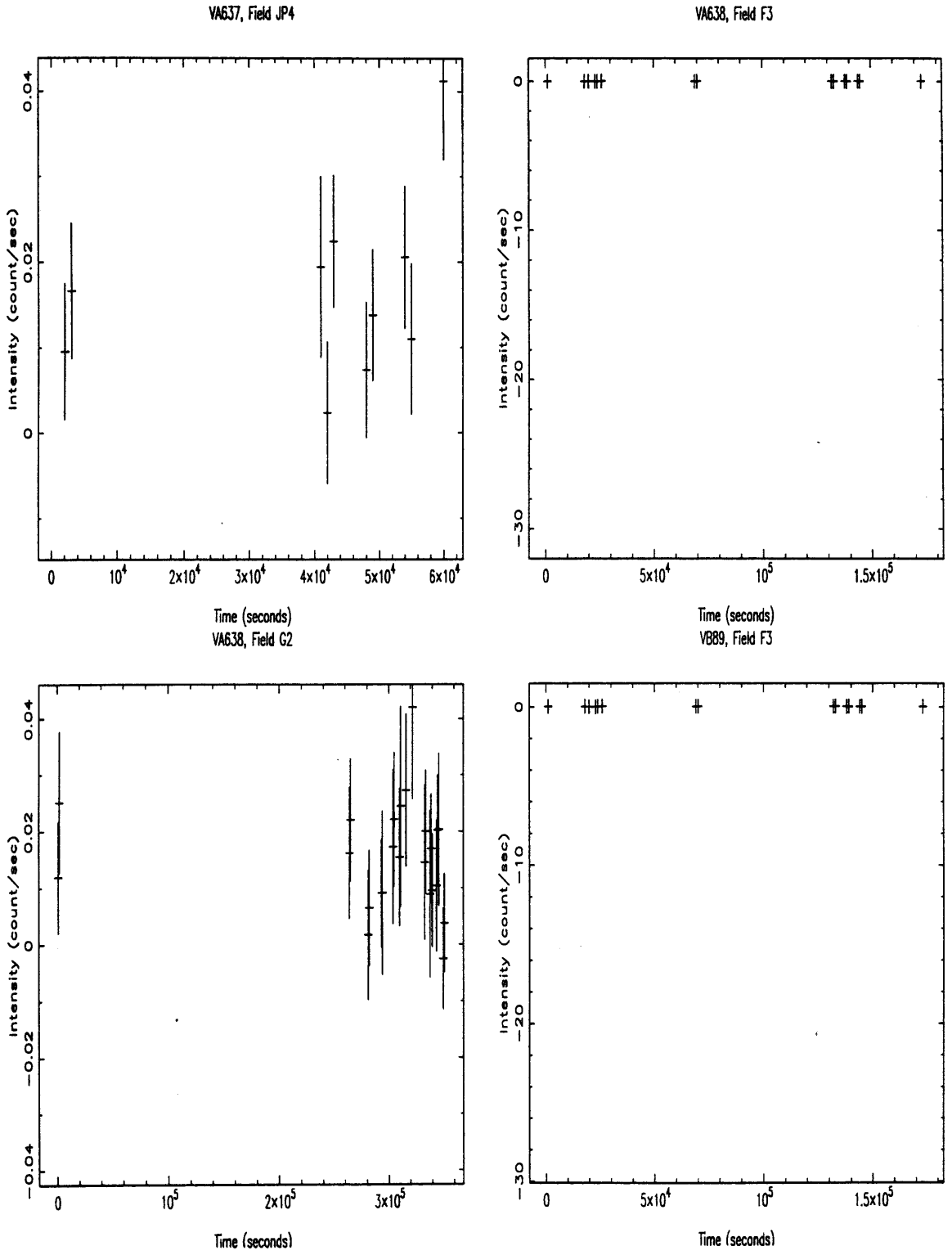

Figure B.22: Hyades PSPC pointed survey lightcurves (see main text).

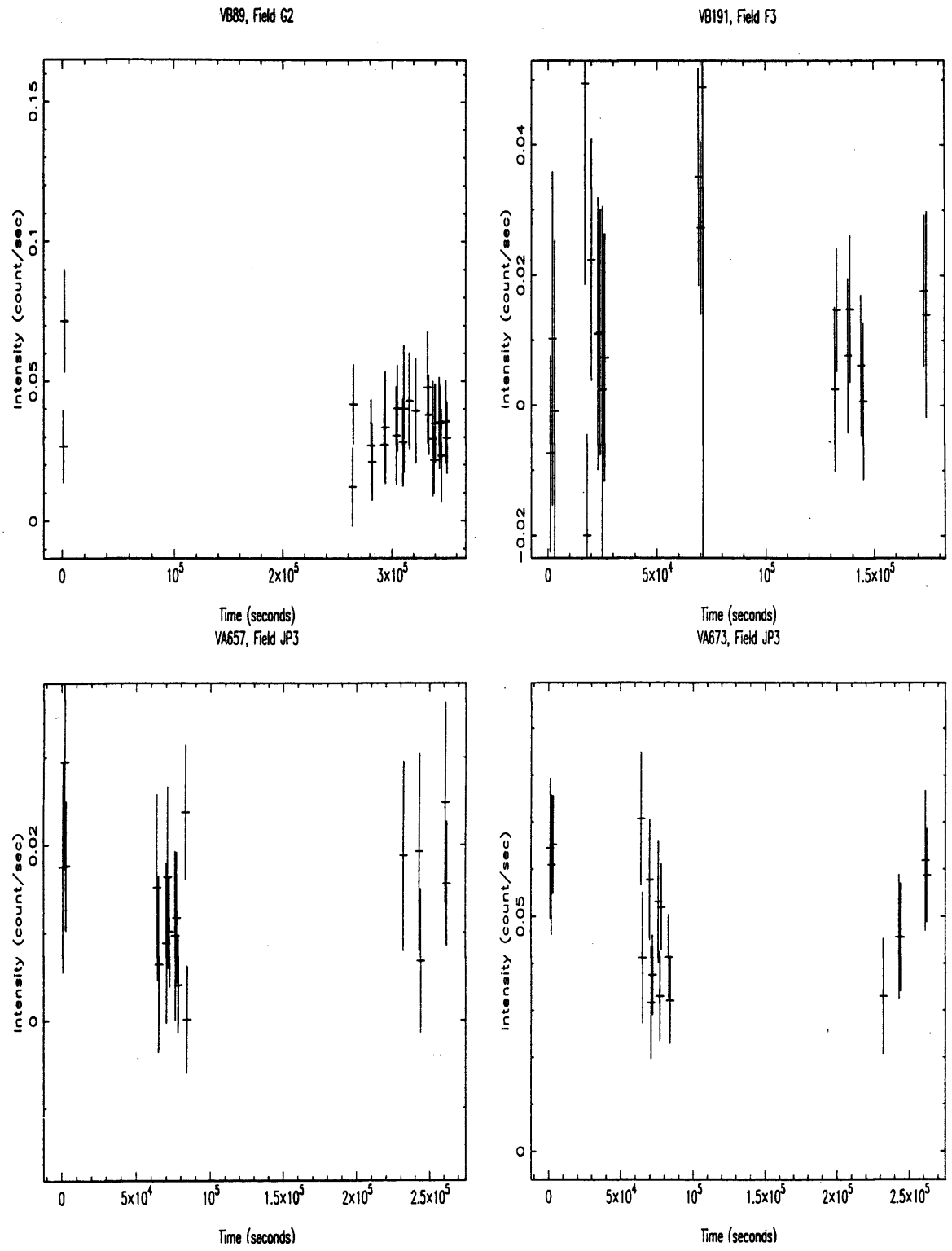

Figure B.23: Hyades PSPC pointed survey lightcurves (see main text).

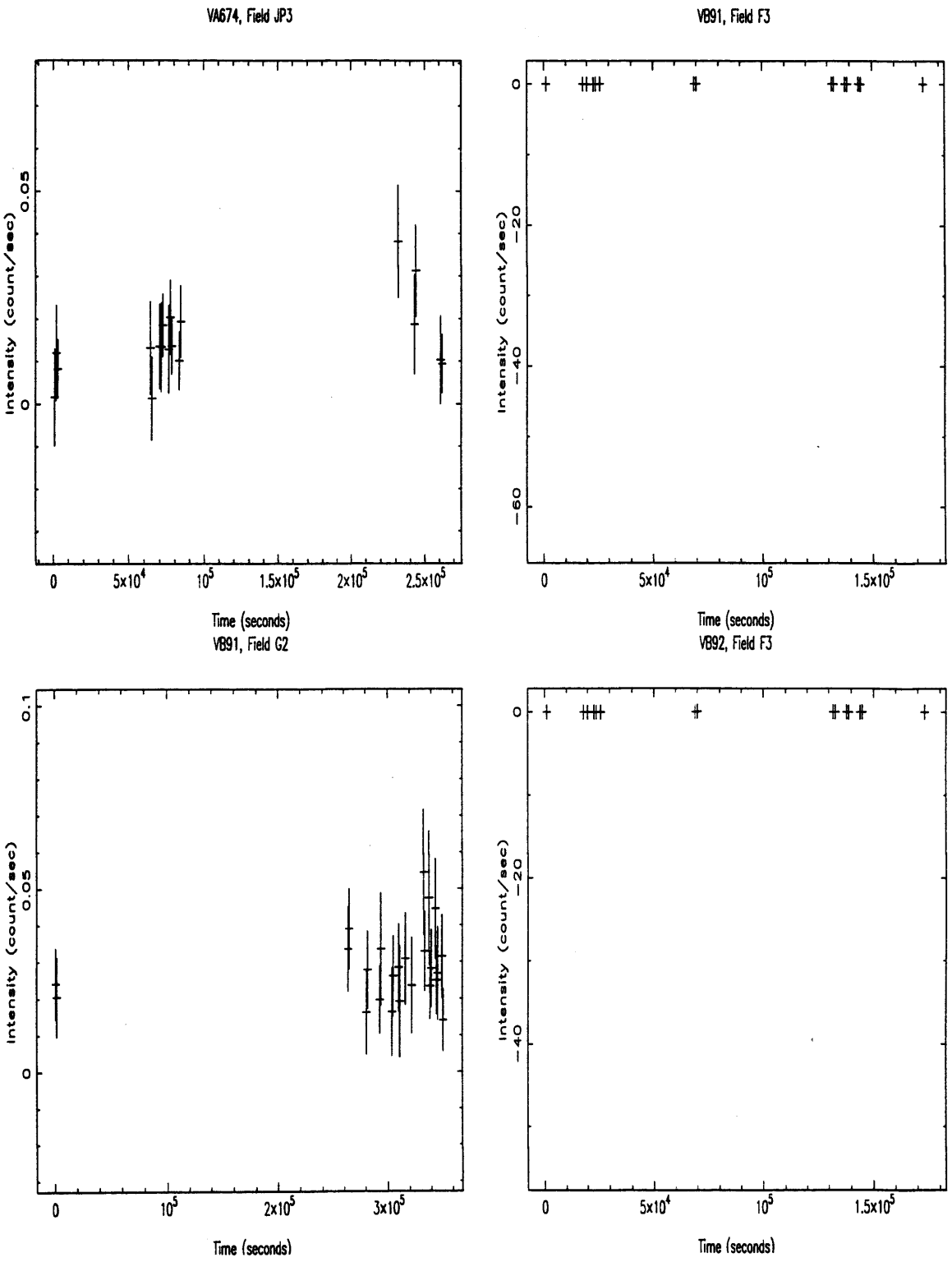

Figure B.24: Hyades PSPC pointed survey lightcurves (see main text).

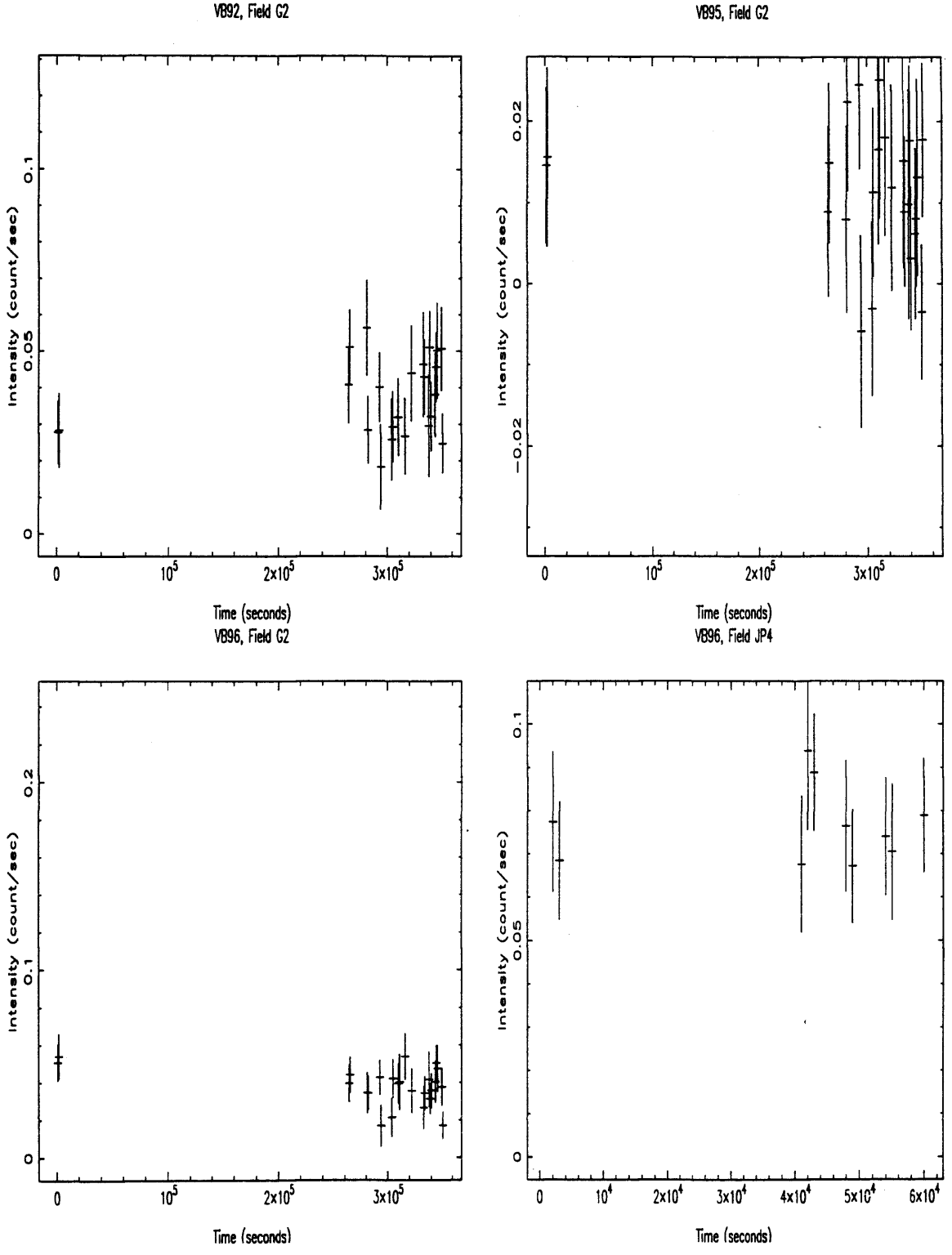

Figure B.25: Hyades PSPC pointed survey lightcurves (see main text).

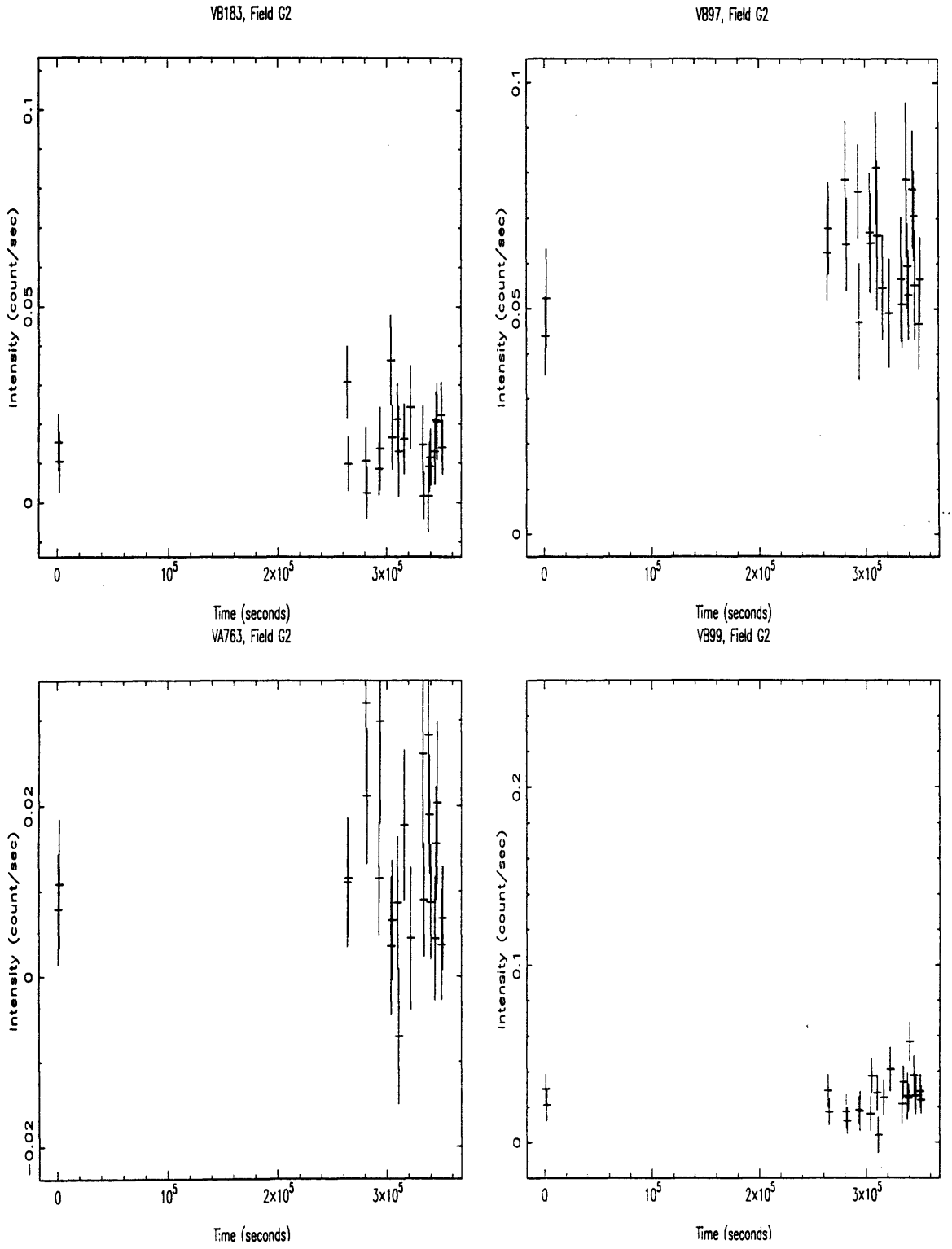

Figure B.26: Hyades PSPC pointed survey lightcurves (see main text).

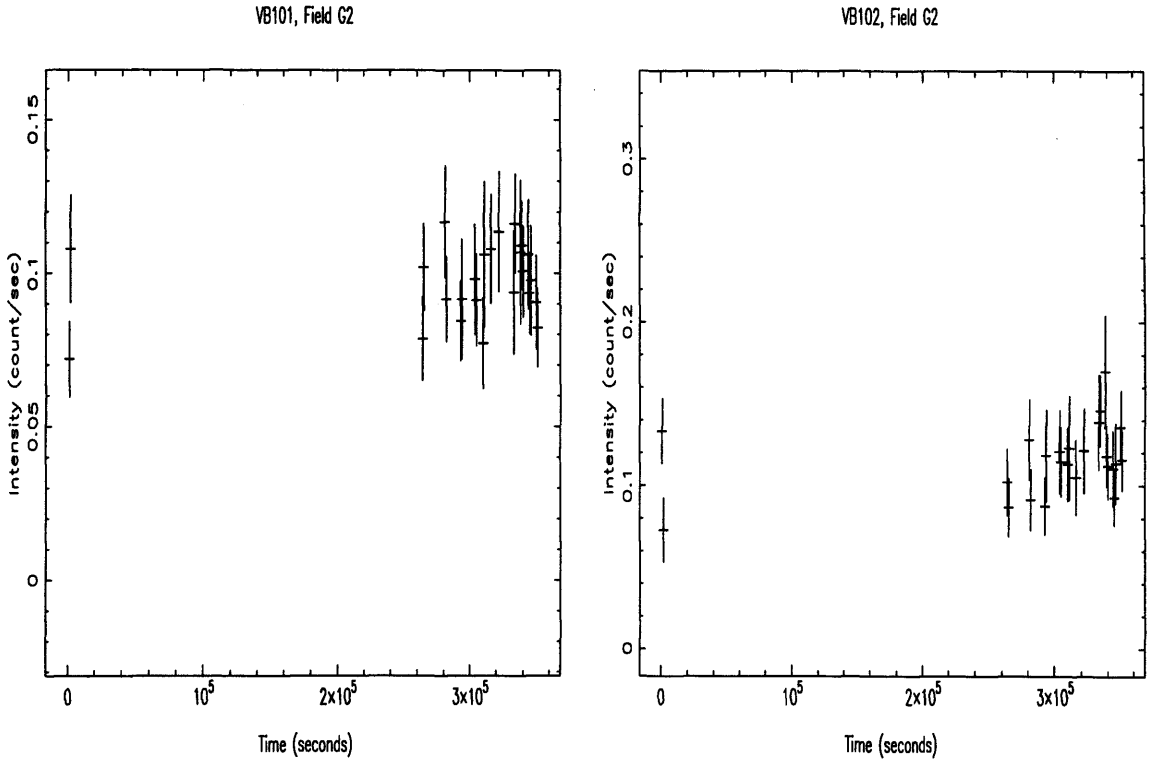

Figure B.27: Hyades PSPC pointed survey lightcurves (see main text).

Appendix C

Hyades PSPC Pointed Survey Source Information

The following pages contain details on the optical and x-ray properties of the stars in the Hyades survey. Optical properties are given for all Hyads and non-Hyads separately, as are x-ray properties. Where no x-ray detection was made of a Hyad, the upper-limits are given.

Table 1. Hyades members in the *ROSAT* PSPC fields: optical properties

Name (1)	VB (2)	VA (3)	H (4)	RA (J2000) (5)	Dec (J2000) (6)	m_V (7)	$B-V$ (8)	Bi (9)	P_{bin} (10)	$v \sin i$ (11)	P_{rot} (12)	Notes
HZ2,EG31,				04 12 44.10	+11 52 01.4	13.86	-0.05	0	0.0	0	0.0	
VB 18	18	60	105	04 14 26.80	+12 26 07.0	8.06	0.64	0	0.0	0	0.0	
VA 68		68	111	04 14 51.50	+13 03 17.0	10.74	1.24	3	0.0	<10	> 3.6	
VA 112		112	169	04 17 39.10	+12 24 54.0	15.34	1.88	0	0.0	0	0.0	
VA 115		115	172	04 17 47.20	+13 39 41.0	12.56	1.47	0	0.0	0	0.0	
VA 118		118	173	04 17 51.00	+15 13 39.0	15.11	1.57	0	0.0	0	0.0	
VA 122		122	176	04 17 55.20	+14 32 47.0	15.00	1.63	0	0.0	0	0.0	
VB 23	23	123	178	04 18 01.40	+18 15 26.0	7.54	0.68	3	75.7	0	0.0	
VA 127		127	181	04 18 08.40	+17 24 60.0	15.90	1.63	0	0.0	0	0.0	
VB 25	25	133	185	04 18 19.00	+16 05 18.0	9.60	0.99	0	0.0	<10	12.6	
VA 135		135	187	04 18 21.50	+17 25 21.0	10.00	1.17	3	0.0	0	0.0	
VA 146		146	192	04 18 45.50	+13 22 13.0	11.99	1.42	0	0.0	<10	> 3.0	
VB 27	27	156	198	04 19 07.60	+17 31 29.0	8.46	0.71	0	0.0	0	0.0	
VA 162		162	203	04 19 20.00	+14 18 59.0	12.81	1.48	0	0.0	0	0.0	
VA 162		162	203	04 19 20.00	+14 18 59.0	12.81	1.48	0	0.0	0	0.0	
VB 28	28	175		04 19 47.50	+15 37 39.0	3.66	0.99	0	0.0	0	0.0	
VB 30	30	182	213	04 19 56.70	+14 02 07.0	5.59	0.28	3	0.0	0	0.0	
VB 30	30	182	213	04 19 56.70	+14 02 07.0	5.59	0.28	3	0.0	0	0.0	
VB 32	32			04 20 24.10	+18 44 35.0	6.11	0.37	3	0.0	0	0.0	
VB 33	33			04 20 35.90	+15 05 44.0	5.26	0.22	0	0.0	0	0.0	
VB 33	33			04 20 35.90	+15 05 44.0	5.26	0.22	0	0.0	0	0.0	
VB 34	34	201	230	04 20 52.50	+13 51 52.0	6.17	0.46	3	3.1	12	3.1	
VB 34	34	201	230	04 20 52.50	+13 51 52.0	6.17	0.46	3	3.1	12	3.1	
VA 203		203	232	04 20 55.50	+14 51 36.0	16.43	1.65	0	0.0	0	0.0	
VA 203		203	232	04 20 55.50	+14 51 36.0	16.43	1.65	0	0.0	0	0.0	
VB 36	36			04 21 31.80	+18 25 05.0	6.80	0.44	0	0.0	0	0.0	
VB 37	37	215	246	04 21 34.20	+14 24 35.0	6.61	0.41	0	0.0	0	0.0	
VB 37	37	215	246	04 21 34.20	+14 24 35.0	6.61	0.41	0	0.0	0	0.0	
VA 216		216	247	04 21 34.50	+14 41 44.0	15.64	1.50	0	0.0	0	0.0	
VA 213		213	242	04 21 34.90	+16 53 42.0	14.97	1.55	0	0.0	0	0.0	
VB 38	38	229	257	04 22 02.80	+14 04 38.0	5.72	0.32	3	2.1	0	0.0	
VB 38	38	229	257	04 22 02.80	+14 04 38.0	5.72	0.32	3	2.1	0	0.0	
VA 242		242	266	04 22 39.70	+18 16 04.0	13.01	1.51	0	0.0	0	0.0	
VA 242		242	266	04 22 39.70	+18 16 04.0	13.01	1.51	0	0.0	0	0.0	
VB 39	39	248	270	04 22 43.90	+16 47 28.0	7.86	0.68	3	2500.0	0	0.0	
VB 40	40	249	271	04 22 44.00	+15 03 23.0	6.99	0.56	3	4.0	8	4.0	
VB 40	40	249	271	04 22 44.00	+15 03 23.0	6.99	0.56	3	4.0	8	4.0	
VB 41	41	256		04 22 55.80	+17 32 34.0	3.77	0.98	3	529.8	0	0.0	
H 282			282	04 22 59.00	+13 18 57.0	13.65	1.65	0	0.0	0	0.0	
VA 260		260	280	04 23 00.90	+15 13 43.0	16.71	1.66	0	0.0	0	0.0	
VA 260		260	280	04 23 00.90	+15 13 43.0	16.71	1.66	0	0.0	0	0.0	
VA 262		262	284	04 23 11.90	+15 42 48.0	15.48	1.66	0	0.0	0	0.0	
VA 262		262	284	04 23 11.90	+15 42 48.0	15.48	1.66	0	0.0	0	0.0	
VA 262		262	284	04 23 11.90	+15 42 48.0	15.48	1.66	0	0.0	0	0.0	
VA 275		275	291	04 23 23.30	+14 25 43.0	14.95	1.56	0	0.0	0	0.0	
VA 275		275	291	04 23 23.30	+14 25 43.0	14.95	1.56	0	0.0	0	0.0	
VA 275		275	291	04 23 23.30	+14 25 43.0	14.95	1.56	0	0.0	0	0.0	
VB 173	173	276	290	04 23 24.80	+15 45 49.0	10.52	1.27	0	0.0	0	14.1	
VB 173	173	276	290	04 23 24.80	+15 45 49.0	10.52	1.27	0	0.0	0	14.1	
VB 45	45	272	288	04 23 24.90	+16 46 39.0	5.64	0.30	3	8.4	0	0.0	

Table 1. *continued*

Name (1)	VB (2)	VA (3)	H (4)	RA (J2000) (5)	Dec (J2000) (6)	m_V (7)	$B-V$ (8)	Bi (9)	$P_{\rm bin}$ (10)	$v \sin i$ (11)	$P_{\rm rot}$ (12)	Notes
VB 46	46	279	292	04 23 31.50	+14 40 14.0	9.11	0.87	0	0.0	0	0.0	
VB 46	46	279	292	04 23 31.50	+14 40 14.0	9.11	0.87	0	0.0	0	0.0	
VA 282		282	294	04 23 42.30	+15 52 53.0	14.83	1.39	0	0.0	0	0.0	
VA 282		282	294	04 23 42.30	+15 52 53.0	14.83	1.39	0	0.0	0	0.0	
VA 288		288	296	04 23 49.80	+14 55 17.0	13.33	1.54	3	0.0	14	1.8	
VA 288		288	296	04 23 49.80	+14 55 17.0	13.33	1.54	3	0.0	14	1.8	
VA 294		294	299	04 23 53.90	+14 03 05.0	10.88	1.31	0	0.0	<10	> 4.0	
VA 292		292	298	04 23 55.50	+16 21 17.0	14.28	-0.01	0	0.0	0	0.0	
VA 292		292	298	04 23 55.50	+16 21 17.0	14.28	-0.01	0	0.0	0	0.0	
VA 297		297	300	04 23 59.10	+16 43 29.0	12.55	1.47	0	0.0	<10	> 2.8	
VB 47	47	301		04 24 05.70	+17 26 39.0	4.80	0.16	0	0.0	0	0.0	
VB 47	47	301		04 24 05.70	+17 26 39.0	4.80	0.16	0	0.0	0	0.0	
VB 50	50	308	308	04 24 11.70	+14 45 30.0	7.62	0.60	3	0.0	0	7.1	
VB 50	50	308	308	04 24 11.70	+14 45 30.0	7.62	0.60	3	0.0	0	7.1	
VB 49	49		307	04 24 12.50	+16 22 45.0	8.24	0.58	0	0.0	0	0.0	
VB 49	49		307	04 24 12.50	+16 22 45.0	8.24	0.58	0	0.0	0	0.0	
VB 174	174	310	312	04 24 16.40	+18 00 10.0	9.99	1.06	0	0.0	0	0.0	
VB 51	51	315	316	04 24 22.30	+17 04 45.0	6.97	0.44	0	0.0	0	0.0	
VA 321		321	321	04 24 28.00	+15 53 03.0	14.98	1.70	0	0.0	0	0.0	
VA 321		321	321	04 24 28.00	+15 53 03.0	14.98	1.70	0	0.0	0	0.0	
VB 52	52	319	320	04 24 28.10	+16 53 10.0	7.80	0.60	3	0.0	8	8.0	
VA 334		334	336	04 24 48.60	+15 52 26.0	11.65	1.42	3	5500.0	0	0.0	
VA 334		334	336	04 24 48.60	+15 52 26.0	11.65	1.42	3	5500.0	0	0.0	
VB 175	175	342	342	04 25 00.20	+16 59 07.0	10.27	1.04	0	0.0	<10	11.9	
VA 351		351	346	04 25 11.80	+17 16 24.0	13.21	1.53	2	0.0	0	0.0	
VA 352		352	348	04 25 15.90	+16 18 09.0	16.27	1.66	0	0.0	0	0.0	
VA 352		352	348	04 25 15.90	+16 18 09.0	16.27	1.66	0	0.0	0	0.0	
VB 57	57	360	357	04 25 37.10	+15 56 28.0	6.46	0.49	3	1900.0	15	2.7	
VA 362		362	360	04 25 46.40	+17 32 42.0	15.32	1.49	0	0.0	0	0.0	
VA 368		368	366	04 25 49.90	+15 00 10.0	14.96	1.97	0	0.0	0	0.0	
VA 382		382	376	04 26 03.70	+17 07 17.0	15.11	1.52	0	0.0	0	0.0	
VA 383		383	378	04 26 04.40	+15 02 32.0	12.19	1.46	0	0.0	<10	> 3.2	
VB 59	59	384	379	04 26 05.60	+15 31 28.0	7.49	0.54	3	2500.0	< 6	5.0	
VB 59	59	384	379	04 26 05.60	+15 31 28.0	7.49	0.54	3	2500.0	< 6	5.0	
VB 141	141	388		04 26 20.70	+15 37 06.0	4.48	0.25	3	0.0	0	0.0	
VB 141	141	388		04 26 20.70	+15 37 06.0	4.48	0.25	3	0.0	0	0.0	
VB 63	63	389	382	04 26 24.10	+16 51 12.0	8.06	0.63	3	2500.0	7	7.7	
VB 64	64	400	388	04 26 40.00	+16 44 49.0	8.12	0.66	0	0.0	5	8.7	
VA 420		420	401	04 27 15.60	+17 14 34.0	13.05	1.48	0	0.0	0	0.0	
VB 65	65	446	415	04 27 35.70	+15 35 21.0	7.42	0.54	0	0.0	9	5.9	
VB 65	65	446	415	04 27 35.70	+15 35 21.0	7.42	0.54	0	0.0	9	5.9	
VB 65	65	446	415	04 27 35.70	+15 35 21.0	7.42	0.54	0	0.0	9	5.9	
VB 189	189	475	422	04 28 10.80	+16 28 18.0	11.08	1.36	0	0.0	0	0.0	
VB 189	189	475	422	04 28 10.80	+16 28 18.0	11.08	1.36	0	0.0	0	0.0	
VB 71	71	489		04 28 34.20	+15 57 45.0	3.85	0.95	3	5760.0	0	0.0	
VB 71	71	489		04 28 34.20	+15 57 45.0	3.85	0.95	3	5760.0	0	0.0	
VA 490		490	435	04 28 38.40	+16 58 16.0	14.02	-0.10	0	0.0	0	0.0	
VB 72	72	491		04 28 39.10	+15 52 16.0	3.41	0.18	3	140.7	0	0.0	
VB 72	72	491		04 28 39.10	+15 52 16.0	3.41	0.18	3	140.7	0	0.0	
VB 73	73	495	439	04 28 47.70	+17 17 09.0	7.85	0.61	0	0.0	7	7.5	

Table 1. *continued*

Name (1)	VB (2)	VA (3)	H (4)	RA (J2000) (5)	Dec (J2000) (6)	m_V (7)	$B-V$ (8)	Bi (9)	P_{bin} (10)	$v \sin i$ (11)	P_{rot} (12)	Notes
VB 190	190	500	441	04 28 50.60	+16 17 21.0	10.70	1.31	3	5400.0	0	3.7	
VB 190	190	500	441	04 28 50.60	+16 17 21.0	10.70	1.31	3	5400.0	0	3.7	
VA 502		502	442	04 28 51.20	+15 58 45.0	11.97	1.42	0	0.0	<10	> 2.9	
VA 502		502	442	04 28 51.20	+15 58 45.0	11.97	1.42	0	0.0	<10	> 2.9	
VB 75	75	511	448	04 28 59.40	+16 09 33.0	6.59	0.53	3	0.0	0	0.0	
VB 75	75	511	448	04 28 59.40	+16 09 33.0	6.59	0.53	3	0.0	0	0.0	
VA 512		512	449	04 28 59.60	+16 20 51.0	14.28	1.52	0	0.0	0	0.0	
VA 512		512	449	04 28 59.60	+16 20 51.0	14.28	1.52	0	0.0	0	0.0	
VA 529		529	456	04 29 12.00	+15 16 44.0	12.42	1.48	0	0.0	0	0.0	
VB 77	77	536	461	04 29 20.10	+17 32 43.0	7.05	0.50	3	238.9	25	2.4	
VB 78	78	544	469	04 29 29.40	+17 51 49.0	6.92	0.45	0	0.0	0	0.0	
VB 181	181	548	472	04 29 30.50	+16 14 43.0	10.34	1.15	0	0.0	<10	11.9	
VB 79	79	547	470	04 29 31.50	+17 53 37.0	8.96	0.83	0	0.0	0	0.0	
VA 575		575	484	04 30 23.50	+17 30 00.0	14.44	1.33	0	0.0	0	0.0	
VB 82	82	584		04 30 33.50	+16 11 39.0	4.78	0.17	1	0.0	0	0.0	
GH7-246				04 30 33.80	+14 44 50.0	14.68	1.56	0	0.0	0	0.0	
VB 182	182	587	491	04 30 35.00	+15 44 02.0	9.01	0.84	3	358.4	0	0.0	
VB 83	83	589	493	04 30 38.90	+15 41 31.0	5.48	0.26	0	0.0	0	0.0	
VB 85	85	597	496	04 30 46.50	+16 08 56.0	6.51	0.43	3	0.0	0	0.0	
VA 610		610	500	04 31 10.50	+16 23 46.0	14.66	1.57	0	0.0	0	0.0	
VA 622		622	505	04 31 28.30	+17 43 11.0	11.91	1.44	0	0.0	<10	> 3.3	
VB 88	88	625	507	04 31 28.90	+13 54 13.0	7.78	0.54	0	0.0	0	0.0	
VA 627		627	509	04 31 36.30	+17 42 34.0	9.53	0.99	3	844.6	0	0.0	
VA 637		637	513	04 31 43.20	+15 02 28.0	12.28	1.48	0	0.0	0	0.0	
VA 637		637	513	04 31 43.20	+15 02 28.0	12.28	1.48	0	0.0	0	0.0	
VA 637		637	513	04 31 43.20	+15 02 28.0	12.28	1.48	0	0.0	0	0.0	
VA 638		638	514	04 31 43.90	+15 37 34.0	12.17	1.46	3	0.0	0	0.0	
VA 638		638	514	04 31 43.90	+15 37 34.0	12.17	1.46	3	0.0	0	0.0	
VB 89	89	644	516	04 31 51.20	+15 51 06.0	6.02	0.34	3	0.0	0	0.0	
VB 89	89	644	516	04 31 51.20	+15 51 06.0	6.02	0.34	3	0.0	0	0.0	
VB 191	191	645	517	04 31 51.80	+15 29 57.0	11.07	1.30	0	0.0	<10	> 3.8	
VB 191	191	645	517	04 31 51.80	+15 29 57.0	11.07	1.30	0	0.0	<10	> 3.8	
VB 191	191	645	517	04 31 51.80	+15 29 57.0	11.07	1.30	0	0.0	<10	> 3.8	
VA 657		657	521	04 32 07.50	+17 39 54.0	14.77	1.47	0	0.0	0	0.0	
VA 673		673	528	04 32 23.40	+17 45 07.0	13.97	0.33	3	0.6	0	0.0	
VA 674		674	530	04 32 28.60	+17 54 18.0	14.80	1.55	0	0.0	0	0.0	
VB 91	91	684	544	04 32 49.40	+16 00 21.0	8.94	0.88	3	5500.0	0	9.4	
VB 91	91	684	544	04 32 49.40	+16 00 21.0	8.94	0.88	3	5500.0	0	9.4	
VB 92	92	692	554	04 32 59.20	+15 49 09.0	8.66	0.74	0	0.0	0	9.0	
VB 92	92	692	554	04 32 59.20	+15 49 09.0	8.66	0.74	0	0.0	0	9.0	
VB 93	93	712	568	04 33 37.30	+16 45 45.0	9.40	0.88	0	0.0	0	0.0	
VB 95	95	725		04 33 50.10	+14 50 41.0	4.66	0.24	3	488.5	0	0.0	
VB 95	95	725		04 33 50.10	+14 50 41.0	4.66	0.24	3	488.5	0	0.0	
VA 726		726	577	04 33 56.40	+16 52 10.0	15.08	1.58	0	0.0	0	0.0	
VB 96	96	727	578	04 33 58.40	+15 09 50.0	8.51	0.84	3	4700.0	0	0.0	
VB 96	96	727	578	04 33 58.40	+15 09 50.0	8.51	0.84	3	4700.0	0	0.0	
VA 731		731	581	04 34 03.70	+14 12 48.0	12.33	1.44	0	0.0	0	0.0	
VB 183	183	747	597	04 34 30.20	+15 50 07.0	9.69	0.91	0	0.0	0	0.0	
VB 97	97	748	598	04 34 34.80	+15 30 17.0	7.94	0.63	0	0.0	0	8.8	
VA 763		763	606	04 35 28.00	+15 23 59.0	14.61	2.54	0	0.0	0	0.0	

Table 1. *continued*

Name (1)	VB (2)	VA (3)	H (4)	RA (J2000) (5)	Dec (J2000) (6)	m_V (7)	$B-V$ (8)	Bi (9)	$P_{\rm bin}$ (10)	$v \sin i$ (11)	$P_{\rm rot}$ (12)	Notes
VB 99	99	778	617	04 36 05.10	+15 41 03.0	9.38	0.85	0	0.0	0	0.0	
VB 101	101			04 36 40.30	+15 52 10.0	6.65	0.43	2	0.0	0	0.0	
VB 102	102			04 37 31.50	+15 08 47.0	7.54	0.60	3	720.0	0	0.0	

Key: (1) star name used,(2) van Bueren (1952) catalogue name, (3) van Altena (1969) catalogue name,(4) Hanson (1975) catalogue name, (5) RA (h m s), (6) DEC (d m s), (7) visual magnitude, (8) B-V colour, (9) Binarity flag (3=definate binary, 2=probable binary, 1=possible binary, 0=no evidence for binarity), (10) binary period, (11) km s^{-1}, (12) rotation period. System parameters courtesy of T. Simon (private communication with J.P. Pye.).

Table 2. Hyades probable non-members in the *ROSAT* PSPC fields: optical properties

Name (1)	VB (2)	VA (3)	H (4)	RA (J2000) (5)	Dec (J2000) (6)	m_V (7)	$B-V$ (8)	Bi (9)	P_{bin} (10)	$v \sin i$ (11)	P_{rot} (12)	Notes
VA 47		47	74	04 12 31.90	+12 00 26.0	11.81	0.64	0	0.0	0	0.0	
VA125AB		125AB		04 18 03.30	+15 31 43.0	11.25	1.29	0	0.0	0	0.0	
VA 131		131	183	04 18 12.40	+16 05 55.0	15.90	1.67	0	0.0	0	0.0	
LP414-158				04 18 33.60	+18 21 56.0	16.09	-9.00	0	0.0	0	0.0	
H196			196	04 18 57.70	+15 08 57.0	16.27	1.74	0	0.0	0	0.0	
H196			196	04 18 57.70	+15 08 57.0	16.27	1.74	0	0.0	0	0.0	
VA 191		191	220	04 20 19.70	+17 30 43.0	12.16	1.08	0	0.0	0	0.0	
LP415-543				04 20 27.30	+18 53 49.0	15.34	1.76	0	0.0	0	0.0	
VA 200		200	229	04 20 47.10	+15 14 11.0	13.85	1.58	0	0.0	0	0.0	
VA 200		200	229	04 20 47.10	+15 14 11.0	13.85	1.58	0	0.0	0	0.0	
VA 211		211	241	04 21 30.90	+14 26 00.0	14.08	1.39	0	0.0	0	0.0	
VA 211		211	241	04 21 30.90	+14 26 00.0	14.08	1.39	0	0.0	0	0.0	
H 264			264	04 22 30.30	+15 13 10.3	14.64	0.84	0	0.0	0	0.0	
H 264			264	04 22 30.30	+15 13 10.3	14.64	0.84	0	0.0	0	0.0	
H 264			264	04 22 30.30	+15 13 10.3	14.64	0.84	0	0.0	0	0.0	
VA 241		241	265	04 22 32.20	+15 51 27.0	14.89	1.73	0	0.0	0	0.0	
VA 241		241	265	04 22 32.20	+15 51 27.0	14.89	1.73	0	0.0	0	0.0	
VA 247		247	269	04 22 40.20	+15 03 46.2	15.47	0.95	0	0.0	0	0.0	
VA 247		247	269	04 22 40.20	+15 03 46.2	15.47	0.95	0	0.0	0	0.0	
VB 172	172	250	272	04 22 44.20	+14 15 22.0	10.15	0.66	0	0.0	0	0.0	
VB 172	172	250	272	04 22 44.20	+14 15 22.0	10.15	0.66	0	0.0	0	0.0	
VA 265		265	285	04 23 16.30	+17 00 42.0	15.90	1.48	0	0.0	0	0.0	
VA 265		265	285	04 23 16.30	+17 00 42.0	15.90	1.48	0	0.0	0	0.0	
VA 305		305	303	04 24 09.00	+15 05 19.0	15.11	1.74	0	0.0	0	0.0	
VA 305		305	303	04 24 09.00	+15 05 19.0	15.11	1.74	0	0.0	0	0.0	
VA 306		306	304	04 24 09.80	+15 28 35.0	14.58	1.64	0	0.0	0	0.0	
VA 306		306	304	04 24 09.80	+15 28 35.0	14.58	1.64	0	0.0	0	0.0	
VA 329		329	330	04 24 37.90	+15 54 36.0	14.81	1.60	0	0.0	0	0.0	
VA 329		329	330	04 24 37.90	+15 54 36.0	14.81	1.60	0	0.0	0	0.0	
VA 366		366	363	04 25 48.60	+15 31 18.0	12.38	1.45	3	0.0	0	0.0	
VA 366		366	363	04 25 48.60	+15 31 18.0	12.38	1.45	3	0.0	0	0.0	
VA 380		380	374	04 26 00.90	+17 16 53.0	13.73	0.87	0	0.0	0	0.0	
VA 413		413	397	04 27 01.50	+15 22 26.0	11.05	1.02	0	0.0	0	0.0	
VA 413		413	397	04 27 01.50	+15 22 26.0	11.05	1.02	0	0.0	0	0.0	
VA 413		413	397	04 27 01.50	+15 22 26.0	11.05	1.02	0	0.0	0	0.0	
VB 188	188	444	413	04 27 32.50	+15 21 45.0	11.07	0.81	0	0.0	0	0.0	
VB 188	188	444	413	04 27 32.50	+15 21 45.0	11.07	0.81	0	0.0	0	0.0	
VB 188	188	444	413	04 27 32.50	+15 21 45.0	11.07	0.81	0	0.0	0	0.0	
VA 478		478	423	04 28 14.20	+16 39 11.0	15.38	1.09	0	0.0	0	0.0	
VB 80	80	569	481	04 30 07.90	+15 38 17.0	5.58	0.32	3	0.0	0	0.0	
VA 578		578	485	04 30 24.70	+17 47 12.0	10.76	0.87	0	0.0	0	0.0	
H495			495	04 30 41.90	+14 39 43.0	16.32	1.97	0	0.0	0	0.0	
H 588			588	04 34 18.30	+14 58 31.0	7.22	1.13	0	0.0	0	0.0	
H 588			588	04 34 18.30	+14 58 31.0	7.22	1.13	0	0.0	0	0.0	
VA 750		750	601	04 34 39.50	+15 12 34.0	12.41	1.45	3	0.0	0	0.0	
VA 750		750	601	04 34 39.50	+15 12 34.0	12.41	1.45	3	0.0	0	0.0	
VA 751		751	600	04 34 41.80	+17 44 55.0	7.75	0.65	0	0.0	0	0.0	

Key: (1) star name used,(2) van Bueren (1952) catalogue name, (3) van Altena (1969) catalogue name,(4) Hanson (1975) catalogue name, (5) RA (h m s), (6) DEC (d m s), (7) visual magnitude, (8) B-V colour, (9) Binarity flag (3=definate binary. 2=probable binary, 1=possible binary, 0=no evidence for binarity), (10) binary period, (11) km s^{-1}. (12) rotation period. System parameters courtesy of T. Simon (private communication with J.P. Pye.).

Table 3. Non-Hyad, catalogued objects in the *ROSAT* PSPC fields: optical properties

Name (1) (7)	RA (J2000) (2)	Dec (J2000) (3)	m_V (4)	m_B (5)	Spec. type (6)
HD 26749	4 14 17.10	+12 20 56.0	6.90	7.60	G2V
SAO 93855	4 18 38.60	+17 50 30.0	8.90	9.60	G0
P NTTS 041559+1716	4 18 51.60	+17 23 15.0	0.00	0.00	
HBC 376	4 18 54.00	+17 22 60.0	12.28	13.41	K7
HD 27296	4 19 9.00	+13 43 16.0	7.76	8.10	F2
HD 27296	4 19 9.00	+13 43 16.0	7.76	8.10	F2
HD 285639	4 20 49.70	+18 35 1.0	0.00	10.10	K5
HD 286678	4 21 14.00	+13 40 24.0	0.00	9.50	G0
HD 285739	4 23 33.00	+17 2 42.0	0.00	10.00	K0
HD 285751	4 23 42.00	+15 37 36.0	0.00	10.00	G5
HD 285751	4 23 42.00	+15 37 36.0	0.00	10.00	G5
HD 285812	4 25 30.60	+15 32 30.0	9.80	10.90	K0
HD 285819	4 25 36.00	+15 11 0.0	0.00	10.00	K0
HD 285819	4 25 36.00	+15 11 0.0	0.00	10.00	K0
HD 28007	4 25 53.20	+17 26 52.0	7.80	7.80	F2V
HD 28124	4 26 51.00	+17 1 45.0	7.10	8.00	K5V
HD 285808	4 27 36.90	+16 1 49.0	10.40	10.90	F5
HD 285808	4 27 36.90	+16 1 49.0	10.40	10.90	F5
HD 28227	4 27 51.60	+15 9 10.0	9.90	10.60	G5
HD 28448	4 29 51.60	+17 4 50.0	8.90	9.50	F8
HD 28448	4 29 51.60	+17 4 50.0	8.90	9.50	F8
HD 28528	4 30 33.50	+14 46 51.0	9.20	9.30	G0
HD 285845	4 31 26.00	+18 16 18.0	0.00	10.36	G6
P NTTS 042835+1700	4 31 27.10	+17 6 25.0	0.00	0.00	
P NTTS 042916+1751	4 32 9.40	+17 57 25.0	0.00	0.00	
NAME FK 1	4 32 15.00	+18 1 42.0	11.60	12.91	K7V
EQ 042921+175524	4 32 15.00	+18 1 42.0	12.15	13.52	K8
V* V826 TAU	4 32 15.00	+18 1 42.0	12.11	13.51	K7
1E 0429.3+1755	4 32 15.00	+18 1 24.0	0.00	0.00	
EQ 042923+181354	4 32 17.00	+18 20 12.0	12.21	13.59	K8
V* V827 TAU	4 32 17.00	+18 20 12.0	12.18	13.58	K7
NAME FK 2	4 32 17.00	+18 20 12.0	11.80	13.11	K7V
1E 0429.3+1813	4 32 17.00	+18 19 30.0	0.00	0.00	
V* GG TAU	4 32 30.00	+17 31 42.0	12.34	13.72	K6V:E
EM* AS 83	4 32 30.00	+17 30 60.0	0.00	11.00	
P NTTS 042950+1757	4 32 43.80	+18 2 58.0	0.00	0.00	
HR 1442	4 33 32.80	+18 1 1.0	6.25	6.32	B9IVN
V* TY TAU	4 34 43.00	+15 15 60.0	11.50	0.00	K0
HBC 412	4 35 24.00	+17 52 0.0	14.12	15.68	M2
HD 29247	4 36 54.80	+15 15 42.0	7.20	7.90	G0

Key: (1) star name, (2)RA (h m s), (3) DEC (d m s), (4) visual magnitude, (5) bolometric magnitude, (6) spectral type. System parameters courtesy of T. Simon (private communication with J.P. Pye.).

Table 4. Hyades members in the *ROSAT* PSPC fields: X-ray properties

Name (1)	Seq. (2)	Xnr (3)	RA (J2000) (4)	Dec (J2000) (5)	Sep. (6)	D/U (7)	ct/ks (8)	err. (9)	L_X (10)	err. (11)	Off. (12)	Rib (13)	* (14)	IPC? (15)
HZ2,EG31,	201748	238	04 12 44.11	+11 52 01.6	0.00	-1	9.3	0.0	1.34	0.00	42.5	1	*	
VB 18	201748	230	04 14 27.47	+12 26 12.4	0.19	0	62.4	2.1	9.05	0.31	0.3	0	*	
VA 68	201748	229	04 14 51.56	+13 03 24.2	0.12	0	20.7	2.1	3.01	0.30	37.5	0	*	
VA 112	201748	232	04 17 42.79	+12 24 47.8	0.91	0	18.7	3.7	2.72	0.53	48.0	0	*	
VA 115	200776	11	04 17 47.14	+13 40 18.0	0.62	0	16.2	2.5	2.34	0.37	46.5	0	*	
VA 118	200775	363	04 17 51.00	+15 13 39.0	0.00	-1	14.1	0.0	2.04	0.00	37.1	0	*	EU
VA 122	200441	248	04 17 54.75	+14 33 47.0	1.00	0	19.0	5.2	2.75	0.76	48.4	0	*	EU
VB 23	201370	120	04 18 04.01	+18 15 06.7	0.70	0	109.7	7.6	15.91	1.11	50.2	0	*	
VA 127	200442	298	04 18 08.40	+17 25 00.1	0.00	-1	55.0	0.0	7.97	0.00	44.3	1	*	EU
VB 25	200775	348	04 18 17.79	+16 05 31.6	0.37	0	26.2	4.3	3.80	0.62	35.2	0	*	
VA 135	200442	285	04 18 21.38	+17 25 06.3	0.25	0	112.5	4.7	16.31	0.68	41.2	1	*	ED
VA 146	200776	25	04 18 45.50	+13 22 13.1	0.00	-1	15.6	0.0	2.26	0.00	42.6	1	*	
VB 27	200442	283	04 19 08.28	+17 31 36.5	0.20	0	34.9	2.4	5.06	0.35	29.5	1	*	ED
VA 162	200776	18	04 19 19.99	+14 18 59.0	0.00	-1	8.0	0.0	1.17	0.00	35.4	1		EU
VA 162	200441	272	04 19 19.99	+14 18 59.0	0.00	-1	7.0	0.0	1.01	0.00	35.6	1	*	EU
VB 28	200775	350	04 19 47.70	+15 37 36.9	0.06	0	392.0	10.7	56.83	1.55	0.2	0	*	ED
VB 30	200776	8	04 19 57.63	+14 02 45.4	0.68	0	96.2	2.3	13.95	0.33	17.4	1	*	EU
VB 30	200441	252	04 19 56.64	+14 02 28.5	0.36	0	89.4	6.3	12.96	0.91	43.5	0		EU
VB 32	201370	117	04 20 25.75	+18 44 26.8	0.41	0	104.9	4.6	15.21	0.67	24.7	1	*	
VB 33	200441	261	04 20 35.90	+15 05 44.2	0.00	-1	5.7	0.0	0.83	0.00	25.3	0	*	EU
VB 33	200775	365	04 20 35.90	+15 05 44.2	0.00	-1	10.0	0.0	1.44	0.00	34.1	1		EU
VB 34	200776	9	04 20 52.60	+13 52 01.1	0.15	0	99.3	2.3	14.39	0.34	0.4	0	*	ED
VB 34	200441	253	04 20 53.20	+13 52 44.6	0.89	0	150.4	10.0	21.80	1.45	49.5	1		ED
VA 203	200441	244	04 20 56.36	+14 51 32.7	0.21	0	3.0	0.7	0.44	0.11	10.3	0	*	EU
VA 203	200775	366	04 20 55.49	+14 51 36.0	0.00	-1	32.9	0.0	4.77	0.00	49.0	1		EU
VB 36	201370	118	04 21 32.16	+18 25 01.2	0.11	0	50.3	2.3	7.30	0.33	0.3	0	*	ED
VB 37	200776	3	04 21 35.13	+14 24 48.1	0.31	0	119.6	3.0	17.34	0.44	34.8	0	*	ED
VB 37	200441	250	04 21 34.71	+14 24 24.5	0.22	0	95.9	4.0	13.90	0.58	18.4	1		ED
VA 216	200441	246	04 21 35.09	+14 41 33.2	0.23	0	6.8	1.0	0.99	0.15	5.6	0	*	EU
VA 213	200442	288	04 21 37.10	+16 53 40.5	0.53	0	21.4	2.5	3.10	0.37	38.6	1	*	EU
VB 38	200776	6	04 22 04.38	+14 04 55.8	0.48	0	33.8	2.0	4.90	0.29	21.9	1		ED
VB 38	200441	251	04 22 03.77	+14 04 30.0	0.27	0	42.7	4.0	6.20	0.58	39.5	0	*	ED
VA 242	201370	119	04 22 40.18	+18 16 17.2	0.25	0	2.4	0.7	0.35	0.10	18.6	1		EU
VA 242	200442	280	04 22 35.32	+18 15 59.8	1.04	0	14.7	3.9	2.14	0.56	48.4	0	*	EU
VB 39	200442	289	04 22 45.33	+16 46 57.5	0.61	0	102.1	6.0	14.80	0.87	50.1	0	*	ED
VB 40	200441	242	04 22 44.36	+15 03 03.7	0.33	0	231.5	6.6	33.56	0.96	30.7	1		ED
VB 40	200020	378	04 22 44.39	+15 03 25.8	0.11	0	191.0	3.3	27.70	0.47	30.5	1	*	ED
VB 41	200442	282	04 22 57.29	+17 32 30.2	0.36	0	17.6	2.1	2.56	0.30	25.1	1	*	ED
H 282	200776	26	04 22 58.99	+13 18 56.9	0.00	-1	22.4	0.0	3.25	0.00	44.8	1	*	
VA 260	200441	259	04 23 00.91	+15 13 43.0	0.00	-1	11.4	0.0	1.66	0.00	41.2	1		EU
VA 260	200020	376	04 23 02.58	+15 13 54.8	0.45	0	6.3	0.9	0.92	0.13	27.2	0	*	EU
VA 262	200777	59	04 23 11.90	+15 42 47.9	0.00	-1	24.4	0.0	3.54	0.00	37.2	0	*	EU
VA 262	200775	359	04 23 11.90	+15 42 47.9	0.00	-1	56.0	0.0	8.11	0.00	49.3	0		EU
VA 262	200020	394	04 23 11.90	+15 42 47.9	0.00	-1	23.5	0.0	3.41	0.00	43.8	0		EU
VA 275	200776	16	04 23 23.30	+14 25 43.0	0.00	-1	47.4	0.0	6.88	0.00	50.0	1		ED
VA 275	200441	249	04 23 22.89	+14 25 30.0	0.24	0	28.7	3.3	4.16	0.48	35.7	0		ED
VA 275	200020	385	04 23 23.56	+14 25 26.0	0.29	0	40.0	2.7	5.80	0.39	45.7	0	*	ED
VB 173	200777	58	04 23 24.79	+15 45 49.0	0.00	-1	34.4	0.0	4.99	0.00	33.3	0	*	ED
VB 173	200020	393	04 23 24.79	+15 45 49.0	0.00	-1	35.5	0.0	5.15	0.00	44.8	0		ED
VB 45	201369	148	04 23 26.59	+16 47 02.0	0.56	0	47.5	3.9	6.88	0.56	42.6	1	*	ED

Table 4. *continued*

Name (1)	Seq. (2)	Xnr (3)	RA (J2000) (4)	Dec (J2000) (5)	Sep. (6)	D/U (7)	ct/ks (8)	err. (9)	L_X (10)	err. (11)	Off. (12)	Rib (13)	* (14)	IPC? (15)
VB 46	200441	247	04 23 31.29	+14 39 29.1	0.75	0	16.0	3.1	2.32	0.45	33.8	1		ED
VB 46	200020	384	04 23 32.56	+14 40 11.9	0.26	0	19.8	1.4	2.87	0.20	31.9	1	*	ED
VA 282	200777	54	04 23 42.29	+15 52 53.0	0.00	-1	7.6	0.0	1.10	0.00	27.6	1	*	EU
VA 282	200020	391	04 23 42.29	+15 52 53.0	0.00	-1	28.0	0.0	4.06	0.00	49.7	0		EU
VA 288	200441	243	04 23 50.37	+14 54 55.7	0.38	0	132.5	6.7	19.21	0.97	40.4	0		ED
VA 288	200020	381	04 23 50.49	+14 55 10.3	0.20	0	92.1	1.9	13.35	0.28	18.1	0	*	ED
VA 294	200776	7	04 23 51.92	+14 03 26.0	0.60	0	11.7	2.2	1.69	0.31	45.1	0	*	EU
VA 292	200777	47	04 23 55.51	+16 21 16.9	0.00	-1	9.1	0.0	1.32	0.00	34.7	1	*	EU
VA 292	201369	178	04 23 55.51	+16 21 16.9	0.00	-1	25.1	0.0	3.64	0.00	46.4	0		EU
VA 297	201369	174	04 23 59.11	+16 43 28.9	0.00	-1	2.9	0.0	0.41	0.00	35.5	1	*	EU
VB 47	201369	159	04 24 05.71	+17 26 39.1	0.00	-1	29.5	0.0	4.27	0.00	48.6	0	*	ED
VB 47	200442	296	04 24 05.71	+17 26 39.1	0.00	-1	39.5	0.0	5.73	0.00	41.7	1		ED
VB 50	200441	245	04 24 11.99	+14 45 31.6	0.08	0	495.3	14.3	71.81	2.07	43.7	1		ED
VB 50	200020	382	04 24 12.31	+14 45 12.9	0.32	0	316.6	3.8	45.90	0.55	22.7	1	*	ED
VB 49	200777	32	04 24 12.97	+16 23 13.3	0.49	0	76.8	3.0	11.13	0.44	33.4	0	*	ED
VB 49	201369	152	04 24 13.27	+16 23 22.6	0.65	0	85.1	4.4	12.34	0.64	41.8	0		ED
VB 174	201370	121	04 24 19.46	+18 00 35.1	0.84	0	22.1	3.6	3.21	0.52	46.9	0	*	EU
VB 51	201369	138	04 24 22.63	+17 04 44.7	0.08	0	43.0	2.7	6.24	0.39	32.1	0	*	EU
VA 321	200777	38	04 24 28.35	+15 53 08.5	0.12	0	3.7	0.9	0.53	0.13	16.6	0	*	EU
VA 321	200020	390	04 24 28.01	+15 53 03.1	0.00	-1	18.8	0.0	2.72	0.00	47.4	1		EU
VB 52	201369	144	04 24 28.77	+16 53 13.4	0.17	0	83.8	4.0	12.16	0.58	27.7	0	*	ED
VA 334	200777	39	04 24 47.62	+15 52 38.7	0.32	0	169.8	3.5	24.63	0.51	12.2	0	*	ED
VA 334	200020	369	04 24 50.38	+15 52 30.7	0.44	0	122.7	4.2	17.79	0.61	46.5	1		ED
VB 175	201369	139	04 25 00.38	+16 58 58.7	0.15	0	10.8	1.4	1.56	0.20	21.5	1	*	EU
VA 351	201369	135	04 25 14.12	+17 16 11.3	0.59	0	154.6	4.2	22.42	0.61	30.2	0	*	ED
VA 352	200777	33	04 25 16.33	+16 18 24.3	0.28	0	11.1	1.4	1.62	0.20	22.5	1	*	
VA 352	201369	153	04 25 15.90	+16 17 51.1	0.30	0	11.0	2.1	1.60	0.31	36.9	1		
VB 57	200777	37	04 25 37.08	+15 56 37.9	0.17	0	218.2	3.9	31.64	0.56	0.3	0	*	ED
VA 362	201369	132	04 25 47.38	+17 32 52.3	0.29	0	8.3	2.7	1.21	0.38	42.8	1	*	EU
VA 368	200020	380	04 25 50.53	+14 59 59.2	0.24	0	4.6	0.5	0.67	0.07	15.7	0	*	EU
VA 382	201369	137	04 26 04.47	+17 07 09.4	0.22	0	23.3	1.6	3.38	0.23	16.8	1	*	ED
VA 383	200020	379	04 26 05.09	+15 02 18.0	0.29	0	24.1	1.1	3.49	0.16	18.4	1	*	ED
VB 59	200777	42	04 26 05.34	+15 31 37.9	0.18	0	193.5	4.8	28.06	0.70	25.8	1		ED
VB 59	200020	372	04 26 06.35	+15 31 15.3	0.28	0	148.3	2.9	21.50	0.41	31.2	1	*	ED
VB 141	200777	40	04 26 20.06	+15 37 14.2	0.21	0	849.4	9.9	123.16	1.43	21.9	1	*	ED
VB 141	200020	370	04 26 21.24	+15 37 06.2	0.13	0	728.5	8.6	105.63	1.25	38.0	1		ED
VB 63	201369	145	04 26 24.73	+16 51 10.6	0.15	0	120.8	2.9	17.51	0.42	0.2	0	*	ED
VB 64	201369	149	04 26 39.89	+16 44 45.0	0.07	0	68.8	2.6	9.97	0.38	7.3	0	*	ED
VA 420	201369	164	04 27 15.60	+17 14 34.1	0.00	-1	4.7	0.0	0.68	0.00	26.6	1	*	EU
VB 65	200777	41	04 27 37.65	+15 35 57.9	0.77	0	56.0	3.1	8.13	0.45	35.7	1		ED
VB 65	201368	84	04 27 35.49	+15 35 43.4	0.38	0	85.8	4.1	12.44	0.60	36.6	1	*	ED
VB 65	200020	371	04 27 36.43	+15 35 03.9	0.34	0	85.5	4.0	12.40	0.58	49.5	0		ED
VB 189	200777	45	04 28 10.80	+16 28 18.1	0.00	-1	15.7	0.0	2.28	0.00	49.0	0		EU
VB 189	201369	151	04 28 09.17	+16 28 40.8	0.55	0	9.3	1.6	1.35	0.23	33.7	0	*	EU
VB 71	200777	36	04 28 34.28	+15 57 34.0	0.18	0	769.3	10.8	111.55	1.56	42.9	1		ED
VB 71	201368	75	04 28 33.86	+15 57 54.3	0.18	0	646.8	8.1	93.78	1.18	29.7	0	*	ED
VA 490	201369	140	04 28 40.45	+16 58 00.7	0.55	0	35.5	2.6	5.15	0.38	33.4	1	*	EU
VB 72	200777	56	04 28 39.10	+15 52 16.0	0.00	-1	57.8	0.0	8.38	0.00	44.2	0		ED
VB 72	201368	76	04 28 39.28	+15 52 38.3	0.37	0	23.8	2.6	3.44	0.38	25.5	1	*	ED
VB 73	201369	134	04 28 48.64	+17 17 00.8	0.26	0	125.9	5.5	18.26	0.80	43.3	0	*	ED

Table 4. *continued*

Name (1)	Seq. (2)	Xnr (3)	RA (J2000) (4)	Dec (J2000) (5)	Sep. (6)	D/U (7)	ct/ks (8)	err. (9)	L_X (10)	err. (11)	Off. (12)	Rib (13)	* (14)	IPC? (15)
VB 190	201368	70	04 28 50.81	+16 17 12.8	0.15	0	208.5	7.2	30.23	1.04	42.9	0	*	ED
VB 190	201369	154	04 28 52.02	+16 17 24.2	0.34	0	178.0	8.1	25.81	1.17	48.9	0		ED
VA 502	200777	49	04 28 51.19	+15 58 45.1	0.00	-1	186.4	0.0	27.03	0.00	47.0	1		EU
VA 502	201368	97	04 28 51.19	+15 58 45.1	0.00	-1	8.2	0.0	1.19	0.00	27.3	1	*	EU
VB 75	200777	35	04 28 59.95	+16 09 44.5	0.23	0	129.1	7.3	18.72	1.06	50.8	1		ED
VB 75	201368	72	04 28 59.47	+16 09 52.4	0.32	0	115.7	4.2	16.77	0.61	35.4	0	*	ED
VA 512	201368	90	04 28 59.59	+16 20 51.0	0.00	-1	97.1	0.0	14.08	0.00	45.4	1	*	ED
VA 512	201369	179	04 28 59.59	+16 20 51.0	0.00	-1	120.4	0.0	17.46	0.00	47.9	0		ED
VA 529	201368	111	04 29 12.00	+15 16 44.0	0.00	-1	10.3	0.0	1.49	0.00	25.4	1	*	EU
VB 77	200443	309	04 29 21.89	+17 32 58.4	0.50	0	159.1	5.8	23.07	0.84	45.1	0	*	ED
VB 78	200443	304	04 29 29.37	+17 52 07.4	0.31	0	95.5	6.1	13.84	0.88	47.8	1	*	ED
VB 181	201368	92	04 29 30.50	+16 14 43.1	0.00	-1	25.6	0.0	3.71	0.00	37.4	1	*	ED
VB 79	200443	316	04 29 31.49	+17 53 37.0	0.00	-1	90.7	0.0	13.15	0.00	48.0	1	*	ED
VA 575	200443	310	04 30 24.43	+17 30 04.5	0.23	0	27.7	1.9	4.02	0.28	30.3	0	*	EU
VB 82	201368	93	04 30 33.50	+16 11 39.1	0.00	-1	19.4	0.0	2.81	0.00	33.9	0	*	EU
GH7-246	200444	343	04 30 33.79	+14 44 49.9	0.00	-1	11.3	0.0	1.64	0.00	28.5	1	*	EU
VB 182	201368	79	04 30 34.31	+15 44 10.0	0.21	0	32.0	1.8	4.65	0.25	8.7	0	*	ED
VB 83	201368	103	04 30 38.90	+15 41 30.8	0.00	-1	0.8	0.0	0.12	0.00	8.3	0	*	EU
VB 85	201368	73	04 30 46.68	+16 08 59.0	0.07	0	224.5	5.4	32.56	0.78	32.0	1	*	ED
VA 610	201368	89	04 31 10.51	+16 23 46.0	0.00	-1	51.8	0.0	7.52	0.00	47.9	1	*	ED
VA 622	200443	321	04 31 28.30	+17 43 10.9	0.00	-1	5.0	0.0	0.73	0.00	18.8	1	*	EU
VB 88	200444	336	04 31 24.76	+13 54 19.0	1.01	0	73.9	7.8	10.72	1.12	50.3	0	*	
VA 627	200443	307	04 31 37.71	+17 42 30.8	0.34	0	54.7	2.2	7.93	0.32	16.6	1	*	ED
VA 637	201368	87	04 31 43.49	+15 01 37.1	0.85	0	35.3	4.6	5.12	0.67	43.5	0	*	
VA 637	201747	222	04 31 43.20	+15 02 28.0	0.00	-1	36.3	0.0	5.26	0.00	49.9	1		
VA 637	200444	330	04 31 44.64	+15 02 16.5	0.40	0	20.2	1.9	2.93	0.28	23.2	1		
VA 638	201368	81	04 31 46.93	+15 37 52.0	0.79	0	11.1	1.8	1.61	0.27	24.0	1	*	EU
VA 638	201747	190	04 31 44.24	+15 38 12.2	0.64	0	16.0	2.0	2.32	0.29	42.2	1		EU
VB 89	201368	77	04 31 51.17	+15 51 00.3	0.09	0	27.6	2.4	4.00	0.35	28.0	0	*	ED
VB 89	201747	184	04 31 52.71	+15 51 53.7	0.87	0	32.5	2.7	4.72	0.40	45.0	0		ED
VB 191	201368	85	04 31 51.97	+15 29 45.0	0.20	0	10.6	1.8	1.53	0.26	26.7	0	*	EU
VB 191	201747	217	04 31 51.79	+15 29 57.1	0.00	-1	8.7	0.0	1.26	0.00	39.6	1		EU
VB 191	200444	337	04 31 51.79	+15 29 57.1	0.00	-1	18.1	0.0	2.63	0.00	48.9	0		EU
VA 657	200443	308	04 32 08.14	+17 39 47.3	0.19	0	8.5	0.8	1.23	0.12	9.7	0	*	EU
VA 673	200443	305	04 32 24.02	+17 44 56.9	0.22	0	45.0	1.9	6.52	0.27	13.3	0	*	ED
VA 674	200443	302	04 32 30.07	+17 54 04.1	0.42	0	20.9	1.9	3.03	0.28	22.3	1	*	ED
VB 91	201368	74	04 32 50.45	+16 00 12.1	0.29	0	40.4	4.4	5.86	0.63	44.9	0	*	ED
VB 91	201747	182	04 32 52.09	+16 01 01.8	0.94	0	46.0	4.1	6.67	0.59	39.8	1		ED
VB 92	201368	78	04 32 56.63	+15 48 50.7	0.69	0	16.5	4.1	2.39	0.60	42.1	1		ED
VB 92	201747	186	04 32 59.34	+15 49 17.2	0.14	0	35.9	1.8	5.20	0.26	30.2	0	*	ED
VB 93	200443	327	04 33 37.30	+16 45 45.0	0.00	-1	32.7	0.0	4.74	0.00	48.7	1	*	ED
VB 95	201747	201	04 33 53.65	+14 50 47.7	0.86	0	12.9	1.8	1.87	0.27	40.5	0	*	EU
VB 95	200444	342	04 33 50.09	+14 50 40.9	0.00	-1	3.9	0.0	0.56	0.00	21.0	1		EU
VA 726	200443	326	04 33 56.40	+16 52 09.8	0.00	-1	22.5	0.0	3.26	0.00	44.6	0	*	
VB 96	201747	197	04 33 58.87	+15 10 00.1	0.20	0	49.1	2.3	7.12	0.34	21.9	1		ED
VB 96	200444	329	04 33 59.83	+15 09 44.2	0.36	0	69.6	3.6	10.09	0.53	35.0	0	*	ED
VA 731	200444	345	04 34 03.70	+14 12 47.9	0.00	-1	5.9	0.0	0.85	0.00	36.8	1	*	
VB 183	201747	185	04 34 33.40	+15 49 52.6	0.81	0	22.6	1.5	3.27	0.22	19.9	1	*	EU
VB 97	201747	193	04 34 35.74	+15 30 18.7	0.23	0	49.1	1.8	7.13	0.27	0.3	0	*	ED
VA 763	201747	195	04 35 28.68	+15 23 49.3	0.23	0	10.0	0.9	1.45	0.13	14.1	0	*	ED

Table 4. *continued*

Name (1)	Seq. (2)	Xnr (3)	RA (J2000) (4)	Dec (J2000) (5)	Sep. (6)	D/U (7)	ct/ks (8)	err. (9)	L_X (10)	err. (11)	Off. (12)	Rib (13)	* (14)	IPC? (15)
VB 99	201747	188	04 36 06.12	+15 41 03.4	0.25	0	28.0	1.8	4.06	0.27	24.4	0	*	EU
VB 101	201747	183	04 36 41.80	+15 51 54.0	0.45	0	116.9	4.0	16.95	0.58	37.4	1	*	
VB 102	201747	198	04 37 32.88	+15 08 24.0	0.51	0	150.9	6.7	21.88	0.97	47.8	0	*	

Key: (1) Source name, (2) field number, (3) arbitrary running number, (4) RA (h m s), (5) DEC (d m s), (6)separation (arcmin) , (7) detection=0, upper limit=1, (8) count rate, (9) count rate error, (10) x-ray luminosity (10^{28}erg/s), (11) x-ray luminosity error (10^{28}erg/s), (12) off-axis angle, (13) rib flag 1=source near rib, 0=source not near rib, (14) asterix indicates best observation of source , (15) EU=Einstein upper limit, ED=Einstein detection.

Table 5. Hyades probable non-members in the *ROSAT* PSPC fields: X-ray properties

Name (1)	Seq. (2)	Xnr (3)	RA (J2000) (4)	Dec (J2000) (5)	Sep. (6)	D/U (7)	ct/ks (8)	err. (9)	L_X (10)	err. (11)	Off. (12)	Rib (13)	* (14)	IPC? (15)
VA 47	201748	236	04 12 31.90	+12 00 25.9	0.00	-1	6.7	0.0	0.98	0.00	38.2	0	*	
VA125AB	200775	361	04 18 03.31	+15 31 43.0	0.00	-1	5.8	0.0	0.85	0.00	25.9	1	*	
VA 131	200775	356	04 18 12.41	+16 05 55.0	0.00	-1	33.1	0.0	4.80	0.00	36.3	0	*	EU
LP414-158	201370	128	04 18 33.60	+18 21 56.2	0.00	-1	6.5	0.0	0.94	0.00	42.3	1	*	
H196	200441	260	04 18 57.70	+15 08 57.1	0.00	-1	8.2	0.0	1.18	0.00	42.2	1	*	
H196	200775	364	04 18 57.70	+15 08 57.1	0.00	-1	10.7	0.0	1.55	0.00	31.3	1		
VA 191	200442	295	04 20 19.70	+17 30 42.8	0.00	-1	0.9	0.0	0.13	0.00	12.5	0	*	
LP415-543	201370	116	04 20 29.68	+18 54 16.1	0.72	0	10.4	1.6	1.50	0.24	32.5	0	*	
VA 200	200441	239	04 20 47.69	+15 14 01.2	0.22	0	17.3	2.3	2.51	0.33	32.6	0	*	
VA 200	200775	351	04 20 47.68	+15 13 59.8	0.23	0	20.4	4.4	2.96	0.63	27.8	1		
VA 211	200776	27	04 21 30.91	+14 25 59.9	0.00	-1	96.9	0.0	14.06	0.00	35.6	0		
VA 211	200441	276	04 21 30.91	+14 25 59.9	0.00	-1	3.2	0.0	0.46	0.00	16.6	0	*	
H 264	200441	255	04 22 30.90	+15 12 30.1	0.69	0	24.5	3.1	3.56	0.45	36.0	0		
H 264	200775	354	04 22 31.15	+15 13 46.2	0.63	0	36.1	7.8	5.23	1.13	46.1	0		
H 264	200020	387	04 22 30.31	+15 13 00.3	0.17	0	27.0	1.4	3.91	0.21	34.5	0	*	
VA 241	200777	57	04 22 32.21	+15 51 27.0	0.00	-1	3.2	0.0	0.46	0.00	44.5	1	*	EU
VA 241	200775	358	04 22 32.21	+15 51 27.0	0.00	-1	11.8	0.0	1.71	0.00	41.8	1		EU
VA 247	200441	278	04 22 40.20	+15 03 46.1	0.00	-1	199.4	0.0	28.92	0.00	30.5	1		
VA 247	200020	412	04 22 40.20	+15 03 46.1	0.00	-1	183.2	0.0	26.56	0.00	31.5	1	*	
VB 172	200776	19	04 22 44.21	+14 15 22.0	0.00	-1	4.7	0.0	0.68	0.00	36.0	1	*	
VB 172	200441	273	04 22 44.21	+14 15 22.0	0.00	-1	4.2	0.0	0.61	0.00	34.7	1		
VA 265	201369	167	04 23 16.30	+17 00 42.1	0.00	-1	8.0	0.0	1.16	0.00	45.9	0		
VA 265	200442	299	04 23 16.30	+17 00 42.1	0.00	-1	3.5	0.0	0.50	0.00	43.0	1	*	
VA 305	200441	262	04 24 09.00	+15 05 19.0	0.00	-1	50.9	0.0	7.38	0.00	48.7	0		
VA 305	200020	377	04 24 09.67	+15 05 13.3	0.19	0	31.2	1.2	4.52	0.17	9.9	0	*	
VA 306	200777	64	04 24 09.79	+15 28 35.0	0.00	-1	1.4	0.0	0.20	0.00	34.7	1		
VA 306	200020	399	04 24 09.79	+15 28 35.0	0.00	-1	0.8	0.0	0.12	0.00	24.6	1	*	
VA 329	200777	52	04 24 37.90	+15 54 36.0	0.00	-1	1.2	0.0	0.17	0.00	14.1	0	*	EU
VA 329	200020	389	04 24 37.90	+15 54 36.0	0.00	-1	53.1	0.0	7.70	0.00	48.7	1		EU
VA 366	200777	43	04 25 48.52	+15 31 23.0	0.09	0	39.1	2.6	5.67	0.38	25.2	1	*	ED
VA 366	200020	373	04 25 51.55	+15 31 10.0	0.72	0	28.7	1.6	4.16	0.23	29.2	1		ED
VA 380	201369	161	04 26 00.89	+17 16 53.0	0.00	-1	1.8	0.0	0.25	0.00	26.5	1	*	
VA 413	200777	65	04 27 01.49	+15 22 26.0	0.00	-1	6.6	0.0	0.96	0.00	39.7	0		ED
VA 413	201368	109	04 27 01.49	+15 22 26.0	0.00	-1	21.4	0.0	3.10	0.00	47.5	1		ED
VA 413	200020	400	04 27 01.49	+15 22 26.0	0.00	-1	16.5	0.0	2.39	0.00	35.6	0	*	ED
VB 188	200777	66	04 27 32.50	+15 21 45.0	0.00	-1	15.1	0.0	2.18	0.00	44.6	0		ED
VB 188	201368	110	04 27 32.50	+15 21 45.0	0.00	-1	18.8	0.0	2.73	0.00	40.8	0		ED
VB 188	200020	401	04 27 32.50	+15 21 45.0	0.00	-1	13.6	0.0	1.97	0.00	42.2	0	*	ED
VA 478	201369	175	04 28 14.21	+16 39 11.2	0.00	-1	2.6	0.0	0.37	0.00	28.9	0	*	
VB 80	201368	80	04 30 08.07	+15 38 25.3	0.14	0	68.2	2.4	9.89	0.34	0.2	0	*	ED
VA 578	200443	318	04 30 24.70	+17 47 12.1	0.00	-1	2.1	0.0	0.30	0.00	33.8	1	*	
H495	200444	332	04 30 41.53	+14 39 20.6	0.38	0	7.9	1.7	1.15	0.24	26.7	1	*	
H 588	201747	223	04 34 18.29	+14 58 31.1	0.00	-1	3.0	0.0	0.44	0.00	31.8	1		
H 588	200444	341	04 34 18.29	+14 58 31.1	0.00	-1	1.7	0.0	0.24	0.00	30.7	1	*	
VA 750	201747	196	04 34 40.17	+15 12 36.2	0.17	0	101.2	2.8	14.68	0.41	17.4	1	*	
VA 750	200444	328	04 34 41.27	+15 13 01.4	0.63	0	83.4	5.8	12.10	0.83	44.2	1		
VA 751	200443	306	04 34 43.60	+17 44 56.4	0.43	0	22.0	2.0	3.19	0.29	34.2	1	*	EU

Key: (1) Source name, (2) field number, (3) arbitrary running number, (4) RA (h m s), (5) DEC (d m s), (6)separation (arcmin) , (7) detection=0, upper limit=1, (8) count rate, (9) count rate error, (10) x-ray luminosity (10^{28}erg/s), (11) x-ray luminosity error (10^{28}erg/s), (12) off-axis angle, (13) rib flag 1=source near rib, 0=source not near rib, (14) asterix indicates best observation of source, (15) EU=Einstein upper limit, ED=Einstein detection.

Table 6. Non-Hyad, catalogued objects in the *ROSAT* PSPC fields: X-ray properties

Name (1)	Seq. (2)	Xnr (3)	RA (J2000) (4)	Dec (J2000) (5)	Sep. (6)	ct/ks (7)	err. (8)	L_X (9)	err. (10)	Off. (11)
HD 26749	201748	1621	4 14 17.50	+12 20 54.2	0.10	1.3	0.4	0.18	0.05	5.9
SAO 93855	200442	658	4 18 39.70	+17 50 9.0	0.44	25.7	2.6	3.73	0.38	40.7
P NTTS 041559+1716	200442	659	4 18 51.58	+17 23 12.1	0.05	50.9	2.7	7.38	0.38	34.6
HBC 376	200442	659	4 18 51.58	+17 23 12.1	0.61	50.9	2.7	7.38	0.38	34.6
HD 27296	200776	1005	4 19 8.68	+13 43 35.4	0.33	22.1	1.6	3.20	0.23	26.5
HD 27296	200776	1006	4 19 8.71	+13 43 34.5	0.32	22.6	1.4	3.28	0.20	26.5
HD 285639	201370	1236	4 20 50.00	+18 34 46.4	0.25	5.2	0.9	0.75	0.13	13.7
HD 286678	200776	1052	4 21 17.24	+13 40 15.7	0.80	15.1	1.0	2.18	0.14	12.8
HD 285739	201369	1300	4 23 31.34	+17 3 9.7	0.61	14.4	2.6	2.09	0.37	43.0
HD 285751	200020	530	4 23 41.77	+15 37 59.1	0.39	133.9	3.0	19.41	0.43	36.0
HD 285751	200777	1101	4 23 40.54	+15 38 20.5	0.82	136.8	3.8	19.84	0.55	33.1
HD 285812	200020	547	4 25 33.50	+15 33 14.9	1.02	2.4	0.8	0.35	0.12	29.2
HD 285819	200020	548	4 25 36.82	+15 10 43.9	0.33	9.4	0.6	1.36	0.09	12.2
HD 285819	200777	1123	4 25 35.82	+15 11 47.1	0.79	19.6	3.1	2.84	0.45	44.6
HD 28007	201369	1329	4 25 52.69	+17 26 15.0	0.63	25.1	2.8	3.65	0.40	36.0
HD 28124	201369	1348	4 26 51.32	+17 1 37.1	0.15	8.4	0.9	1.22	0.14	12.5
HD 285808	200777	1141	4 27 34.69	+16 1 23.9	0.68	19.3	2.3	2.80	0.33	29.0
HD 285808	201368	1167	4 27 36.57	+16 2 18.2	0.49	21.4	4.4	3.11	0.63	43.4
HD 28227	201368	1169	4 27 50.10	+15 9 25.7	0.45	18.7	4.2	2.71	0.61	43.9
HD 28448	200443	767	4 29 50.96	+17 4 23.2	0.47	19.7	3.1	2.85	0.45	47.1
HD 28448	200443	768	4 29 51.01	+17 4 26.9	0.41	23.6	3.7	3.42	0.54	47.0
HD 28528	200444	860	4 30 35.38	+14 47 29.0	0.78	15.4	2.2	2.23	0.31	28.5
HD 285845	200443	778	4 31 25.08	+18 15 50.3	0.51	134.4	6.3	19.48	0.91	46.8
P NTTS 042835+1700	200443	779	4 31 25.56	+17 6 12.8	0.42	17.1	1.8	2.49	0.26	30.0
P NTTS 042916+1751	200443	786	4 32 10.11	+17 57 18.1	0.20	83.2	3.7	12.06	0.53	26.0
NAME FK 1	200443	790	4 32 16.55	+18 1 28.3	0.43	84.9	3.1	12.31	0.45	29.9
EQ 042921+175524	200443	790	4 32 16.55	+18 1 28.3	0.43	84.9	3.1	12.31	0.45	29.9
V* V826 TAU	200443	790	4 32 16.55	+18 1 28.3	0.43	84.9	3.1	12.31	0.45	29.9
1E 0429.3+1755	200443	790	4 32 16.55	+18 1 28.3	0.37	84.9	3.1	12.31	0.45	29.9
EQ 042923+181354	200443	791	4 32 17.60	+18 20 18.9	0.18	68.8	5.3	9.98	0.77	48.6
V* V827 TAU	200443	791	4 32 17.60	+18 20 18.9	0.18	68.8	5.3	9.98	0.77	48.6
NAME FK 2	200443	791	4 32 17.60	+18 20 18.9	0.18	68.8	5.3	9.98	0.77	48.6
1E 0429.3+1813	200443	791	4 32 17.60	+18 20 18.9	0.83	68.8	5.3	9.98	0.77	48.6
V* GG TAU	200443	797	4 32 30.63	+17 31 40.0	0.15	6.2	0.7	0.90	0.10	0.2
EM* AS 83	200443	797	4 32 30.63	+17 31 40.0	0.68	6.2	0.7	0.90	0.10	0.2
P NTTS 042950+1757	200443	802	4 32 44.03	+18 2 44.4	0.23	13.5	1.6	1.96	0.23	31.1
HR 1442	200443	816	4 33 33.35	+18 0 48.4	0.25	197.5	4.8	28.63	0.69	32.6
V* TY TAU	201747	1553	4 34 43.45	+15 15 59.6	0.11	21.1	1.2	3.06	0.17	14.1
HBC 412	200443	841	4 35 27.91	+17 52 17.9	0.98	59.5	4.5	8.63	0.65	46.8
HD 29247	201747	1570	4 36 56.48	+15 15 43.1	0.41	11.2	1.7	1.62	0.24	36.8

Notes: Key: (1) Source name, (2) field number, (3) arbitrary running number, (4) RA (h m s), (5) DEC (d m s), (6)separation (arcmin) , (7) count rate, (8) count rate error, (9) x-ray luminosity (10^{28}erg/s), (10) x-ray luminosity error (10^{28}erg/s), (11) off-axis angle.

REFERENCES.

Allan D.J., Ponman T.J., Jeffries R.D., 1995,

Allen C.W., 1973, Astrophysical Quantities. Athlone Press, London

Ambruster C.W., Sciortino S., Golub L., 1987, ApJS, 65, 273

Anders E., Grevasse N., 1989, GCA, 53, 197

Ayres T.R., Linsky J.L., Vaiana G.S., Golub L., Rosner R., 1981, ApJ, 250, 293

Barbera M., Micela G., Sciortino S., Harnden F.R., Rosner R., 1993, ApJ, 414, 846

Barstow M.A., Schmitt J.H.M.M., Clemens J.C., Pye J.P., Denby M., Harris A.W., Pankiewicz G.S., 1992, MNRAS, 255, 369

Batten A.H., Fletcher J.M., Mann P.J., 1978, Pub. Dom. Astr. Obs., 15

Belloni T., Mereghetti S., 1994, A&A, 286, 935

Bignami G.F., Caraveo P.A., Mereghetti S., 1993, Nature, 361, 704

Boyle B.J., McMahon R.G., Wilkes B.J., Elvis M., 1995, MNRAS, 272, 462

Bradt H., Ohashi T., Pounds K.A., 1992, in Maran S.P., ed., The Astronomy and Astrophysics Encyclopedia. CUP

Branduardi-Raymont G., Mason K.O., Warwick R.S., Carrera F.J., et al., 1994, MNRAS, 270, 947

Brickhouse N., Edgar R., Kaastra J., Kallman T., et al. 1995, Legacy, 6, 4

Brickhouse N., Raymond J.C., Smith B.W., 1995, ApJS, 97, 551

Bromage G.E., Kellet B.J., Jeffries R.D., Innis J.L., Matthews L., Anders G.J., Coates D.W., 1992, ASP Conf. Ser. 26, p. 80

Burke E.W., Jr et al., 1992, IBVS 3722

Carrol R.W., et al., 1980, ApJ, 235, L77

Catura R.C., Acton L.W., Johnson H.M., 1975, ApJ, 196, L47

Collura A., Pasquini L., Schmitt J.H.M.M., 1988, A&A, 205, 197

Cruddace R.G., Dupree A.K., 1984, ApJ, 227, 263

Day C., Arnaud K., Ebisawa K., Gotthelf E., Ingham J., Mukai K., White N., 1994, The ABC Guide to ASCA Data Reduction.

Dempsey R.C., Linsky J.L., Fleming T.A., Schmitt J.H.M.M., 1993a, ApJS, 86, 599

Dempsey R.C., Linsky J.L., Fleming T.A., Schmitt J.H.M.M., 1994, in Caillault J.P., ed., Cool Stars, Stellar Systems and the Sun. ASP Conf. Ser., vol 64, p.74

Dere K.P., Mason H.E., Monsignori Fossi B.C., Waljeski K.H., 1994, AAS 25, 1459

Favata F., Micela G., Sciortino S., 1995, A&A, 298, 482

Fleming T.A., Gioia I.M., Maccacaro T., 1989, ApJ, 340, 1011

Fleming T.A., Scmitt J.H.M.M., Giampapa M.S., 1995, ApJ, 450, 401

Fossi B.C.M., Landini M., 1994, Solar Physics, 152, 81

Frisch P.C., York D.G., 1983, ApJ, 271, 59

Gagné M., Caillault J.P., Stauffer J.R., 1995, ApJ, 450, 217

Georgantopolous I., Saxton R.D., Pye J.P., 1992, The ROSAT PSPC PSF. University of Leicester X-ray Astronomy Group.

Gioia I.M., Henry J.P., Maccacaro T., Morris S.L., et al., 1990, ApJ, 356, 35

Gioia I.M., Maccacaro T., Schild R., Stocke J.T., Morris S.L., Henry J.P., 1990, ApJS, 72, 567

Golub L., Rosner R., Vaiana G.S., Weiss N.O., 1981, ApJ, 243, 309

Guillout P., Haywood M., Motch C., Robin A.C., 1996, A&A, in press

Guinan E.F., Giménez A., 1993, in Sahade J., et al., eds., The Realm of Interacting Binary Stars. Kluwer, Dordrecht, p. 51

Haisch B.M., 1983, in Byrne P.B., Rodono M, eds, ASSL 102. Activity in Red Dwarf Stars. Reidel, Dordrecht, p. 255

Haisch B., Linsky J.L., 1976, ApJ, 205, L39

Hasinger G., Burg R., Giacconi R., Hartner G., et al., 1993, A&A, 275, 1

Hertz P., Grindlay J.E., 1984, ApJ, 278, 137

Hertz P., Grindlay J.E., 1988, AJ, 96, 233

Hodgkin S.T., 1995, PhD Thesis, University of Leicester

Holt S.S., White N.E., Becker R.E., Boldt E.A., Mushotsky R.F et al., 1979, ApJ, 234, L65

Humphreys R.A., Landau R., Ghigo F.D., Zumach W., 1991, AJ, 102, 395

Innes D., Hartquist T., 1984, MNRAS, 209, 7

Jeffries R.D., Bromage G.E., 1993, MNRAS, 260, 132

Kaastra J.S., Mewe R., 1994, Legacy, 3, 16

Kashyap V., Rosner R., Micela G., Sciortino S., et al., 1992, ApJ, 391, 667

King I.R., Raff M.I., 1977, PASP, 89, 120

Kürster M., 1994, in Caillault J.P., ed., Cool Stars Stellar Systems and the Sun, ASP Conf. Ser. 64, p. 104

Liedahl D.A., Osterhead A.L., Goldstein W.H., 1995, ApJ, 438, L115

Lin R.P., Schwartz R.A., Kane S.R., Pelling R.M., Hurley K.C., 1984, ApJ, 283, 421

Linsky J.L., 1990, in Elvis M., ed., Imaging X-ray Astronomy. CUP, p. 39

Linsky J.L., Haisch B.M., 1979, ApJ, 229, L27

Majer P., Schmitt J.H.M.M., Golub L., Harnden F.R. Jr., Rosner R., 1986, ApJ, 300, 360

Maoz E., Grindlay J.E., 1995, ApJ, 444, 183

Masai K., 1994, Jour. Quan. Spec. & Rad. Trans. 51, 211

Maxson C.W., Vaiana G.S., 1977, ApJ, 215, 919

McGale P.A., Pye J.P., Hodgkin S.T., 1996, MNRAS, in press

Mewe R., 1991, A&AR, 3, 127

Mewe R., Gronenschild E.H.B.M., van den Oord G.H.J., 1985, A&AS, 65, 511

Micela G., Sciortino S., Vaiana G.S., Schmitt J.H.M.M., Stern R.A., Harnden F.R. Jr., Rosner R., 1988, ApJ, 325, 798

Motch C., Belloni T., Buckley D., et al., 1991, A&A, 246, 24

Motch C., Guillout P., Haberl F., Pakull M.W., Pietsch W., Reinsch K., 1996, A&A, in press

Pallavicini R., et al 1981, ApJ, 248, 279

Pallavicini R., Monsignori Fossi., Landini M., Schmitt J.H.M.M., 1988, A&A, 191, 109

Pallavicini R., Tagliaferri G., Stella L., 1990, A&A. 228, 403

Pan H.C., Jordan C., 1995, MNRAS, 272, 11

Paresce F., 1984. AJ, 89, 1022

Parker E.N., 1988, ApJ, 330, 474

Pfeffermann E., et al., 1986, Proc. SPIE, 733, 519

Pye J.P. Hodgkin S.T., Stern R.A., Stauffer J.R., 1994, MNRAS, 266.798

Radick R.R., Lockwood G.W., Baliunas S.L., 1990. Science, 4938, p. 39

Raymond J.C., 1988, in Pallavicini R., ed., Hot Thin Plasmas in Astrophysics. Kluwer. Dordrecht, p. 3

Raymond J.C., Smith B.W., 1977. ApJS, 35, 419

Reale F., Serio S., Peres G., 1993, A&A, 272, 486

Reeves E.M., 1976, Solar Phys., 46. 53

Rong-Xian Z., et al., 1992. IBVS 3772

Rosner R., 1980. in Dupree A.K., ed., Cool Stars Stellar Systems and the Sun. Smithson. Astron. Obs. Spec. Rep., No. 389. p. 79

Rosner R., Tucker, W.H., Vaiana G.S., 1978, ApJ, 220, 643

Rucinski D., Bzowski M., 1995, A&A, 296, 248

Schmitt J.H.M.M., 1991, IAU General Assembly Proceedings (August)

Schmitt J.H.M.M., 1996, A&A, in press

Schmitt J.H.M.M., Golub L., Harnden F.R. Jr., Maxson C.W., Rosner R., Vaiana G.S., 1985, ApJ, 290, 307

Schmitt J.H.M.M., Haisch B., Barwig H., ApJ, 1993, 419, 81

Sciortino S. et al. 1990, ApJ, 361, 621

Singh K.P., Drake S.A., White N.E., 1996, AJ, 6, 2415

Skumanich A., 1972, ApJ, 171, 565

Snowden S.L., Cox D.P., McCammon D., Sanders W.T., 1990, ApJ, 354, 211

Snowden S.L., Plucinsky P.P., Briel U., Hasinger G., Pfefferman E., 1992, ApJ, 393, 819

Stark A.A., Gammie C.F., Wilson R.W., Bally J., et al., 1992, ApJS, 79, 77

Stauffer J.R., Caillault J.P., Gagné M., Prosser C.F., Hartmann L.W., 1994, ApJS, 91, 625

Stern R.A., Antiochos S.K., Harnden F.R. Jr., 1986, ApJ, 305, 417

Stern R.A., Schmitt J.H.M.M., Kahabka P., 1995, ApJ, 448, 683

Stern R.A., Uchida Y., Tsuneta S., Nagase F., 1992, ApJ, 400, 321

Stern R.A., Underwood J.H., Antiochos S.K., 1983, ApJ, 264, L55

Stern R.A., Zolcinski M.C., Antiochos S.K., Underwood J.H., 1981, ApJ, 249, 647

Swank J.H., 1985, in The Origin of Nonradiative Heating/Momentum in Hot Stars. p. 86

Trümper J., 1983, Adv. Space Res., 2, 241

Tsuru T., Makashima K., Ohashi T., 1989, Pub. Astr. Soc. Japan, 41, 679

Tsuru T., Makashima K., Ohashi T., Sakao T., Pye J.P., et al., 1992, MNRAS, 225, 192

Ulmschneider P., 1991 in Ulmschneider P., Priest E., Rosner R., eds, Mechanisms of Chromospheric and Coronal Heating. Springer, Berlin, p. 328

Vaiana G.S., Reidy W.P., Zehnpfennig T., Van Speybroeck L., Giacconi R., 1968, Science, 161, 564

Vaiana G.S., Davis J.M., Giacconi R., Krieger A.S., Silk J.K., Timothy A.F., Zombeck M.V., 1973, ApJ, 185, L47

Vaiana G.S., 1990, in Elvis M., ed., Imaging X-ray Astronomy. CUP, p. 61

van den Oord G.H.J., Mewe R., 1988, A&A, 213, 245

Vilhu O., Heise J., 1986, ApJ, 311, 937

Vilhu O., Caillault J.P., Heise J., 1988, ApJ, 330,922

Walter F.M., Bowyer S., 1981, ApJ, 245, 671

Warwick R.S., Barber C.R., Hodgkin S.T., Pye J.P., 1993, MNRAS, 262, 289

Weiss N.O., 1993, in Linsky J.L., serio S., eds, Physics of Solar and Stellar Coronae: G.S. Vaiana Memorial Symposium. Kluwer, Dordrecht, P. 541

Westergaard N.J., Norgaard-Nielsen H.U., Hansen L., Jorgensen H.E., Rasmussen I.J., Schnopper H.W., 1985, in Cosmic X-ray Spectroscopy Mission. ESA SP-239

White N.E., 1995, ApJ, 445, 125

White N.E., Marshall F.E., 1983, ApJ, 268, L117

White N.E., Parmar A.N., Culhane J.L., Kellett B.J., Kahn S., 1986, ApJ, 301, 262

White N.E., Shafer R.A., Parmer A.N., Horne K., Culhane J.L., 1990, ApJ, 350, 776

Wilson O.C., 1978, ApJ, 226, 379

Wilson O.C., Woolley R., 1970, MNRAS, 148, 463

Withbroe G.L., 1981, in Solar Active Regions (Boulder, Colorado Assoc. University Press), p.199

Acknowledgements.

In producing any thesis, more than one person is usually involved. As such, I'd like to thank John Pye for his supervision and patience over the years. Thanks to Bob Warwick for early supervision and the initial offer of my place at Leicester, Ken Pounds for being an great head of department and Martin Ward who seems to have taken over admirably.

Thanks also to Geoff and Geoff for the almost continuously functioning computers, Simon Hodgkin for being the only other cool-stars student around, Julian Osborne for the ASCA help and Jeremy Ashley for the occasional Asterix patch.

To all those I've crossed paths and raised a glass with over the years, cheers. A thesis can be hard work and everybody needs friends to get them through. Notable among the motley crew I have called 'friends' have been, Fred, Kevin and Simon (for that pre-Leicester connection), Keith and Liz, John and Lisa (for being cosistantly couply, though amusingly not so for Keith and Liz by the time I got to do my corrections), Rowan (for numerous lunchtime chats), Matt (for always being ready for a night out) Tim (for looking like Elvis), Dennis (for being cool), Ian (although he works so hard he puts us to shame) and the younger boys, Gareth and Dobbie (for asking questions which allow us old guys to look smart).

To prove I have friends outside of work I'd also like to thank Christine (for being my one true love), Mike and Geoff (for comradeship at GM Hall), Roseanna (for mentioning me in her dissertation), Vicky (for becoming a trekkie), Kai and the gang of '96 for laughs aplenty, and the role-playing bunch for removing me from reality on a regular basis. Finally Christine (a different one... without whom I'd have finished the thesis much sooner), thanks for teaching me about determination. Rest in peace.